
Dissertation submitted in fulfilment of the requirements for the degree

## Master of Science in Engineering

Department of Mechanical Engineering

University of Cape Town

# INFLUENCE OF LASER SCAN RATE ON THE MECHANICAL PROPERTIES OF SLM Ti6Al4V ALLOY

Lehlomelo Matjelo

**October 2018**

# PLAGIARISM DECLARATION

I know the meaning of plagiarism and declare that all the work in the document, save for that which is properly acknowledged, is my own. This thesis/dissertation has been submitted to the Turn-it-in module (or equivalent similarity and originality checking software) and I confirm that my supervisor has seen my report and any concerns revealed by such have been resolved with my supervisor.

Signed by candidate

Lehlomelo Matjelo Raymond

October 2018

# ABSTRACT

The influence of laser scan speed on the resulting axial tensile, fracture toughness and fatigue crack growth rate (FCGR) properties has been investigated on samples produced by the selective laser melting (SLM) process from a Grade 5 Ti6Al4V metal powder; the laser scan speed was varied from 1.5 m/s to 4 m/s, while other process parameters were kept constant. Test procedures and specimens were designed in accordance with the ASTM E8/E8M, ASTM E399 and ASTM E647 standards and the corresponding microstructural characterisation carried out using optical microscopy in bright field mode. The bulk densities were investigated in line with ASTM B962-15 (Standard test method for density of compacted or sintered powder metallurgy (PM) products, using Archimedes' principle) and varied from 96% to near-100%.

The ultimate tensile strength (UTS) for the as-built SLM Ti6Al4V uniaxial tensile specimens ranged from 1007 MPa to 1333 MPa, with the total elongation at failure (ductility) ranging from 4% to 9%. Nevertheless, there was generally very poor correlation between scan rate, density and measured mechanical properties. Consequently, it was proposed that the form and distribution of porosity would be more likely suited to explaining the mechanical property data. This led to a second batch of samples being produced at 3 m/s and 4 m/s for the sole purpose of investigating the influence of pores on the mechanical properties for the now stress-relieved (650°C for 4 hours in vacuum, furnace cooled) SLM Ti6Al4V samples. The uniaxial tensile test, fracture toughness test and the 3-point bend fatigue crack initiation test results were studied in conjunction with the X-ray computed tomography scans (X-ray CT scans), which were done prior to testing, and fractography carried out using the secondary scanning electron microscope (SEM) images.

The UTS for the stress-relieved SLM Ti6Al4V dropped to a range of 1000 MPa – 1120 MPa, while the ductility for samples fabricated at 3 m/s was improved (7±3% to 12±2). Comparison across the 3-point bend fatigue test results for specimens fabricated at 3 m/s and 4 m/s indicated highly variable resistance to crack initiation.

The results and analysis for the as-built and stress-relieved SLM Ti6Al4V mechanical test specimens led to the conclusion that the scattered mechanical measurements observed in this project could be attributed to variable porosity in samples, which overshadowed any correlation to be made between the laser scan speed and the measured mechanical properties; severe porosity in mechanical specimens played a major role in their mechanical response.

# ACKNOWLEDGEMENTS

The following individuals, departments and companies are acknowledged for the crucial role they played during the course of this project:

- My supervisor, Prof. Robert Knutsen, for all his guidance and support.

- CSIR (NCL), through Danie Louw, for a brief introduction into the additive manufacturing technology (SLM) and for producing my test specimens.

- The financial assistance provided by the Department of Science and Technology through the CPAM programme.

- The financial assistance of the National Research Foundation (NRF) towards this research is hereby acknowledged. Opinions expressed, and conclusions arrived at are those of the author and are not necessarily to be attributed to the NRF

- CME personnel help and support during my lab work:
  - Penny Louw
  - Soraya Von Willingh
  - Richard Curry

- Workshop personnel for their endless help in the machining of samples:
  - Pierre Smith
  - Dillon Jacobs

- The UCT Electron Microscope Unit (EMU) for their help and my introduction to the Nano SEM machine.

- Stellenbosch University, CT scanner Facility (Department of Forestry), for help with the X-ray-computed tomography scans and results analysis.

- Friends and family for their support; most especially to my mother and girlfriend for all their prayers and support and for always being there for me.

# TABLE OF CONTENTS

# LIST OF FIGURES

# LIST OF TABLES

# 1. INTRODUCTION

Titanium exists in two types of crystal structures, the hexagonal close-packed (HCP) structure, termed α-phase, and the body-centred cubic (BCC) structure, termed β – phase. This allows titanium to offer quite a variety of alloys with distinct characteristics through alloying elements or heat treatment processes. Within this wide range of titanium alloys is the Ti6Al4V alloy, which was developed in the early 1950s, specifically for aerospace applications, because of its high specific strength, corrosion resistance and low specific weight [1,2].

The traditional processing methods, like casting, incur significant manufacturing expenses, as complex and special moulds need to be made. Furthermore, the Ti6Al4V alloy has an oxidation problem and casting needs to be carried out under a controlled environment. In addition, grain growth is more prone in casting, owing to the high temperature holding time involved during the process [2]. For these reasons, various methods need to be devised to reduce the manufacturing costs and also the machining time of Ti6Al4V alloy products and these include the additive manufacturing technique.

The additive manufacturing techniques, the selective laser melting (SLM) process in this case, are characterised by extreme localised heat inputs in short time intervals and this has a direct and significant influence on the resulting microstructure [3]. The product during the SLM is formed by selectively melting layer upon layer of powder (Ti6Al4V powder) of a predetermined thickness by exposure to a thermal laser beam. The powder is heated and melted with sufficient laser power for a liquid pool to be formed, which, upon rapid cooling, solidifies, whereupon the material starts to form a product profile.

At the end of a single cross-sectional scan of a powder layer with the laser beam, the build platform is lowered by a predetermined layer thickness and a new layer of powder is deposited for scanning. This process is repeated until the full product is completed.

In most instances, the preferred scan rate for producing Ti6Al4V components by selective laser melting (additive manufacturing) is of the order of 0.2 m/s – 1.6 m/s [4,5,6]. This scan rate

provides the optimum window for obtaining the lowest porosity and good mechanical properties that are comparable with wrought metal components. However, the situation is more complex in that scan rate is not an isolated variable and hence energy density is also considered, which takes into account scan rate and laser power. Consequently, it may be possible to scan at higher rates by moderating the power input to obtain the optimum energy density for developing good microstructural integrity. Furthermore, variation in process parameters can have a proportional influence on the microstructure and density of the final part, which will result in distinct mechanical properties. In this regard, the advantages of the SLM process can be recognised only if the mechanical properties of the final part compete with or match the mechanical properties produced when using conventional methods.

Therefore, the aim of this project is to investigate and characterise the influence of laser scanning speed on the mechanical properties and the corresponding microstructure of the Ti6Al4V alloy, as produced by the selective laser melting (SLM) process. This involves carrying out mechanical tests, such as tensile and fracture toughness tests as well as the fatigue crack growth rate test, on the as-built SLM Ti6Al4V alloys. Investigation on the influence of post-build heat treatments (stress relief annealing) on the mechanical properties with reference to the wrought or cast titanium alloys will also be carried out.

The report presents the mechanical tests carried out to achieve the set project objectives and the corresponding microstructural evolution, owing to the different laser scanning speeds employed. The microstructural evolution is investigated using the optical microscope in bright field mode to identify the effect of the post heat treatment processes employed on the mechanical properties, such as the stress relief anneal carried within the $\alpha + \beta$ region. The secondary electron SEM images are used to investigate failure modes on the surfaces of the fractures for the tensile and fracture toughness specimens.

Therefore, the project was broken down into the following set objectives:

1. To perform the following mechanical tests on samples machined to comply with the ASTM standards:
    i. Tensile testing (ASTM E8/8M)
    ii. Fatigue strength testing (ASTM E399)
    iii. Fatigue crack growth rate (ASTM E647)

2. To carry out stress relief annealing at 650°C for approximately four hours.
3. To perform a microstructural evolution investigation to draw comparisons between the as-built and the heat treated samples.
4. To investigate and characterise porosity in all the samples.
5. To perform mechanical tests on the heat-treated samples and comment on any changes that are observed in the properties.
6. To attempt to establish correlation between scan rate, heat treatment, density and porosity distribution, and measured mechanical properties.

The report is structured to address the above objectives as follows:

- Chapter 2 presents the literature surveyed on past research that is relevant to the task at hand.
- Chapter 3 describes the experimental apparatus and procedures used.
- Chapter 4 summarises the experimental results for the mechanical tests carried out and further characterises the role of microstructural integrity on the mechanical properties observed.
- Chapter 5 provides an in-depth analysis of the results presented in Chapters 4.
- Chapter 6 concludes the findings in the project, and
- Chapter 7 presents recommendations based on the findings and the conclusions drawn.

# 2. LITERATURE REVIEW

## 2.1. INTRODUCTION TO THE ADDITIVE MANUFACTURING TECHNIQUE

The additive manufacturing technique, as defined by the ASTM standards, is said to be "a process of joining materials to make objects from 3D (three-dimensional) model data, usually layer upon layer, as opposed to subtractive manufacturing methodologies" [7]. The additive manufacturing technique is among the most studied processes [3, 8 - 20] as it provides low cost production of components made from relatively expensive materials, such as titanium alloys.

Moreover, additive manufacturing aims at zero waste manufacturing by producing near net-shape components to reduce extensive machining [11, 12]. The additive manufacturing technique offers several other advantages, such as the ability to manufacture almost any regular open porous structure with high repeatability, giving full design freedom and hence total control over the mechanical properties and geometrical properties [8, 10]. Nevertheless, there are still challenges in the process, which include the chemistry control during melting, solidification cracking and contamination issues [21].

## 2.2. ADDITIVE MANUFACTURING TECHNIQUES

There are several additive manufacturing techniques that can produce complex shapes; these are generally classified according to the feeding technique and the thermal energy source. The main techniques are the powder bed, blown powder and the wire feed and all these use a thermal energy source supplied either by an electron beam, a laser or an electric arc [11]. The powder bed fusion process is commonly used in selective laser melting (SLM) and electron beam melting (EBM), while the blown powder technique is used in laser metal deposition (LMD) or the laser cladding (CLAD) techniques.

### 2.2.1. Selective laser melting (SLM)

The selective laser melting (SLM) process is an additive manufacturing technique through which components are built layer by layer by selectively melting the powder with a focused laser beam. This process involves localised high heat inputs that lead to steep thermal gradients, rapid solidification and fast cooling [20, 4]. Figure 1 depicts the schematic representation of the SLM process apparatus.

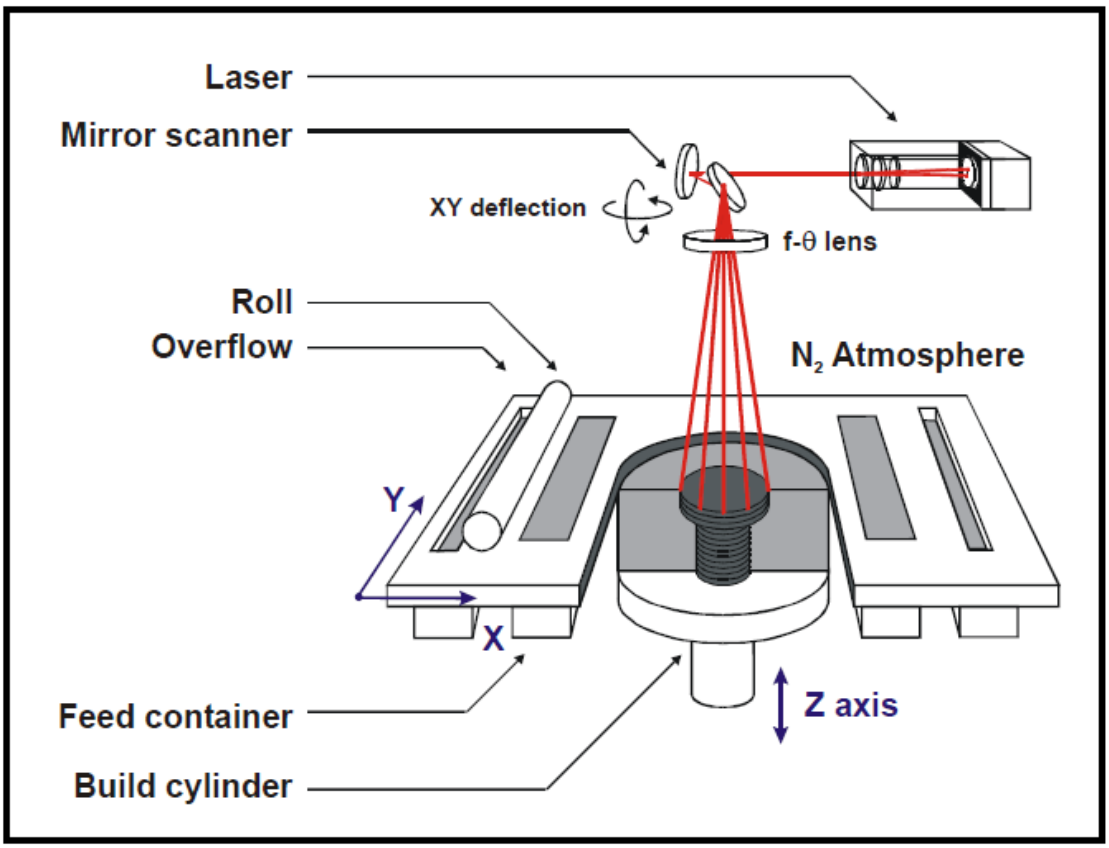


**Figure 1: The schematic diagram of the SLM process [3, 22, 23]**

The SLM machine incorporates a computer-aided drawing (CAD) software model, used to send signals to a laser scanner, which consolidates the predetermined profile by selectively melting a layer of metal powder using the thermal energy supplied by the focused laser beam and direction control by the deflection lenses. Each successive layer of powder, generally between 20 to 150 µm, is deposited on the movable platform (which has the degree of freedom in the *z* direction to facilitate powder layer deposition), using either a roller or scraper [23]. The process is carried out in a controlled environment containing either Argon (Ar) or Nitrogen ($N_2$) and the type of laser power used depends also on the type of commercial machine used [23].

The SLM process has advantages over the conventional production techniques as it offers fewer production steps and near net shape production, as well as high material use efficiency during production. Furthermore, owing to its layer by layer built nature, SLM enables the production of parts with complex geometries. However, non-optimal scan parameters may cause melt pool instabilities during the process, which can result in increased porosity and an undesirable surface finish [4].

### 2.2.2. Electron beam melting (EBM)

The electron beam melting process (EBM) is an additive manufacturing technique through which 3D components are fabricated layer by layer to near net shaped parts, directly from computer models [9]. Figure 2 is a schematic representation of the EBM machine.

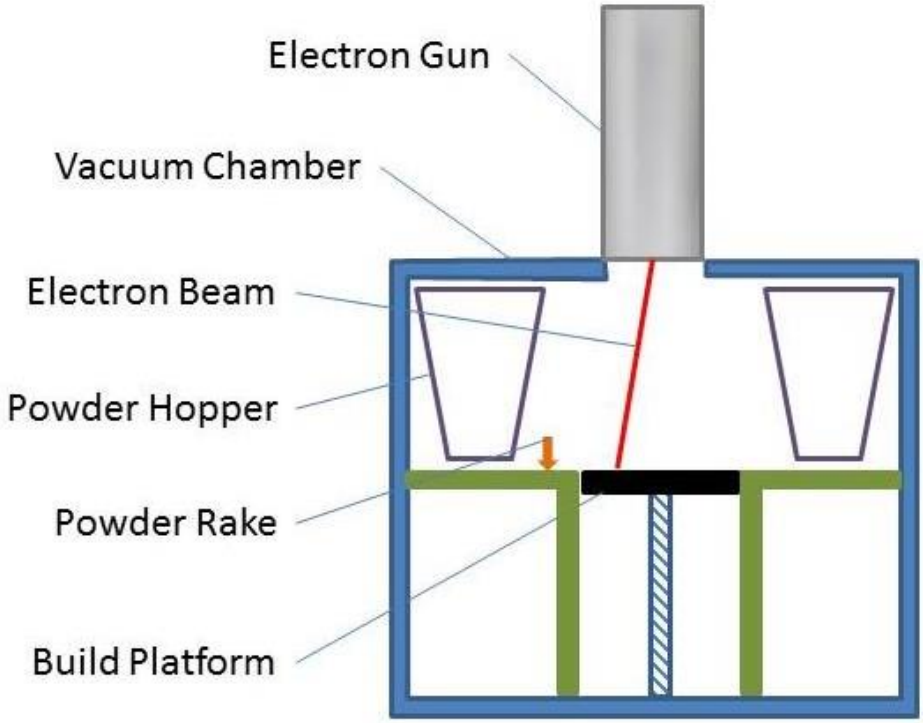


**Figure 2: The schematic diagram of the EBM process [24]**

Components with complex geometries are fabricated by the EBM process through consecutive cycles, layer after layer. The layering process is the same as the SLM, but the source of thermal energy used for melting is an electron beam emitted from a tungsten filament. The beam is controlled by two magnetic coils, whose major input is to control the beam's position and diameter.

Work by Gong *et al*. [25] showed that Ti6Al4V samples produced by both the EBM and SLM techniques had comparable fatigue strengths, hardness and ductility. However, SLM samples showed higher yield and tensile strengths than those produced using EBM, where lower temperature gradients were involved, the powder bed being maintained at 675° C. This was due to the predominant presence of martensitic α' microstructure, caused by higher temperature gradients in the SLM process.

## 2.3. THE SLM PROCESSING PARAMETERS

Yadroitsev and Smurov [15, 16] studied different processing parameters, such as the effects of the scanning speed, the powder layer thickness and the laser power. In both studies, it was reported that by using the optimal processing parameters, together with proper scanning strategies, components with mechanical properties close to those produced using wrought materials could be produced. This further suggested that different SLM process parameters could have a substantial influence on the resulting microstructure, the surface roughness and the density, which in turn would have a direct impact on the mechanical characteristics of the SLM Ti6Al4V product [3]. As an example, Zhang *et al*. [26] observed that increasing the hatch spacing (gap between two successive scan lines) reduced the Young's modulus of the SLM Ti6Al4V alloys, while the material's porosity increased.

### 2.3.1. Effects of SLM scanning strategy

Different scanning strategies can result in different microstructure and surface finish, as melt pool boundaries introduced during the SLM process may introduce unwanted anisotropic properties into the finished part [14, 15, 27].

The scanning strategy has a significant influence on the direction of elongated columnar grains formed and the local heat dissipation during the SLM process [3]. Figure 3 illustrates the different scanning strategies that can be employed during the SLM process, namely the zigzag, unidirectional and the cross-hatching laser scan strategies.

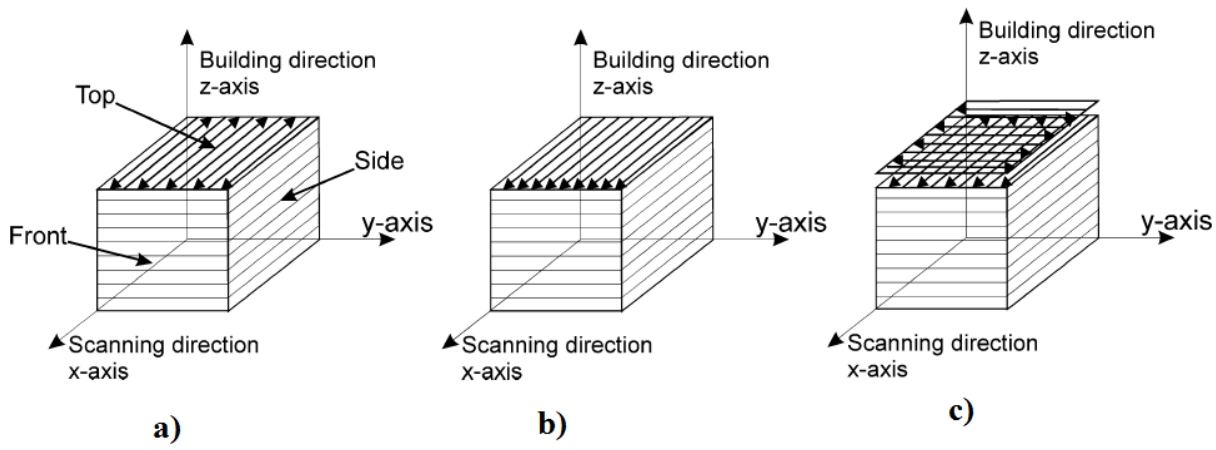


**Figure 3: Scanning strategies: a) Zigzag; b) unidirectional; c) cross – hatching [3].**

Yadroitsev *et al*. [15] investigated two distinct scanning strategies to determine their influence on the resulting microstructure of the SLM Ti6Al4V alloy produced, as shown in Figure 4.

Figure 4(a) shows the two scanning strategies used. For Strategy A, each powder layer is processed twice by the laser beam. The second laser beam is passed between the previously melted tracks of the same layer and by so doing re-melts the two neighbouring tracks. The second strategy (Strategy B) is meant to minimise the influence of the heat-affected zone (HAZ). In this case, the second layer is scanned with a shift from laser scan lines on the previous layer, as shown schematically in Figure 4(a).

Figure 4(b) depicts the corresponding micrographs of the two scanning strategies. There is no significant difference between the two micrographs. The white arrows on Figure 4(b) indicate the melt pool boundaries of tracks, with strategy B showing more melt pool boundaries than strategy A.

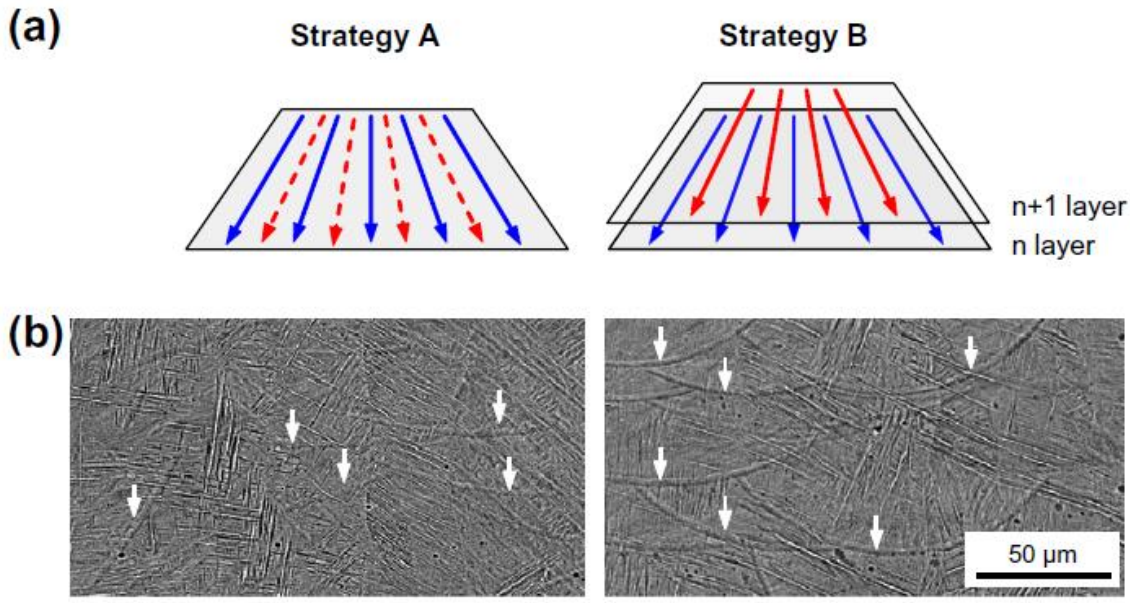


**Figure 4: SLM scanning strategies: a) Scanning strategies; b) Resulting SEM micrographs [15]**

On the other hand, Van Hooreweder *et al*. [26] used the island scanning strategy and sub-optimum parameters to show the effect on the resulting microstructural defects. In this scanning strategy, small distinct islands were scanned at various directions in a single layer, to eradicate the residual strain effect on the final product.

Figure 5(a) shows the resulting microstructure of the island scanned sample and clearly reveals pores aligned in a particular direction, which could be due to inferior or inadequate melting, caused by the overlapping between the islands. Figure 5(b) further illustrates the microstructure of the SLM Ti6Al4V alloy, produced using sub-optimum scanning parameters. In this case, process parameters, apart from those specified for the SLM machine, were employed, which

resulted in a considerable number of pores, leading to the material being more prone to fatigue crack initiation and rapid propagation.

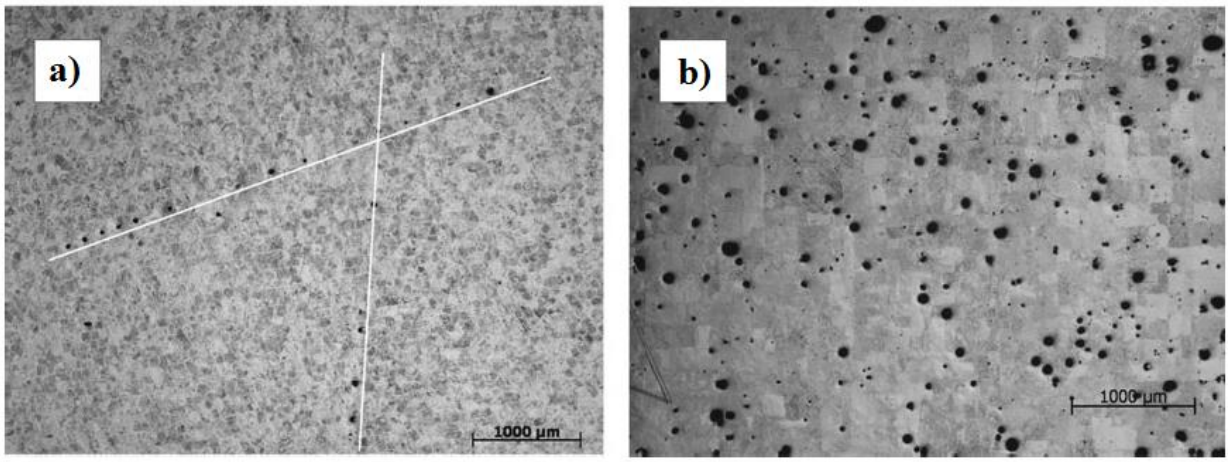


**Figure 5: Pores in SLM Ti6Al4V: a) Island scanned; b) sub-optimum parameters [26]**

### 2.3.2. Effects of the scanning speed and the laser power

The scanning speed has an inversely proportional influence on the energy density, which is defined as the average applied energy per volume of material during a single layer scanning of the material [3]. This is governed by the equation:

$$\mathrm{E} = \frac{P}{v \times h \times \mathrm{t}}$$ **(Equation 1: The energy density equation [3,28])**

where $E$ is the energy density ($J/m^3$), $P$ is the power ($J.s^{-1}$), $v$ is the scanning speed (m/s), $h$ is the hatch spacing ($m$) and $t$ is the layer thickness ($m$).

Thijs *et al*. [3] compared the influence of the laser scanning speed on the resulting microstructures of SLM Ti6Al4V alloys from 0.02 m/s to 0.005 m/s, where the power, hatch spacing, and the layer thickness were kept constant. The irregular scan tracks observed suggested that the melt pool was less stable at extremely low laser scan rates (0.005 m/s) and resulted in microstructural coarsening more significant than that at higher laser scan rates.

Song *et al*. [2] investigated the effects of processing parameters on the mechanical properties and the corresponding microstructure. It was reported that the densification and the microstructure of the SLM Ti6Al4V alloys were strongly influenced by the laser scanning speed and the laser power.

Figure 6 depicts the 27 single track set process parameters employed by Song *et al*. [2]. The second zone (Zone II) was reported to have yielded the optimum results. Examples of the corresponding microstructures observed for Zones I, II and III are shown in Figure 7 (a – c).

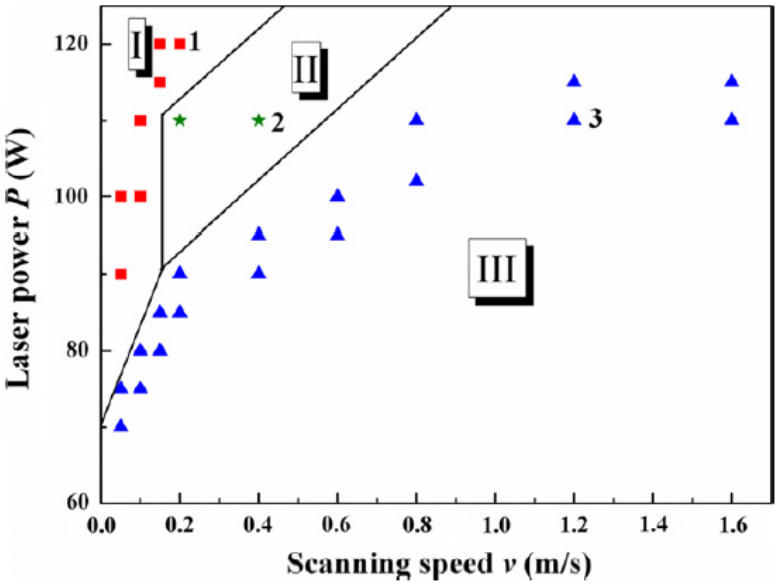


**Figure 6: Mechanisms of single tracks for SLM Ti6Al4V [2].**

Figure 7(a) signifies a high energy input zone (Zone I in Figure 6) with a relatively low scanning speed. The single track was completely melted, owing to the high energy applied, but this resulted in considerable residual stresses, leading to visible fractures. Figure 7(b) depicts a lower laser power with a higher scanning speed (110 W, 0.4 m/s, compared to 120 W, 0.2 m/s). A continuous track was achieved with no visible residual cracks and fewer pores (Zone II in Figure 6). Lastly, Figure 7(c) shows that the higher scanning speed employed limited the energy interaction with the Ti6Al4V powder and resulted in partial melting with a honeycomb-like morphology (Zone III in Figure 6).

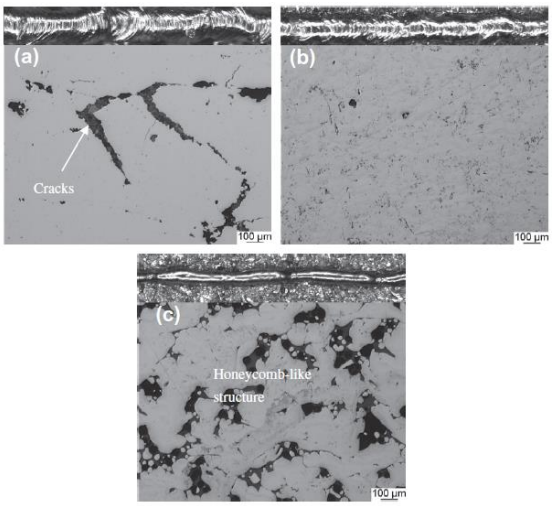


**Figure 7: micrographs of single tracks (top insert) and cross-sectional Ti6Al4V parts produced by different processing parameters: (a) 120 W, 0.2 m/s; (b) 110 W, 0.4 m/s; (c) 110 W, 1.2 m/s [2].**

Work done by Song *et al*. [2] is consistent with the observation by Gong *et al*. [29], who reported on several SLM Ti6Al4V samples that were produced at different process parameter settings with the laser scan speed and the laser power being varied one at a time. The process parameters in this study [29] were believed to yield a specific pore morphology characterisation, as summarised in Figure 8.

According to Figure 8, there exist distinct porosity mechanisms, owing to parameter settings, that generate different defects in SLM Ti6Al4V alloys. This process window has four melting zones: Zone I, which represents a fully dense SLM Ti6Al4V alloy, Zone II, which represents over melting, Zone III, which corresponds to incomplete melting, and Zone IV (OH), which corresponds to overheating (See Section 2.5 for a more detailed account of the defect evolution.).

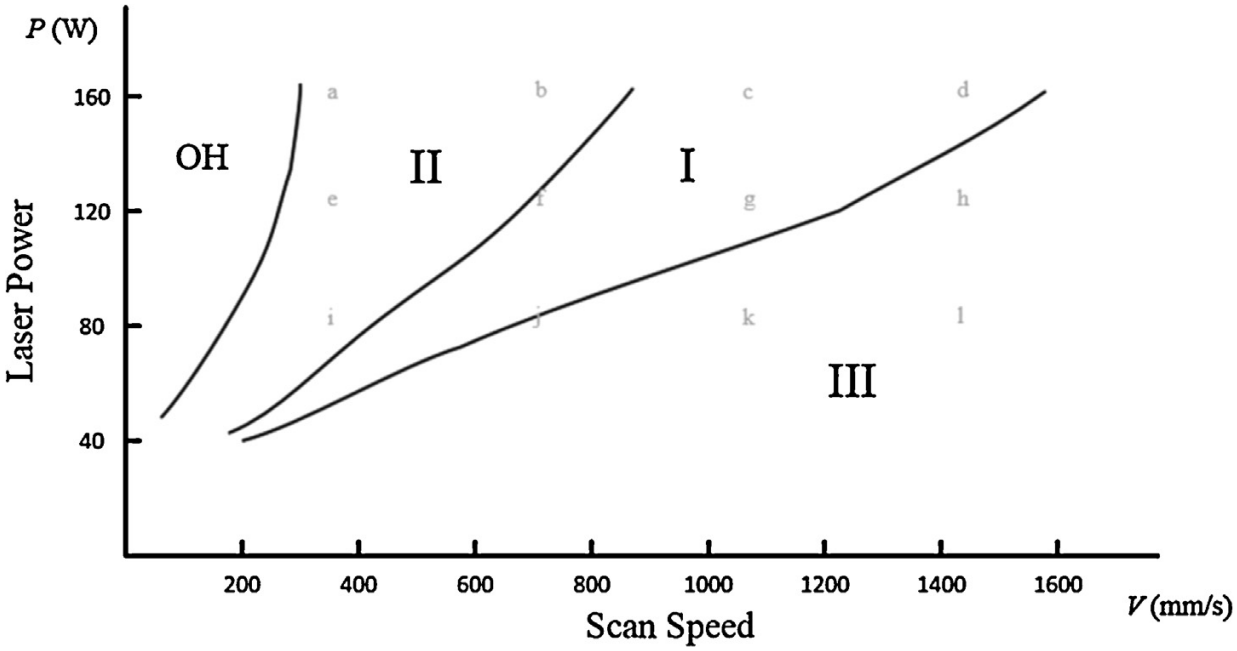


**Figure 8: Process window for Ti6Al4V [29]**

Bartolomeu *et al*. [28] also investigated the influence of the scanning speed, the laser power and the hatch spacing on the resulting strength and density of the SLM Ti6Al4V alloy. The model observed suggested that increasing the energy density by varying the laser scan rate while other parameters were kept constant resulted in higher shear strength, hardness and density. On the other hand, further increase in laser scan rate resulted in lower values of shear strength, hardness and density, with other parameters kept constant. This correlates well with the work of Sun *et al*. [30], who observed that the density increased with increasing energy density until it reached some optimum value then dropped again. Perhaps the reason for this

was that there was no linear relationship between the available supplied energy density and the resulting densification, as shown by Song *et al*. [2] and Gong *et al*. [29].

Kasperovich *et al*. [31] investigated the relationship between a range of process parameters and the resulting pore morphologies. A particular effect was observed as the laser power and laser scan speed were varied while the other parameters were held constant and the results are as shown in Figure 9.

Figure 9 indicates two SLM process parameters that influence the porosity of the SLM Ti6Al4V alloy. Figure 9(a) suggests there is a significantly large amount of energy density at lower laser scan speeds and high laser power, which results in high porosity. This reduces as the laser scan speed is increased, with a corresponding decrease in energy density, resulting in optimum process parameters (laser scan speed of 0.5 m/s, with constant laser power and hatch spacing of 175 W and 100 µm, respectively) that yield the least porosity. Further increase in laser scan speed results in less energy density and melt pool overlap is not effective, which results in elongated pores. Figure 9(b) shows that power fluctuation between 100 W and 110 W at 100 µm hatch spacing and 0.6 m/s laser scan speed yield considerable porosity. Nevertheless, a wide window is provided, with low sensitivity to variation between 120 W and 190 W.

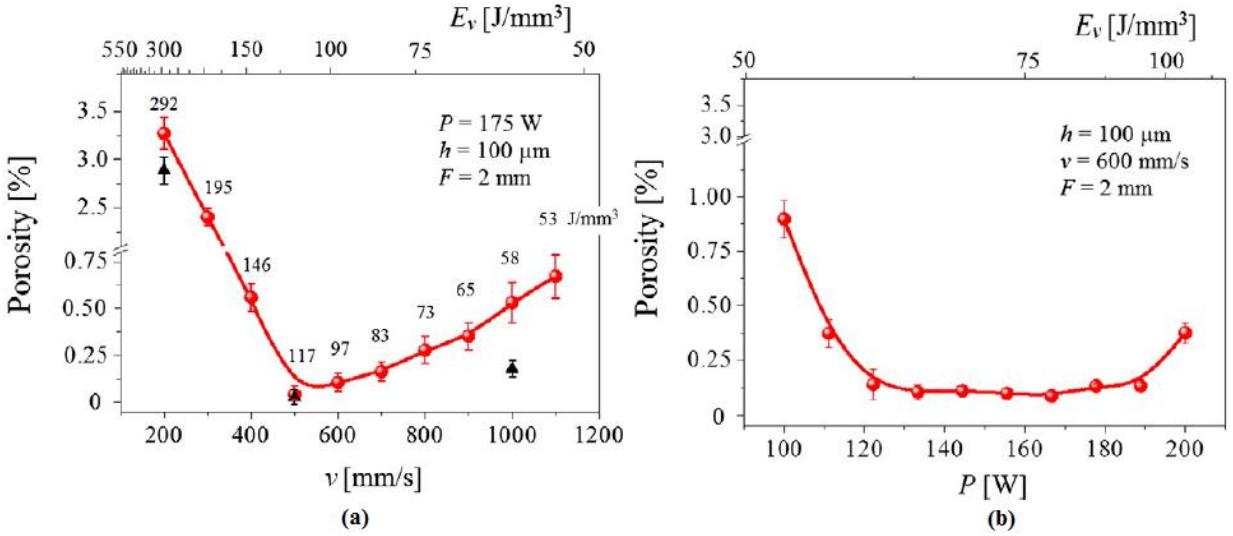


**Figure 9: Influence of process parameters on porosity: (a) Scanning speed; (b) laser power [31]**

It should be noted that, generally, similar energy densities can be achieved by various SLM process parameter combinations and their effects behave in a non-predictive manner. Therefore, a comparison according to the energy density is highly unreliable and misleading [31, 32]. On the other hand, the available energy density has been found to be the main contributor in powder layer melting, the laser scan rate and the laser power being the main contributors [33]. Ferrar *et al*. [34] reported that the method in which the inert gas was delivered across the build platform could influence the reproducibility of products across the

build area. This suggested that there were many process parameters that contributed to the optimum SLM process, in addition to the available energy density.

## 2.4. EFFECTS OF SLM ON Ti6Al4V PRODUCTS

Vrancken *et al*. [4] investigated the effect of several heat treatments on the microstructure and the mechanical properties of SLM Ti6Al4V alloys. The study revealed that the process resulted in a crystallographic texture, which can be attributed to different build directions. This further influenced the mechanical properties as the textures would be aligned in a certain direction if no post heat treatment were carried out. Thijs *et al*. [3] further observed specific microstructures on the parts produced by the SLM process, owing to the high temperature gradients involved, hence resulting in strong crystallographic textures that had a direct and significant influence on the mechanical properties. Furthermore, although the additive manufacturing technique provided higher quality net-shape components, with complex geometries [10, 4], there was a major challenge with respect to residual stresses generated during the fabrication process, which gave rise to unacceptable mechanical properties [10,20].

### 2.4.1. The mechanical properties

Vrancken *et al*. [20] and Cain *et al*. [17] both observed the anisotropic behaviour upon investigation of the fatigue crack growth rate of SLM Ti6Al4V samples, carried out in different orientations with reference to the build direction. Edwards and Ramulu [5] also observed anisotropic behaviour in fatigue performance on their samples, even though a systematic multi-directional scanning strategy was used, whereby the laser direction was rotated 65° at each layer. It was believed that this would reduce the residual stresses, as well as the anisotropic properties, owing to the crystallographic texture. Work by Van Hooreweder *et al*. [26] revealed that the resulting microstructure from the SLM process was the key controller of the mechanical properties (fracture toughness and the fatigue crack growth rate properties) of the SLM Ti6Al4V samples, as all samples produced were closer to the density of the bulk titanium products (99.73±0.036%).

The crystallographic textures inherent in the SLM process are not the only challenges facing the powder metallurgy (additive manufacturing) industry. In recent studies, densification of the final SLM part has been shown to be a major concern. Murr *et al*. [19] and Gong *et al*. [25] reported that the density of the part produced by the SLM was critical for titanium alloys, since the porosity of such parts had a detrimental effect on the mechanical properties.

Further research on the effects of pores (less dense SLM products) on the mechanical integrity of SLM products revealed that their presence was detrimental to the mechanical properties of

the SLM part. As an example, Facchini *et al*. [35] observed low ductility in SLM products, which was attributed to the martensitic morphology, the residual stresses, as well as to the presence of micro cracks and pores, within the SLM specimens.

### 2.4.2. The resulting microstructure

Solidification of Ti6Al4V produced through the SLM process occurs in epitaxial growth, meaning the melt solidifies with the same crystal orientation as the solute substrate [8,26]. Furthermore, since the melting of the metal powder occurs layer by layer, hence forming minute melt pools that rapidly solidify, the resulting microstructure is unique, with directional growth features that are far from thermodynamic equilibrium [14].

Figure 10 depicts the as-built micrographs that Vrancken *et al*. [4] observed when investigating the mechanical and microstructural evolution of SLM Ti6Al4V products that had been exposed to different heat treatments. The island scanning strategy used resulted in a chessboard pattern, as shown in Figure 10(a), while Figure 10(b) reveals long columnar grains at low magnification and oriented in the building direction, as indicated by the arrow, and the primary β grains, which grow epitaxially owing to successive layer deposition during the SLM process [4].

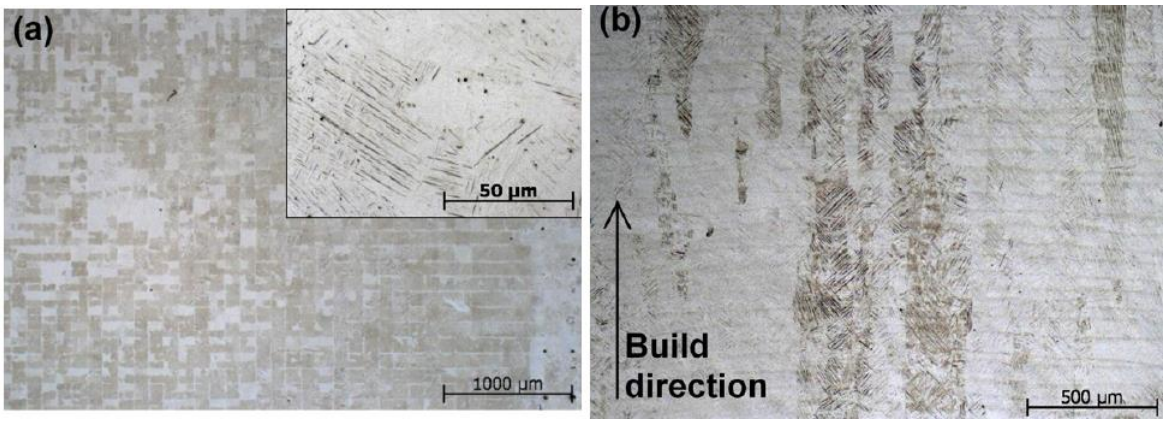


**Figure 10: SLM Ti6Al4V products micrographs taken: a) Perpendicular; b) parallel to with respect to the build direction [4].**

## 2.5. DEFECTS INCURRED BY THE SLM TI6AL4V ALLOY PROCESSING

The properties of the final SLM product highly depends on the in-layer scan strategy and the successive layer-to-layer properties [16]. Further to this, the SLM process is prone to process instabilities, owing to non-optimum process parameters, which result in near nominal density products [21] with some porosity due to entrapped gas bubbles or unmolten particles. Porosity is a crucial quality indicator in metal additive manufacturing technology [31,36].

Gong *et al*. [25] reported that the morphology of pores present in SLM Ti6Al4V products had a direct correlation with the amount of energy density supplied. The spherical pores were due to entrapped gas from local overheating, while the irregular and elongated pores could have arisen from unmelted particles, owing to insufficient fusion. Furthermore, the pore's location and distribution gave an indication of the process conditions. To further understand the role of different process parameter settings on the nature and morphology of defects in SLM Ti6Al4V alloy samples, Gong *et al*. [29] varied both the laser power and the laser scan speed, one at a time, and studied the morphology of pores formed. They further hypothesised that the generated defect could be caused by one of the following phenomena:

1. **Material vaporisation**: This is due to a high laser energy density being applied to the melt pool, causing gas bubbles and resulting in spherical defects. The vaporisation of a low melting point constituent within the Ti6Al4V powder normally takes place at the bottom of a melt pool and, since the process is associated with a high solidification rate, the gas bubbles get entrapped inside the substrate material as an inclusion, as indicated in Figure 11 [29,6].

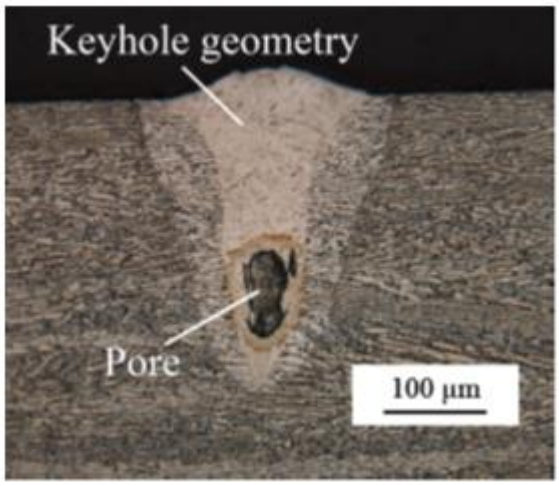


**Figure 11: Material vaporisation phenomena [29]**

2. **Mass transfer phenomena**: The intense laser energy also generates excessive thermal energy that evaporates molten material to the top surface. This further generates recoil pressure, which sometimes leads to the molten material being ejected and solidifying rapidly at the surface and partially welded to the melt pool as a spherical particle (satellite phenomena). The partially-welded particles remain on the surface and those larger than the layer thickness will be removed by the recoating blade, which will result in surface pits being left behind, as shown in Figure 12 [29,37].

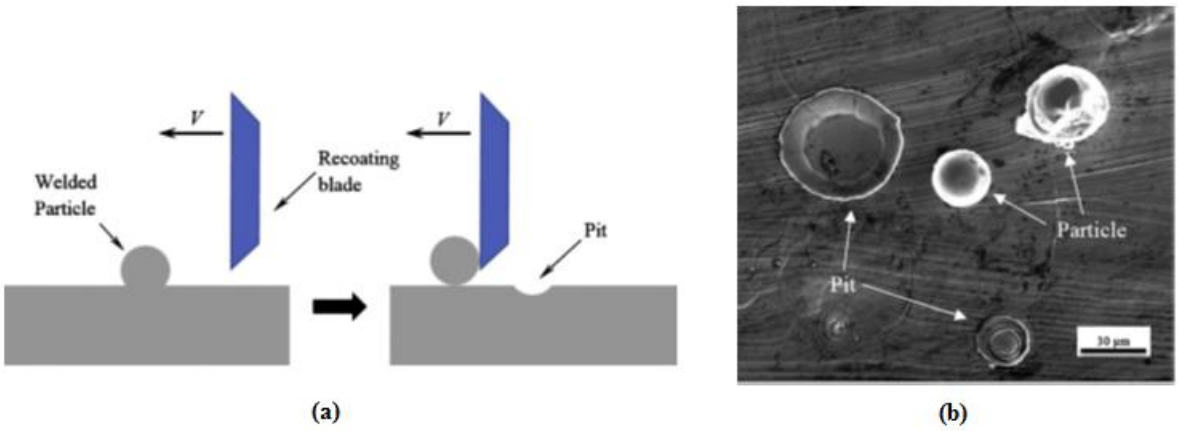


**Figure 12: Surface pits formation on SLM Ti6Al4V alloy: (a) Schematic; (b) SEM image [29]**

3. **Melt pool discontinuity**: The lack of melt pool overlap is the primary cause of porosity defects associated with lower energy densities or large hatch spacing. This lack of overlap results in poor wetting and thermal conduction of the melt pool, which further results in insulation of the previous layer by unmelted powder particles and promotes surface tension phenomena prone to the formation of voids and pores. This effect is illustrated in Figure 13.

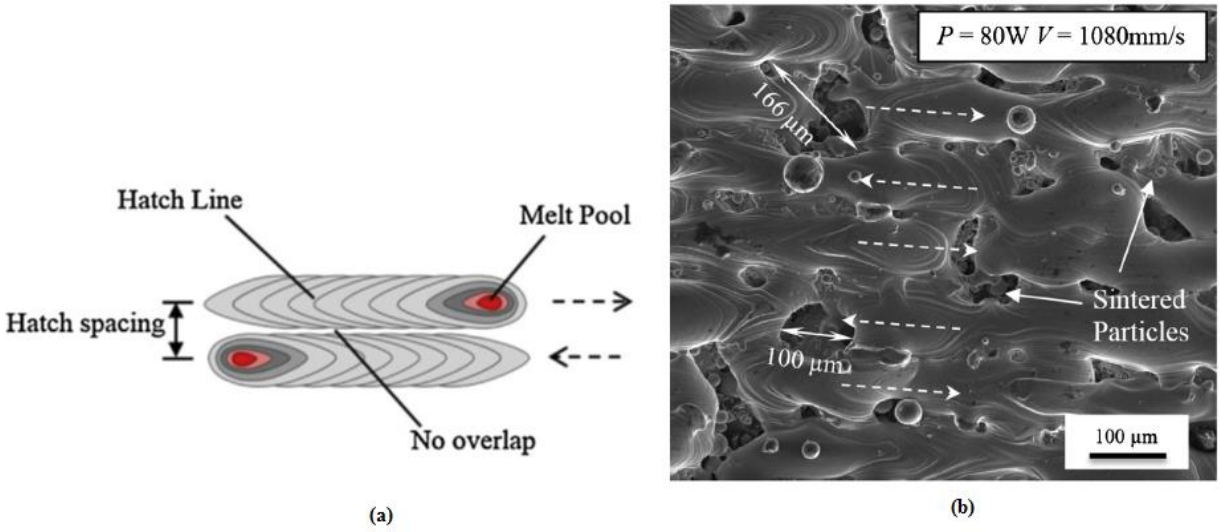


**Figure 13: Melt pool discontinuity: (a) poor melt pool overlap; (b) Resulting microstructure (dotted arrows indicates scan directions) [29].**

4. **Process instability**: At times, the manufacturing process itself can experience malfunctions or the raw material may exhibit inferior properties. In the first case, the instability in laser power may aggravate the melting problem, especially if the fluctuation is significantly large, leading to poor penetration depth and therefore resulting in unmelted powder particles entrapped under the melt pool [6]. Moreover, the surface and microstructural integrity of SLM

parts can be improved by increasing the inert gas flow across the build chamber to help remove excess process fumes and fine powders from the substrate [34].

Work by Xia *et al*. [38] showed that the increase in laser scan speed, with other parameters kept constant, introduced undesirable defects, like pores and unfused particles. In this case, the laser scan speed was varied from 0.2 m/s to 0.5 m/s. The observation is shown in Figure 14.

Figure 14 shows the pore morphologies of the SLM Inconel 718 super-alloy, processed at laser scan rates from 0.2 m/s to 0.5 m/s. The morphology in Figure 14(a) represents the microstructural outcome when the laser scan speed was lowest (0.2 m/s) and indicates only minor defects that occurred during fabrication (metallurgical porosity, which can be attributed to the high energy density delivered, which results in entrapped gases within the molten pool). Increasing the laser scan speed to 0.3 m/s (Figure 14(b)) resulted in more process pore defects (open porosity, owing to low energy density, hence a lack of melt pool overlap) being introduced into the final microstructure. Further increasing the laser scan speed to 0.4 m/s saw an escalating incidence of open porosity and of the formation of satellites and balling phenomena. Finally, increasing the laser scan speed to 0.5 m/s resulted in more unfused powder particles and open porosities were observed on a larger scale.

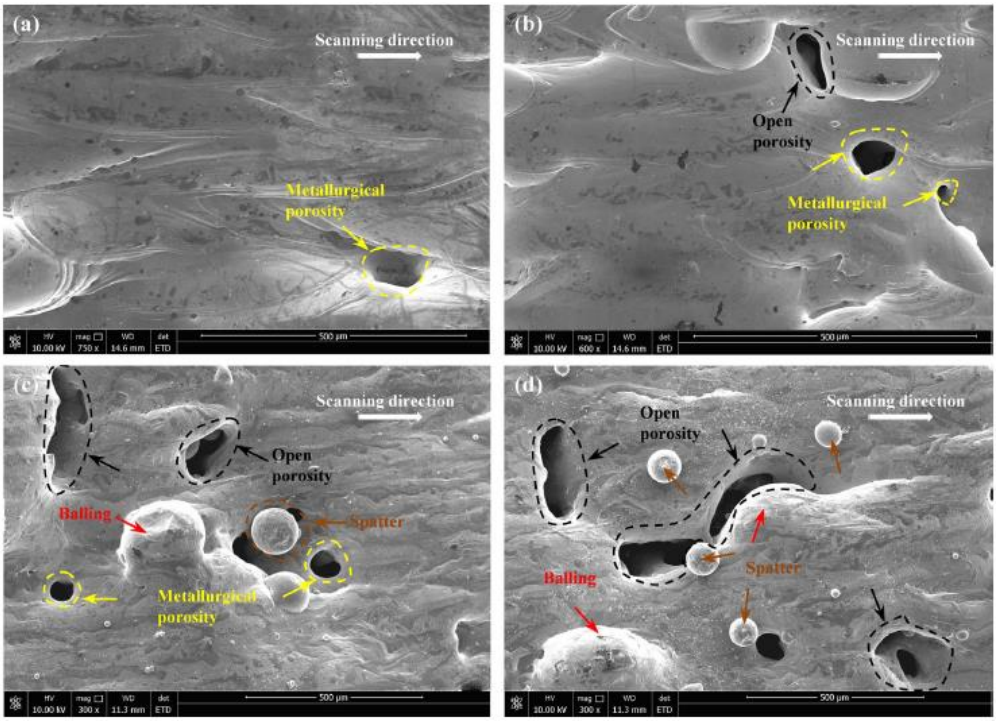


**Figure 14: Field emission SEM images of SLM Inconel 718 super-alloy fabricated at: (a) 0.2 m/s; (b) 0.3 m/s; (c) 0.4 m/s; (d) 0.5 m/s [38].**

It is apparent from Figure 14 that the scanning speed has a direct influence on the nature of defects within the SLM fabricated product, with more defects being present at higher laser scan speeds. This is because high laser scan rates (hence lower available energy density) tend to increase the capillary instability within the melt pool, which results in small liquid droplets being splashed to the surface, as reported by Kruth *et al*. [37]. Moreover, this will decrease the operating temperature within the molten pool and subsequently the viscosity of the molten flow will increase, which leads to improper wetting.

Figure 15 indicates two types of SLM process pore morphologies. Figure 15(a) shows the spherical gas pores and the balling effect, as well as the satellite formation. Figure 15(b) shows the non-sintered zone. The spherical pores are due to one of the following: to the entrapped inert gas, to metal gas evaporation owing to high laser power or to solidification of the inert gas dissolved in liquid melt and released on solidification. On the other hand, the balling effect and the satellite formation are due to insufficient fusion, as presented earlier in this section [9,29,37].

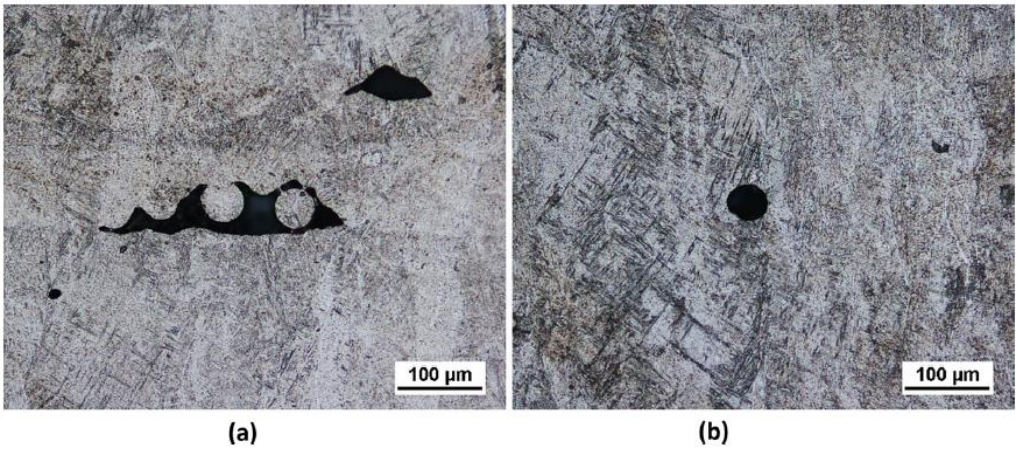


**Figure 15: SLM process defects: (a) gas pores; (b) non-sintered area or delamination [9].**

Gu *et al*. [39] varied the laser scan rate from 0.1 m/s to 0.4 m/s while other parameters were held constant. The final resultant microstructures of the pure titanium were found to depend on the process parameters employed, as shown in Figure 16.

Figure 16(a) shows narrow micro-cracks produced at low laser scan speed (higher energy density) between layers and these could be thermal cracks, owing to the residual thermal stresses as a result of rapid shrinkage during densification once the powder is fully molten [39]. Increasing the scan speed from 0.2 m/s to 0.3 m/s (Figure 16(b) and Figure 16(c)) resulted in a transition from a stable solidification front to an uneven distribution state of the layers. This phenomenon is characterised by solidified melt pools being elongated along the laser scan

direction, as indicated in Figure 16(c). Irregular micro pores are observed at even higher scan speed (lowest energy density), as indicated in Figure 16(d).

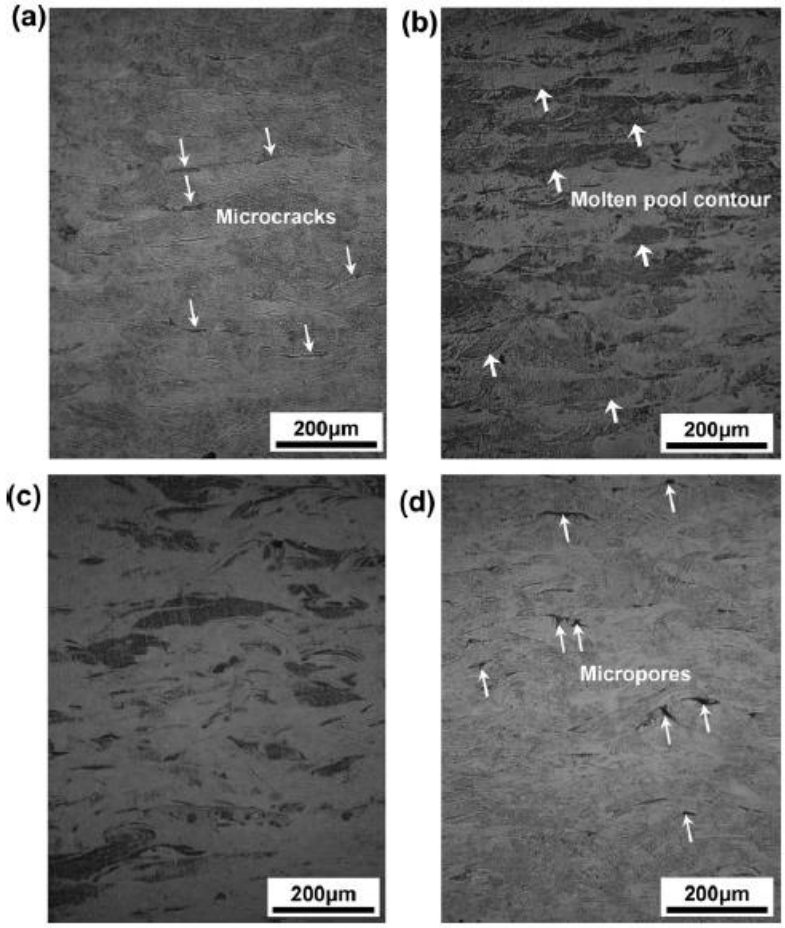


**Figure 16:Optical SLM Ti micrographs at: (a) 0.1 m/s; (b) 0.2 m/s; (c) 0.3 m/s; (d) 0.4 m/s [39]**

### 2.5.1. Influence of SLM process defects on the tensile and fatigue properties

Shifeng *et al*. [27] showed that the substantial decrease in ductility of SLM products could be attributed to the inevitable presence of melt pool boundaries where crack initiation took place when external load was applied. Specimens were built in two different directions, vertical and horizontal, after which the fractured edges and surfaces were investigated with optical microscopy and scanning electron microscopy respectively.

Figure 17 shows two optical micrographs taken on a fractured edge after tensile tests. Figure 17(a) shows a fractured tensile specimen that was built in the horizontal direction (Z-direction). The fractured edge has a saw tooth morphology as it fractured along the track-to-track melt pool boundary. The fractured tensile specimen built in the vertical direction (Z-direction), shown in Figure 17(b), indicates a smooth curve shape, owing to plastic deformation. Note that the tensile axis is indicated by the F-direction.

Further comparison between the fractured surfaces of the horizontally- and vertically-built tensile specimens by SEM imaging, shown in Figures 17(c) and 17(d), reveal major differences in fracture modes. Low energy to fracture cleavage surfaces can be identified on the fracture surface of the horizontal specimen, owing to brittle failure and low elongation while, on the other hand, the fracture surface of the vertical-built specimen exhibits fine dimples that are due to the moderate ductility.

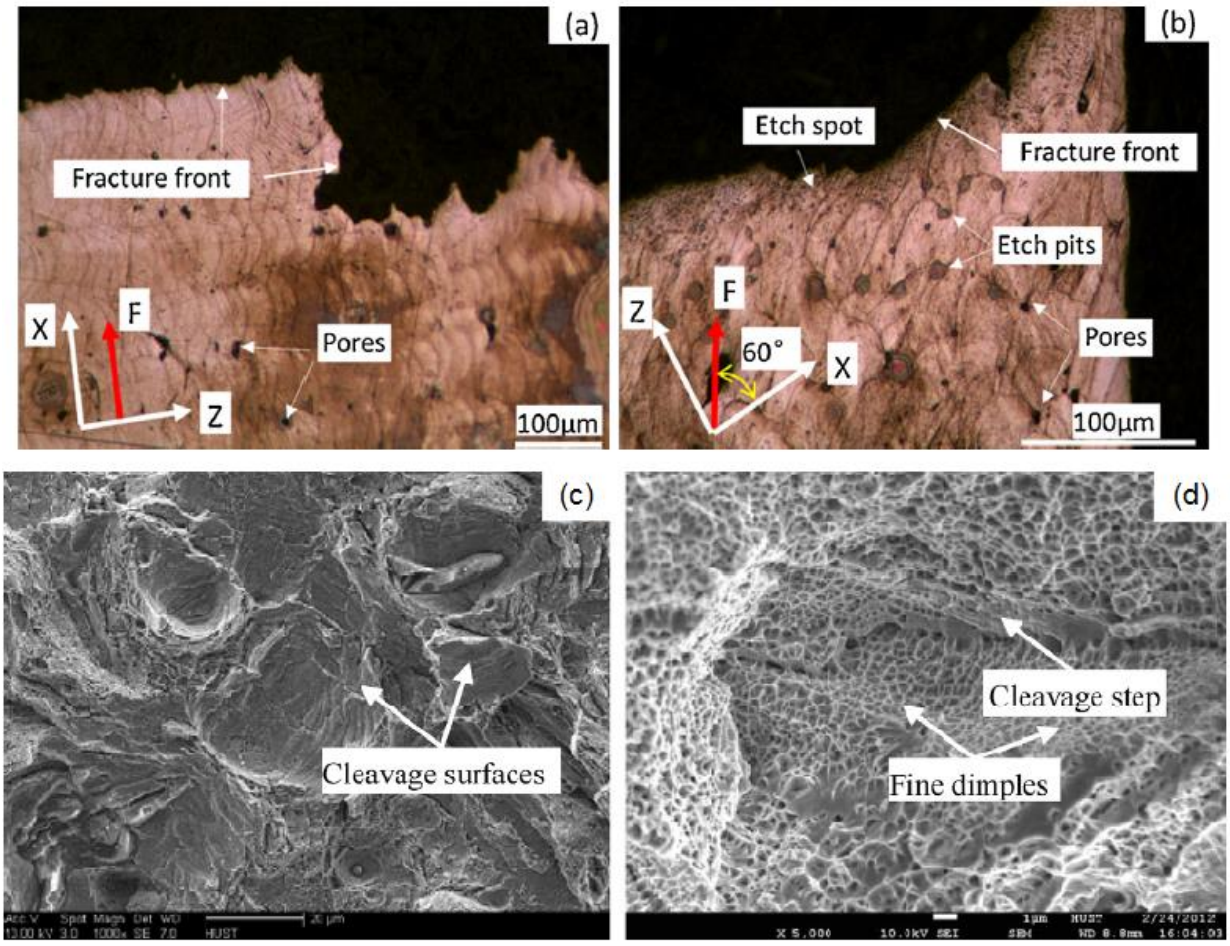


**Figure 17: Optical and SEM micrographs of the fractured edges after tensile testing: (a & c) Horizontal; (b & d) Vertical directions [27]**

Furthermore, work by Facchini *et al*. [35] revealed that the sudden loss in ductility in SLM Ti6Al4V specimens could be attributed to the presence of extreme-sized pores, which generally exhibited poor strain hardenability.

Figures 18(a) and 18(b) show that the deformation of the SLM Ti6Al4V alloy is predominantly ductile, confirmed by the amount of dimple profile on the surfaces, but the presence of cleavage surfaces is also visible around the pre-existing pores and cracks, indicating brittle fracture and hence poor work hardenability.

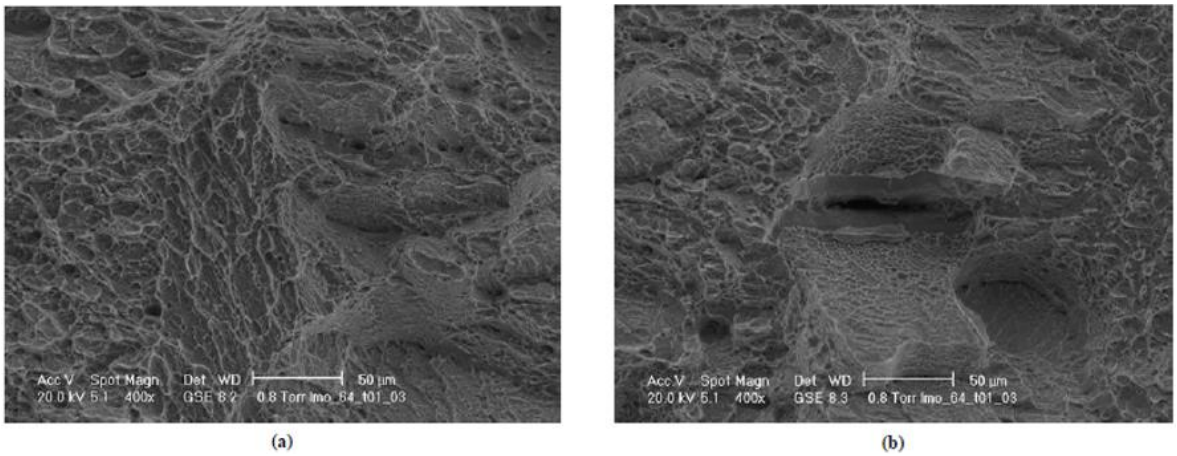


**Figure 18: SEM images of the tensile fractured surface on the SLM Ti6Al4V alloys [35]**

Sterling *et al*. [40] also showed that the sudden loss in ductility in the additive manufactured Ti6Al4V alloys was due to the undesirable presence of defects. This was investigated using the secondary electron SEM images (shown in Figure 19) and revealed the presence of more defects on the specimen that exhibited poor plastic deformation (ductility).

From Figure 19, it is evident that Specimen 1 possessed large pores, this may have been the reason why its ductility was poor as compared to Specimens 2 and 3. This correlates very well with findings reported by Formanoir *et al*. [41], who investigated the sudden loss of ductility in one of the EBM fabricated Ti6Al4V samples. Fractographs revealed that the sample with the lowest ductility had a considerable number of unfused powder particles as compared to other samples, as shown in Figure 20(b).

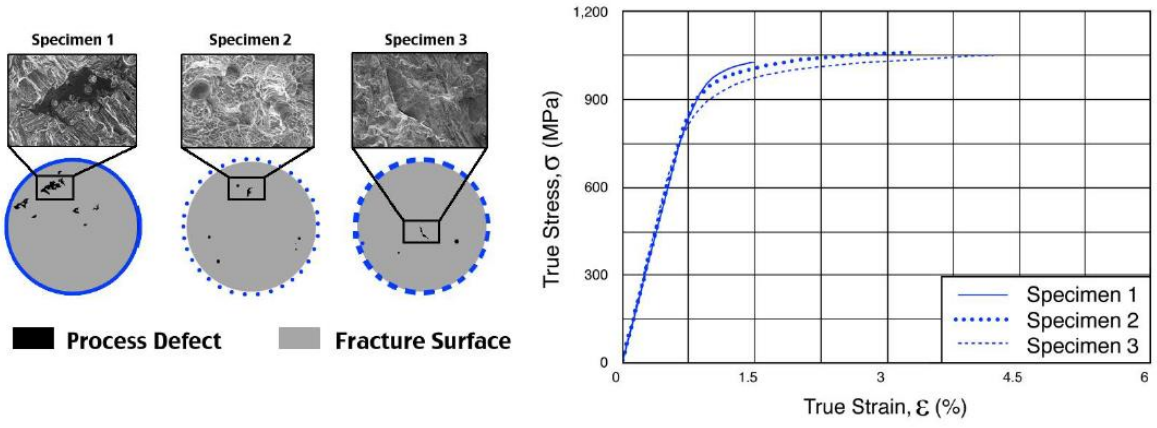


**Figure 19: Tensile tests results and fractographs carried out on three specimens fabricated with different process parameters [40]**

Specimens were built in different directions, namely, parallel to the build (Z) direction, at the X-Y plane, 45° between the X-Y direction (Xv) and in the X-Y plane, parallel to the X-direction. Figure 20(a) shows the tensile test results of the three specimens and it is apparent

that the specimen built in the X-Y direction exhibit a substantial loss in ductility, as compared to the other two specimens.

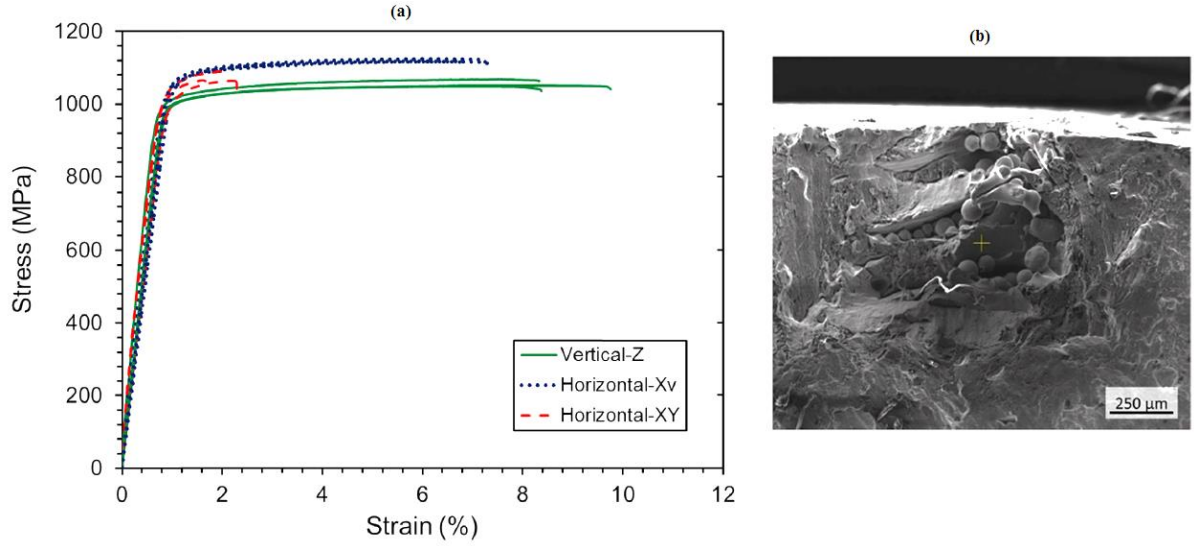


**Figure 20: Tensile results and SEM Fractographs of TI6Al4V alloy fabricated in XY direction by EBM [41]**

Casati *et al*. [42] investigated the effect of build orientation on the mechanical and microstructural properties of SLM 316L austenitic stainless steels. As other authors had observed [35,40,41], it was reported that the sudden loss in both the specimen's strength and ductility was due to the presence of pores and unmelted powder particles, which were observed in the SEM secondary electron images, as shown in Figure 21.

As Figure 21 shows, specimens produced parallel to the build direction (Z-axis, vertical orientation) resulted in the lowest strength and undesirable scatter in ductility. Further investigation into the fractured surfaces revealed unmelted particles within the specimen. This resulted in reduced strength during tensile loads, owing to reduced effective cross-sectional area [42].

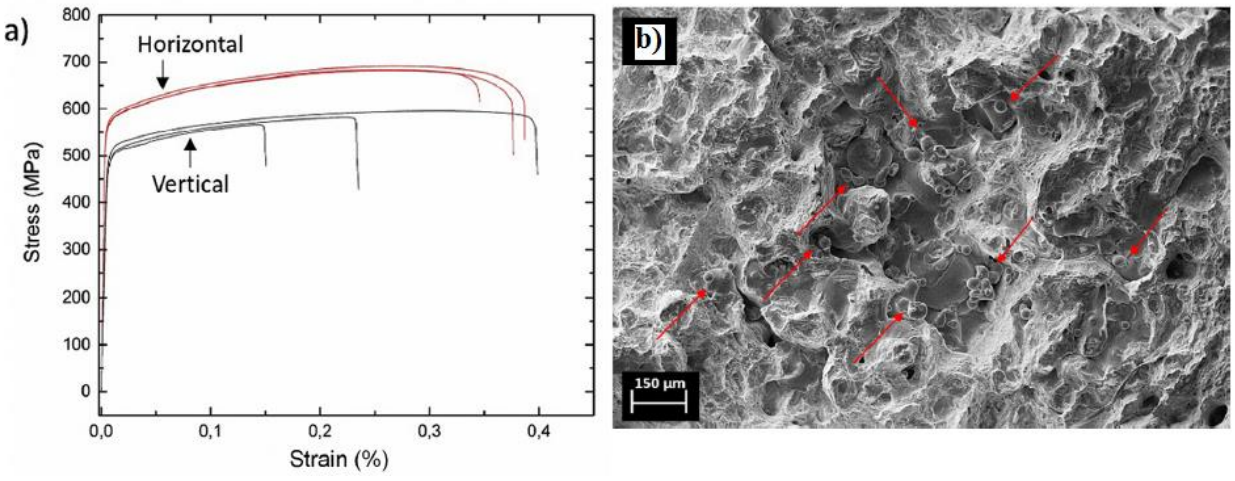


**Figure 21: SEM Fractographs for specimen produced in vertical direction [42].**

The inevitable presence of defects and micro voids during the SLM process has been proved to be the major reason for the loss of ductility in most SLM Ti6Al4V alloys, as presented in this section. Quantitative work by Krakhmalev *et al*. [43] to investigate the source of fracture in SLM Ti6Al4V samples, using X-ray computer tomography ( X-ray CT) scans, led to the conclusion that most of the necking during tensile testing was due to the initial micro pores' coalescence. Using the reconstruction of tensile specimens in micro CT, the area prone to necking on the as-built samples differed significantly from the one in a stress relieved state, both being pre-strained at 8.25% and 8.95% respectively, as shown in Figure 22.

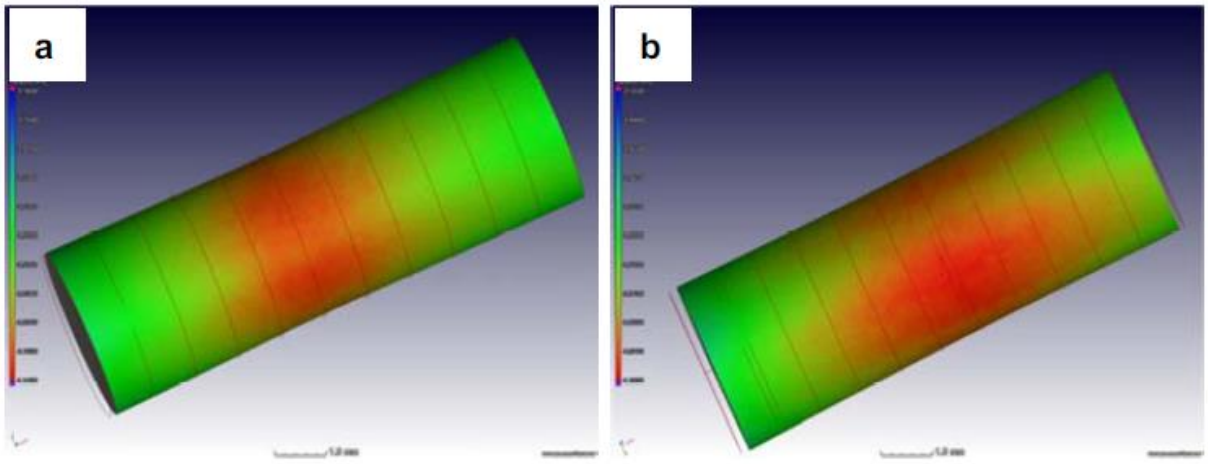


**Figure 22: Possible necking reconstruction: (a) after 8.25% pre-strain in as-built; (b) after 8.95% pre-strain in stress relieved state [43].**

The difference in necking locations may be due to the extreme deformation localisation, which is as a result of severe residual stresses that cause different pore morphologies, as compared to the stress relieved samples [43]. The pore evolution was also studied by capturing the micro CT scans before and after pre-stressing the as-built and stress relieved samples to identify any changes that could have arisen. As the specimen was strained, pore coarsening was observed to be dominant around the necking area and comparison was made before and after straining, using the micro CT scan, as presented in Figure 23.

Figure 23(a) depicts the porosity distribution along the gauge lengths for the as-built and stress relieved tensile samples. Moreover, the pore morphologies are also shown (Figure 23a(ii) and Figure 23a(iii)), which indicate elongated pores. Figure 23(b), on the other hand, depicts the pore sizes for both the as-built and the stress relieved tensile samples, before and after pre-straining; micro pore coarsening was predominant around the centre of the tensile specimens. Comparison between Figure 23a(i and ii) and Figure 23b(iii and iv) reveals that the pore morphology changed as the tensile specimen was pre-strained for both the as-built and the stress relieved tensile specimens, but perhaps more noticeably for the as-built condition.

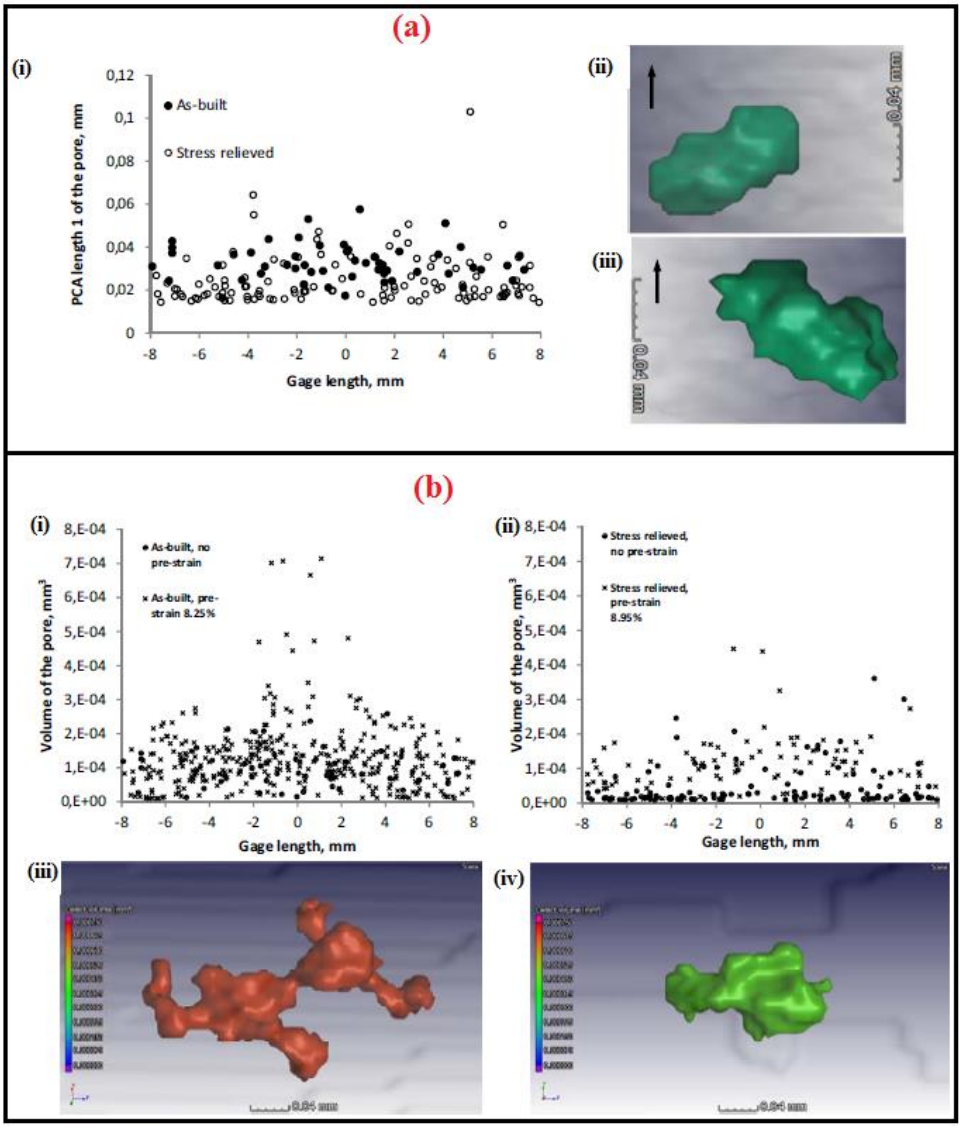


**Figure 23: Evolution of micro pores: (a) as-built and stress relieved before pre-strain; (b) after 8.25% pre-strain in as-built (i & iii) and after 8.95% pre-strain in stress relived state (ii & iv) [43].**

The porosity within SLM fabricated parts also has a significant influence on the material's fatigue properties. The size, distribution, location and shape of the voids present will affect the fatigue life of such a material [40]. This was further validated by Chastand *et al*. [44], who observed that the fatigue failure of the SLM Ti6Al4V alloy was not entirely due to the amount of porosity present, but a combination of the pore size, porosity distribution and the amount of other process defects present in the alloy, as shown in Figure 24.

Fractographs presented in Figure 24 show that most of the sample failure is attributed to the position of defects near to or at the surface. In this zone the crack can easily initiate and propagate [44].

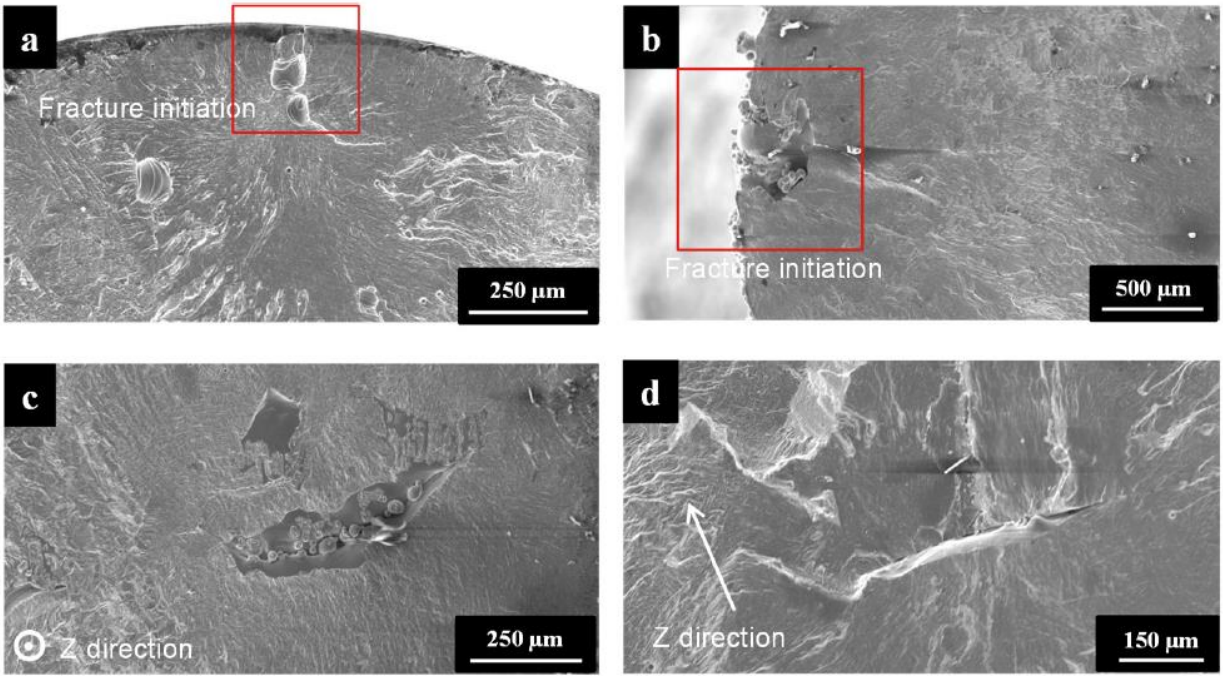


**Figure 24: Types of defects which influence fatigue properties of SLM Ti6Al4V alloys: (a) location of porosity; (b) Surface defects; (c) Unmelted zones in XY plane parallel to the X-axis and (d) XZ plane parallel to the build direction (Z-axis) [44].**

Work by Wycisk *et al*. [45] showed that the fatigue life of Ti6Al4V fabricated by laser additive manufacturing was negatively influenced by the inevitable presence of process defects, both internal and external. The SEM images shown in Figure 25 reveal two crack initiation sites both internally and on the fabricated specimen's surfaces. Although a good surface finish may improve the mechanical properties of SLM fabricated alloys, as advocated by Formanoir *et al*. [41], Mower and Long [46] found no particular difference in the fatigue behaviour of their direct laser metal sintered (DLMS) Ti6Al4V samples after polishing, as it was reported that the internal voids resulting from the fabrication process kept showing after polishing and acted as surface defects and potential crack nucleation sites.

Figure 25(a) depicts that the crack initiation was due to internal process bonding defects, which acted as stress raisers for easy facilitation of crack initiation, as indicated by red arrows. Figure 25(b and c) indicates that the surface defects on the laser addictive manufactured Ti6Al4V specimen provided crack initiation sites, as indicated by red arrows in both figures.

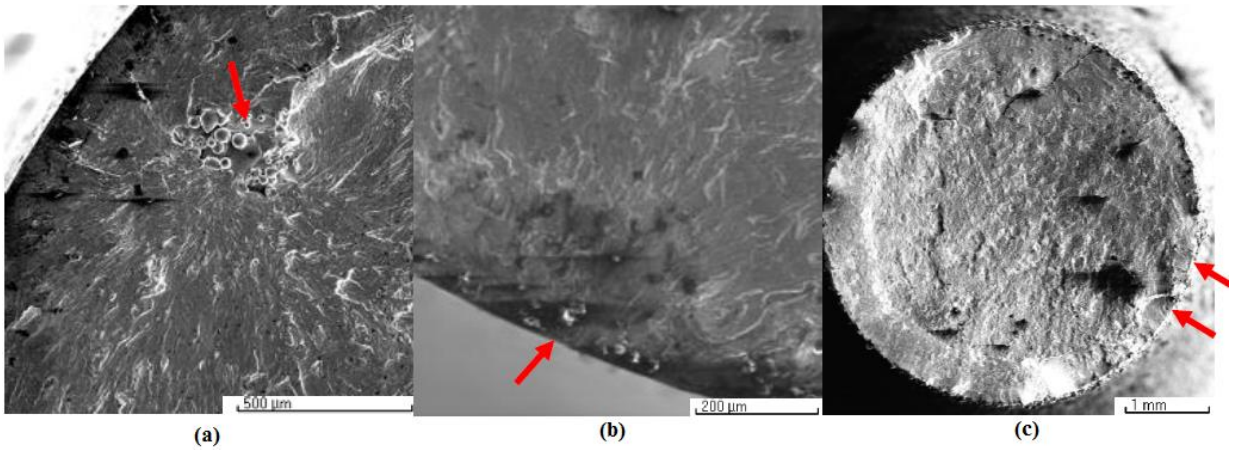


**Figure 25: SEM images showing fatigued laser addictive manufactured Ti6Al4V fractured surface [45]**

## 2.6. PORE CHARACTERISATION USING THE X-RAY COMPUTED TOMOGRAPHY

The influence of pores, shape and distribution cannot be overlooked as this has a significant correlation with the mechanical properties of products. The presence of pores not only leads to a reduction in the effective load bearing area, but also facilitates crack initiation and propagation, especially if the nature or morphology of pores present is irregular or micro pores are clustered and provide high stress concentrations [47]. Therefore, it is crucial to detect and characterise internal voids and the porosity of such products to appreciate the integrity of the resulting mechanical properties, especially for industrial applications [48].

Figure 26 shows reconstructed projections, with segmented pores labelled in red. Figure 26(a) depicts lower resolution X-ray CT scans, the whole volume of the fabricated cuboid was scanned with 9.9 µm voxel size. Figure 26(b) shows two sections taken on the same cuboid (labelled in blue in Figure 26a)) with 2.1 µm voxel size which also depicts the morphology and size of pores present within the cuboid.

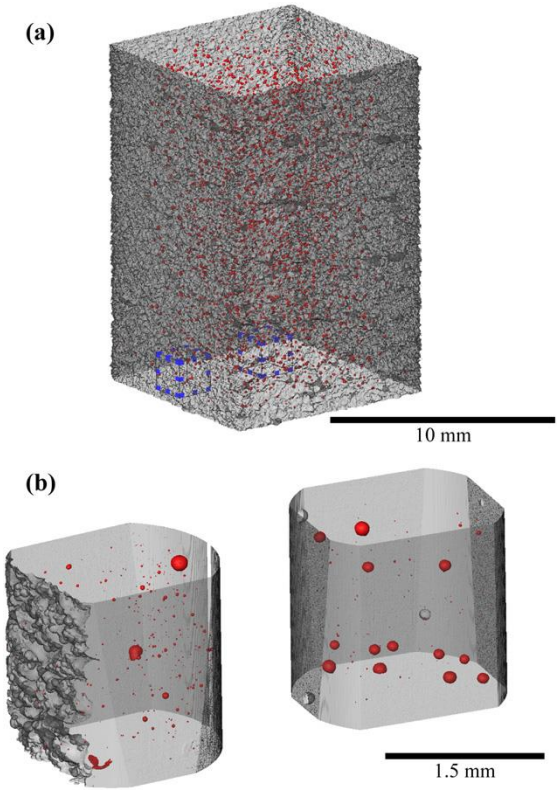


**Figure 26: Example of X-ray CT datasets: (a) cuboid obtained with 9.9 µm voxel size; (b) sections taken on the edge and the centre of the cuboid with 2.1 µm voxel size [49].**

The X-ray computed tomography method has earned the reputation of being a crucial tool in detecting and characterising the porosity within materials. This process involves scanning the material in question with an X-ray beam and collecting data through the detector. These data can now be manipulated by the data acquisition system in order to reconstruct the scanned material and visualise defects in 3-D. The porosity distribution and other quantitative data processing can then be retrieved, as illustrated in Figure 27.

This quantitative analysis prevents over-emphasis on the pore volume fraction, which may be portrayed to the naked eye because the reconstructed images are projections. Hence, a more statistical analysis is crucial to characterise the spatial distribution and density of the part in question [49].

Ziółkowski *et al*. [50] studied the porosity detection in 316L stainless steels fabricated by the SLM process using X-ray tomography. Figure 27(i) depicts the reconstructed SLM 316L stainless steel samples that were fabricated in different orientations with respect to the build direction. The porosity distribution is qualitatively observed and it is clear that Sample A and Sample B have more pores distributed homogeneously along the samples, compared to Sample C, which tends to reveal pores at the extreme ends.

The average pore size, shown in Figure 27(ii), indicates the directionality in which the pores are elongated. The pores in the X and Y directions are larger than in the Z direction, indicating

that most of the pores are elongated in the X and Y directions. In addition to this, sphericity ratio (*S*) is used to indicate a three-dimensional shape that approximates a perfect sphere (whereby $S = 1$ is a perfect sphere) and this is used to identify the nature of pores present, as shown in Figure 28(i).

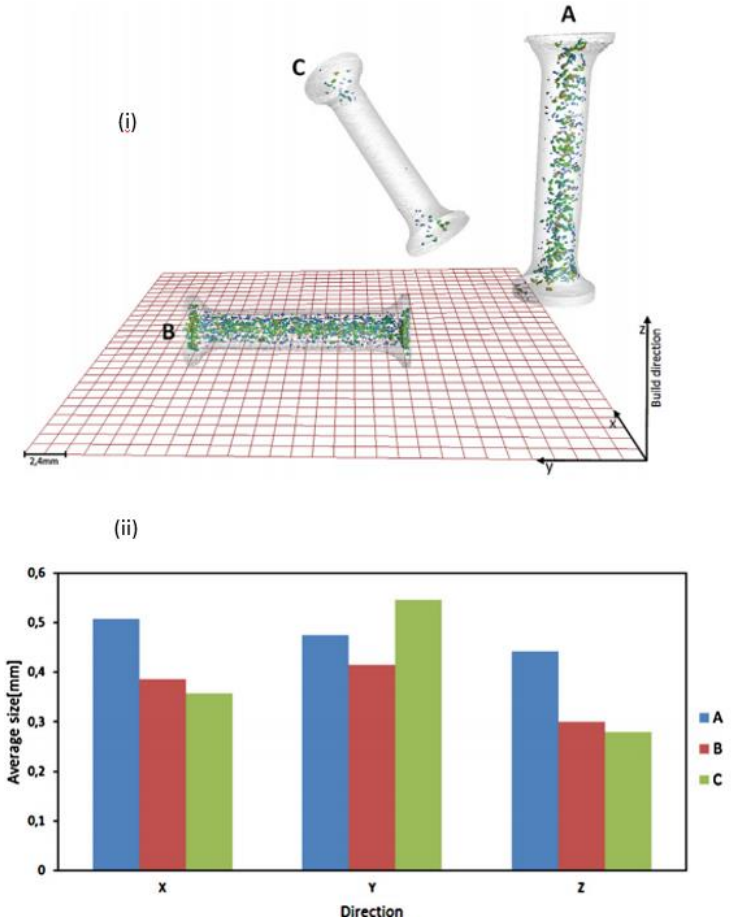


**Figure 27: Porosity characterisation in SLM 316L steel: (i) specimen reconstruction; (ii) average pore size in x, y and z directions [50].**

The pore size distribution shown in Figure 28(ii) is used to indicate the average porosity in each sample. In this case, the average porosity ranged between 330 µm and 540 µm and further showed that most pores greater than 1 mm were found only in Sample A and Sample B.

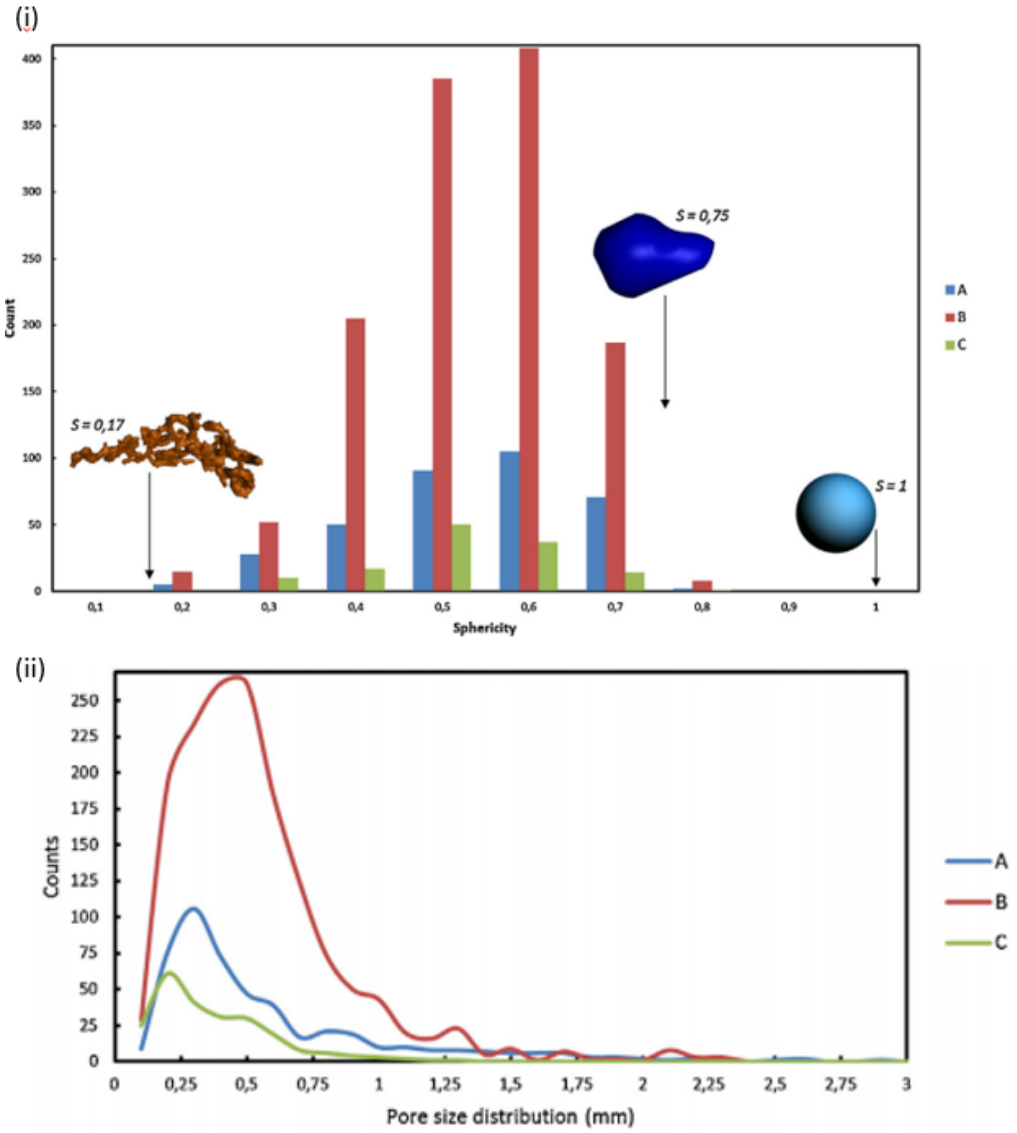


**Figure 28: Porosity characterisation in SLM 316L steel: (i) sphericity distribution; (ii) pore size distribution histogram; [50].**

Maskery *et al*. [47] characterised and quantified SLM Al–Si10–Mg porosity using X-ray computed tomography. In this research, the post heat treatments that were carried out were reported not to yield any difference in the pore size and morphology. Samples with dimensions of 5 $mm^3$ were fabricated using the SLM process and the defects incurred were investigated using X-ray CT scans. The number of pores were characterised, as shown in Figure 29.

Figure 29 depicts a plot of the number of pores, porosity, mean area and the median area against increasing sample height (z-axis). Figure 29(a) illustrates the number of pores detected over the sample height and it is evident that there exist uneven pore distributions per sampled CT layer and, furthermore, the number of pores increases with build distance. This is validated by the first-order polynomial fit, which indicates a slope of pores per layer per micrometre. However, the porosity level throughout the sample did not increase, as Figure 29(b and c)

depicts. The peaks in layer porosity indicate large pores present along the sample height, which are primarily responsible for porosity variation and also serve as an indication of the separation between these pores.

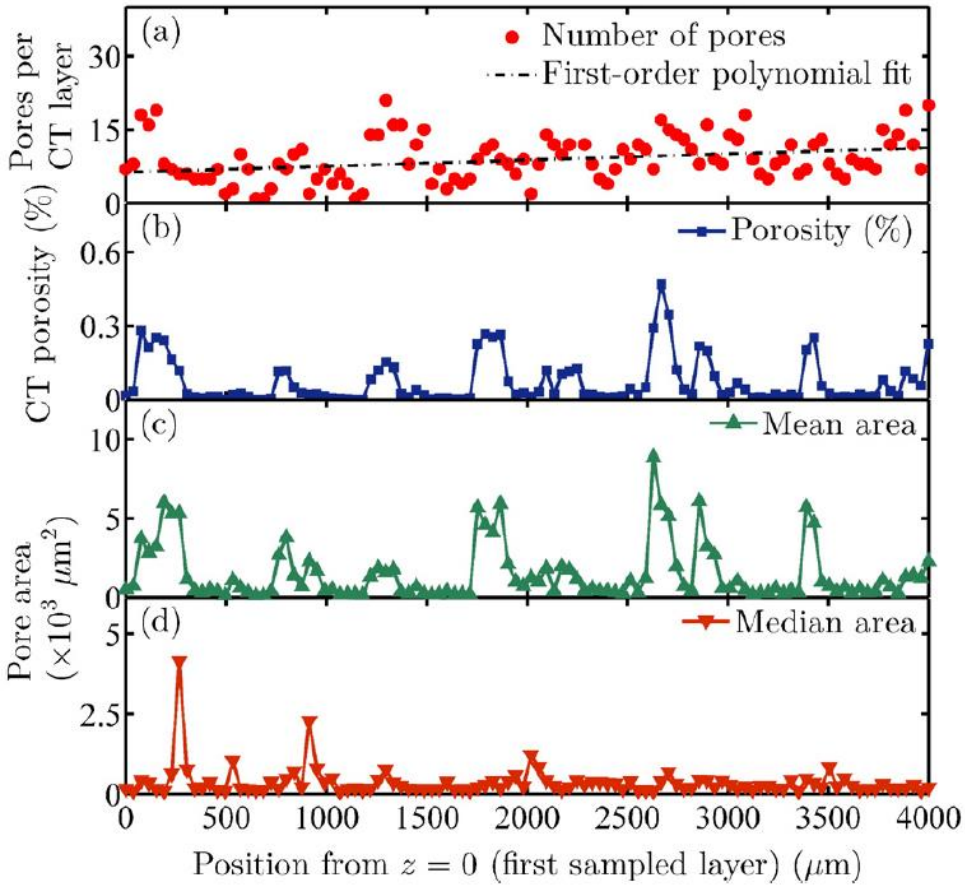


**Figure 29: Pore areas at increasing height in the SLM sample: (a) number of pores; (b) porosity; (c) mean; (d) median [47].**

Further investigation into the pore morphology revealed the anisotropic nature of the pores present after sample reconstruction, using the acquisition system as indicated in Figure 30(a). Larger pores were flat when viewed in the XY plane and at the same time had long and thin profiles when viewed in the ZX plane. A more quantitative analysis is provided by Figure 30(b), which depicts that the sphericity (*f* aspect) of pores in the XY plane is quite high (approximating a circular/spherical structure), as compared to the ZX plane

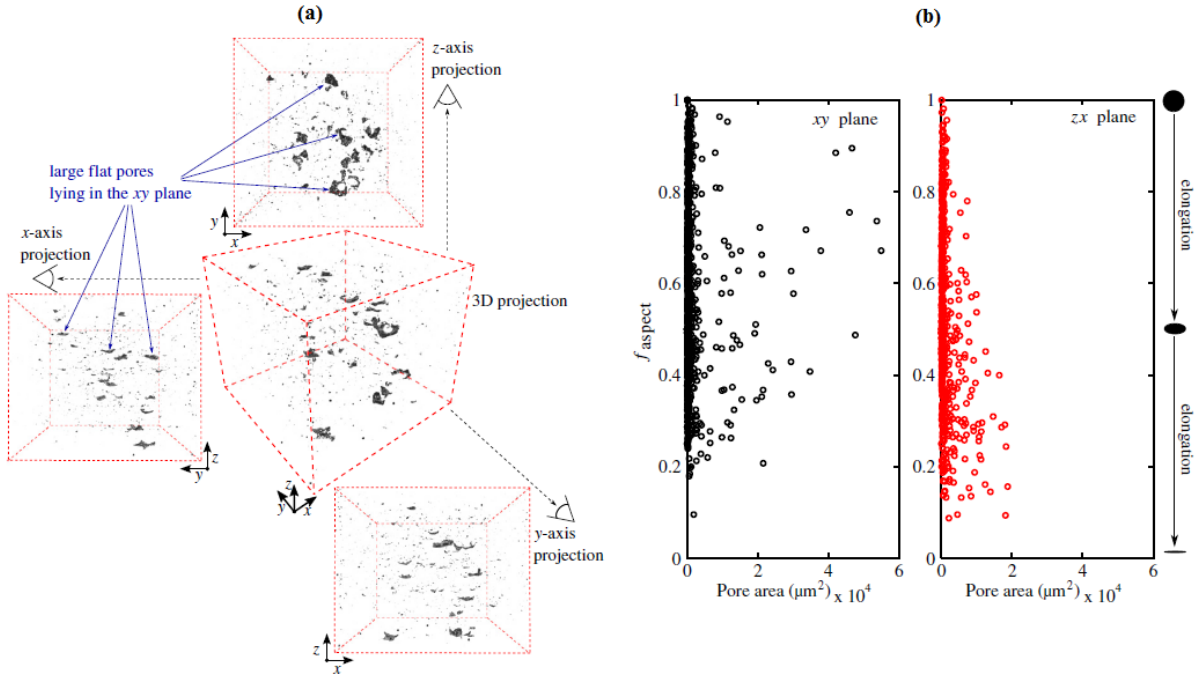


**Figure 30: Pore morphologies: (a) Reconstructed sample; (b) sphericity distribution [47]**

Zhang *et al*. [51] also used the X-ray CT technique to investigate the role of porosity in the Fe-based amorphous coating in the prevention of corrosion. It was reported that the amount and location of porosity present on the coating facilitated direct paths between the corrosive environment and the substrate. The X-ray CT was used to reconstruct 3D isometric projections of the selected area close to the region where the coating and the substrate met, after which statistical analysis was carried out to quantify and characterise the pores present, as shown in Figure 31.

The 3-D X-ray CT reconstructed projections are seen in Figure 31(a). The pores are dark-coloured, owing to their weak X-ray absorption, as compared to the fully dense substrate. Further manipulation of the dataset by the acquisition system revealed pores within the coating, from the smallest pore to the largest pore detected, their size and spatial distribution, as in Figure 31(b). The statistical analysis shown in Figure 31(c) is an indicative analysis of the porosity frequency against the average pore diameter and this shows that the pores present were generally less than 20 μm, with the peak diameter of around 6 μm present. Figure 31(d) depicts the porosity distribution along the coating and it is evident that there was a high porosity zone near the coating and the substrate interface. This is further validated by Figure 31(b), in which extremely large pores can be seen around the coating-substrate interface, which may have resulted from improper wetting.

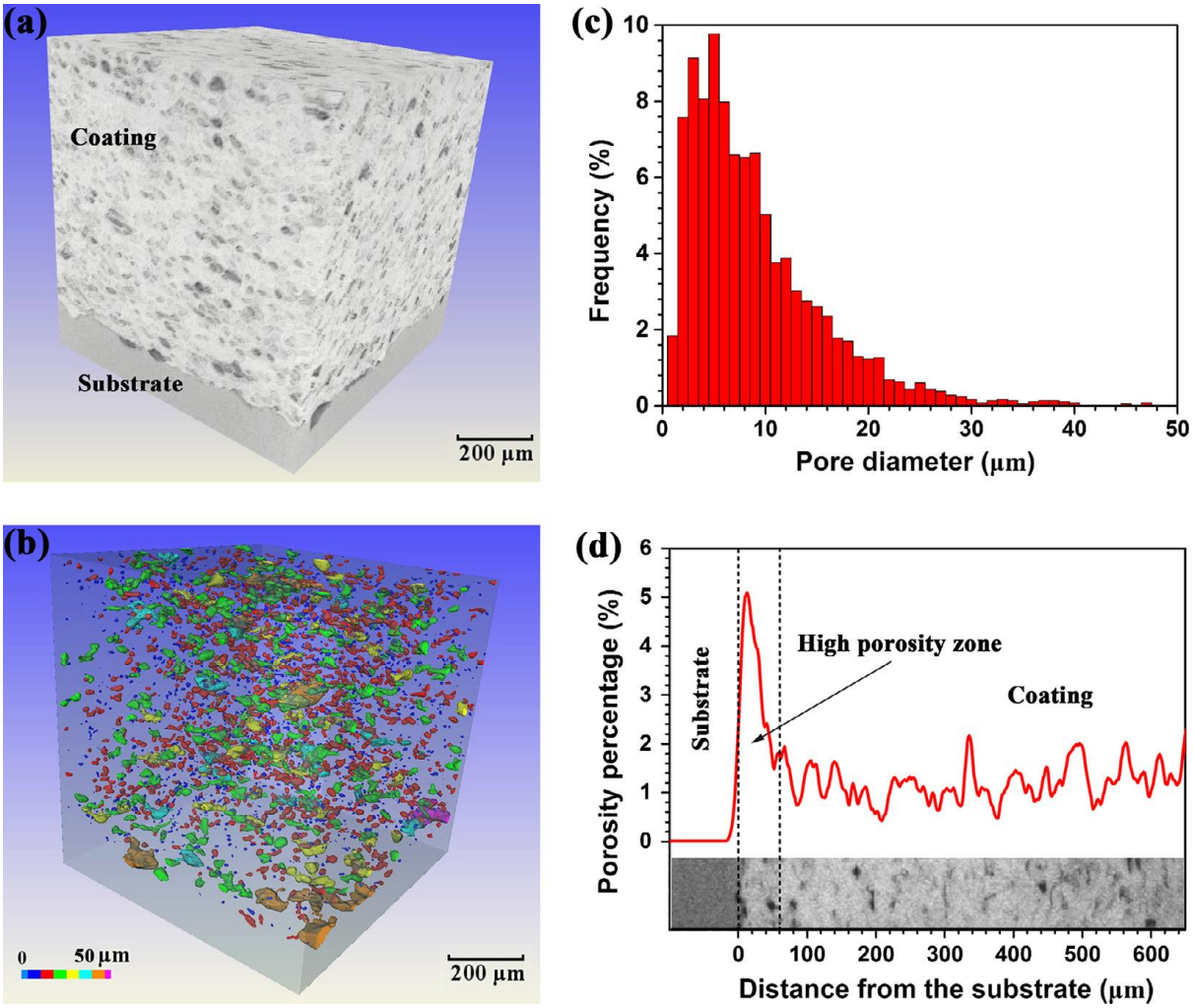


**Figure 31: Porosity distribution in Fe-based amorphous coating: (a & b) X-ray CT 3-D reconstruction showing the coating and substrate together with porosity distribution; (c) porosity size distribution; (d) porosity percentage change along the coating [51].**

The X-ray computer tomography can also be used in conjunction with other software analysis, like the finite element analysis (FEA) technique. Wicke *et al*. [52] characterised casting pores on a Fe-rich Al-Si-Cu alloy, using both the X-ray micro CT method and applying the finite element analysis technique on the reconstructed pores revealed by the X-ray CT technique, as shown in Figure 32. The results showed that shrinkage pores, which are irregular, act as stress raiser and potential nucleation sites for cracks.

Figure 32(a and b) depicts the X-ray CT slice that shows the presence of irregular pores from the stacked slices developed and an isolated pore, respectively. The isolated pore was inserted as a cavity in an FE model of a cylindrical volume representing the material and a uniaxial displacement simulated as a quasi-static tensile test to monitor the stress level on the pore. Figure 32(c) shows the resultant FEA computed stress distribution model and indicates that

high stress levels will be experienced in the internal pore surface with respect to the applied load direction.

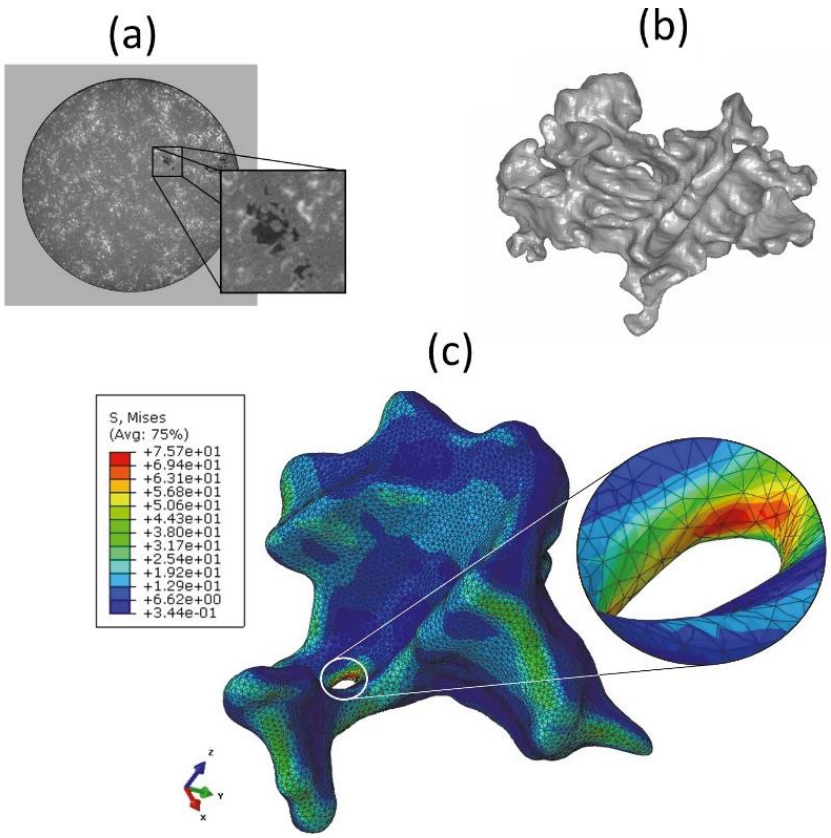


**Figure 32: Shrinkage pores in a cast Al-Si-Cu alloy: (a) pore identification in one of the stacked layers in X-ray CT; (b) Isolation and reconstruction of the pore by X-ray CT; (c) FEA model of the reconstructed pore [52].**

The X-ray CT scan can also be used to assess the quality of cast products, as the process is susceptible to shrinkage and air pores. Niklas *et al.* [53] studied the effect of solution heat treatment on gas porosity and mechanical properties in a die cast step test part (shown schematically in Figure 33(a)), manufactured with AlSi10MnMg (Fe) secondary alloy, whereby the porosity was investigated using the fractographic and metallographic analysis of the tensile samples. The results showed that the elongation in tensile samples decreased significantly as the sample's porosity increased.

The two-dimensional (2D) cross sections shown in Figure 33(b) reveal that only samples produced with a thickness between 10 mm and 15 mm show detectable pores in the X-ray CT scan, whereas Figure 33(c) depicts a reconstructed 3D view from the X-ray CT scan and clearly shows the spatial porosity distribution on samples that exhibited more pores. In this regard, samples produced with a thickness between 10 mm and 15 mm showed shrinkage pores.

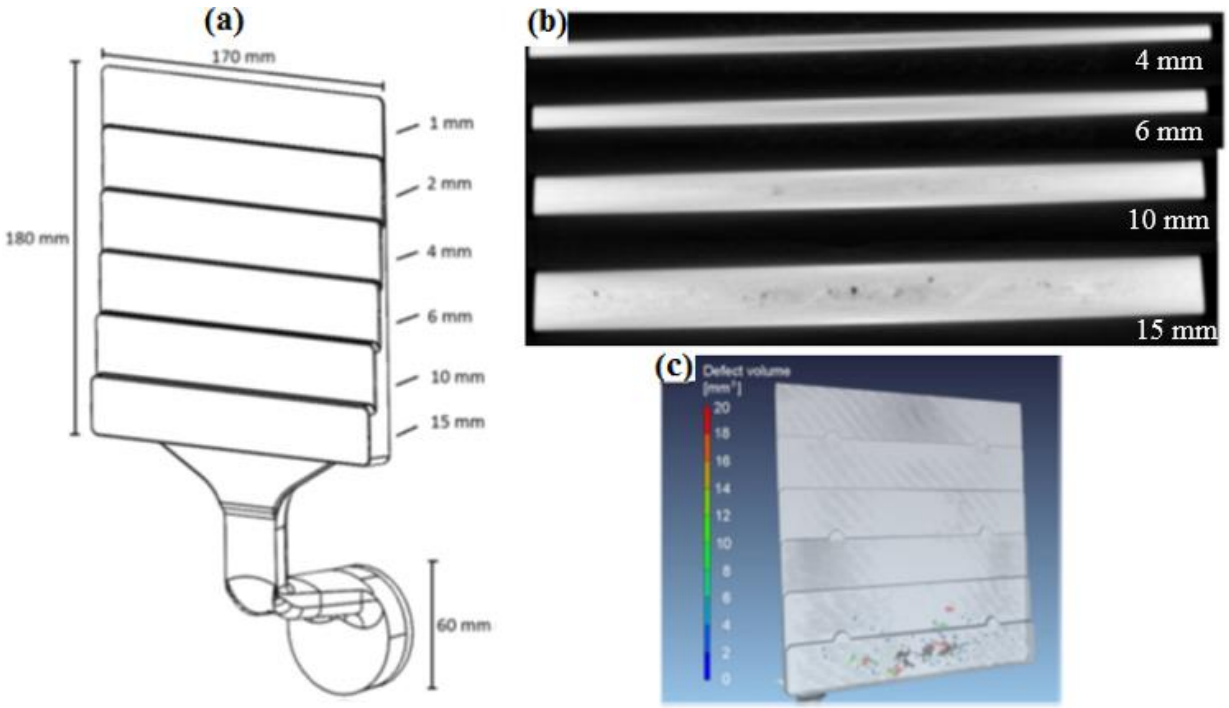


**Figure 33: (a) High pressure die casting design of the step part; the X-ray CT scan for porosity analysis: (b) 2-D slices each with different thicknesses; (c) reconstructed X-ray CT [53].**

Therefore, it is evident that the role that the porosity distribution, pore size and location play on the SLM Ti6Al4V products cannot be overlooked, as the mechanical properties of such products are affected, especially the ductility and fatigue properties [54, 55]. Contrary to all the above regarding the role of porosity and other process defects on the fatigue behaviour of the SLM fabricated material, Benedetti *et al*. [56] observed no particular influence of voids on crack initiation in SLM Ti6Al4V samples, even though pores were observed on the fractured surfaces. Perhaps the work by Wang *et al*. [57] can explain this as pores were also present in the A 319 alloy (Al-Si alloy) samples produced by the lost foam casting process. However, both the experimental and numerical tests revealed that extremely large pores were more likely to generate strain localisation zones for crack initiation. This correlates very well with the work done by Wicke *et al*. [52], who also observed that the fatigue life of cast Fe-rich Al-Si-Cu alloy was limited by the presence of extremely large and irregular pores, especially those close to the material's surface, which act as stress raisers.

## 2.7. MECHANICAL PROPERTIES OF SLM Ti6Al4V PRODUCTS

Several authors [19, 4, 26, 25] have considered different optimum SLM process parameters to produce a comparable product to that produced by conventional methods. A summary of all the work by these authors is presented in Table 2 for easy reference. Although the aim is to produce SLM product with less porosity (hence denser products) that yields better mechanical

characteristics, Gong *et al*. [25**]** reported that density contribution towards the SLM product quality assessment was inadequate as there could be unmolten powder particles within the product that contributed to the density but not the strength.

### 2.7.1. Tensile properties of SLM Ti6Al4V alloy

Murr *et al*. [19] reported a tensile strength of 1450 MPa, with a corresponding percentage elongation of 4.4%, when investigating the mechanical behaviour of Ti6Al4V, produced by rapid layer manufacturing. This is consistent with what Vrancken *et al*. [4] observed, as the tensile strengths were reported to be around 1000 MPa with the ductility (percentage elongation) less than 10% (7.28±1.12). Edwards and Ramulu [5] reported percentage elongation of 3.3 ±0.76, with the corresponding ultimate tensile strength and the yield strength of 1035±29 MPa and 910±9.9 MPa respectively. Cain *et al*. [17] also reported an average tensile strength of 1279 MPa, with an elongation to failure of 6%. Leuders *et al*. [13] reported an average tensile strength of 1080 MPa, with a corresponding elongation to failure of about 1.6%.

Gong *et al*. [25] studied the effects of different scan speeds, hence different energy densities, on the tensile properties of SLM and EBM Ti6Al4V samples. The results are shown in Figure 34. Table 1 shows the corresponding process parameters used. The laser power, hatch spacing, and layer thickness were kept constant at 120 W, 0.1 mm and 0.03 mm respectively.

**Table 1: Process parameters used for SLM Ti6Al4V samples [25]**

| Sample identification | Scan speed (mm/s) | Energy density (J/mm$^3$) |
|---|---|---|
| SLM – OP 1 | 960 | 42 |
| SLM – MP 2 | 540 | 74 |
| SLM – MP 3 | 400 | 100 |
| SLM – MP 4 | 1260 | 32 |
| SLM – MP 5 | 1500 | 27 |

Figure 34(a) to Figure 34(c) show process parameters from the optimum to excessive energy density. The overall ultimate tensile strength is seen to drop as the energy density increases, with a detrimental effect on the process reproducibility. On the other hand, Figure 34(d) and

Figure 34(e) represent tensile properties at lower energy densities and show a further drop in the UTS, with Figure 34(e) further indicating a substantial drop in elongation. In general, the effect of excessive energy density has less effect on the sample's mechanical properties as compared to that produced with inadequate energy density [24]. This is because insufficient fusion incurs defects like delamination and satellite formation, which have a direct impact on the SLM Ti6Al4V alloy's ductility.

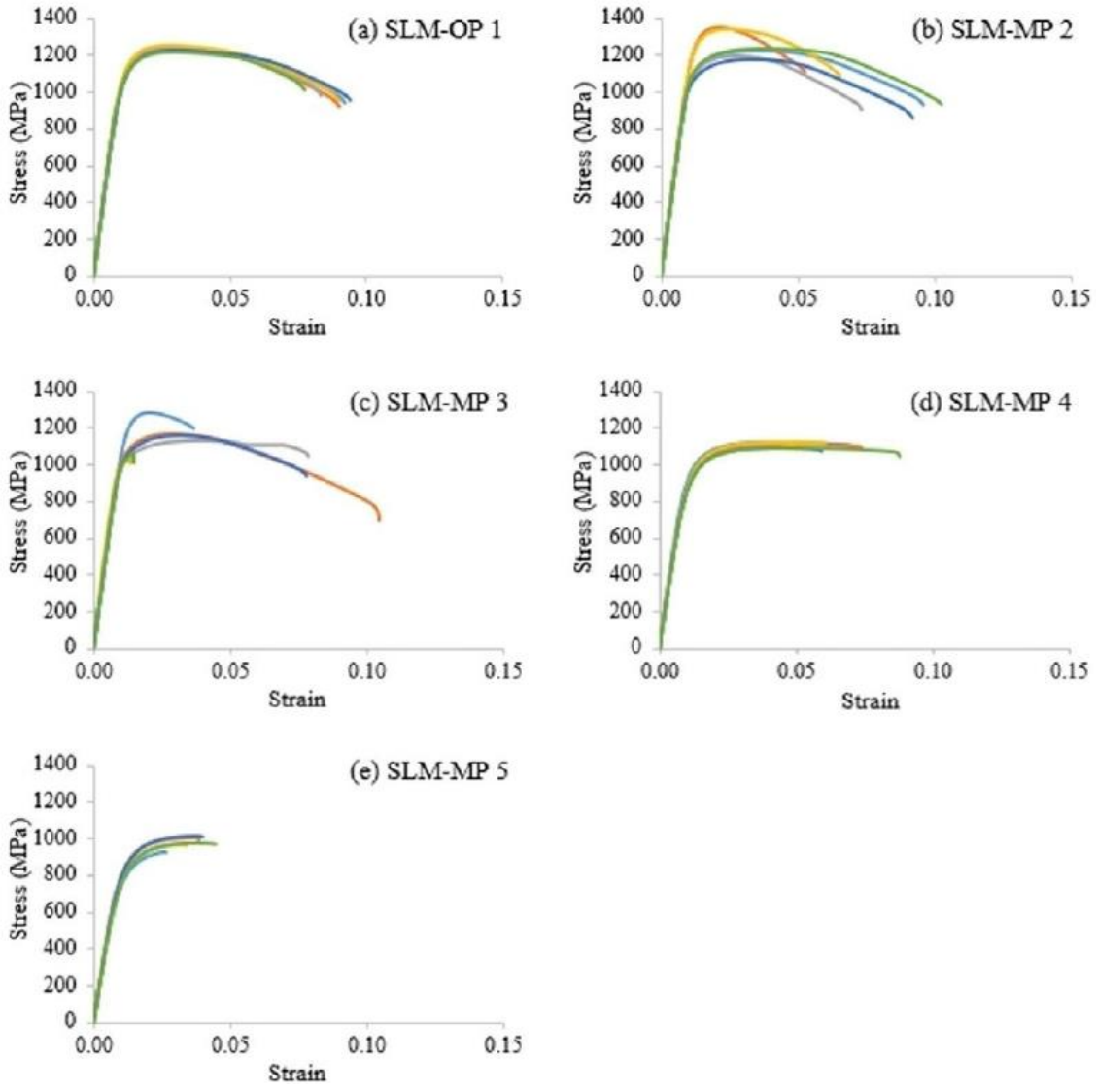


**Figure 34: Stress – strain graphs of SLM Ti6Al4V samples produced at different scan speeds [25].**

### 2.7.2. Fracture toughness properties

Vrancken *et al*. [20] observed fracture toughness values in the range 28 ± 2 MPa. $m^{0.5}$ in the X-Y direction with respect to the build direction (Z axis). On the other hand, Van Hooreweder *et al*. [26] reported a fracture toughness of 52.4±3.48 MPa. $m^{0.5}$ for the samples produced, while

Cain *et al*. [17] reported 28±2 MPa. $m^{0.5}$. The difference between Van Hooreweder *et al*. [26], Vrancken *et al*. [20] and Cain *et al*. [17] may have arisen from different densifications achieved or build orientations during fabrication.

### 2.7.3. Fatigue crack growth rate properties (FCGR)

Van Hooreweder *et al*. [26] suggested that the fine-grained microstructure produced during the SLM process, even though it led to low fracture toughness properties, gained advantage with respect to fatigue crack growth rate, as there were higher number of grain boundaries acting as obstacles for crack propagation.

Figure 35 shows the fatigue crack growth rate comparison plot between the SLM Ti6Al4V and the bulk (wrought or cast) titanium products. Using the Paris equation, Van Hooreweder *et al*. [26] reported two Paris constants *m* and *C* as 3.376 and $5x10^{-12}$ *m*.$cycle^{-1}$ respectively, compared to the bulk Ti6Al4V, whose *m* and *C* constants were 4.757 and $4x10^{-14}$, respectively. This further showed that the SLM Ti6Al4V alloy experienced better and slower crack propagation properties as compared to the bulk Ti6Al4V alloys.

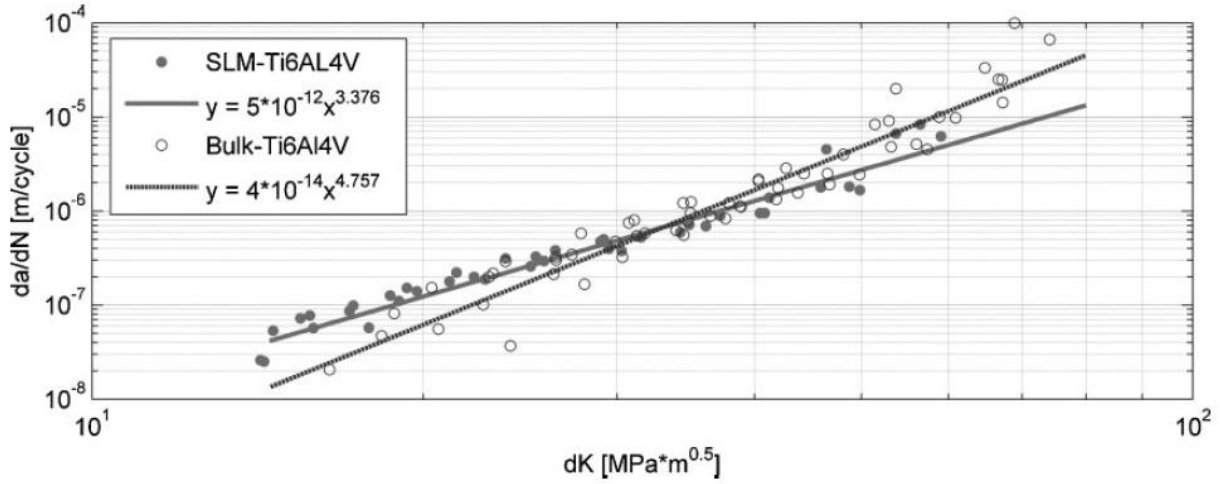


**Figure 35: Crack growth da/dN versus stress intensity range dK for VAR and SLM-Ti6Al4V [26]**

### 2.7.4. Summary on SLM Ti6Al4V mechanical properties as reported by other authors

The extensive work done by several researchers is consistent and there are acceptable differences in the mechanical properties reported. The major difference observed is with the ductility and the fracture toughness properties of the as-built SLM Ti6Al4V alloys and this may

be due to the build direction employed, as well as to the nature of defects incurred during the SLM process. Table 2 serves as a summary that compares work by several researchers.

**Table 2: SLM Ti6Al4V mechanical properties**

| Author | Tensile properties | | Fracture Toughness ($MPa.m^{0.5}$) | FCGR | |
|---|---|---|---|---|---|
| | UTS (MPa) | Elongation (%) | | *m* | C |
| Murr et al. **[19]** | 1450 | 4.4 | - | - | - |
| Vrancken et al. **[4]** | 1000 | 7.28 | - | - | - |
| Edwards and Ramulu **[5]** | 1035 | 3.3 | - | - | - |
| Cain et al. **[17]** | 1279 | 6 | 28 | 3.37 | $5.79 \times 10^{-12}$ |
| Leuders et al. **[13]** | 1080 | 1.6 | - | - | - |
| Vrancken et al. **[20]** | - | - | 28 | - | - |
| Van Hooreweder et al. **[26]** | - | - | 52.4 | 3.376 | $5 \times 10^{-12}$ |
| **Bulk Ti6Al4V** | 1006 | 8 | 69.98 | 4.757 | $4 \times 10^{-14}$ |

## 2.8. POST SLM HEAT TREATMENT PROCESSES

Several authors have investigated the effects of post heat treatments on SLM products [4, 15, 17-18]. Optimisation of mechanical properties by the heat treatment of parts produced by the SLM process is profoundly different when compared to Ti6Al4V products manufactured by conventional process. This is attributed to the unique microstructure produced by the SLM process, which requires specific heat treatments to optimise the material's mechanical properties [4]. Moreover, the original fine needle martensitic α' – phase provides nucleation sides for the α – phase at their grain boundaries when the SLM Ti6Al4V alloy is heated, which leads to the vanadium atoms being expelled and the formation of the β – phase at the newly formed α – phase boundaries [4].

### 2.8.1. Annealing

An ideal combination of homogeneous properties, high ductility and good strength is achieved by proper annealing, which is carried out when the Ti6Al4V alloy is heated just below the β – transus temperature (indicated in Figure 36), permitting a small amount of the α – phase to remain and prevent grain growth [15, 18]. It should be noted that the β – transus temperature for Ti6Al4V is typically about 1000°C.

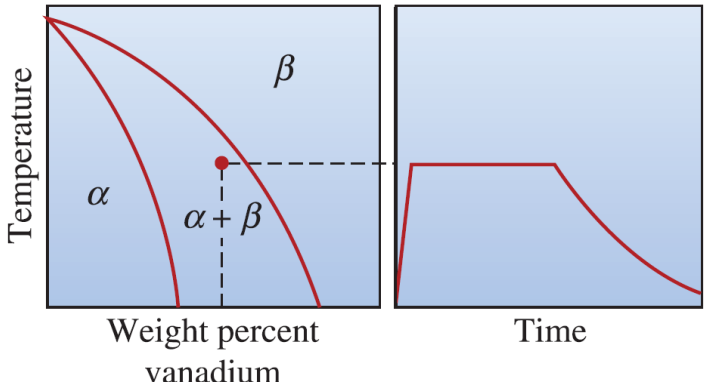


**Figure 36: Ti6Al4V annealing process [18]**

Yadroitsev *et al*. [15] reported that annealing the SLM Ti6Al4V alloy at 800°C for four hours, followed by furnace cooling, resulted in a lamellar structure with very few fine nuclei of equiaxed α – phase. Furthermore, maintaining the temperature well below the β – transus eliminated excessive grain growth and yielded better mechanical properties. This was observed by Cain *et al*. [17] in respect of microstructural development, as shown in Figure 37.

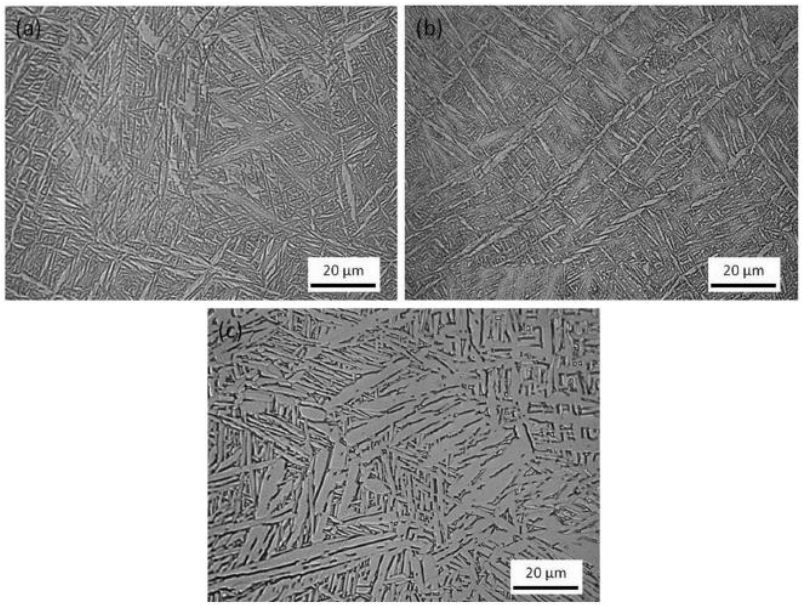


**Figure 37: Microstructural evolution of SLM Ti6Al4V: a) as build; b) after 4 hrs at 650°C; c) after 2 hrs at 890°C [17].**

Figure 37(a) on the previous page shows the martensitic α' – phase structure, which is similar to that reported by Yadroitsev *et al*. [15], owing to the SLM process. The martensitic structure decomposed as the sample was heated at 650°C for four hours into acicular α – phase, as shown in Figure 37(b). Further exposure to elevated temperature (890°C) for two hours resulted in the formation of the Widmanstätten structure on cooling the reformed β – phase, as shown in Figure 37(c).

### 2.8.2. Water quenching

Heating SLM Ti6Al4V alloy to α + β region (800°C), followed by water quenching, results in the formation of a metastable hexagonal α' – martensite and some residual α – phase at grain boundaries [15, 18].

Figure 38 depicts the results Yadroitsev *et al*. [15] observed when the SLM Ti6Al4V alloy was heated to 840°C and 960°C then water quenched, respectively. Both micrographs show a lamellar structure, with the specimen quenched from 840°C showing a finer lamellar structure than the one quenched to 960°C, perhaps owing to coarsening phenomena [15].

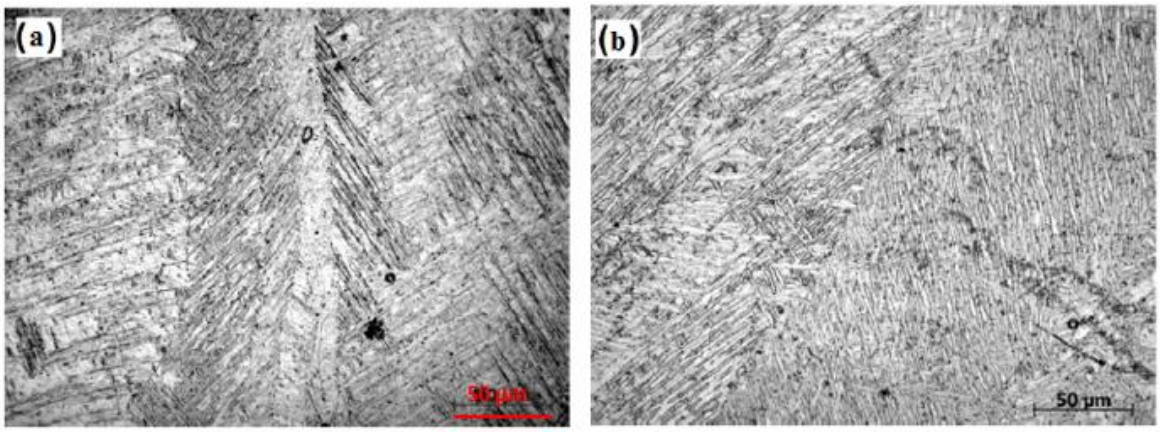


**Figure 38: Microstructural evolution of SLM Ti6Al4V alloy: a) WQ at 840°C; b) WQ at 960°C [15]**

### 2.8.3. Water quenching followed by tempering

The process of heating and quenching followed by tempering of Ti6Al4V alloys is governed by the phase diagram shown in Figure 39.

The martensite start line ($M_s$) provides reference for quench and temper treatment. When the SLM Ti6Al4V alloy passes through the $M_s$ line, the β – phase transforms to α' – phase martensite during quenching. Reheating the supersaturated phase (α' – phase martensite) results in tempering, with β – phase precipitation from α' – phase martensite, which increases the strength of the alloy [15, 18].

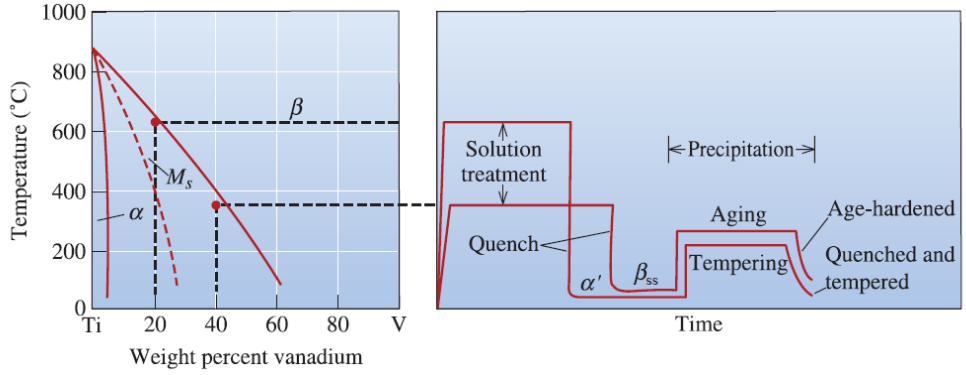


**Figure 39: Phase diagram for Ti6Al4V (heating, quenching and tempering) [18]**

Yadroitsev *et al*. [15] heated samples at 840°C and 960°C, followed by water quenching and tempering at 600°C for four hours. The microstructural evolution of the SLM Ti6Al4V alloy is shown in Figure 40.

Heating the SLM Ti6Al4V alloy sample to the α + β region, but above the $M_s$ (martensite start) line, followed by water quenching and annealing at 600°C for four hours, resulted in two distinct microstructures, as shown in Figure 40. The difference arose as a result of the different annealing temperatures of 840°C and 960°C. The amount of β-phase formation increased with increasing the annealing temperature, which led to greater modification of the as-built α' martensitic microstructure.

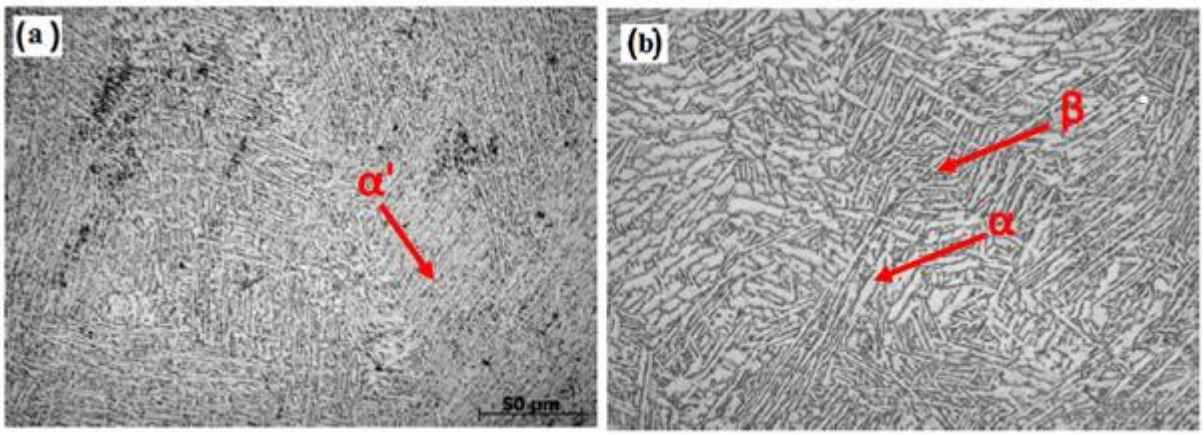


**Figure 40: Microstructural evolution of SLM Ti6Al4V alloy: a) WQ at 840°C, temp at 600°C for 4 hours; b) WQ at 960°C, temp at 600°C for 4 hours [15]**

## 2.9. INFLUENCE OF POST PROCESSING HEAT TREATMENT VARIABLES ON THE MICROSTRUCTURE

In general, the recrystallisation kinetics for the α to β phase ratio is controlled by the temperature and the holding time in the α + β region. Several investigations [4, 15, 17-18] have been carried out with respect to different post heat treatments of the SLM Ti6Al4V alloy to yield desirable microstructural integrity and hence the optimum mechanical properties that can compete with the titanium alloys produced using conventional methods.

### 2.9.1. Influence of temperature

Vrancken *et al*. [4] carried out post heat treatment processing on the SLM Ti6Al4V alloy at 780°C, 843°C and 1015°C, soaked for two hours, followed by furnace cooling. The resulting microstructures are presented in Figure 41.

Figure 41a) shows that the supersaturated martensitic α' – phase has been transformed after two hours at 780°C into a mixture of a fine needle-shaped α – phase (dark colonies) and β – phase (light colonies). Comparing Figure 41(a) with Figures 41(b) and (c), it is evident that the 'β' plates become significantly coarser as the temperature is increased. Furthermore, when the SLM Ti6Al4V alloy is heated above the β – transus temperature, a homogeneous β – phase results and a lamellar α + β mixture is later formed during furnace cooling, as shown in Figure 41(c).

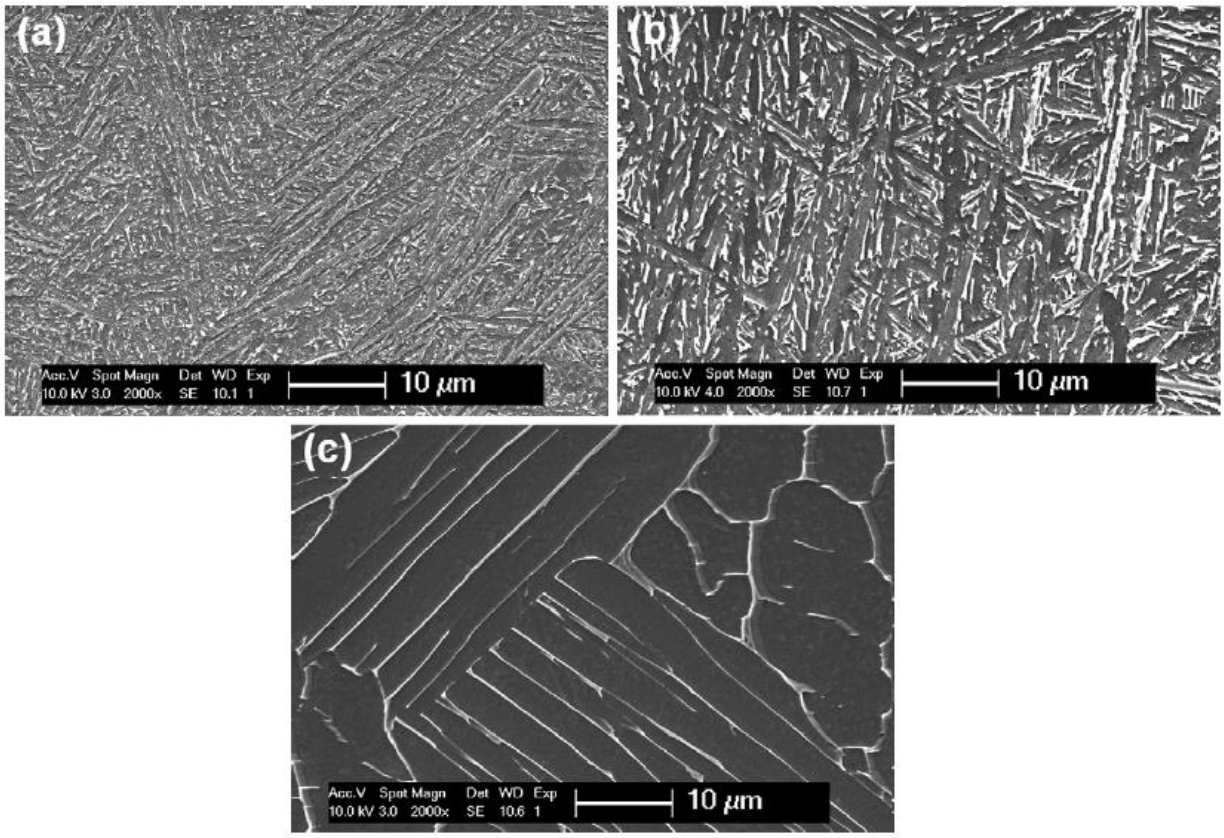


**Figure 41: SEM images of SLM Ti6Al4V soaked for 2 hours at: a) 780°C; b) 843°C and c) 1015°C [4]**

### 2.9.2. Influence of the soaking or residence time

In general, the soaking time, especially at high temperatures, influences grain coarsening. This was reported by Vrancken *et al*. [4] when the SLM Ti6Al4V alloy was held at different temperatures within the α + β region. At this region, both the α - phase and the β – phase tended to coarsen but ultimately hinder each other, thereby limiting the grain growth. Furthermore, the residence time dependency increased as the temperature approached the β – transus temperature of the SLM Ti6Al4V alloy, as shown in Figure 42.

Figures 42(a) and 42(b) show the microstructural transition from the as-built SLM Ti6Al4V alloy soaked at constant temperature for two distinct times. The black arrows show that the α –

phase started to globularise at some locations after being held for 20 hours at 940°C. (The α – phase are the lighter colonies while the β – phase are the darker colonies.)

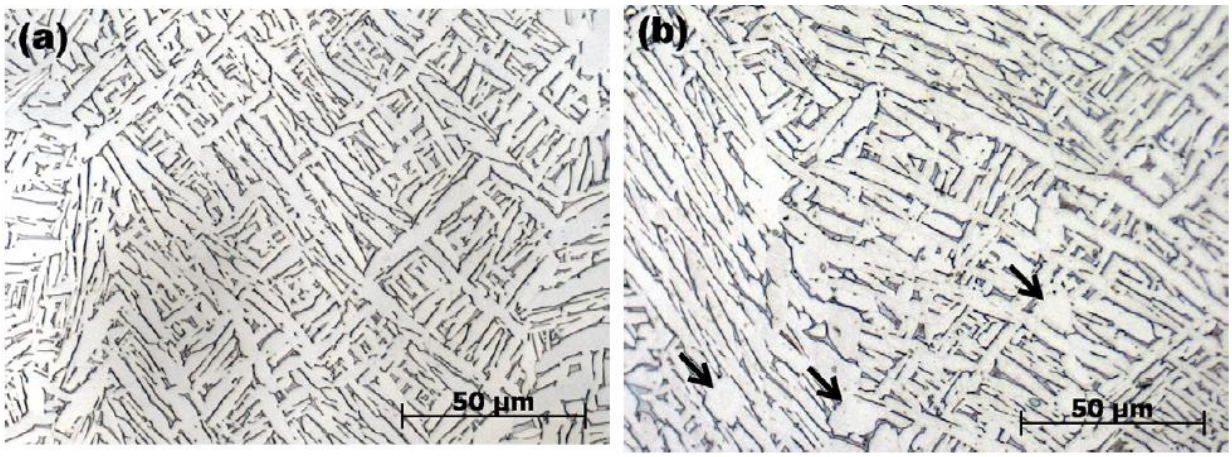


**Figure 42: The α plate size heat treated at 940°C and held for: a) 2 hours; b) 20 hours followed by furnace cooling [4]**

### 2.9.3. Influence of the cooling rate

Yadroitsev *et al*. [15] advocated that the transformation of the β – phase under cooling was highly dependent upon the cooling rate. Furthermore, the cooling rate became an important parameter when the SLM Ti6Al4V alloy was heated above the β – transus temperature, which determined the final morphology and dimensions of the α – phase [4].

Vrancken *et al*. [4] investigated the effect of the cooling rate on the SLM Ti6Al4V alloy heated at 850° for two hours, followed by furnace cooling, air cooling and water quenching. The results are shown in Figure 43.

Micrographs in figure 43 show minor differences, as the α – phase needle widths are similar in all three. In addition, the influence of the cooling rate at this temperature (850°C) is minimal, as the α fraction is fairly large [4]. This α fraction decreases as the temperature escalates towards the β – transus. The effect of the cooling rate also increases. When the SLM Ti6Al4V alloy is heated above the β – transus temperature, the cooling rate determines the final morphology and colony size of the α-phase. High cooling rates lead to the formation of fine α - phase nuclei and furnace cooling results in an α + β lamellar structure, while air cooling results in an α-Widmansttaten microstructure [4].

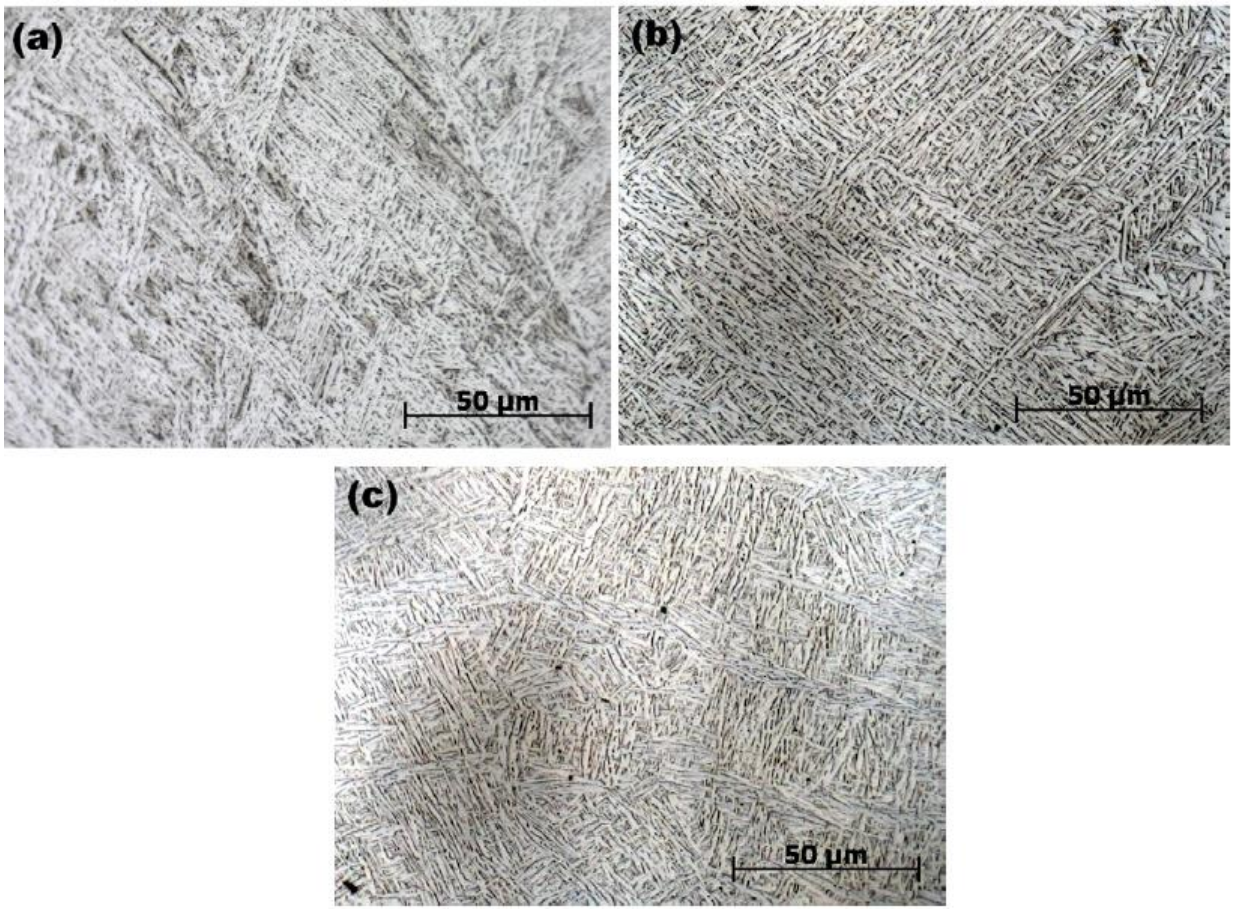


**Figure 43: Microstructure of SLM Ti6Al4V alloy after 2 hours at 850°C followed by: a) furnace cooling; b) air cooling and c) water quenching [4]**

## 2.10. INFLUENCE OF POST PROCESSING HEAT TREATMENTS ON THE MECHANICAL PROPERTIES

Lütjering [58] reported that the α colony size was the important microstructural parameter that determined the mechanical properties of α – β titanium alloys. The reduced α colony size improved the ductility, the crack nucleation and crack propagation resistances.

### 2.10.1. Tensile properties

Vrancken *et al*. [4] carried out several heat treatments and measured the corresponding influence on the mechanical properties. The study is summarised in Table 3.

Cain *et al*. [17] observed a slight decline in the tensile strength between the as-built and the samples stress relieved at 650°C for four hours (1171 MPa from 1248 MPa), with a slight increase in percentage elongation. The tensile strength further declined when samples were heated at 890°C for two hours and the elongation was reported also to have dropped. This could be attributed to the coarsening of the two phases, hence reducing the ductility, as was observed by the premature failure in Sample 3, as shown in Table 3 by Vrancken *et al*. [4]. On the other

hand, Leuders *et al*. [13] also heat treated SLM Ti6Al4V samples at 800°C for two hours and reported a slight decline in the ultimate tensile strength from 1080 MPa as-built to 1040 MPa, with a higher percentage to failure (5% as compared to 1.6% as-built).

**Table 3: Mechanical properties of SLM Ti6Al4V alloy following different heat treatments [4]**

| # | Temp. (°C) | Time (hours) | Cooling rate | E(GPa) | $\sigma_y$ (MPa) | UTS (MPa) | E (%) |
|---|---|---|---|---|---|---|---|
| **1** | 540 | 5 | WQ | 112.6±30.2 | 1118±39 | 1223±52 | 5.36±2.02 |
| **2** | 850 | 2 | FC | 114.7±3.6 | 955±6 | 1004±6 | 12.84±1.36 |
| **3** | 850 | 5 | FC | 112.0±3.4 | 909±24 | 965±20 | Premature failure |
| **4** | 1015 for 5 hrs followed by 843 for 2 hrs | - | AC followed by FC | 114.9±1.5 | 801±23 | 874±23 | 13.45±1.18 |
| **5** | 1020 | 2 | FC | 114.7±0.9 | 760±19 | 840±27 | 14.06±2.53 |
| **6** | 705 | 3 | AC | 114.6±2.2 | 1026±35 | 1082±34 | 9.04±2.03 |
| **7** | 940 for 1 hr followed by 650 for 2 hrs | - | AC followed by AC | 115.5±2.4 | 899±27 | 948±27 | 13.59±0.32 |
| **8** | 1015 for 0.5 hour followed by 730 for 2 hrs | - | AC followed by AC | 112.8±2.9 | 822±25 | 902±19 | 12.74±0.56 |

**WQ = water quench; FC = furnace cool; AC = air cool**

### 2.10.2. Fracture toughness properties

According to Van Hooreweder *et al*. [26], inferior fracture toughness values observed could be attributed to the microstructural morphology of the SLM Ti6Al4V products. The fine α' – martensitic phase gave rise to increased brittleness. This could be eliminated by the post heat treatments to improve the products ductility, which would lead to improved fracture toughness. This was further validated by Cain *et al.* [17], whose results are summarised in Table 4.

**Table 4: Fracture toughness for the as-built and heat treated SLM Ti6Al4V alloy [17]**

| Heat process | Temperature (°C) | Time (hours) | Fracture toughness, $K_{1C}$ (MPa.m$^{0.5}$) |
|---|---|---|---|
| Stress relieve anneal | 650 | 4 | 28±2 |
| Full anneal | 890 | 2 | 41±2 |

### 2.10.3. Fatigue crack growth rate properties

The acicular α – phase microstructure inherent in SLM process is prone to fatigue crack initiation, but cracks follow meandering and tedious paths along the boundaries between α and β phases. This results in a low fatigue crack growth rate and good fracture toughness, as well as a good resistance to creep [15, 18]. This was further validated and confirmed by Cain *et al*. [17], who observed the slowest crack propagation in XY orientation (built on the XY plane, perpendicular to the build direction, Z-axis) for the as-built SLM Ti6Al4V sample and the fastest crack propagation in the stress relieved sample, as shown in Figure 44.

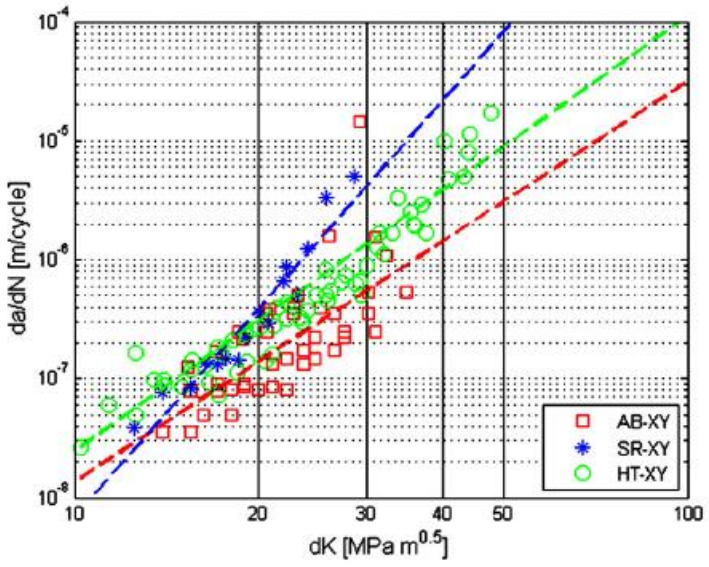


**Figure 44: Crack growth d*a*/d*N* versus stress intensity range d*K* for samples built in the XY orientation [16]**

Vrancken *et al*. [20] investigated the fatigue crack growth rate of SLM Ti6Al4V samples fabricated in three different orientations with reference to the build direction. The as built SLM Ti6Al4V samples were compared with the stress relief annealed samples (soaked at 650°C for four hours, followed by furnace cooling). The results are shown in Figure 45.

It is evident from Figure 45 that the XY orientation, as reported by Cain *et al*. [17], indicates an increase in the fatigue crack growth rate after the stress relieve anneal, as compared to the other two orientations, which show a decrease in the fatigue crack growth rate after the stress relief anneal. This may be attributed to the initial compressive stresses associated with the SLM built

process that were relieved during annealing, which would otherwise have slowed down the crack growth if still present [20].

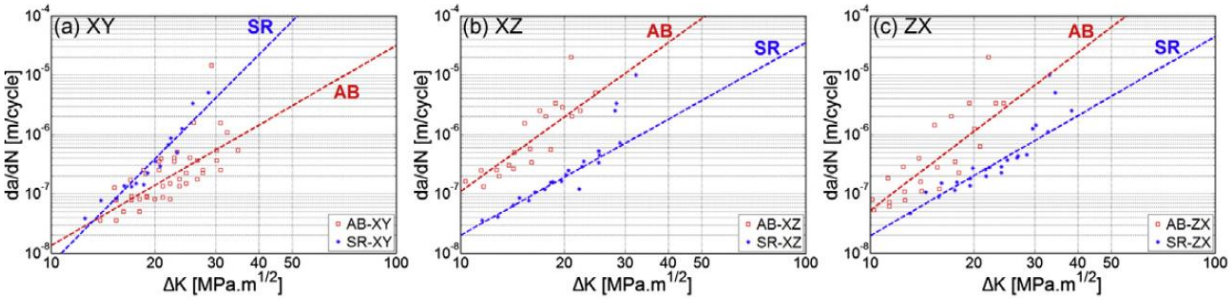


**Figure 45: The FCGR curves for the as-built (AB) and the stress relieve annealed (AR) in three orientations [20]**

## 2.11. CONCLUDING REMARKS

A brief account of literature has been presented focusing mainly on topics such as the microstructural characterisation of the SLM Ti6Al4V alloys and the corresponding mechanical properties, as well as several distinct heat treatment processes that can be carried out to improve the mechanical properties of SLM products and hence can compete with the wrought or cast titanium alloys.

### 2.11.1. Importance of SLM process optimisation

Extensive research has been carried out by several researchers [35, 43, 59, 60] to optimise the SLM process for a better microstructural integrity of products, which would compete with that of products produced by conventional methods. For example, the elimination of the oxide layer on the underlying substrate by re-melting plays a crucial role for proper wetting and spreading of the molten metal on the substrate to reduce delamination and balling phenomena. In addition, the presence of α – stabilisers as interstitial elements (oxygen and nitrogen) distorts the HCP lattice structure and therefore limits the dislocation movement, leading to material embrittlement. This is due to the α – phase being less ductile than the β – phase [35, 43, 59, 60]. The irregular surface of the SLM layer also hinders the efficient melting of powder particles as there will be inadequate laser energy in the region where the powder layer exceeds the set layer thickness, leading to an insufficient pool to penetrate and wet evenly throughout the substrate, resulting in unmolten powder particles [60].

### 2.11.2. Post SLM heat treatments

The review in this section has indicated that the final microstructural morphology of the SLM fabricated products generally depends on the holding time and the maximum temperature for the heat treatment within the (α + β) region. Furthermore, the annealing process in the range 650°C - 1050°C has been used in recent research [4,17] not only to relieve residual stresses formed during the SLM process, but also to modify the microstructural morphology of the SLM Ti6Al4V alloy and produce an α + β lamellar structure, which gives rise to a good combination of strength and toughness.

# 3. EXPERIMENTAL PROCEDURE

This chapter serves as a detailed account of the research experimental procedures that were performed and the equipment that was used. It presents the experimental techniques used to collect all information essential to this project. The results will be comprehensively presented in Chapter 4.

## 3.1. MANUFACTURING OF SLM Ti6Al4V SAMPLES

All the SLM Ti6Al4V samples were produced at the CSIR National Laser Centre in Pretoria by a zig-zag scanning strategy using the OPTOMEC® additive manufacturing system's laser engineered net shaping (LENS®), Model 850R. The setup, shown in figure 46, consisted of the following when SLM Ti6Al4V samples were built:

1. A dedicated SLM powder bed assembly which was designed and built by the National Laser Centre, the assembly had the following components:
   i. A scan lab XYZ mirror scanner.
   ii. A powder piston which lowers after each layer is selectively fused.
   iii. A scraper built with powder holder to scrap each layer and apply a new layer for the next scan.
   iv. Two linear motors driving the scraper and the powder piston. A titanium base plate with integrated powder seal was attached to the powder piston.
   v. A LENS interface to move the setup easily into and out of the LENS, and
   vi. A vacuum cleaner to remove dust and smoke away from the scan area.

2. The OPTOMEC LENS, Model 850R system, with its tilt-rotate table removed and the XYZ gantry parked in the top corner away from the viewing window. This was essentially used as a hermitically sealed class 1 laser glove box to ensure an oxygen free environment when processing samples. The ante-chamber of the LENS assisted in moving samples and base plates into and out of the oxygen free environment.
3. An IPG 5kW fibre optic cable with fibre feed that plugs into the scan lab XYZ mirror scanner.
4. An IPG laser chiller which dissipates excess heat gained in the generation of the laser light.

5. A dedicated software, developed by the National Laser Centre, which interfaced the scraper and the powder piston motors with the laser power directed by the scan lab XYZ scanner.

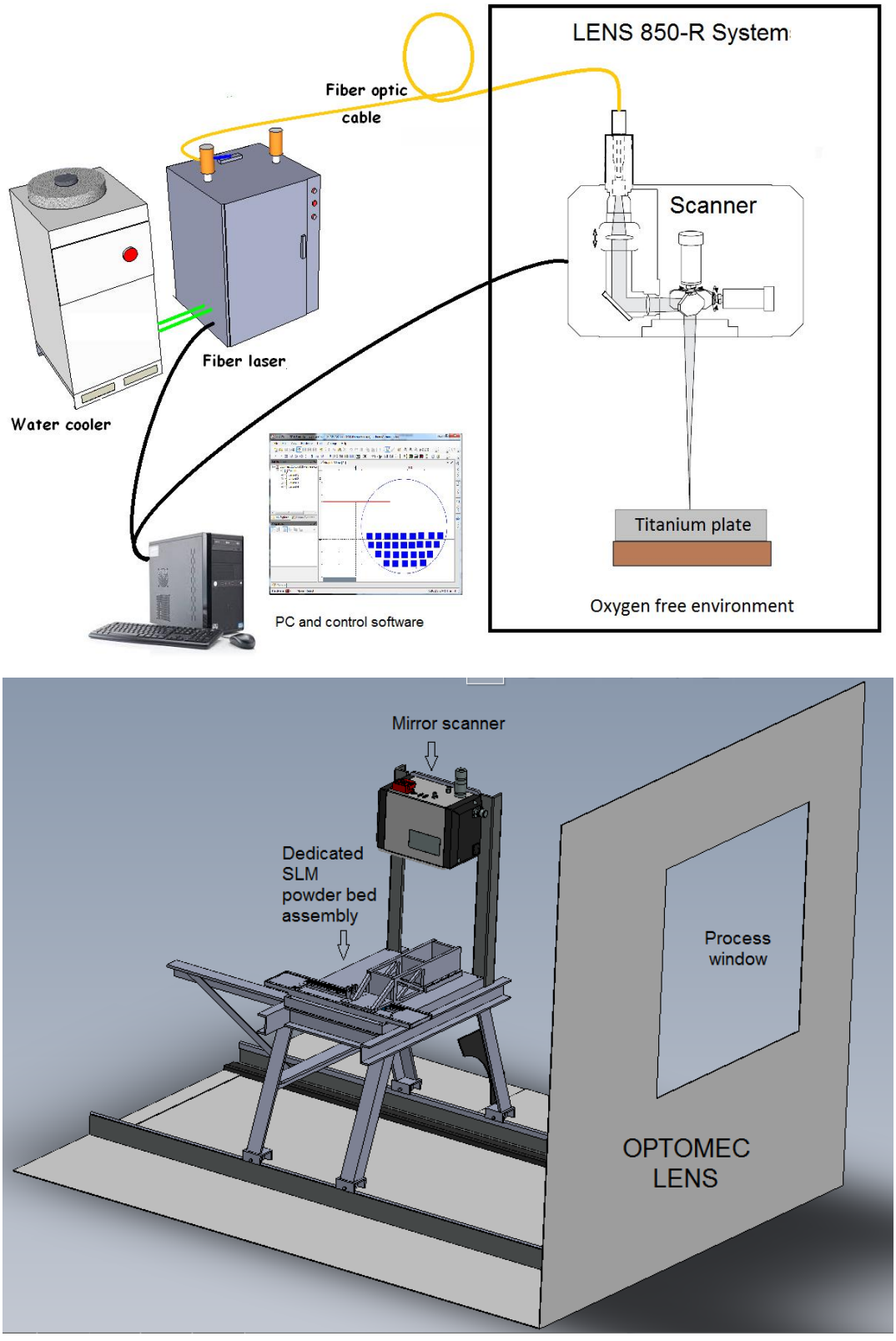


**Figure 46:Setup used to fabricate SLM Ti6Al4V samples: Schematic representation (top image); powder bed assembly fed into the LENS (bottom image)**

Samples were produced from Grade 5 Ti6Al4V powder with an average particle diameter of 50 µm, the scanning parameters are indicated in Table 5.

**Table 5: The SLM scanning parameters used to produce Ti6Al4V samples**

| Laser power (kW) | Layer Thickness (µm) | Hatch spacing (µm) | Laser spot size (µm) | Laser scan speed (m/s) |
|---|---|---|---|---|
| 0.65 | 50 | 120 | 240 | 1.5 |
| 0.65 | 50 | 120 | 240 | 1.75 |
| 0.65 | 50 | 120 | 240 | 2.0 |
| 1.3 | 50 | 120 | 240 | 2.5 |
| 1.3 | 50 | 120 | 240 | 3.0 |
| 1.3 | 50 | 120 | 240 | 3.5 |
| 1.3 | 50 | 120 | 240 | 4.0 |

Each layer was scanned using the zig-zag scanning strategy as shown in Figure 47(a). Samples fabricated for mechanical tests (tensile, fracture toughness and fatigue crack growth tests) were produced in the XY plane with respect to the build direction (Z-direction), as indicated by Figure 47(b and c). These samples were fabricated as blocks, after which mechanical specimens were machined according to ASTM standards.

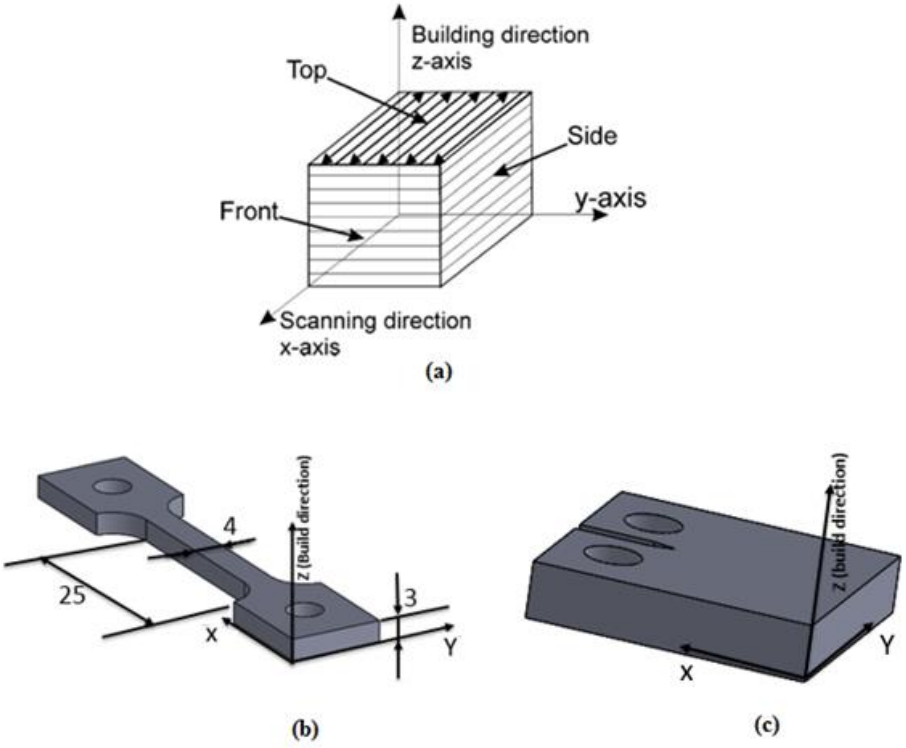


**Figure 47: Sample fabrication: (a) scanning strategy employed [2]; (b) & (c) samples produced in X-Y orientation.**

## 3.2. POROSITY TESTS

Bulk porosity measurements were conducted using the Archimedes' principle, which involved recording both the mass and volume measurements of the SLM Ti6Al4V samples and calculating the respective densities. An experimental study carried by Wits *et al*. [36] revealed that the Archimedes' principle and the computer tomography methods gave the same value (though differences could be minor) for the determination of the density of SLM Ti6Al4V samples. The investigation further revealed the importance of both methods as they were considered as non-destructive, volume-based methods whose difference in density/porosity measurement arose from the nature of the tests. On the other hand, the Archimedes' principle only provided general information about the total void content and left out crucial information about the shape and distribution of such voids [48].

In accordance with the ASTM B962-15 (Standard test method for density of compacted or sintered powder metallurgy (PM) products using Archimedes' principle), the SLM Ti6Al4V samples were first weighed in air, followed by 30 minutes of oil impregnation at room temperature to seal off surface porosity. Lastly, the impregnated samples were weighed while fully immersed in distilled water contained in a glass beaker. (Between 0.05 and 0.1 volume percent of a wetting agent was added to reduce the effect of surface tension.) The part density was measured using the equation:

$$D_s = \frac{A\rho_w}{B - F}$$ ***(Equation 2: Determination of density using Archimedes' principle [64])***

where: $A$ was the mass of the SLM Ti6Al4V sample, $\rho_w$ was the density of water in g/cm$^3$ at a specific determined temperature, $B$ was the mass of the oil-impregnated sample and $F$ was the mass of the oil-impregnated sample immersed in distilled water.

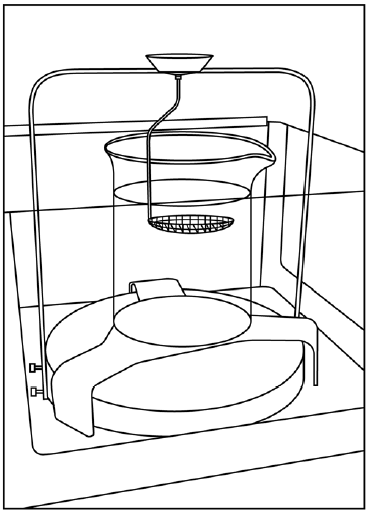

**Figure 48: Porosity measurement apparatus**

The porosity of the SLM Ti6Al4V sample was then calculated using $porosity = 1 - \frac{D_s}{D} \times 100$, where $D_s$ was the density of the SLM part and $D$ was the density of a fully dense part.

### 3.3. MECHANICAL TESTING

Mechanical tests were carried out to investigate the mechanical integrity of the SLM Ti6Al4V alloy corresponding to the observed microstructure and to compare with titanium alloys produced by conventional methods. In this project three mechanical tests were carried out, the uniaxial tensile test, the fatigue crack growth rate (FCGR) test and the fracture toughness test. At least three (3) repeat tests were done for each set of parameters.

#### 3.3.1. Tensile testing

The SLM Ti6Al4V samples were manufactured using parameters as presented in Table 5. All samples were produced with the tensile axis in the XY-direction (parallel to the scan direction, X-axis) with respect to the build direction (Z-direction) as shown previously in Figure 47(b).

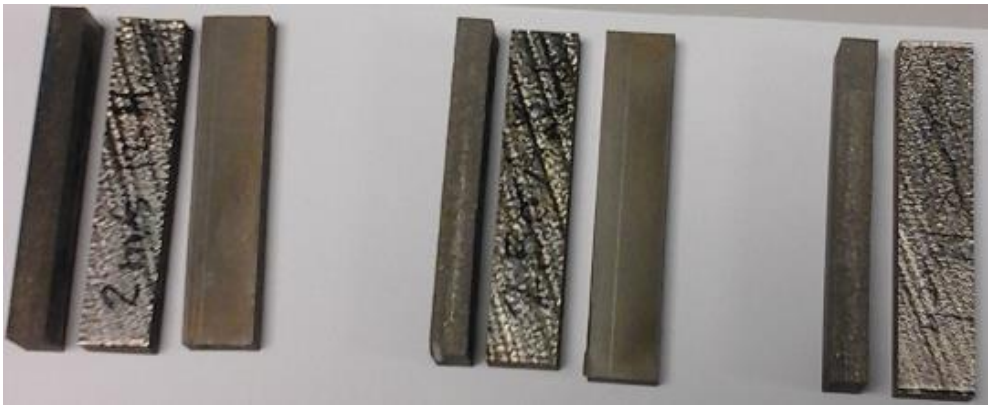

**Figure 49: The SLM Ti6Al4V tensile samples fabricated in the X-Y direction**

The SLM Ti6Al4V tensile samples were fabricated as bars with dimensions of 67 mm x 14 mm x 7 mm (as depicted in Figure 49) and were machined to dog-bone tensile specimens, shown in Figure 50, in line with the ASTM E8/E8M standard. Because of the poor surface integrity of the SLM fabricated parts, tensile specimens were machined and ground to a fine surface finish to reduce or eliminate poor ductility that could have arisen owing to poor surface finish, as reported by Formanoir *et al*. [41].

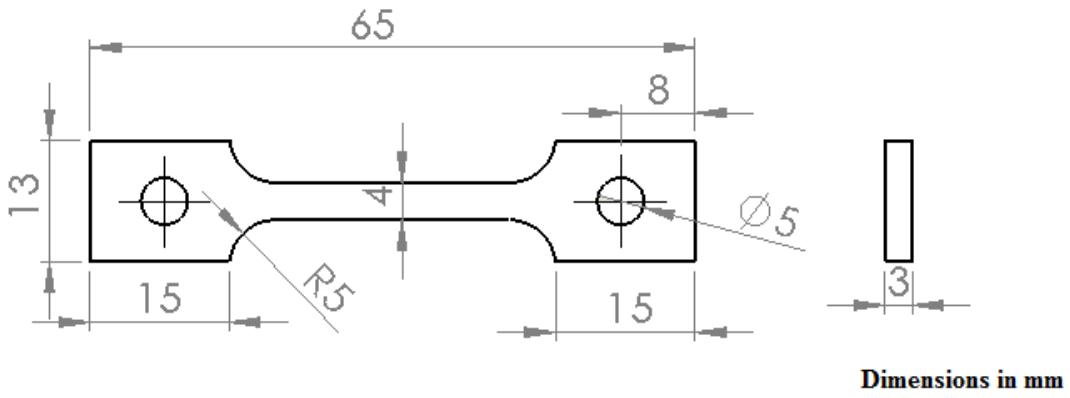


**Figure 50: The tensile specimen geometry**

The geometry shown in Figure 50 was chosen to facilitate efficient pin joints between the specimen and the grips of the tensile tester, as sub-sized specimens had to be machined owing to the dimensional constraints of the produced SLM Ti6Al4V samples. Two of the machine's grips had to be redesigned and machined using the M300 ultra high strength steel to accommodate the sub-sized samples on the Zwick universal tester.

Tensile testing was carried out using the Zwick universal tester. The equipment is shown in Figure 51. Hardened and ground pins with Vickers hardness 698 (HV = 698), corresponding to Rockwell hardness number 60, were used to facilitate a pin joint between the tensile tester and the tensile specimens.

The Zwick universal tester consists of a movable cross head and a stationary load cell. A suitable preload (50 N) was introduced to take up slack in the test setup prior to commencing the tensile test to failure. The specimen's gauge length (extensometer) was set to 22 mm with a cross sectional area of approximately 12 $mm^2$ (3 mm x 4 mm) and the extensometer used up to fracture. The cross head was set to move at 1 mm/min, in accordance with the ASTM E8/E8M standard. From the uniaxial tensile test results the elastic modulus (E), the ultimate tensile strength (UTS), 0.2% proof stress ($\sigma_y$) as well as the percentage elongation, were measured.

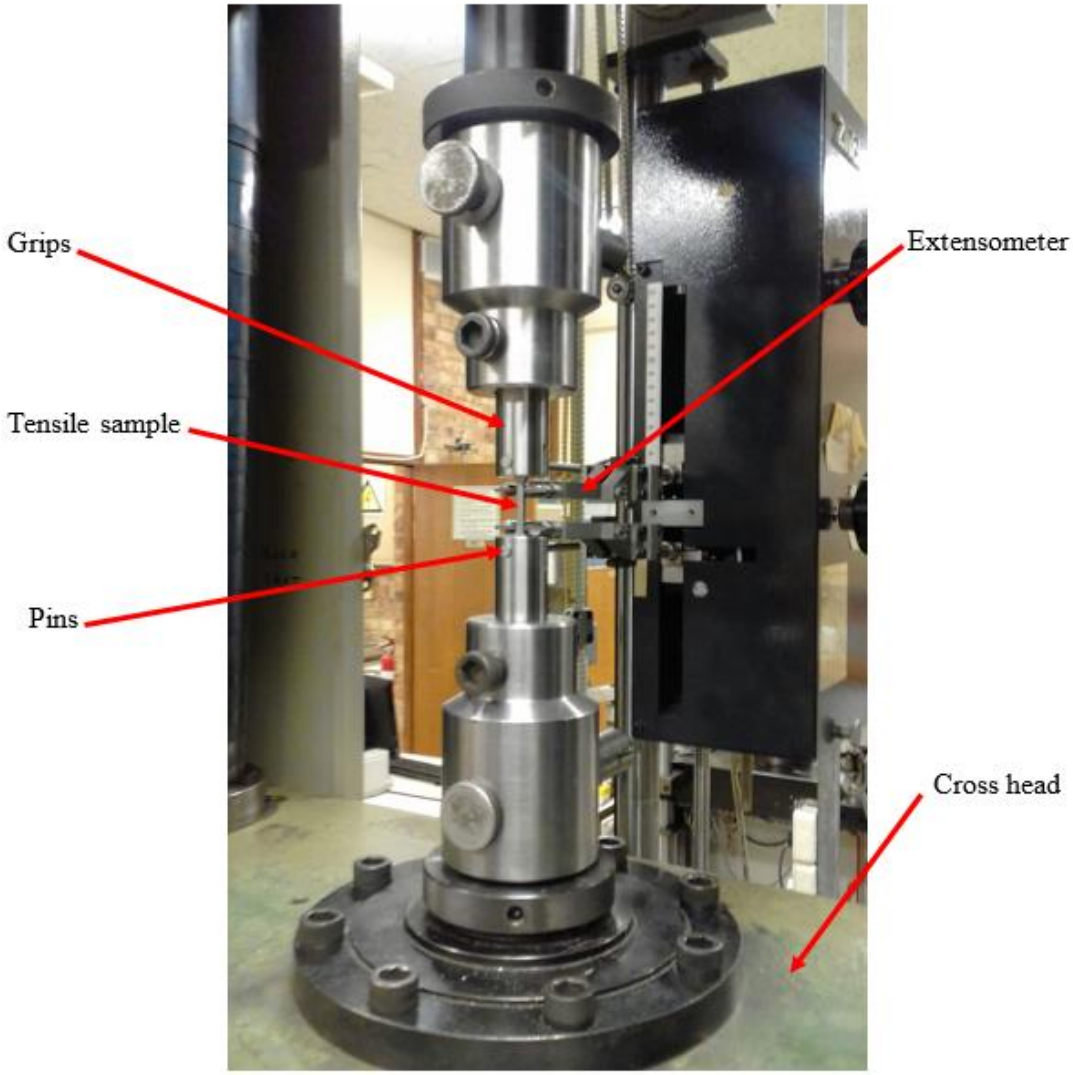


**Figure 51: Tensile testing experimental apparatus**

### 3.3.2. Fatigue crack growth rate (FCGR) testing

FCGR specimens were produced using parameters as presented in Table 6 and in the XY plane and parallel to the scan direction (X-axis), with respect to the build direction (Z-axis), as indicated in Figure 47(c). The FCGR measurement grid was machined in line with the ASTM 647 standard, as shown in Figures 52(a) and 52(b). The sample notch was produced using Electric Discharge Machining (EDM) wire cutting technology.

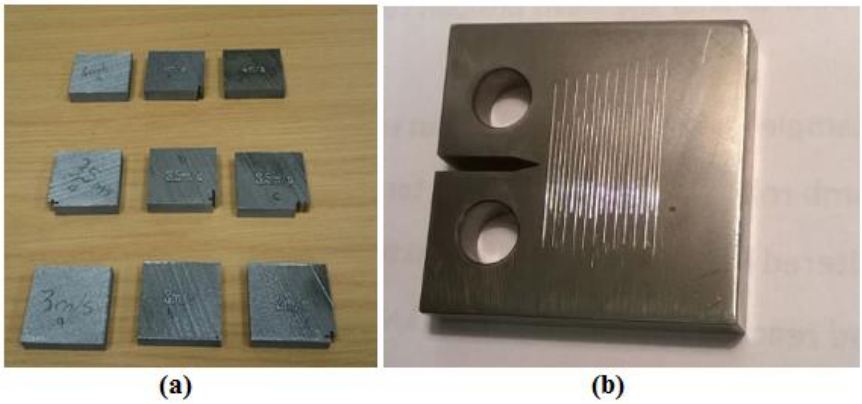


**Figure 52: The SLM Ti6Al4V FCGR samples: (a) as build; (b) After machining**

After machining to dimensions in accordance to the ASTM 647 standard, as shown in Figure 52, the FCGR samples were ground, using 800, 1200, 2400 and 4000 grit silicon abrasives consecutively. This gave rise to a smooth mirror-like surface finish, line patterns were made at 0.5 mm intervals from the notch for the crack propagation inspection during testing, as shown in Figure 52(b).

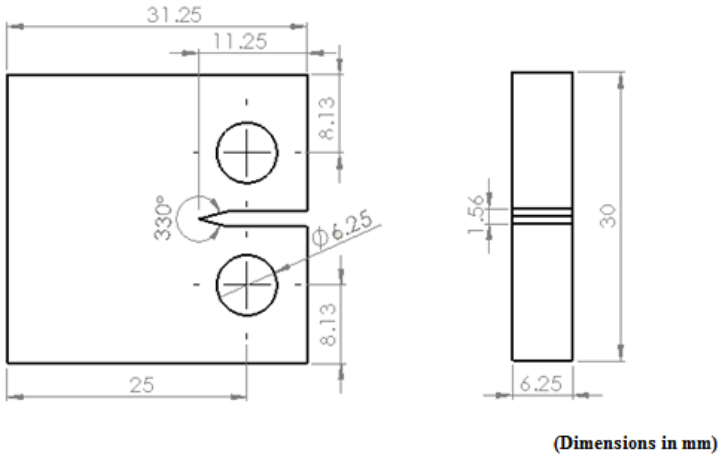


**Figure 53: The FCGR specimen dimensions**

The pre-crack growth and the actual FCGR measurement were carried out using a 45 kN servo-hydraulic machine shown in figure 54. A 1 mm long pre-crack was developed at the notch root by a fully reversed cyclic loading at 7 Hz and the crack length was monitored visually using a camera system, as shown in Figures 54(a and b).

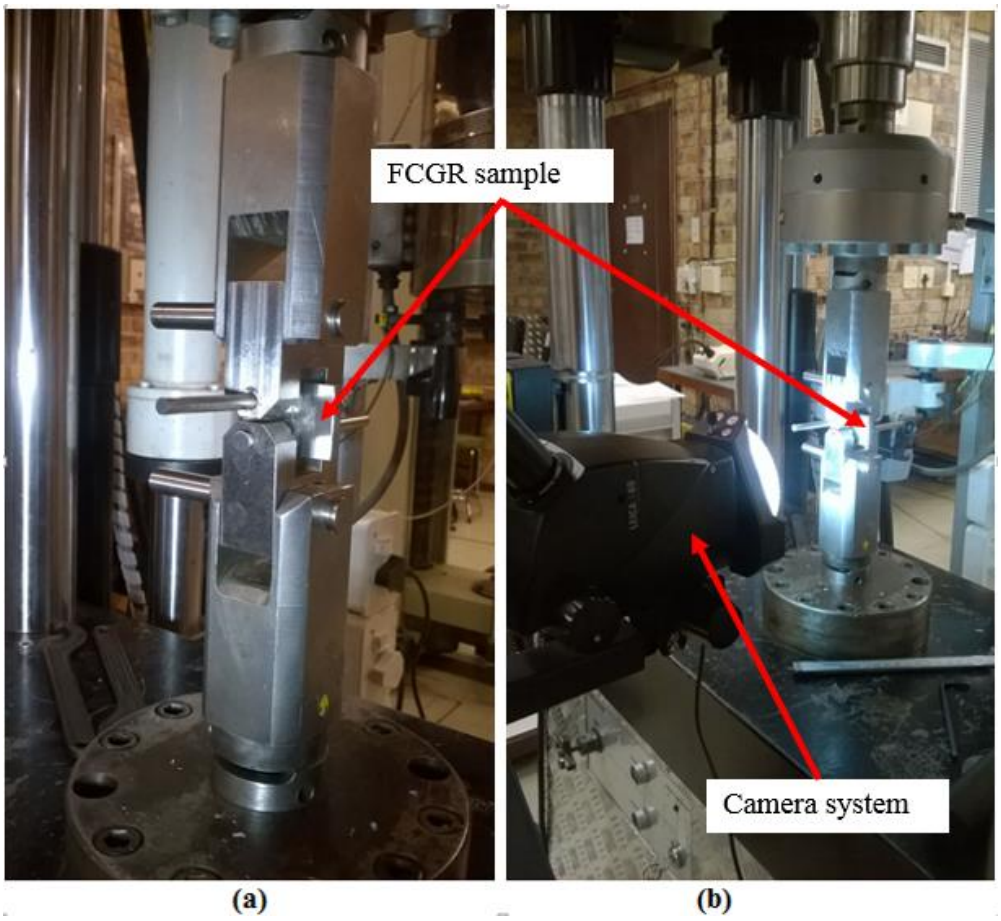


**Figure 54: The FCGR apparatus: servo-hydraulic test machine equipped with 45 kN load cell.**

The actual FCGR measurements were carried out using a cyclic load in tension (R = 0.1) with a fixed cyclic frequency of 5Hz and fixed amplitude $\Delta P$. The crack propagation was visually inspected by the camera system.

### 3.3.3. Fracture toughness testing

Fracture toughness specimens were produced using parameters as presented in Table 6, with variation in laser scan speed from 3.0 m/s to 4.0 m/s (3.0, 3.5 and 4.0 m/s) and in the XY plane, parallel to the scan direction (X-axis) with respect to the build direction (Z-axis), as indicated in Figure 47. Fabricated blocks with dimensions of 40 mm x 40 mm x 15 mm were machined in line with the ASTM E399 standard, as shown in Figures 55(a) and 55(b). The sample notch was produced using Electric Discharge Machining (EDM) wire cutting technology.


**Figure 55: The SLM Ti6Al4V fracture toughness samples: (a) as build; (b) After machining**

Figure 56 illustrates the dimensions used to machine the fracture toughness samples in accordance with the ASTM E399 standard. The surface roughness ($R_a$) values were inspected using the optical profilometer and they conformed to the ASTM E399 standard.

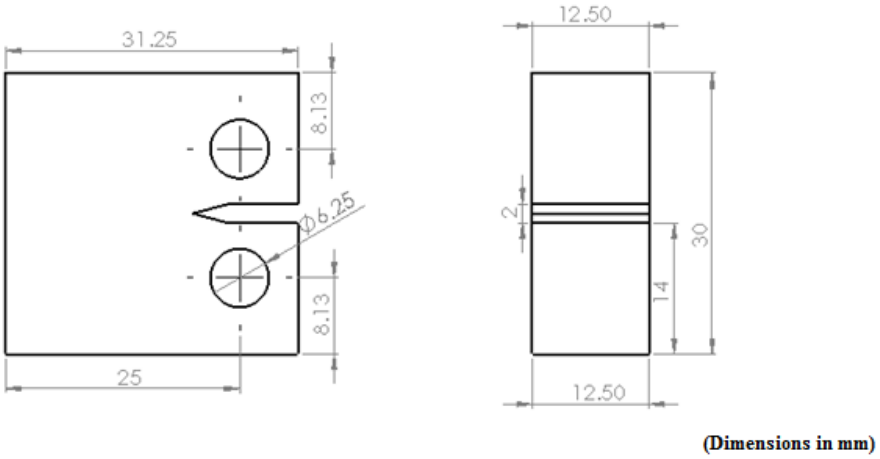


**Figure 56: The fracture toughness specimen dimensions**

Figure 57 illustrates the apparatus used to carry out the fracture toughness test. A 7 mm long pre-crack was developed and monitored visually using a camera system. After pre-crack development, fracture toughness was measured in tension at a displacement speed of 1 mm per minute until the specimen fractured. The fracture toughness test conditions adhered to the ASTM E399 standard.


**Figure 57: The fracture toughness apparatus**

After the fracture toughness testing, all the relevant raw data were extracted from the machine's data acquisition system and analysed in accordance with the ASTM E399 for proper validation of the results and hence a determination of the fracture toughness of the samples.

### 3.3.4. Three-point-bend fatigue testing

Three-point bend fatigue testing was carried out to investigate the role porosity played in the mechanical properties of SLM Ti6Al4V samples. Samples were fabricated by SLM at 3 m/s and 4 m/s laser scan speed in bars with dimensions of 13 mm x 13 mm x 65 mm, from which three-point bend fatigue samples were machined as rods with 12 mm diameter and 65 mm length. Note that the bars were fabricated with the longer axis in the XY-direction (parallel to the scan direction, X-axis) with respect to the build direction (Z-direction).

The actual test was carried out on a 45 kN servo-hydraulic machine, using a cyclic load at 10 Hz in compression (R = -0.1) and with fixed amplitude $\Delta P$. Samples were exposed to cyclic compressive loads with corresponding stresses between 1200 MPa to 1400 MPa for 100 000 cycles and with a span length (S) of 40 mm to provide at least 10 mm overhang at both ends.

The crack initiation and propagation were monitored using the camera system, in conjunction with a 45° mirror, as shown in Figure 58**.**

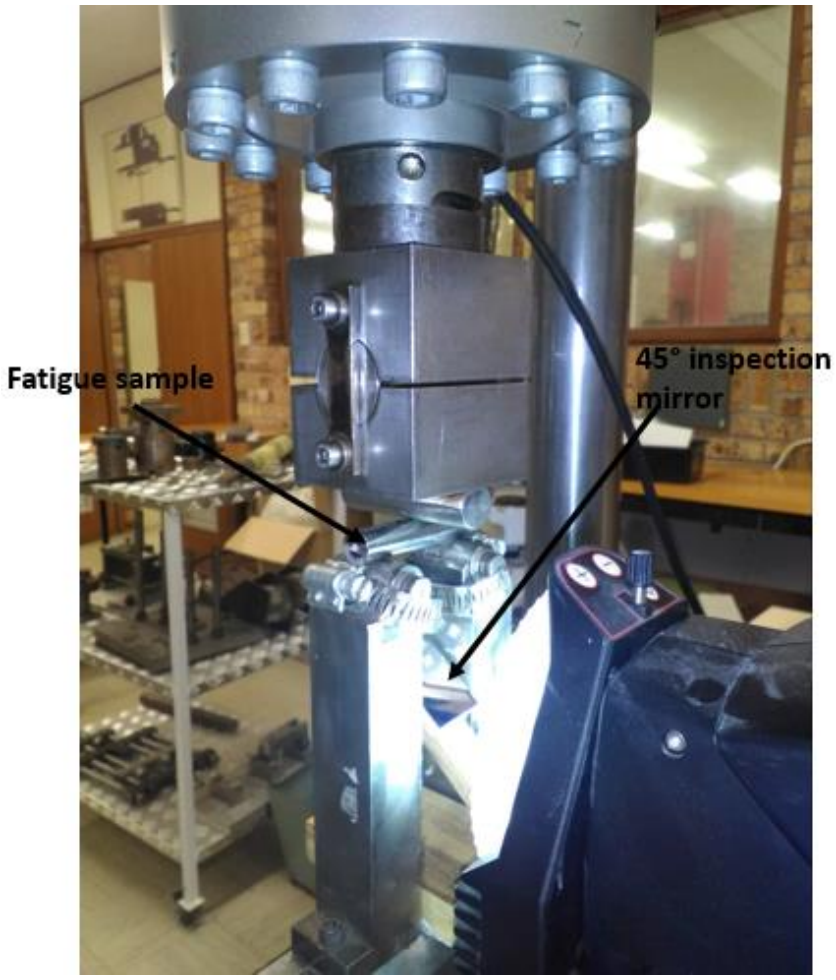


**Figure 58: The three-point bend test apparatus**

Prior to testing, samples were first quantitatively investigated for porosity and other surface defects, using X-ray micro computed tomography, which showed the spatial distribution of all micro pores and enabled the identification of the position of the largest pore(s) in each sample. Moreover, samples were polished to a mirror-like surface finish using abrasive silicon carbide papers up to 4000 grit to eliminate any surface defects before the X-ray micro computed tomography scans were carried out.

## 3.4. METALLURGICAL INVESTIGATIONS

Metallurgical samples were prepared to investigate the microstructural integrity of the SLM Ti6Al4V samples before and after fracture. The microstructural characterisation, both parallel and perpendicular to the build direction, was performed using the bright field light microscope, whereas the tensile fractured surfaces were investigated using secondary electron imaging in the scanning electron microscope (SEM).

### 3.4.1. Sample preparation for optical light microscopy

Sample preparation for metallurgical investigation can generally be classified into sectioning, grinding, polishing and etching (where necessary). The SLM Ti6Al4V samples were prepared as briefly represented in Table 6.

**Table 6: Grinding and polishing steps for Ti6Al4V alloy**

| Process | Abrasive medium | Speed (rpm) | Applied force (N) | Lubricating medium | Duration (minutes) |
|---|---|---|---|---|---|
| Grinding | SiC 800 | 150 | 30 | Water | 5 |
| | SiC 1200 | 150 | 30 | Water | 5 |
| Polishing | MD DUR/DAC | 150 | 30 | 9µm diamond suspension | 15 |
| | MD DUR/DAC | 150 | 30 | 3µm diamond suspension | 5 |
| | MD NAP | 150 | 30 | Attack solution | 5 |
| | PG – Pap #120 | 150 | 30 | Water | 5 |

#### 3.4.1.1. Sectioning

A small representation of each sample was made through sectioning by the EDM wire cutter and by the abrasive cutter where appropriate. Care was taken not to overheat both the cutting tool and the samples by introducing a cutting fluid that served as a coolant. Overheating the specimen can result in unwanted artefacts, such as wrong microstructural representation owing to recrystallisation. For each set process parameter, sections were cut both parallel and perpendicular to the build direction to thoroughly investigate the resulting SLM Ti6Al4V microstructural integrity.

#### 3.4.1.2. Mounting

Samples were selected and mounted using polymeric powder under the influence of both pressure and heat for a short time (14 minutes at 2kN load). This facilitated ease to handle the specimens during grinding and polishing. Sample clips were employed to hold specimens in chosen appropriate positions during mounting, as shown in Figure 59.

**Figure 59: Mounted samples**

#### 3.4.1.3. Grinding

Grinding was done using rotating discs covered with silicon carbide paper with water introduced as a coolant and lubricant. 800 and 1200 grit papers were used respectively, with a slight pressure at the centre of the specimen being applied. The specimens were ground until all the blemishes had been removed, the sample surface was flat, and all the scratches occurred in a single orientation. To move to the next abrasive paper grade, it was necessary to wash the sample in water before moving to the next grade, orienting the scratches from the previous grade normal to the rotation direction. When the grinding was completed, the samples were washed with water and alcohol, followed by warm air drying.

#### 3.4.1.4. Polishing

An automatic polisher was employed for the polishing steps, as presented in Table 7. The main purpose was to get rid of all scratches imposed on the specimen during grinding. The samples were thoroughly cleaned using water and alcohol, followed by warm air drying, before moving on to the final stage. The polished surfaces had a mirror-like profile.

#### 3.4.1.5. Etching (for optical microscopy only)

The purpose of etching is that the etchant attacks surfaces with the highest energy, leading to corrosion on such surfaces and revealing surface defects that can easily be distinguished in optical microscopy.

Furthermore, operations carried out before etching (grinding and polishing) may produce highly deformed thin layers on the surface. These can be removed chemically during etching.

All samples were etched using Kroll's reagent (100 ml distilled water, 2 ml HF and 5 ml $HNO_3$) and rinsed with either hot water or distilled water, thoroughly washed in ethanol and lastly dried, using warm air.

### 3.5. POST SLM STRESS RELIEF HEAT TREATMENT

The undesirable microstructural integrity of the SLM Ti6Al4V alloy can be manipulated using post heat treatment to yield better microstructures that will have correspondingly improved mechanical properties, comparable to the titanium alloys produced by conventional methods. The purpose of performing the post SLM heat treatment, stress relief annealing in this case, is to get rid of the acicular needle-shaped α' – phase morphology, which is martensitic and brittle, and also to relieve residual stresses, which are inevitable owing to the nature of the SLM process.

The SLM Ti6Al4V samples were soaked for four hours at 650°C in a vacuum environment to prevent sample oxidation and then furnace cooled, the set temperature being reached at the rate of 5°C/min as shown in Figure 60. The experimental calibration curve was used to determine the thermostat temperature. In this case, in order to have an actual furnace temperature set at 650°C, the thermostat was set to 750°C, using the experimental calibration curve provided.

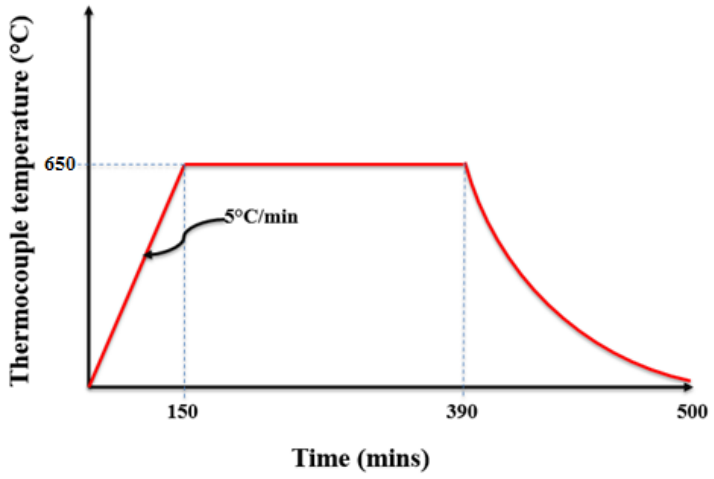


**Figure 60: Stress relief annealing curve carried out for SLM Ti6Al4V samples**

The stress relief vacuum furnace apparatus is shown in Figure 61. This consists of an electric furnace whose maximum operating temperature is 1000°C and the samples are put inside a glass tube. The vacuum is facilitated by a turbo pump and backed up by a vacuum (scroll) pump for consistent vacuum effect. To prevent oxidation, as this would result in undesirable

consequences such as embrittlement, the vacuum environment was regulated in the range *5.4 x $10^{-5}$ mbar – 6.9 x $10^{-6}$ mbar*.

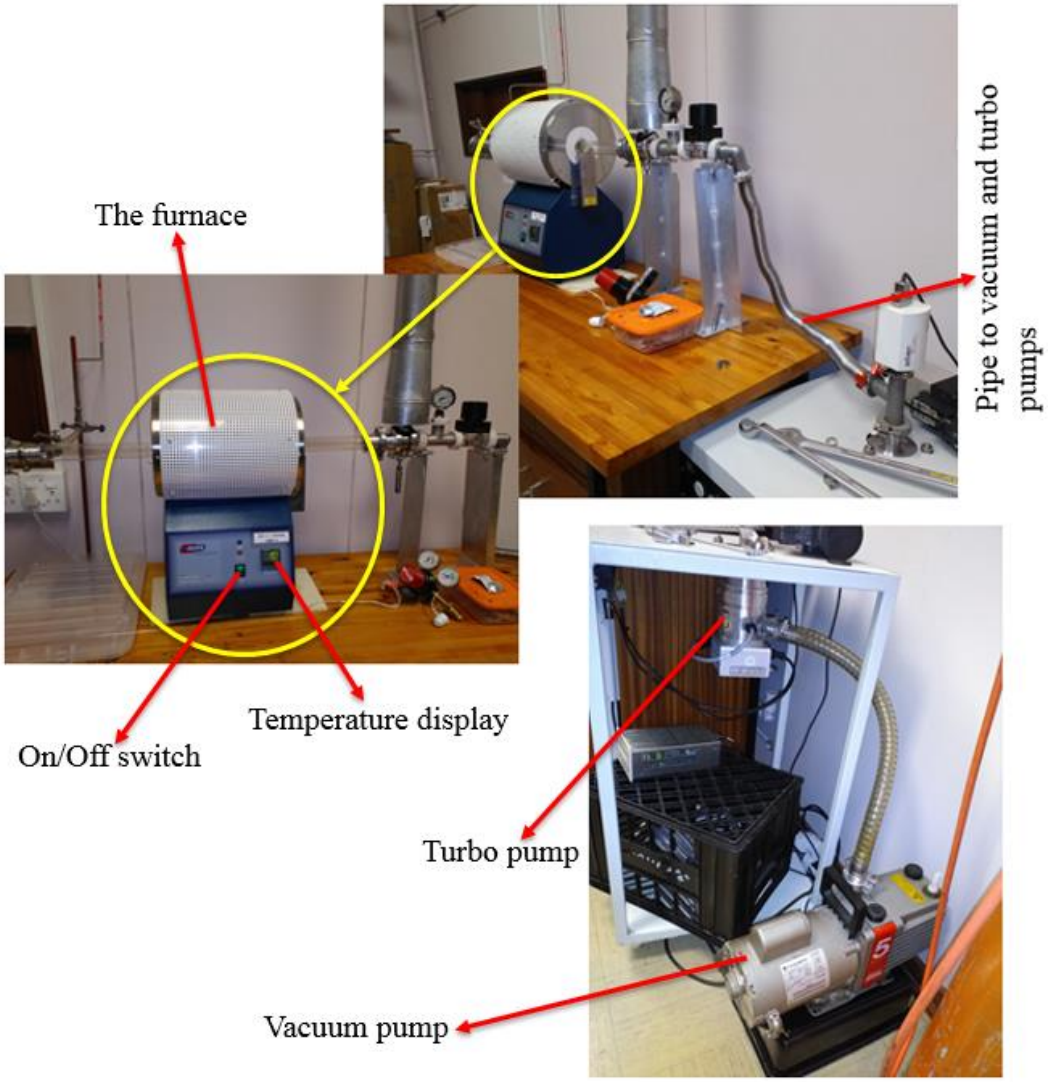


**Figure 61: The vacuum furnace apparatus used for stress relief anneal**

### 3.6. X-RAY COMPUTER TOMOGRAPHY (X-RAY CT) SCAN

The X-ray micro CT scans were carried out at the Stellenbosch University CT Scanner Facility (Department of Forestry). This facility houses a walk-in cabinet for samples in the range of 10 mm up to 300 mm on their longest axis [61]. The equipment is manufactured by General Electric Sensing and Inspection Technologies/Phoenix X-ray in Germany. The micro CT scanner is equipped with two X-ray tubes, the transmission target and the reflection-type target, with maximum operating voltages of 180 kV and 240 kV respectively. This equipment allows users to carry out non-destructive quantification and characterisation of pores and their spatial distribution.

Figure 62 depicts a schematic representation of the X-ray CT scan used in this study. A sample is placed on a platform that is free to rotate and is located between the X-ray source and the detector. The distance between the sample and the detector will depend on the required field of view and resolution. A narrow beam of X-rays is aimed towards the sample as the platform rotates, producing signals that are picked up by the detector located opposite the X-ray source and transmitted to the data acquisition system. After a complete specimen/platform rotation the computer acquisition system constructs a 2D image slice (tomographic image) and the image is temporarily stored. The platform is moved by a minute increment for the next scan to commence. The X-ray scan is then repeated as before to produce another tomographic image. This is done repeatedly until the desired area is fully scanned.

Once the sample is fully scanned, it is removed from the platform and the Volume Graphics VGStudioMax 2.2 software package is used to reconstruct stacked images to produce a full 3D image.

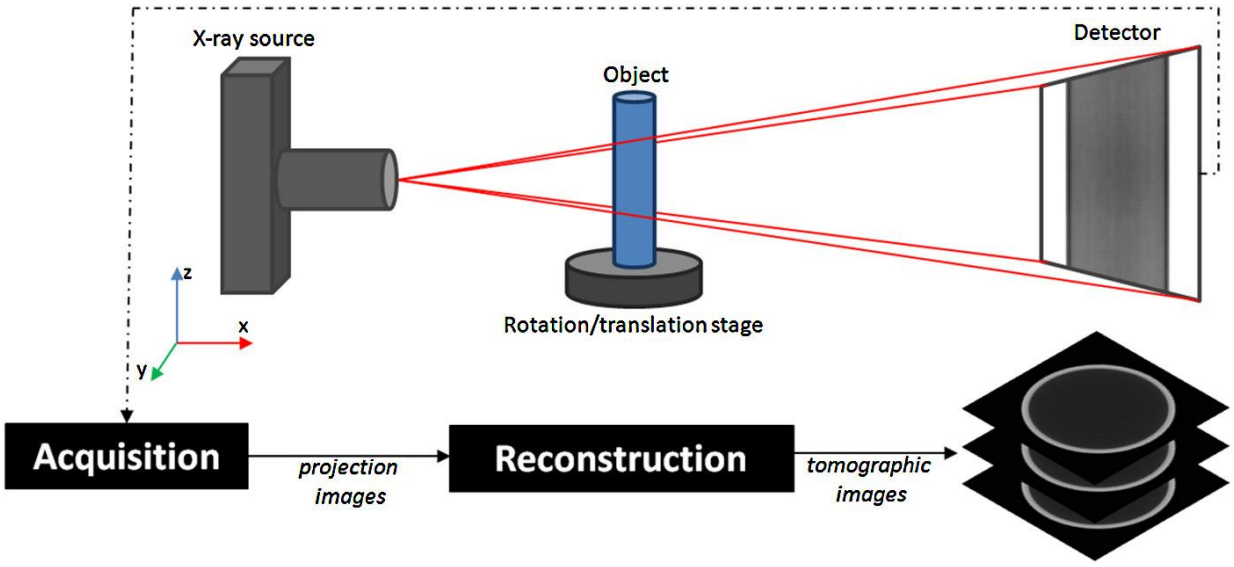


**Figure 62: The X-ray CT schematic [50].**

The X-ray micro CT scans reported were carried out with the 160 kV X-ray source and up to 120 µA current, with the beam being filtered by a 0.5 mm copper beam filter with 1000 stacked layers per image. Scans with voxel size of approximately 8 µm were carried out in this study, with a resolution of 16.67 µm to pick up pores that were more than 50 µm in diameter. The X-ray scanner field of view was restricted within the gauge length or area of interest, so that the effects of pores could be quantitatively investigated, as shown in Figure 63.

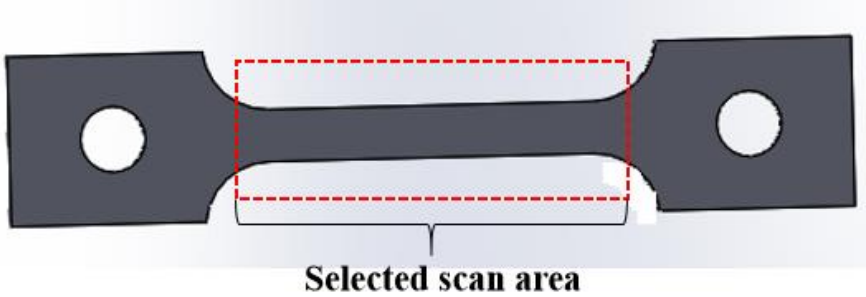


**Figure 63: Selected CT scan area on the tensile sample**

Post scan analysis was performed using the Volume Graphics VGStudioMax 2.2 software package, which contained a full volume of data (in Microsoft Excel) and myVGL, which is a free viewer programme, useful in reviewing all the tomographic images in the 2D and 3D reconstructed images. Standard segmentation methods were employed for porosity analysis, whereby the desired area was isolated so that the custom defect mask method could be applied. The software was also used to identify the large pore(s) through the stacked tomographic images, which was then exported and saved for reporting purposes.

The volume of data captured can be used to extract quantitative information on pore size and its location, as well as a pore's sphericity, which can be plotted in Excel for the user to have better insight into the location of the biggest pore within the scanned area. Table 7 shows a portion of data received from the software, to serve as an example.

**Table 7: Example of part of the data captured by the Volume Graphics software.**

| Diameter [mm] | Volume [mm³] | Surface [mm²] | Sphericity | Pos. x [mm] | Pos. y [mm] | Pos. z [mm] | Projected area (yz-plane) [mm²] | Projected area (xz-plane) [mm²] | Projected area (xy-plane) [mm²] |
|---|---|---|---|---|---|---|---|---|---|
| 0.4177 | 0.00804 | 0.36444 | 0.53 | -1.6017 | -1.5547 | -7.4023 | 0.0616 | 0.07236 | 0.04361 |
| 0.5188 | 0.01504 | 0.63278 | 0.47 | -0.7051 | -1.411 | -13.2885 | 0.10306 | 0.10451 | 0.07521 |
| 0.2359 | 0.00238 | 0.14333 | 0.6 | -1.6677 | -1.315 | -11.023 | 0.02361 | 0.02847 | 0.02229 |
| 0.5492 | 0.01349 | 0.64167 | 0.43 | 1.5809 | -1.2613 | -10.0737 | 0.0884 | 0.12618 | 0.07181 |
| 0.1826 | 0.00141 | 0.09333 | 0.65 | 0.1657 | 1.002 | -5.3575 | 0.01465 | 0.01986 | 0.01361 |
| 0.5145 | 0.00942 | 0.44556 | 0.48 | 0.1763 | -1.4068 | 2.7133 | 0.06722 | 0.09139 | 0.05597 |
| 0.2392 | 0.00185 | 0.12167 | 0.6 | -0.4808 | -1.5255 | -6.986 | 0.02264 | 0.02472 | 0.01569 |
| 0.2543 | 0.00273 | 0.16 | 0.59 | 0.9845 | -1.3676 | -12.7557 | 0.02493 | 0.03611 | 0.01951 |
| 0.19 | 0.00146 | 0.09667 | 0.64 | 1.6574 | -0.1195 | -9.4243 | 0.01757 | 0.01792 | 0.01396 |
| 0.4673 | 0.0034 | 0.21889 | 0.5 | 1.4224 | -1.3392 | 0.3287 | 0.04139 | 0.04667 | 0.02097 |
| 0.1353 | 0.00056 | 0.04944 | 0.66 | 0.9571 | -1.1474 | -14.626 | 0.00847 | 0.00785 | 0.00924 |
| 0.1655 | 0.00094 | 0.07389 | 0.63 | 1.2254 | 0.5144 | -5.4001 | 0.01257 | 0.01528 | 0.01153 |

| | | | | | | | | | |
|---|---|---|---|---|---|---|---|---|---|
| 0.3406 | 0.00549 | 0.295 | 0.51 | -1.4339 | -1.3525 | -14.0895 | 0.04681 | 0.05444 | 0.03785 |
| 0.309 | 0.00318 | 0.19667 | 0.53 | 1.7942 | -1.3999 | -1.954 | 0.03111 | 0.04097 | 0.02354 |
| 0.2373 | 0.00185 | 0.11944 | 0.61 | -1.11 | -1.3471 | -10.5558 | 0.02222 | 0.02458 | 0.01417 |
| 0.3595 | 0.00378 | 0.22556 | 0.52 | 1.5639 | -1.4894 | 4.8815 | 0.03819 | 0.04625 | 0.02632 |
| 0.2625 | 0.00215 | 0.13778 | 0.59 | 1.1461 | -1.5097 | 4.365 | 0.02069 | 0.03333 | 0.01729 |

From the above data, to identify the large pore within the gauge length (Z-axis), the plot of pore diameter versus the position in Z-direction (Pos. Z) is used, as shown in Figure 64.

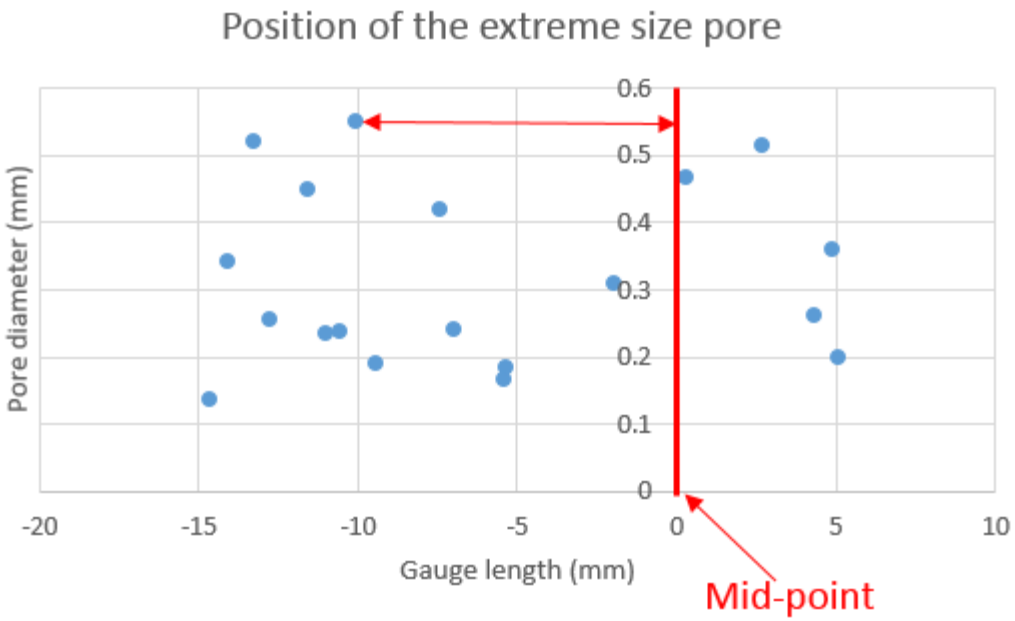


**Figure 64: Position of the extreme size pore (example)**

The large pore is as highlighted in Table 8 and can be further seen on the plot in Figure 64 (indicated by the red arrow showing its position with reference to the mid-point of the scanned area). It is also possible to export the porosity distribution data into an Excel spreadsheet to customise the pore size versus the number of counts.

The sphericity ratio, which is the comparison between a perfect sphere (S = 1) and an irregular shaped profile (S ≤ 0.7), was calculated using the equation:

$$S = \frac{\pi^{1/3}(6V)^{2/3}}{A} \qquad (\textit{Equation 3: The sphericity ratio [51, 5]})$$

where $V$ and $A$ were the volume and area of the pore in question. This quantity can also be plotted as a function of the pore diameter, to indicate pictorially the shape of pores present within a sample.

# 4. EXPERIMENTAL RESULTS

This chapter comprehensively presents the observed experimental results that characterise the mechanical and microstructural properties of SLM Ti6Al4V specimens, fabricated at distinct laser scan rates while other process parameters were kept constant. A thorough analysis of the results follows in Chapter 5.

## 4.1. BULK SAMPLE CHARACTERISATION

For one to appreciate the integrity of the "as-built" SLM Ti6Al4V specimens produced, both the microstructural investigation and porosity tests were conducted. The microstructural investigations were conducted using the light optical microscope in bright field mode, while porosity tests were carried out using the Archimedes' principle. X-ray computed tomography scans were further used for the quantitative analysis of porosity in the SLM Ti6Al4V samples.

### 4.1.1. Porosity analysis of SLM Ti6AlV samples

Prior to the machining of various mechanical test specimens in accordance with ASTM standards, bulk sample densities were determined using the Archimedes' principle. The densification varied from 92% to near 100% for all the bulk SLM Ti6Al4V samples, as presented in tables 8 to 10. Some of the as-built SLM Ti6Al4V bars presented in table 10 were further machined to produce three (3) axial tensile test samples per bar.

**Table 8: Bulk density measurements for fracture toughness SLM Ti6Al4V samples**

| laser scan speed (m/s) | Sample number | mass of sample in air, A (kg) | Mass of oil-impregnated sample, B (kg) | Mass of oil-impregnated sample immersed in water, F (kg) | Density of sample (kg/m$^3$) | Densification |
|---|---|---|---|---|---|---|
| 3 | 1 | 0.104 | 0.1042 | 0.0803 | 4342.54 | 0.98 |
| | 2 | 0.104 | 0.1041 | 0.0802 | 4342.54 | 0.98 |
| 3.5 | 1 | 0.104 | 0.1041 | 0.0801 | 4338.31 | 0.98 |
| | 2 | 0.104 | 0.1041 | 0.0801 | 4324.45 | 0.98 |
| 4 | 1 | 0.106 | 0.106 | 0.082 | 4393.75 | 0.99 |
| | 2 | 0.103 | 0.1042 | 0.08 | 4233.73 | 0.96 |
| | 3 | 0.106 | 0.106 | 0.082 | 4393.75 | 0.99 |

All density measurements were carried out at room temperature (22°C - 24°C) and the density of the distilled water used was $\rho_w$ = 997.95 kg/m$^3$. The density of wrought Ti6Al4V was taken as 4420 kg/m$^3$.

**Table 9: Bulk density measurements for the FCGR SLM Ti6Al4V samples**

| Laser scan speed (m/s) | Sample number | Mass of sample in air, A (kg) | Mass of oil-impregnated sample, B (kg) | Mass of oil-impregnated sample immersed in water, F (kg) | Density of sample ($kg/m^3$) | Densification |
|---|---|---|---|---|---|---|
| 3 | 1 | 0.064 | 0.065 | 0.0501 | 4286.50 | 0.97 |
| | 2 | 0.068 | 0.0682 | 0.0527 | 4378.10 | 0.99 |
| | 3 | 0.066 | 0.0652 | 0.05 | 4333.20 | 0.98 |
| 3.5 | 1 | 0.069 | 0.0691 | 0.0533 | 4358.14 | 0.99 |
| | 2 | 0.066 | 0.068 | 0.0528 | 4333.20 | 0.98 |
| | 3 | 0.062 | 0.0635 | 0.0489 | 4237.87 | 0.96 |
| 4 | 1 | 0.067 | 0.0675 | 0.052 | 4313.72 | 0.98 |
| | 2 | 0.066 | 0.068 | 0.0528 | 4333.20 | 0.98 |
| | 3 | 0.065 | 0.066 | 0.051 | 4324.45 | 0.98 |

**Table 10: Bulk density measurements for the SLM Ti6Al4V uniaxial tensile test samples**

| Laser scan speed (m/s) | Sample number | Mass of sample in air, A (kg) | Mass of oil-impregnated sample, B (kg) | Mass of oil-impregnated sample immersed in water, F (kg) | Density of sample (kg/m3) | Densification |
|---|---|---|---|---|---|---|
| 1.5 | 1 | 0.041 | 0.0412 | 0.03181 | 4357.40 | 0.99 |
| | 2 | 0.04 | 0.0402 | 0.0311 | 4386.59 | 0.99 |
| 1.75 | 1 | 0.04 | 0.0405 | 0.03109 | 4242.08 | 0.96 |
| | 2 | 0.041 | 0.0411 | 0.0316 | 4306.94 | 0.97 |
| 2 | 1 | 0.042 | 0.0421 | 0.0325 | 4366.03 | 0.99 |
| | 2 | 0.041 | 0.0412 | 0.0318 | 4352.76 | 0.98 |
| | 3 | 0.028 | 0.03 | 0.0232 | 4109.21 | 0.93 |
| | 4 | 0.029 | 0.0312 | 0.0242 | 4134.36 | 0.94 |
| | 5 | 0.028 | 0.03 | 0.0231 | 4049.65 | 0.92 |
| 2.5 | 1 | 0.029 | 0.0312 | 0.0243 | 4194.28 | 0.95 |
| | 2 | 0.029 | 0.031 | 0.0242 | 4255.96 | 0.96 |
| | 3 | 0.028 | 0.0302 | 0.0235 | 4170.54 | 0.94 |
| 3 | 1 | 0.03 | 0.0305 | 0.0235 | 4276.93 | 0.97 |
| | 2 | 0.027 | 0.028 | 0.0216 | 4210.10 | 0.95 |
| | 3 | 0.028 | 0.0291 | 0.0219 | 3880.92 | 0.88 |
| | 4 | 0.04 | 0.0402 | 0.0311 | 4386.59 | 0.99 |
| | 5 | 0.04 | 0.0401 | 0.0309 | 4338.91 | 0.98 |
| 3.5 | 1 | 0.039 | 0.0392 | 0.0302 | 4324.45 | 0.98 |
| | 2 | 0.04 | 0.0403 | 0.0312 | 4386.59 | 0.99 |
| 4 | 1 | 0.04 | 0.041 | 0.0319 | 4386.59 | 0.99 |
| | 2 | 0.038 | 0.0395 | 0.0308 | 4358.86 | 0.99 |

Since the method was volume-based and provided only general information on the porosity of the specimen in question, the X-ray computed tomography (X-ray CT) scan was employed to get more information on the distribution, size and the location of the largest pores. The X-ray CT scans were carried out only on the uniaxial tensile samples and fatigue crack initiation samples, all which were stress relieved and polished prior to the scans.

### 4.1.2. X-ray computed tomography (X-ray CT) scans

A series of ***X-ray CT scans were performed on the stress relieved*** tensile test specimens prior to mechanical testing, as shown in Figure 65 through to Figure 70. Pores ranging from 50 µm and close to 1 mm were detected using the X-ray CT scanner, where most of the smaller pores occurred throughout the scanned volume. In some specimens, the largest pores were isolated from the smaller pores, while in others there were several clustered micro pores next to the surface. It is important to recall that all specimens had been polished to a mirror-like surface finish, using abrasive silicon carbide papers up to 4000 grit, to eliminate any surface defects before the X-ray micro computed tomography scans were carried out.

***Uniaxial tensile test samples fabricated at 3 m/s laser scan speed.***

Figure 65 shows the X-ray CT scan results for the 3D reconstructed views in XZ plane (2D view) of the stress relieved SLM Ti6Al4V uniaxial tensile samples, fabricated at 3 m/s laser scan speed. The largest pores (0.3 mm – 1 mm) appear as red dots within the scanned volume and in some instances, are located next to the surface of the tensile sample. Hence, the sample was prone to premature failure during testing as this could act as a stress concentration area.

Figure 66 further shows pore size distribution parallel to the scanned area and their location along the gauge length, Z-axis. The X-ray CT scan reveals that pores in the range 0.12 mm – 0.16 mm were dominant for all the uniaxial tensile test specimens, while small pores ($\leq$ 0.1 mm in this case) were clustered and distributed throughout the gauge length. The largest pores (0.3 mm – 0.95 mm) were isolated in most of the specimens and a thorough investigation and comprehensive analysis of their location will be presented on the next page.

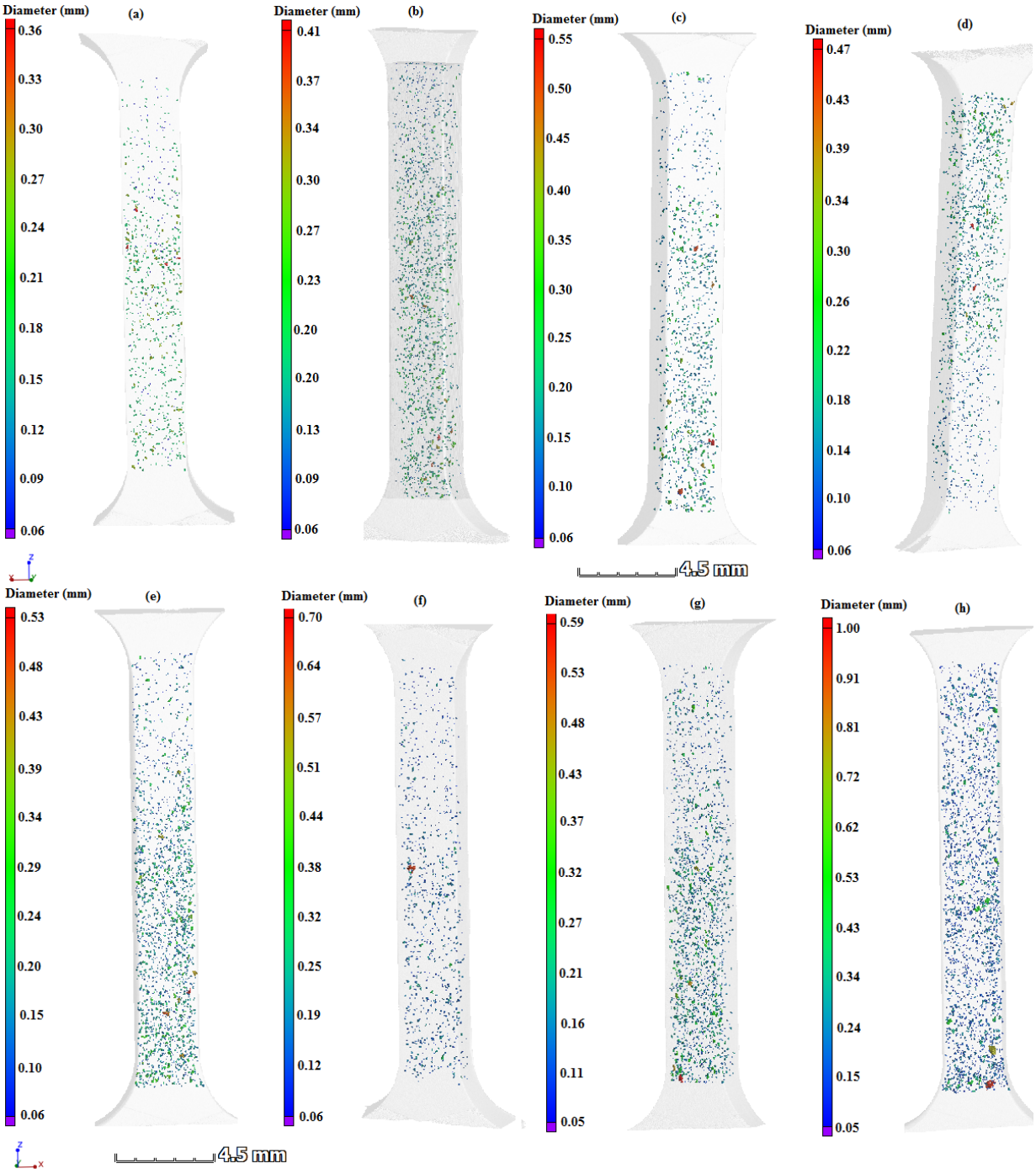


**Figure 65: The X-ray CT scan of stress relieved SLM Ti6Al4V uniaxial tensile samples fabricated at 3 m/s: (a) sample 2; (b) Sample 7; (c) Sample 3; (d) Sample 4; (e) Sample 5; (f) Sample 1; (g) Sample 6; (h) Sample 8.**


**Figure 66: Pore size distribution for stress relieved SLM tensile samples fabricated at 3 m/s: (a) Sample 2; (b) Sample 7; (c) Sample 3; (d) Sample 1; (e) Sample 8.**

Figure 67(a) depicts some of the surface defects (surface pore and crack) revealed by the X-ray CT scan in the stress relieved Ti6Al4V tensile samples fabricated at 3 m/s (sample 1). In addition, 2D images from the stacked X-ray CT slices (shown in Figure 67(b)) reveal near surface pores and clustered pores in some samples. The pores, as indicated in Figure 66, are clustered micro pores evenly distributed throughout the specimen's gauge length. In some cases, the largest pore was isolated and located near the surface of a specimen, as was the case with the specimen in Figure 67b(i).

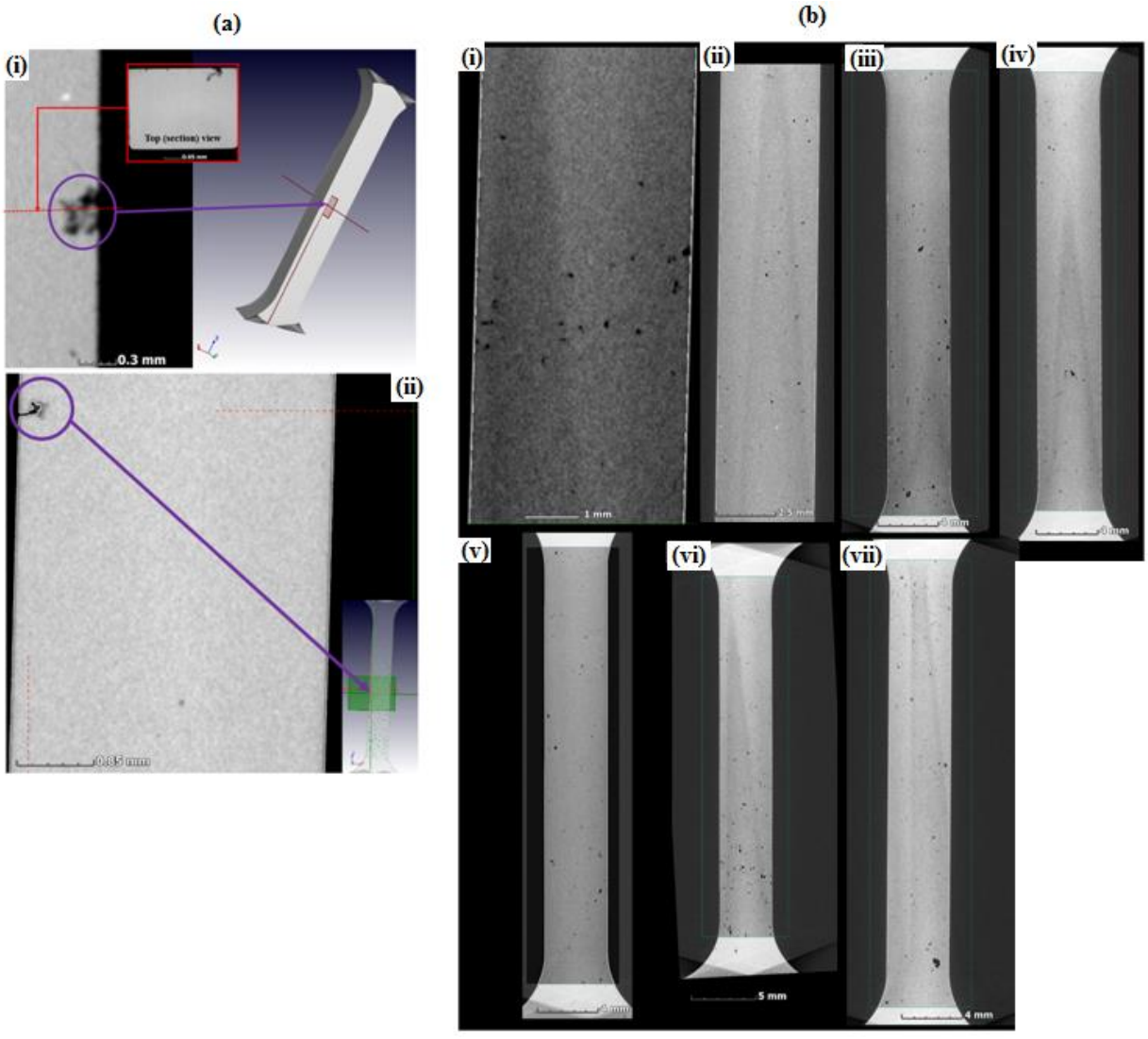


**Figure 67: 2-D X-ray CT scan cross- sections showing porosity on stress relieved SLM Ti6Al4V tensile samples: (a) and b(i) Sample 1; b(ii) Sample 2; b(iii) Sample 3; b(vi) Sample 7; b(vii) Sample 8.**

Figure 65(a), Figure 66(a) and Figure 67b(ii) represent Sample 2 within the stress relieved SLM Ti6Al4V, fabricated at 3 m/s, and show a lower porosity compared to the rest of the samples. This example does not necessarily indicate a trend in porosity versus the laser scan speed, but rather highlights the ability of the X-ray CT method to distinguish the porosity character of different samples.

### *Uniaxial tensile test samples fabricated at 4 m/s laser scan speed*

Figure 68 shows the X-ray CT scans for SLM Ti6Al4V uniaxial tensile samples, fabricated at 4 m/s, in 3D reconstructed views. These specimens were also stressed relieved at 650°C for four hours in a vacuum furnace. In comparing the nature of defects present in specimens fabricated at 3 m/s (Figure 65) and 4 m/s (Figure 68), one can qualitatively observe that the number of pores increased at higher laser scan rates, which may be attributable to less energy density available as the laser scan speed is increased, but this needs thorough investigation.

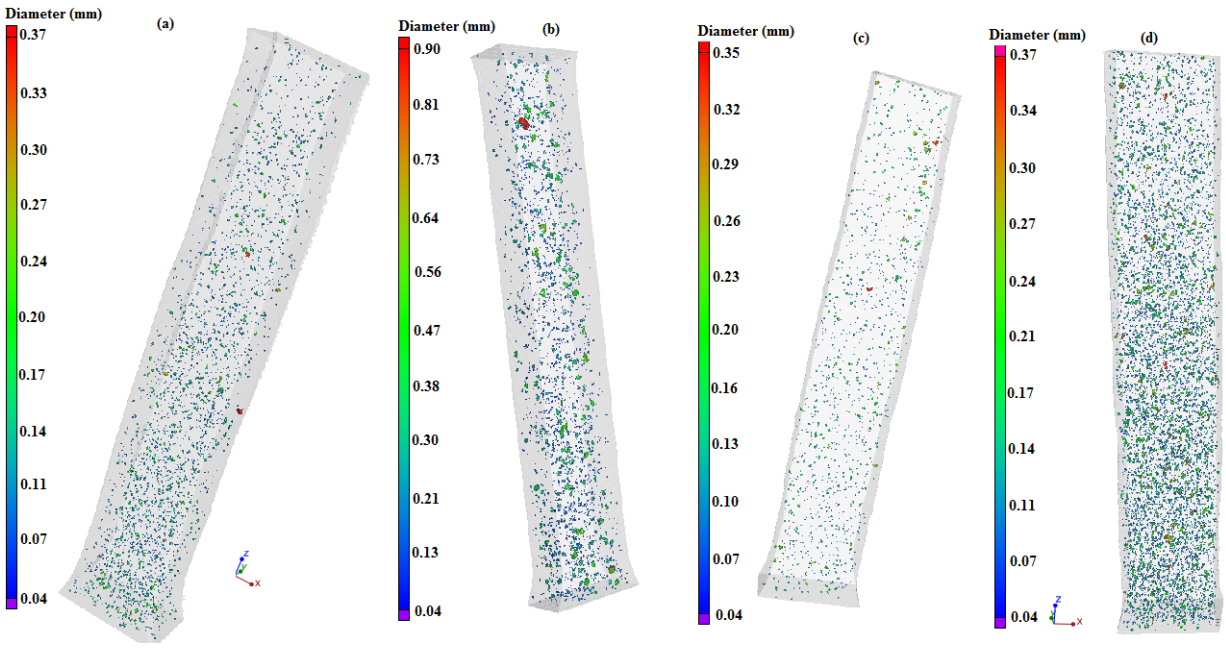


**Figure 68: The X-ray CT scan of stress relieved SLM Ti6Al4V uniaxial tensile samples fabricated at 4m/s: (a) Sample 4; (b) Sample 3; (c) Sample 2; (d) Sample 1**

The pore size distribution plot for the stress relieved SLM Ti6Al4V uniaxial tensile test specimens, fabricated at 4 m/s, is presented in Figure 69. The number of detected pores increased substantially from 80 – 200 counts for specimens fabricated with 3 m/s laser speed to 130 – 470 counts for those fabricated at 4 m/s. Nevertheless, the largest pores were still isolated, as observed previously, while pores less than 0.1 mm were seen clustered and distributed throughout the gauge length, with pores in the range 0.12 mm – 0.14 mm in diameter being dominant. It is important to note at this juncture that for both laser scan speeds (3 m/s and 4 m/s), there existed an isolated large pore close to 1 mm in diameter and its significance will be investigated in the resulting mechanical tests.

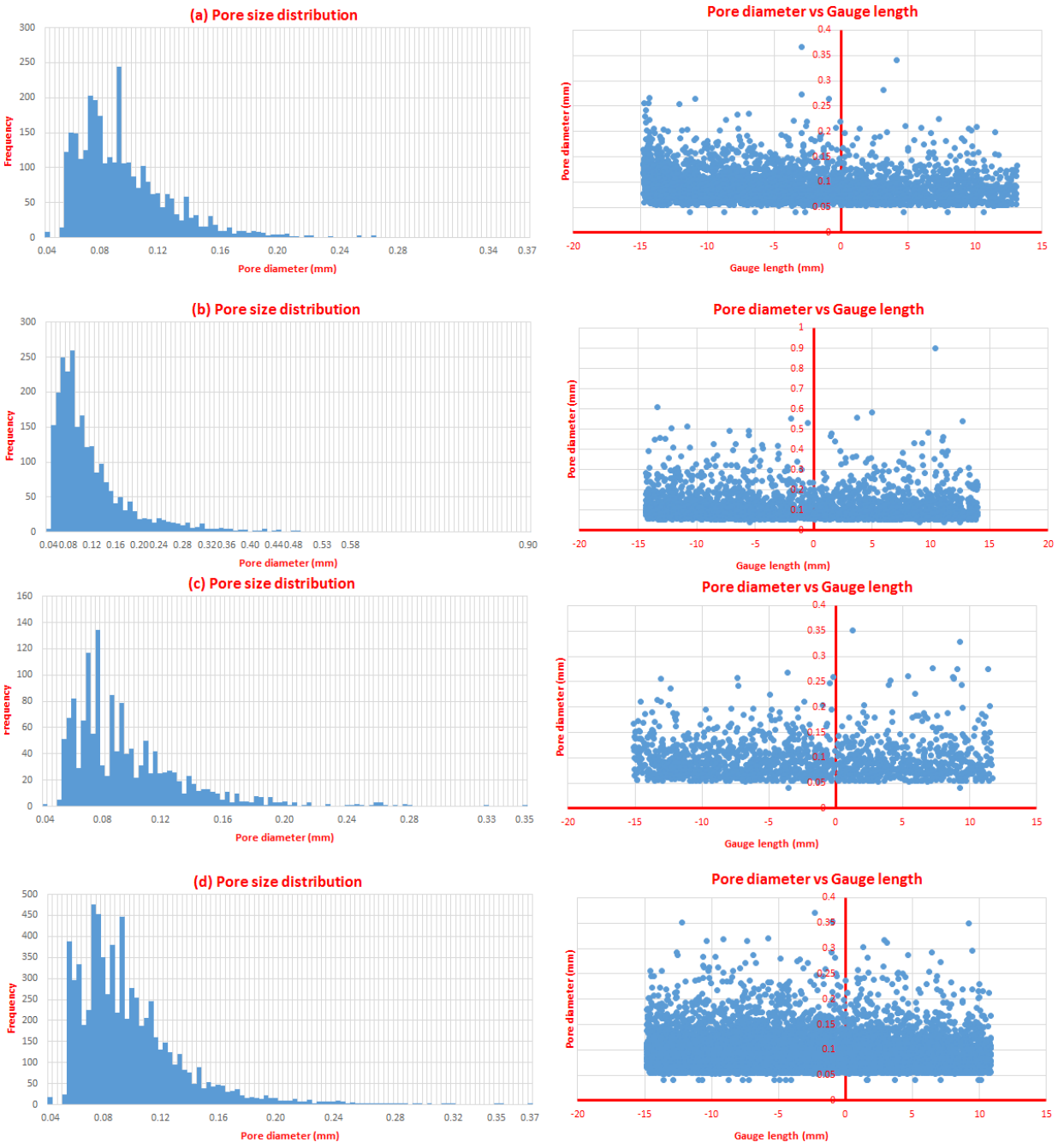


**Figure 69: Pore size distribution for stress relieved SLM tensile samples fabricated at 4 m/s: (a) Sample 4; (b) Sample 3; (c) Sample 2; (d) Sample 1**

Figure 70 shows the 2D image slices extracted from the X-ray acquisition software and reveals SLM process defects near the surface of the uniaxial tensile samples. Figure 70(a) shows that the largest pore in the uniaxial tensile sample was next to the centre of the specimen (X-direction) and this is validated by Figures 68(c) and 69(b), which further show that the large pore was 10 mm from the centre of the specimen along the gauge length (Z-direction).

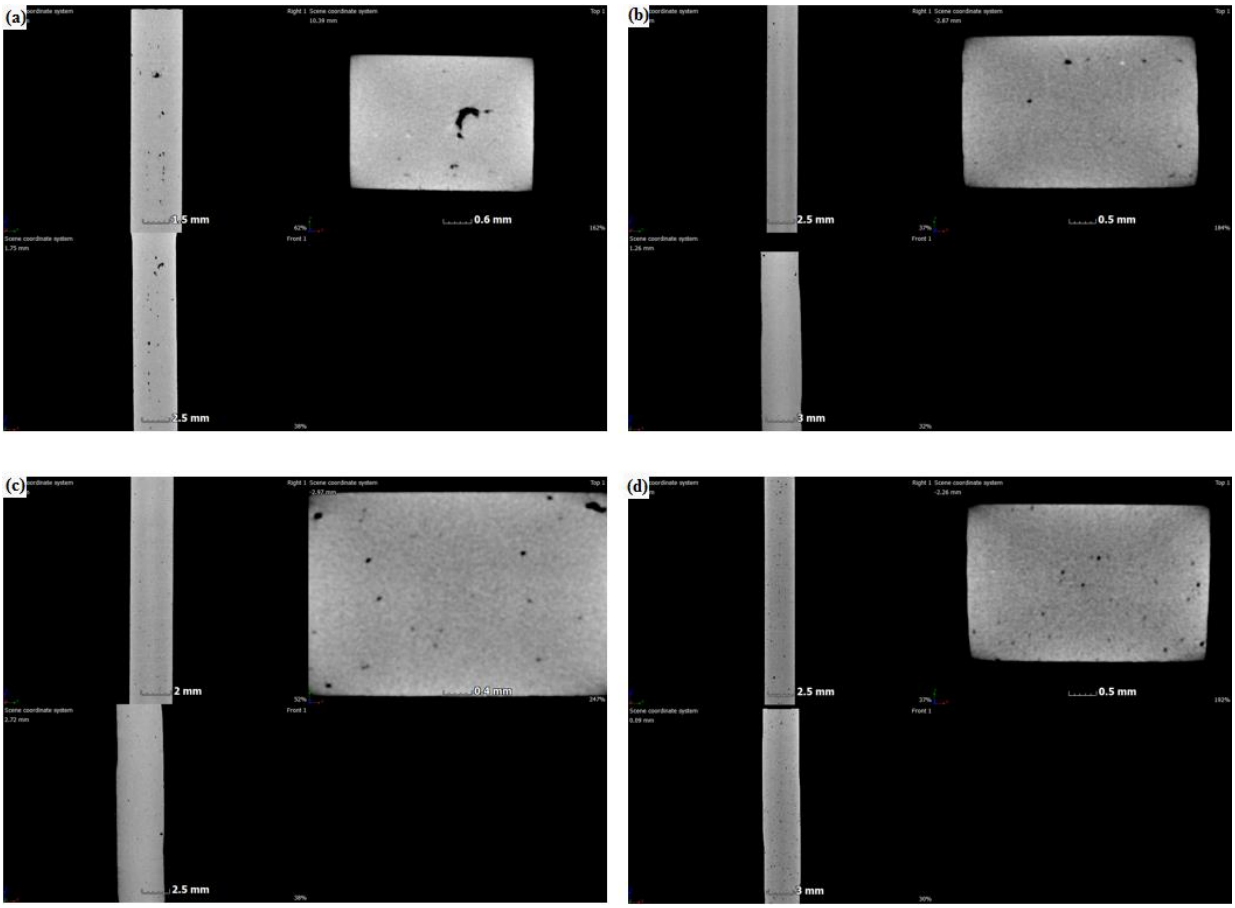


**Figure 70: 2-D slices for the stress relieved SLM Ti6Al4V tensile samples fabricated at 4 m/s: (a) Sample 3; (b) Sample 2; (c) Sample 1; (d) Sample 4**

Apart from the specimens presented in Figures 70(b), 68(c) and 69(c), which correspond to Sample 2, all the specimens fabricated at 4 m/s laser scan rate exhibit considerable clustered micro pores, with some located next to the specimen surface.

Resistance to fatigue crack initiation for the stress relieved SLM Ti6Al4V alloy fabricated at 3 m/s and 4 m/s scan rates had to be investigated to analyse the influence of SLM process defects on fatigue properties. Figure 71 shows three-point bend fatigue crack initiation samples, fabricated at 3 m/s and 4 m/s and stressed relieved at 650°C for four hours in a vacuum, followed by furnace cooling. In the majority of the samples most pores were clustered and located nearer to the sample's surfaces and as Figure 71(h) depicts, there is a clear indication of defects. Clustering of porosity was confined to a single build layer or successive build layers, with pores elongated parallel to the scan direction.

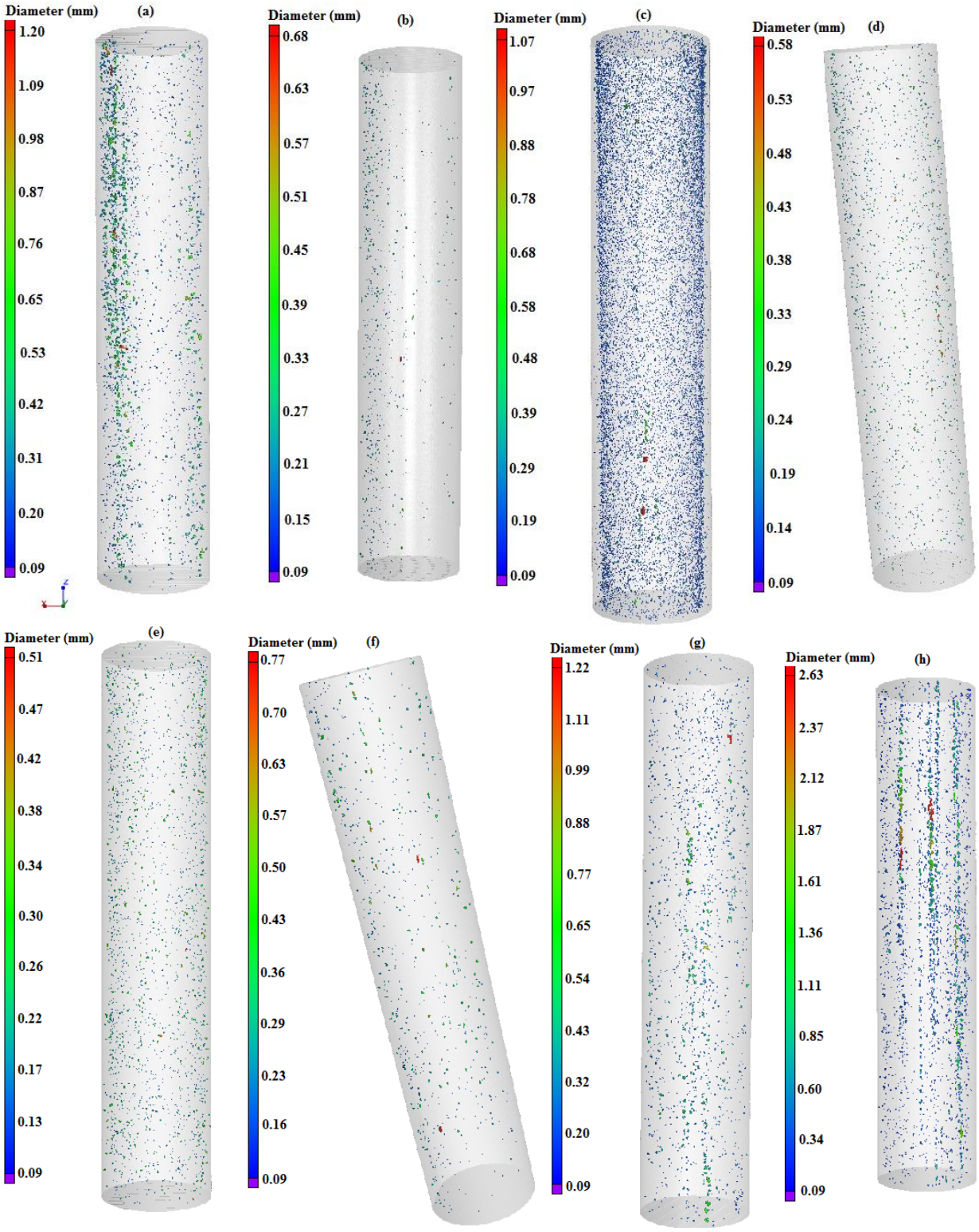


**Figure 71: The X-ray CT scan of stress relieved SLM Ti6Al4V 3-point bend fatigue samples: 3 m/s (a-Sample 4, b-Sample 2, c- Sample 1, d-Sample 3); 4m/s (e-used for experimental settings, f-Sample 3, g-Sample 1, h-Sample 2)**

It is important to note that the fatigue crack initiation samples in Figure 71(a, c and h) exhibit most SLM process defects, as well as extreme pore size, far greater than the 1 mm large pore presented previously in uniaxial tensile test specimens. In addition, large pores are among the

clustered micro pores and this could result in catastrophic failure during the fatigue test. The porosity distribution for the four samples is shown in Figure 72.

As Figure 72 depicts, pores in the range 0.18 mm – 0.28 mm were predominant and clustered in all four cases. The effects of these defects (pores) on the fatigue properties of the stress relieved SLM Ti6Al4V rod will be studied in proceeding chapters. In general, there was an unpredictable variation in the nature of defects that occured during the sample fabrication, which could not be correlated directly with the laser scan speed.


**Figure 72: Pore size distribution for stress relieved SLM fatigue crack initiation samples fabricated at: 3 m/s (a- Sample 4 ,b- Sample 1, d- Sample 2); 4 m/s (c-Sample 2)**

Scanning through the 2D stacked images, there were a significant number of surface pores in some samples (See Figure 73(b and c)), compared to the sample shown in Figure 73(a). There was also a noticeable alignment of defects parallel to the scan direction that were close to the specimen's surface, as illustrated by Figure 73(b). Figures 71(b) and 73(a) show a fairly clean specimen in terms of the porosity character, as compared to the others and the largest pore was located at the centre of the specimen, as indicated in Figures 72(d) and 73(a).

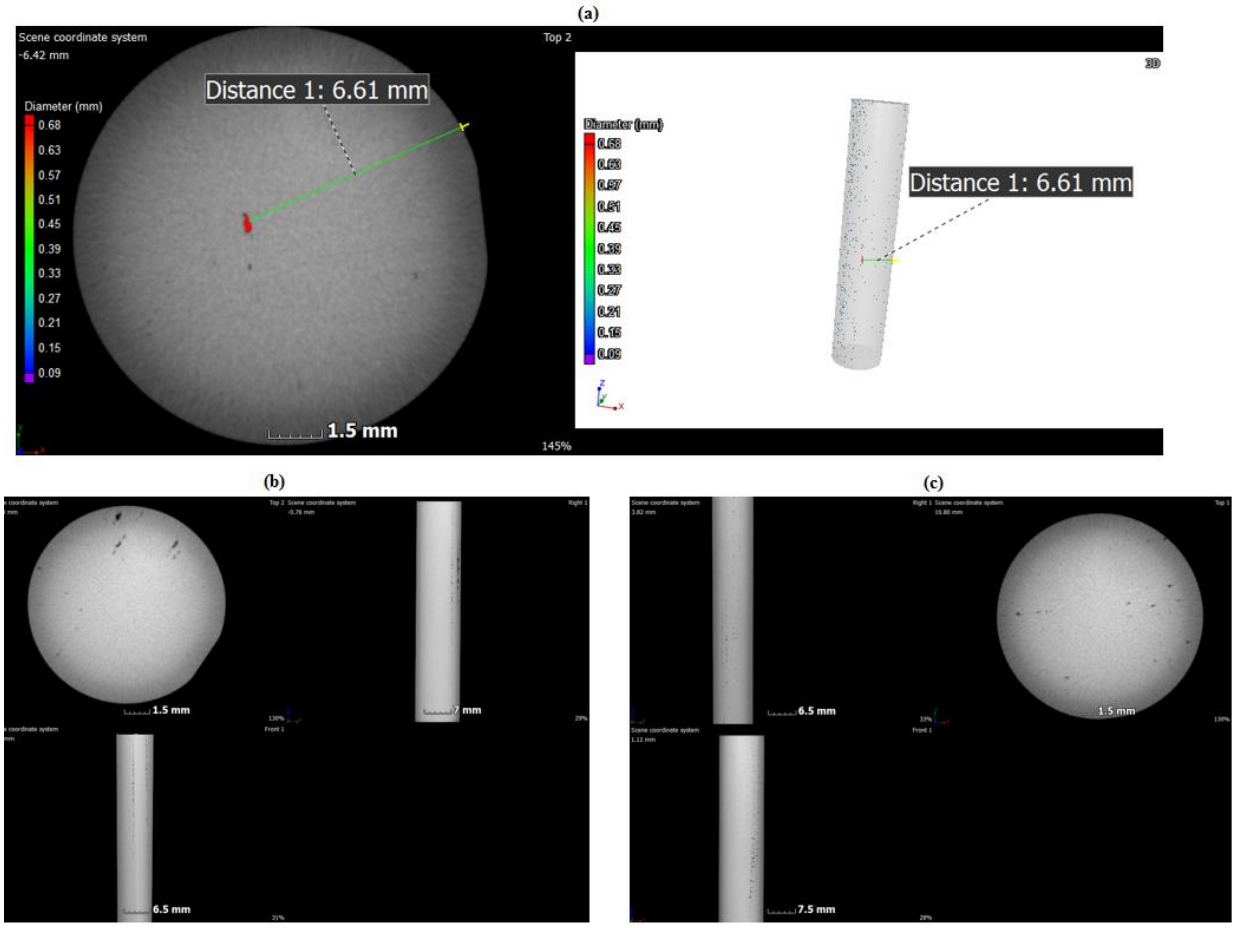


**Figure 73: 2-D slices for the stress relieved SLM Ti6Al4V tensile samples fabricated at: (a) 3 m/s (sample 2); (b) 3 m/s (sample 1); 4 m/s (sample 2).**

The X-ray CT scans also revealed that the sphericity/aspect ratio for all SLM Ti6Al4V samples approached 0.8 for pores less than 0.02 mm and most of the pores were elongated ($f \leq 0.7$). This is illustrated in Figure 74.

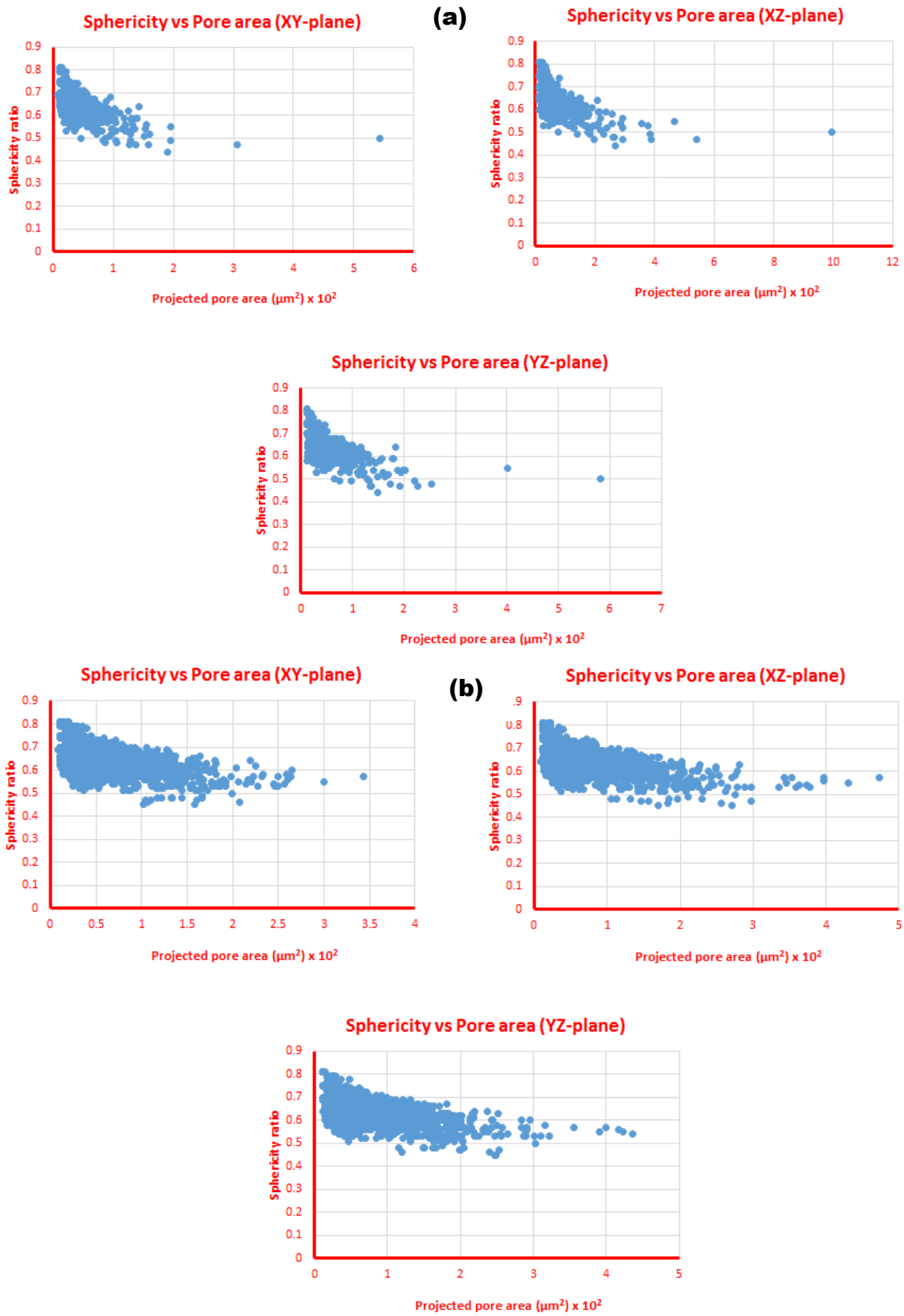


**Figure 74: The sphericity ratio for the stressed relieved SLM Ti6Al4V samples fabricated at 3 m/s and 4 m/s**

### 4.1.3. Microstructure of SLM Ti6Al4V samples (as-built and stress relieved state)

The microstructural integrity of each sample was investigated in both the as-built and stress relieved state. As is common for the SLM Ti6Al4V specimens, columnar grain structures were visible in each micrograph taken parallel to the build direction, because of the epitaxial grain growth resulting from successive layer deposition. Micrographs taken perpendicular to the build direction mainly had track-to-track melt pool features, owing to the zig-zag scanning strategy. Optical micrographs are presented in Figure 75 for the as-built SLM Ti6Al4V, fabricated at 1.5 m/s and 2.5 m/s laser scan rates.

The layer-to-layer melt pool boundaries are indicated by the yellow dotted lines on the micrographs taken parallel to the build direction. In all the micrographs taken, there exists a fine needle-shaped α' martensitic phase, which is due to short laser power interaction times and localised high heat input leading to high temperature gradients and rapid solidification.

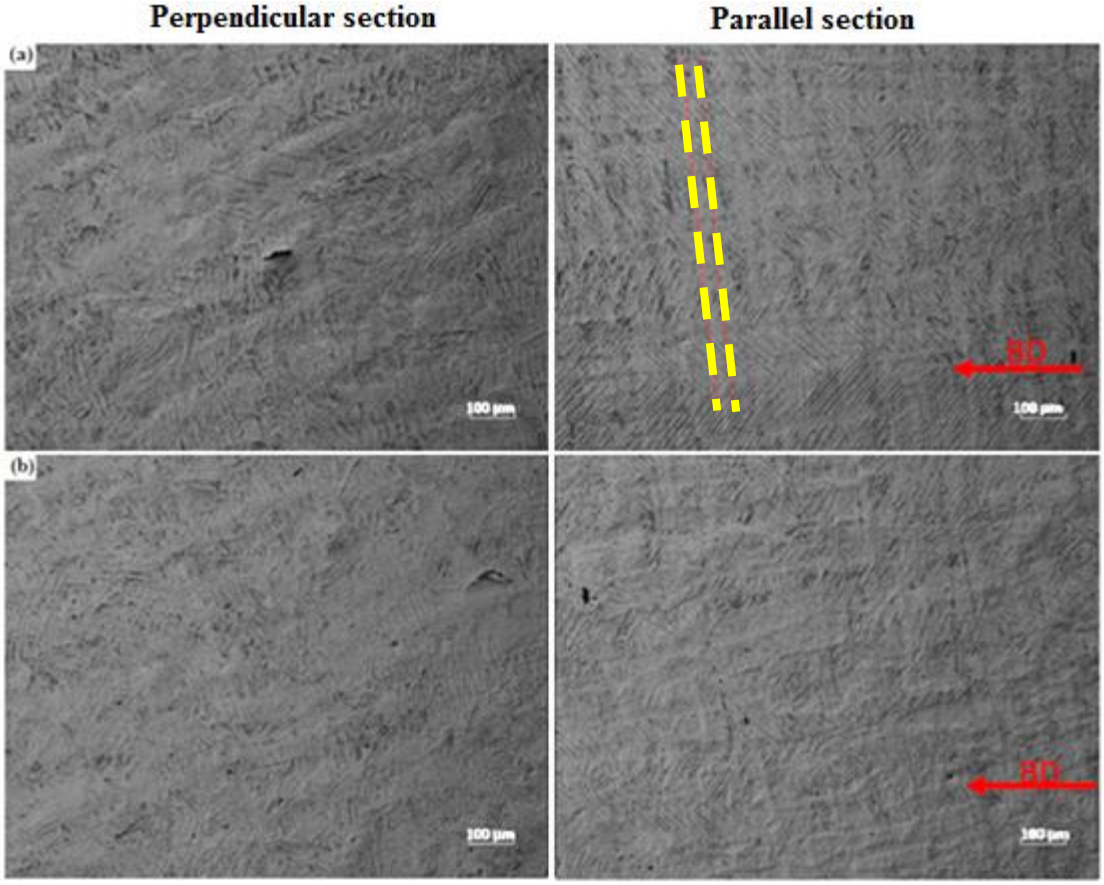


**Figure 75: SLM Ti6Al4V microstructures perpendicular and parallel to build direction fabricated at: (a) 1.5 m/s; (b) 2.5 m/s.**

A closer look at the overall microstructural morphology resulting from the SLM process also reveals the prior – β columnar grains, as well as the martensitic α' platelets on the section cut parallel to the build direction as shown in Figure 76. Black arrows indicate the direction of growth for the prior – β columnar grains, owing to successive layer-to-layer deposition.

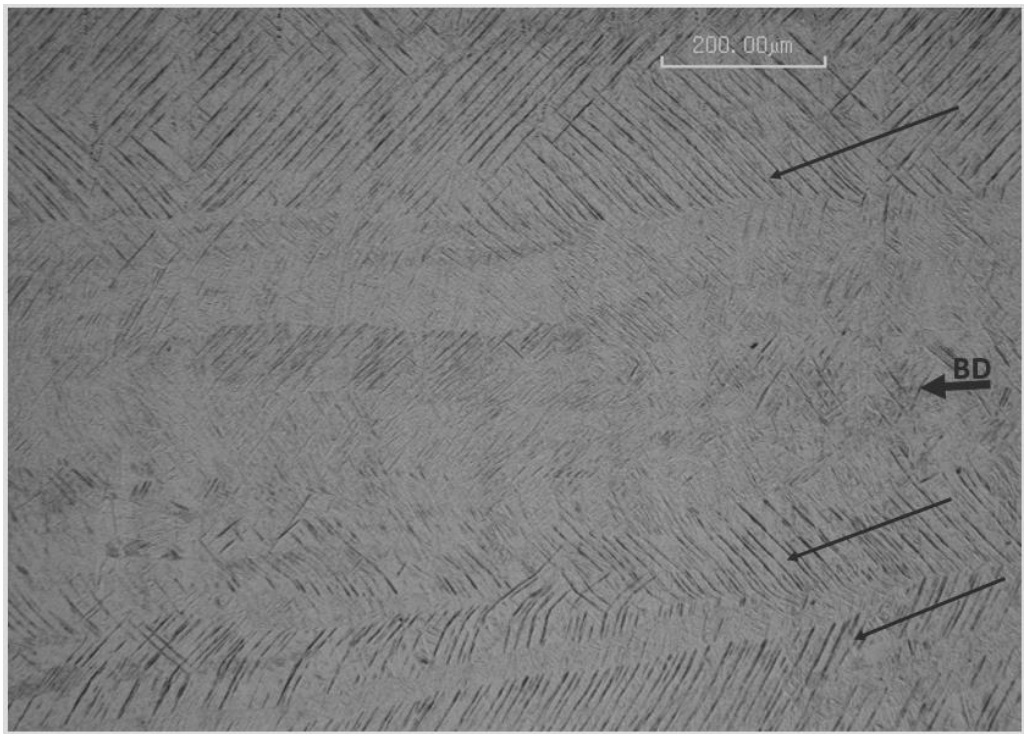


**Figure 76: SLM Ti6Al4V microstructures parallel to build direction.**

Micrographs were also taken on the stressed relieved Ti6Al4V samples, as illustrated in Figure 77. The inevitable presence of martensitic α' platelets is still visible on the section taken perpendicular to the build direction as depicted by the micrograph on the left. Further to this, the presence of micro pores and unmelted zones (indicated by white arrows) are evident, as seen in (Figure 77) on the as-built SLM Ti6Al4V micrographs.

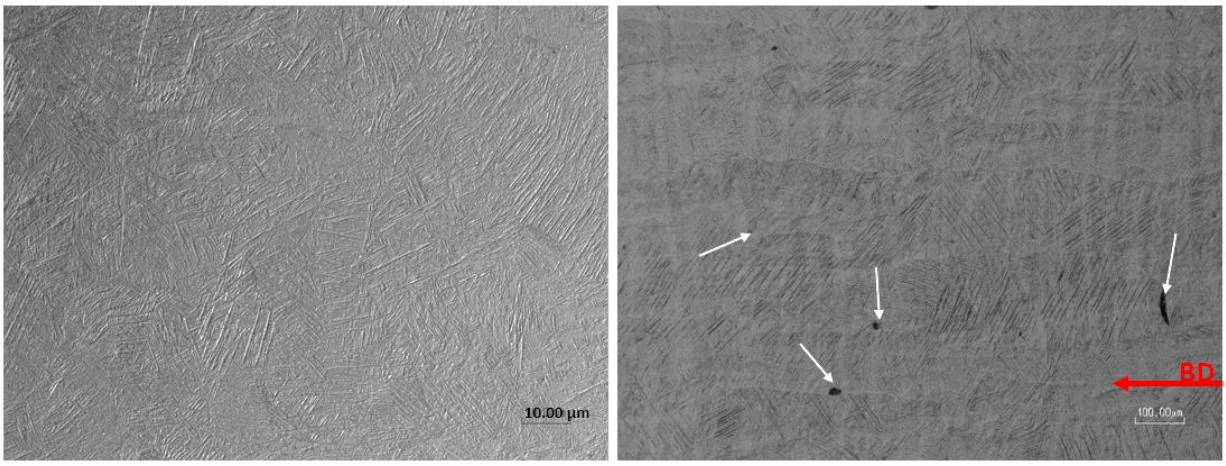


**Figure 77: Micrographs for the stress relieved SLM Ti6Al4V specimen fabricated at 3 m/s.**

The SLM process is conducive to defects, which may either be due to sub-optimum process parameters being used or to environmental contamination. Therefore, the optimum combination of process parameters and inert environment is essential to achieve decent microstructural integrity, thereby enabling comparable mechanical properties with specimens produced by

conventional methods. Figure 78 illustrates most of the defects observed in different set process parameters, from 1.5 m/s to 4 m/s laser scan rates, while other parameters (power, hatch spacing, layer thickness) were kept constant, hence a variation in energy density supplied to the atomised powder.

Figure 78(a-d) shows defects present as a result of a specific set of parameters and/or environmental contamination. Figure 78(a) shows an unstable melt pool boundary morphology, which could be due to excessive energy density delivered to the powder (low laser scan speeds with high laser power). Figure 78(b) shows two phenomena, firstly the balling effect, which is characterised by minor cracks perpendicular to the build direction, and secondly, circular-shaped pores (indicated by white arrows), which are as a result of excessive energy density.

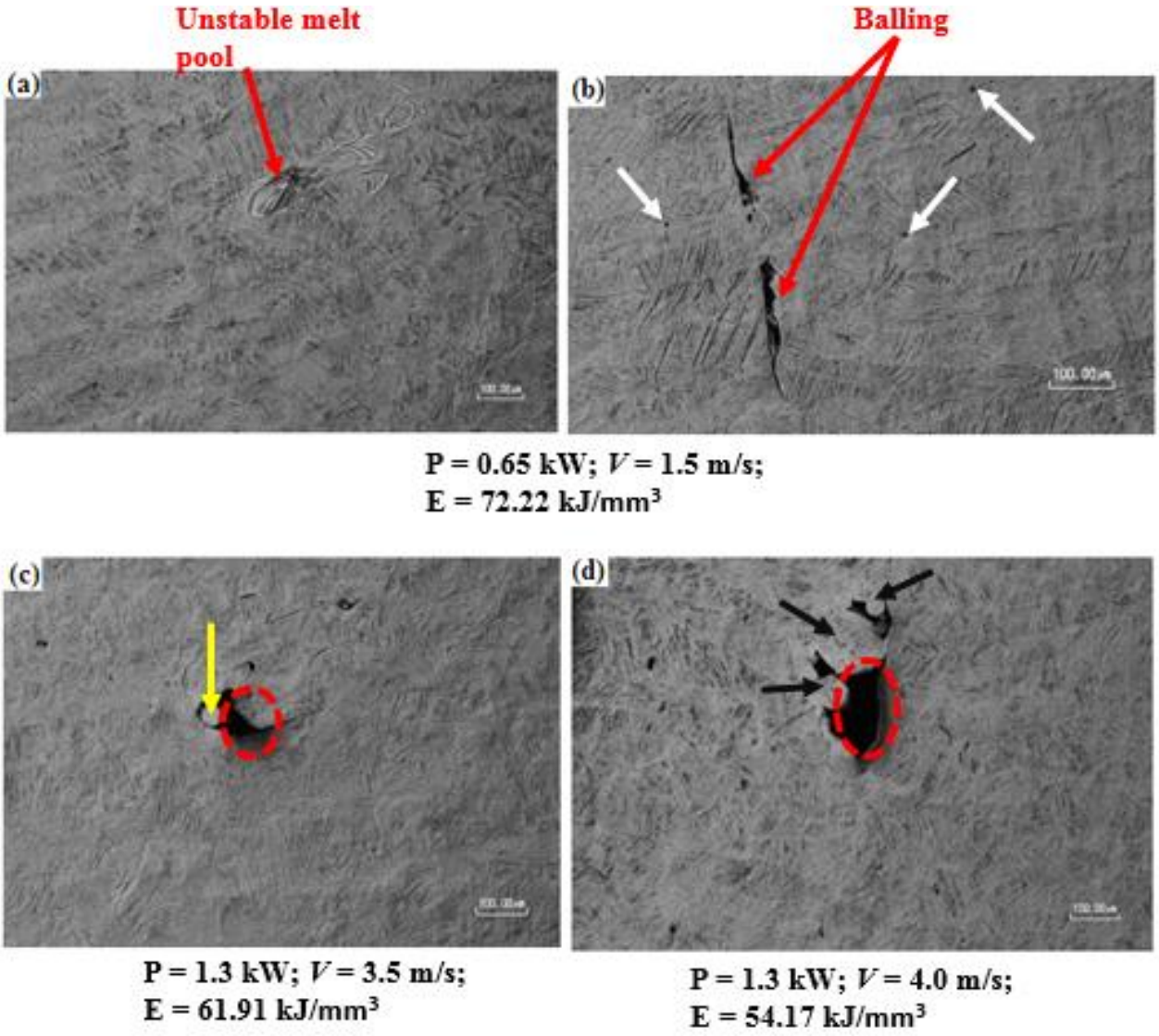


**Figure 78: Defects on the SLM Ti6Al4V specimens (etched) at distinct parameter settings**

On the other hand, Figure 78(c-d) illustrates low energy density defects, namely the unmelted zone (circled in red), the satellites formation (black arrows in figure 78(d)), as well as unmelted

particles (yellow arrow). The above is because of inadequate energy density, as some of the powder will not be fully molten and will be attached on to the melt pool, whereas the unmelted zone and delamination effects are due to improper wetting of the substrate material by the melt pool.

The delamination effect was also observed on the as-built SLM Ti6Al4V samples, as shown by red arrows in Figure 79. This may be attributed to the residual stresses build-up as the substrate's thickness increased. These two FCGR samples had to be discarded and were not used.

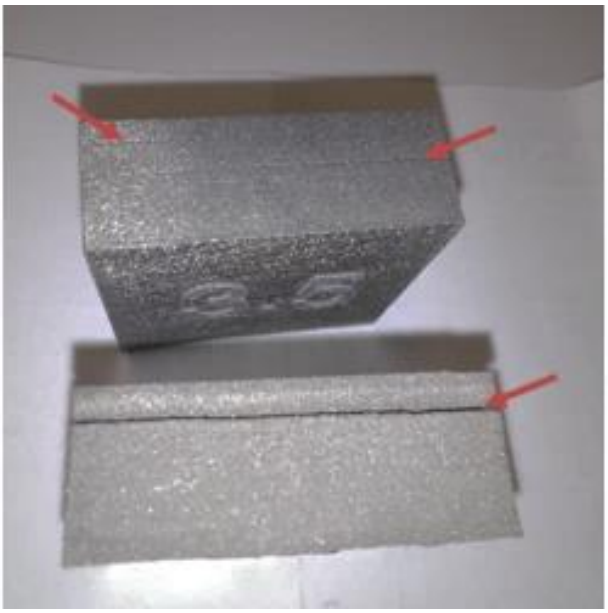

**Figure 79: The delamination phenomena on the as build SLM Ti6Al4V specimens**

There is no direct correlation between the laser scan speed and the nature of process defects present in each sample for this project. The variation in pores across the sample range is significant to the extent that the SLM process itself becomes unpredictable for porosity measurements.

## 4.2. MECHANICAL PROPERTY MEASUREMENT

Mechanical properties for the as-built and stress relieved SLM Ti6Al4V alloy, fabricated at different laser scan rates, are presented in this section. The property tests that were carried out included uniaxial tensile testing, fracture toughness and the fatigue crack growth rate tests, as well as the three-point bend fatigue crack initiation tests. All the specimens were machined and tests were in line with the ASTM standards.

### 4.2.1. Uniaxial tensile test results for the as-built and stress relieved SLM Ti6Al4V samples

The uniaxial tensile mechanical properties for the as-built SLM Ti6Al4V specimens, fabricated at different scan rates, are shown in Figure 80. For easy reference, Table 11 serves as a general summary of the tensile properties at different scan rates. Very little necking of the specimens was noticed by the naked eye during testing. With reference to Table 11 and Figure 80, there was no obvious relationship that could be drawn regarding the influence of laser scan rate and the measured mechanical properties. This is investigated further in Figures 81 and 82.

**Table 11: Summary of tensile mechanical properties for the as-built SLM Ti6Al4V at different scan rates.**

| Laser scan speed (m/s) | Energy density ($kJ/mm^3$) | Young's/ Elastic modulus (GPa) | UTS (MPa) | 0.2% proof stress (MPa) | Elongation at failure (%) |
|---|---|---|---|---|---|
| 1.5 | 72.22 | 114 ± 12 | 1030 ± 68 | 773 ± 48 | 7 ± 3 |
| 1.75 | 61.91 | 112 ± 18 | 1022 ± 93 | 760 ± 72 | 8 ± 4 |
| 2.0 | 108.33 | 119 ± 20 | 1007 ± 123 | 640 ± 76 | 6 ± 3 |
| 2.5 | 86.67 | 144 ± 5 | 1333± 23 | 893 ± 23 | 4 ± 1 |
| 3.0 | 72.22 | 118 ± 9 | 1094 ± 60 | 800 ± 49 | 7 ± 2 |
| 3.5 | 61.91 | 110 ± 22 | 1052 ± 124 | 740 ± 104 | 9 ± 2 |
| 4.0 | 54.17 | 115 ± 29 | 988 ± 145 | 728 ± 131 | 8 ± 4 |

Figure 80 shows a series of tensile stress-strain curves for the as-built SLM Ti6Al4V specimens fabricated at different scan rates, from 1.5 m/s to 4 m/s, with other process parameters kept constant. This increase in laser scan rate has an indirect proportionality to the corresponding energy density, hence resulting in energy density deterioration. The Ultimate Tensile Strength (UTS) for the as-built SLM Ti6Al4V samples varied from 1000 MPa to 1333 MPa, while the percentage elongation varied from 4% to 9%, but this change could not be associated with the laser scan rate as there was a significant scatter in data. The scatter in data worsened as the laser scan speed was increased above 3 m/s (Refer to Figure 80).

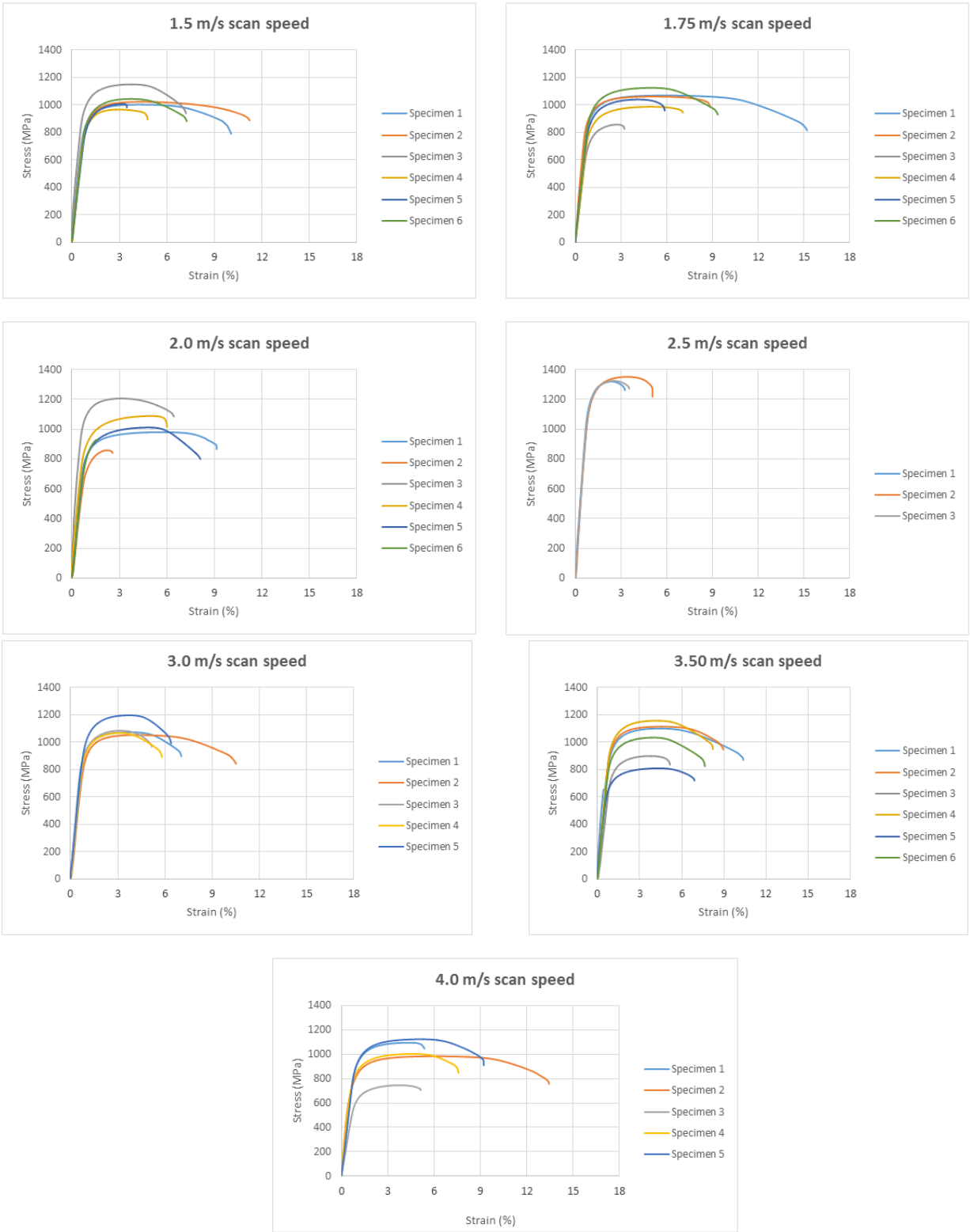


**Figure 80: Tensile stress – strain curves for the as-built SLM Ti6Al4V at different scan rates**

To appreciate the scattered data in the mechanical results, histograms were used, as presented in Figure 80 and Figure 81. These show the influence of laser scan rate on the UTS, elongation and the 0.2% proof stress for the as-built Ti6Al4V tensile samples, fabricated at laser scan rates ranging from 1.5 m/s to 4 m/s.

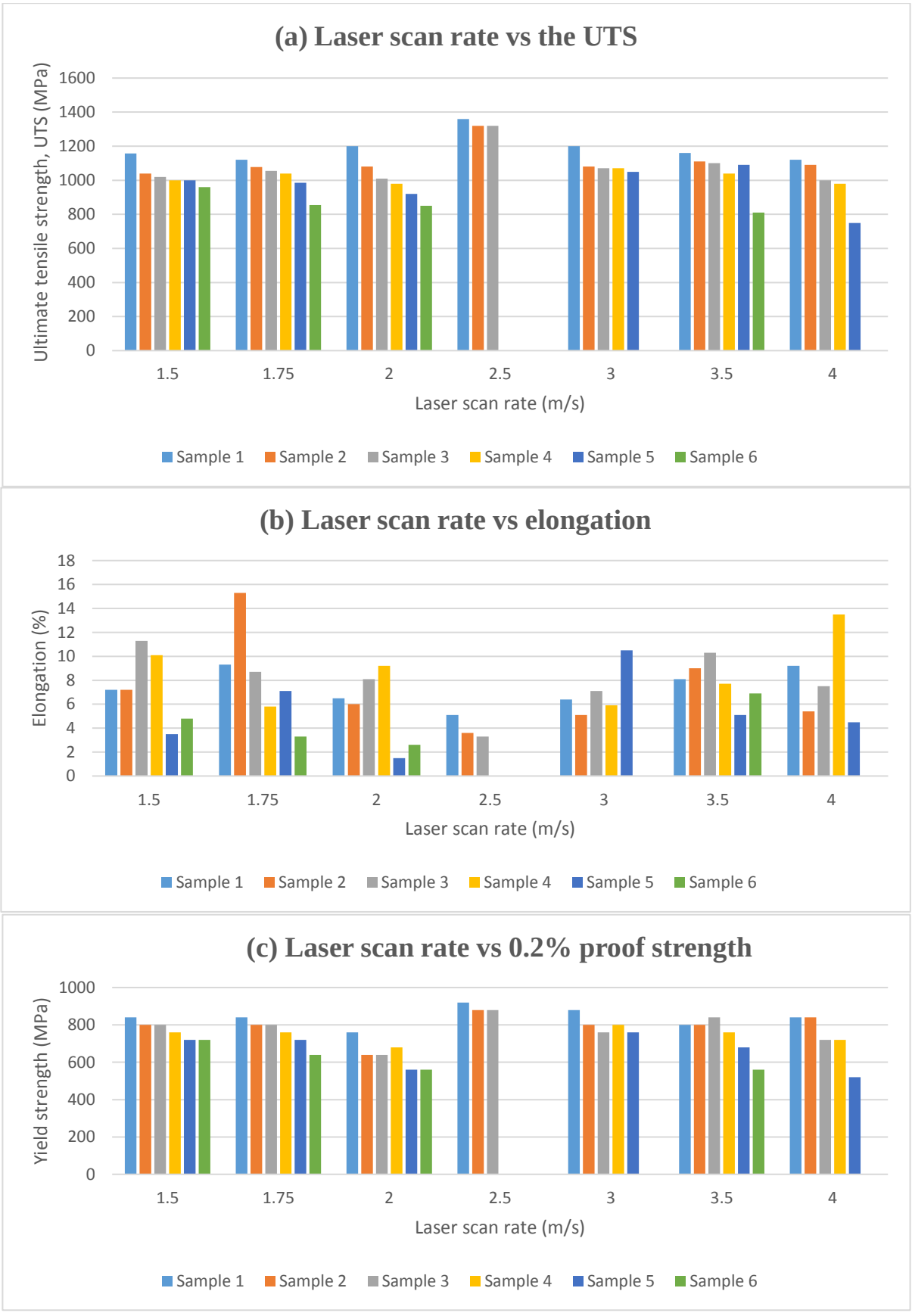


**Figure 81: The laser scan rate plot for the as-built SLM Ti6Al4V samples against: (a) UTS; (b) elongation; (c) Yield strength.**

Figure 81(a) shows the ultimate tensile strengths (UTS) for all the as-built Ti6Al4V uniaxial tensile specimens fabricated at 1.5 m/s up to 4 m/s. There was a 26% difference in the range of measured UTS values, owing to the inconsistent mechanical measurements observed. This means that for a given set of specific process parameters there was a significant scatter of data, which overshadowed the relationship between the measured UTS and the laser scan speed. The scatter in measured mechanical properties became significant for the percentage elongation (ductility), as there was a 55% variation as shown in Figure 81(b) and in this instance no relationship could be concluded between ductility and the laser scan speed. Lastly, Figure 81(c) shows the range of measured 0.2% proof stress values for different scan rates. The yield strength for these as-built SLM Ti6Al4V samples ranged from 640 MPa to 893 MPa.

As Figure 82 shows, there is generally very poor correlation between the laser scan speed and the tensile mechanical properties due to scatter in results.

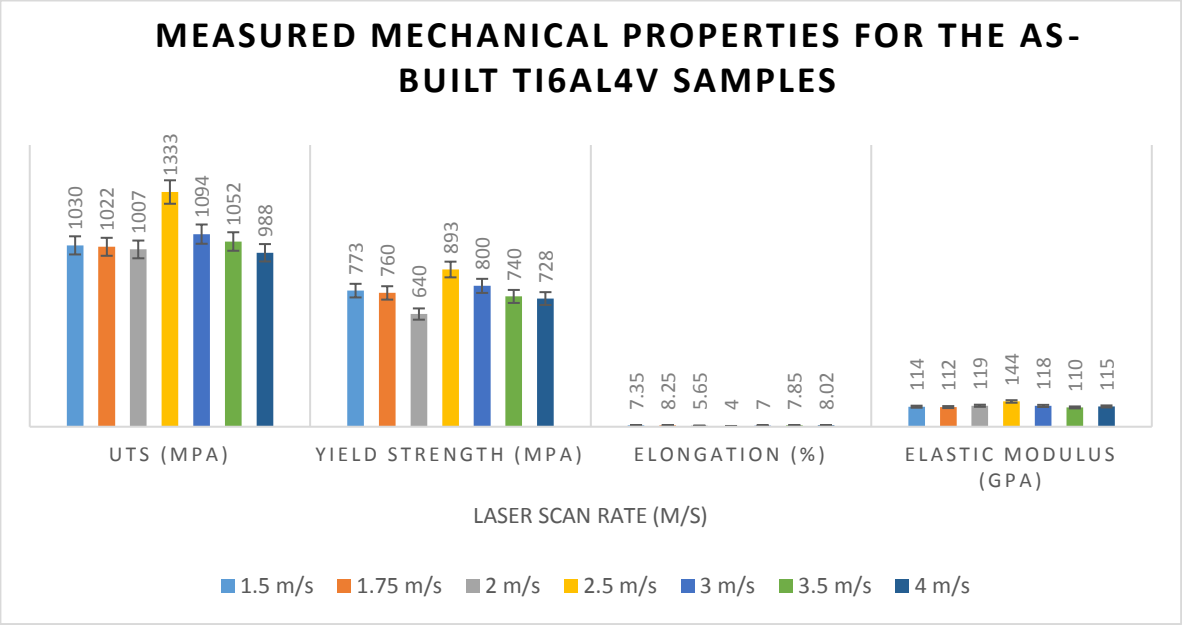


**Figure 82: Measured mechanical properties for the as-built SLM Ti6Al4V samples fabricated at different laser scan rates.**

Residual stresses inherent in the SLM process have a direct impact on the mechanical properties of the SLM part [20, 26] and hence the need to carry out the post SLM stress relief anneal heat treatment. Tensile tests were carried out on the stress relieved samples and the tensile stress-strain results are presented in Figure 83 for the stress relieved SLM Ti6Al4V samples fabricated at 3 m/s and 4 m/s.

Figure 83 show improvement in the overall elongation (7±3% to 12±2) for tensile samples fabricated at 3 m/s laser scan speed. After annealing however, samples fabricated at 4 m/s show a slight deterioration in elongation (8 ± 4% to 6 ±3%).

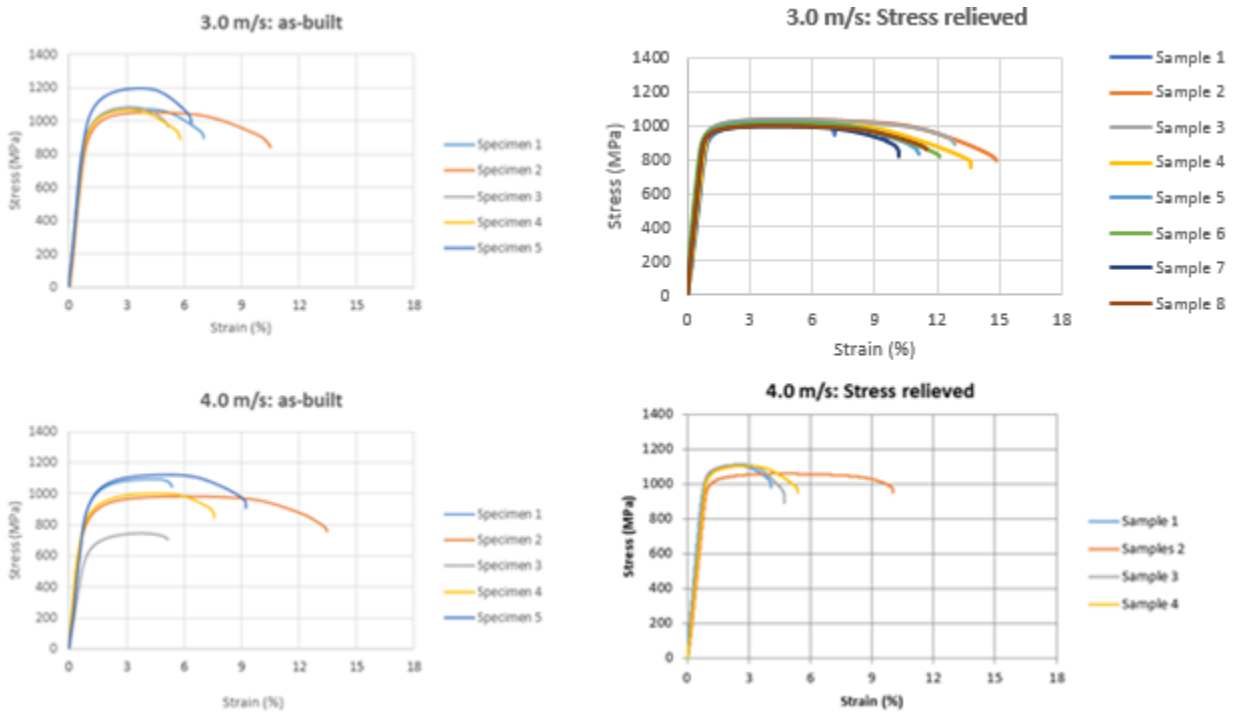


**Figure 83: Tensile stress-strain curves for the SLM Ti6Al4V samples: (a) as-built and stress relieved (3 m/s); (b) as-built and stress relieved (4 m/s).**

For easy reference, Table 12 presents data points extracted from the tensile stress-strain graphs in Figure 83. There was a slight improvement in the ultimate tensile strength and the proof strength as the laser scan rate was increased from 3 m/s to 4 m/s, but the ductility decreased considerably.

**Table 12: Tensile mechanical properties for stressed relieved SLM Ti6Al4V uniaxial tensile samples.**

| Sample # | E (GPa) | UTS (MPa) | 0.2% proof strength (MPa) | Elongation (%) |
|---|---|---|---|---|
| **3 m/s** | | | | |
| 1 | 128.1 | 1000 | 830 | 9.7 |
| 2 | 130.2 | 1036 | 810 | 14.8 |
| 3 | 115.96 | 1037 | 850 | 13 |
| 4 | 105.93 | 1016 | 820 | 13.5 |
| 5 | 138.45 | 1026 | 800 | 11 |
| 6 | 133.6 | 1000 | 850 | 12.1 |
| 7 | 122.4 | 1019 | 830 | 10.2 |
| 8 | 124.67 | 1000 | 820 | 11.6 |
| **Average** | **125 ± 10** | **1017 ± 16** | **826 ± 18** | **12 ± 2** |
| **4 m/s** | | | | |
| 1 | 138.633 | 1120 | 960 | 4.1 |
| 2 | 101.741 | 1060 | 920 | 10 |
| 3 | 123.429 | 1120 | 960 | 4.8 |
| 4 | 111.812 | 1100 | 940 | 5.4 |
| **Average** | **119 ± 16** | **1100 ± 28** | **945 ± 19** | **6 ± 3** |

This is further validated by Figure 84(d). In general, Figure 84 illustrates that stress relieving the as-built Ti6Al4V uniaxial tensile samples and testing the stress relieved samples fabricated between 3 m/s and 4 m/s may have resulted in improved UTS and yield strength with a corresponding loss in ductility, but the data points are inadequate to reach such a conclusion as there were only two parameters used (3 m/s and 4 m/s). Furthermore, there is still a significant variation in the measured mechanical results, approximating 4% and 35% for the UTS and elongation, respectively.

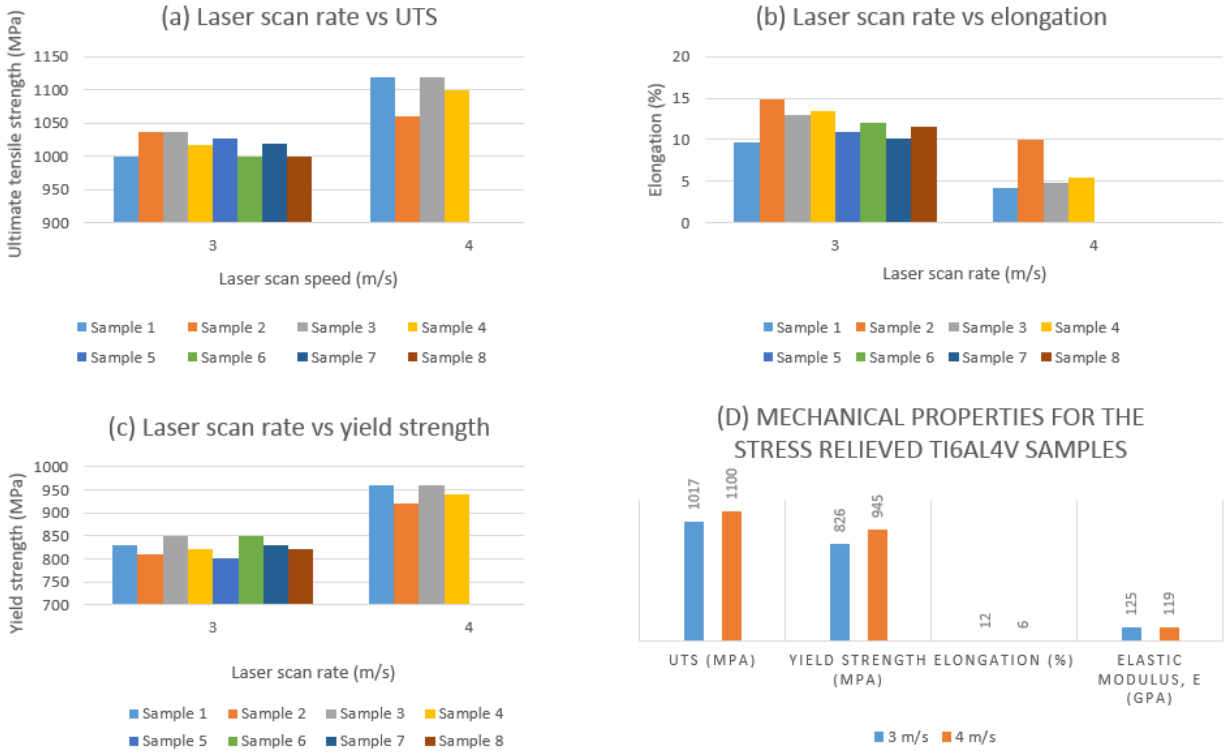


**Figure 84: Measured tensile mechanical properties for the stressed relieved SLM Ti6Al4V samples fabricated at 3 m/s and 4 m/s: (a) UTS; (b) elongation; (c) 0.2% proof stress; (d) comparison of average mechanical properties for each laser scan speed.**

In general, the uniaxial tensile test measurements in this project did not show direct correlation with the change in laser scan speed. Therefore, the nature of pores present in these samples will be used to explain the mechanical data.

### 4.2.2. Fracture toughness test results

Fracture toughness tests were carried out to investigate the resistance of the stress relieved SLM Ti6Al4V samples to fracture when a defect or crack was present in the material. The specimens under investigation were subjected to the formation of a predetermined pre-crack length, after which the actual fracture toughness test was carried out by increasing force until the specimen fractured.

Fracture toughness results for the SLM Ti6Al4V (stress relieved) are summarised in Table 13. Samples were fabricated using laser scan rates between 3 m/s and 4 m/s, each scanning process setting with two samples. It is important to note at this point that two samples fabricated at 3 m/s and 3.5 m/s fractured prematurely during pre-cracking and therefore had to be discarded and the cause of this investigated.

Nevertheless, as Table 13 shows, the fracture toughness values varied from 37 MPa.m$^{0.5}$ to 48 MPa.m$^{05}$ and no trend or influence of the laser scan speed on the fracture toughness properties could be detected as there were insufficient data points.

**Table 13: Fracture toughness values for the stress relieved SLM Ti6Al4V samples.**

| Laser scan rate (m/s) | Configuration correction factor: $Q_{CT}(a/w)$ | Load level, $P_Q$ (N) | $\sigma_Q$ (MPa) | $K_Q$ (MPa. m$^{0.5}$) | $P_{max}$ (N) | $\frac{P_{max}}{P_Q}$ | $L_Q$ (mm) | $K_{1C}$ (MPa.m$^{0.5}$) |
|---|---|---|---|---|---|---|---|---|
| **3** | 7.348 | 8202 | 26.246 | 37.446 | 8513 | 1.04 | 5.214 | **37** |
| **3,5** | 7.348 | 8642 | 27.654 | 39.455 | 8685 | 1.00 | 5.788 | **39** |
| **4** | 7.348 | 9838 | 31.482 | 44.916 | 10026 | 1.02 | 7.501 | **45** |
| | 7.348 | 10592 | 33.894 | 48.358 | 10741 | 1.01 | 8.695 | **48** |

As it is a prerequisite to validate captured experimental data in line with the ASTM E399 standards, indicators were used as presented in both Table 13 and Figure 85, which helped to calculate respective fracture toughness values.

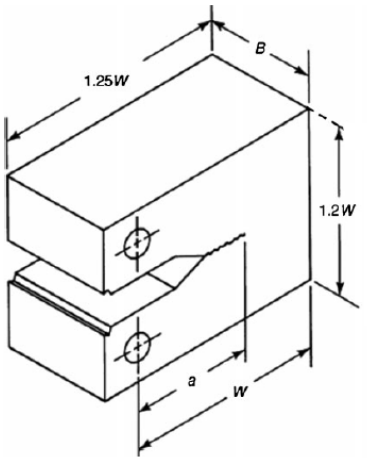


| a (mm) | W (mm) | W-a (mm) | B (mm) | 0.2% Yield strength offset (MPa) |
|---|---|---|---|---|
| 12 | 25 | 13 | 12.5 | 820 |

**Figure 85: Standard ASTM compact tension (CT) specimen for fracture toughness tests [26].**

The procedure to calculate the fracture toughness variable was as follows:

After pre-cracking, a clip gauge was attached on knife edges attached to the notch opening and the necessary settings done to allow data capture by the acquisition system as the specimen was fractured with escalating force. These data would help to develop a load displacement curve, as shown in Figure 86.

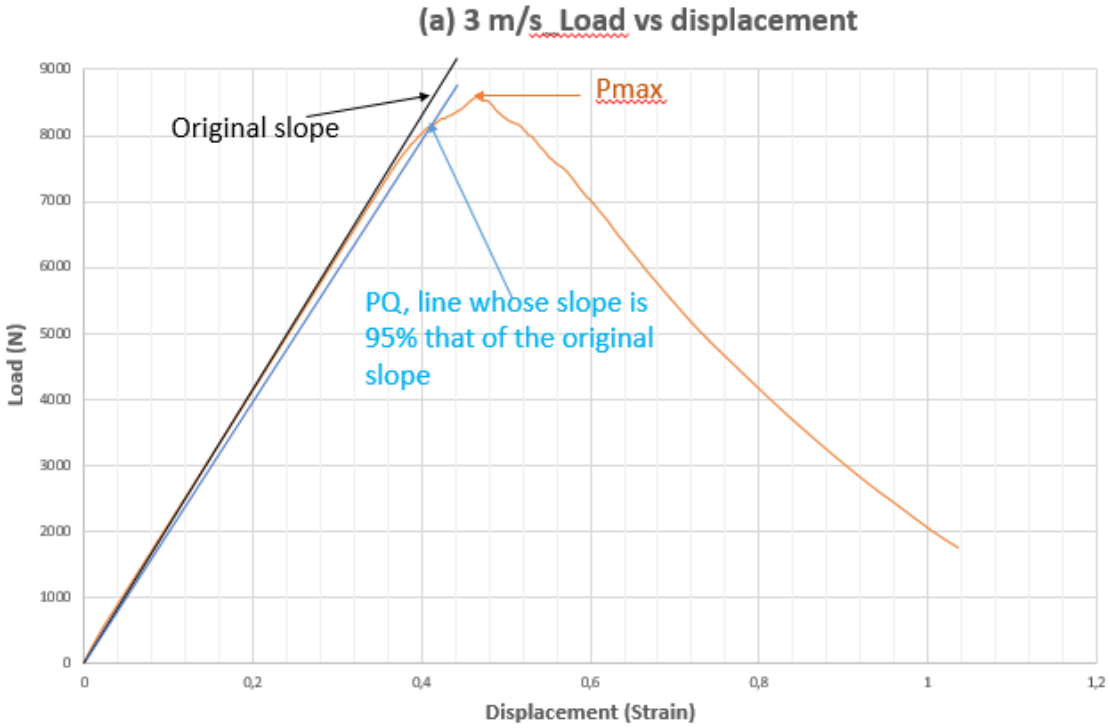


**Figure 86: Load vs Displacement (crack mouth opening) used to determine $P_{max}$ and $P_Q$**

Procedure to calculate the fracture toughness variable, $K_{1C}$:

1. The crack length variable, *'a'*, is measured. This is the initial crack length (notch) plus the pre-crack length on the fractured sample. Other variables, like the sample width (*B*), '*w*'**,** as well as '*w-a*' can also be determined in accordance with the CT specimen geometry, as provided by the ASTM E399 standard.
2. From the Load vs Displacement curve extracted from the raw data acquisition system, the maximum force endured during fracture ($P_{max}$) can be determined, as well as the force ($P_Q$), as indicated in Figure 86. This is followed by determining the ratio $\frac{P_{max}}{P_Q}$; this should be less than 1.10, as outlined by the ASTM E399 standard.
3. Determine the configuration correction factor ($Q_{CT}$) for a CT specimen geometry:

$$Q_{CT} = 16.7 - 104.7\left(\frac{a}{w}\right) + 369.9\left(\frac{a}{w}\right)^2 - 573.8\left(\frac{a}{w}\right)^3 + 360.5\left(\frac{a}{w}\right)^4$$

4. A conditional value, $K_Q$ is then calculated using the formula: $K_Q = Q_{CT} \times \sigma_Q \times \sqrt{\pi a}$, where the variable $\sigma_Q = \frac{P_Q}{Bw}$

5. Finally, the quantity $L_Q = 2.5\left(\frac{K_Q}{\sigma_Y}\right)$, where $\sigma_y$ is the 0.2% offset yield strength in tension, is determined and if this quantity is less than the specimen ligament size (*w-a*) then $K_Q$ is equal to the specimen's fracture toughness $K_{1C}$.

### 4.2.3. Fatigue crack growth rate (FCGR) results

The fatigue crack growth rate testing measures the rate at which a crack propagates through a material by subjecting a pre-cracked specimen to cyclic loading at constant force. The crack length versus the number of cycles to failure for the SLM Ti6Al4V specimens fabricated at distinct laser scan rates is presented in Figure 87. As the Figure indicates, most of the specimens failed after 63 000 cycles at a constant applied load, while some specimens failed after only 50 000 cycles.

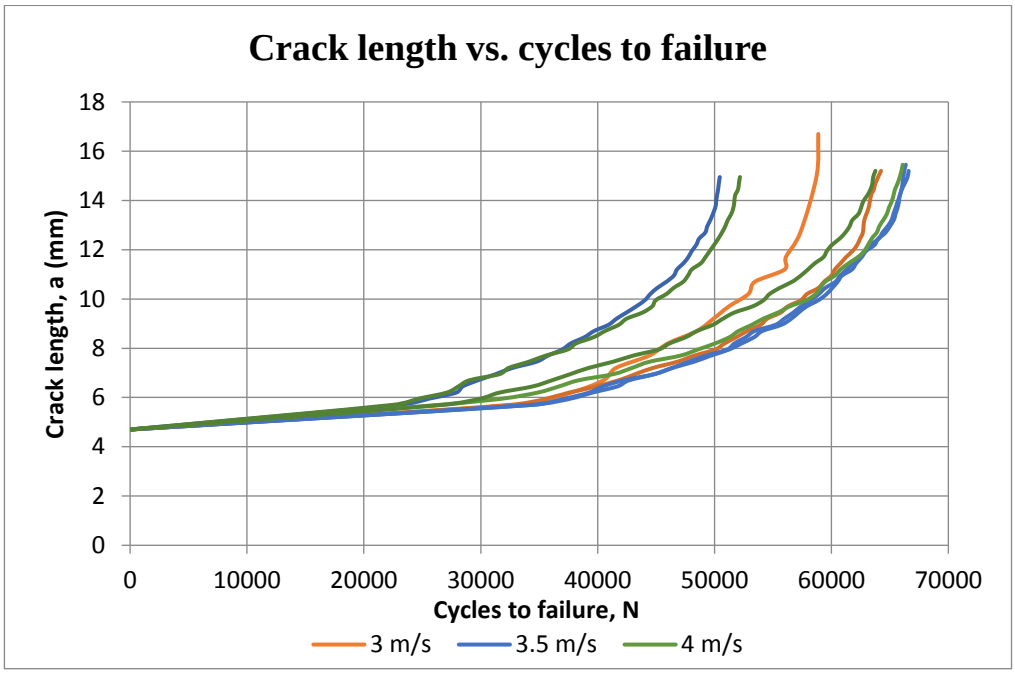


**Figure 87: Crack length (a) versus number of cycles to failure (N) for SLM Ti6Al4V fabricates at different scan rates**

It is also crucial to note in Figure 87 that the two specimens fabricated at 3.5 m/s and 4 m/s, which failed just after 50 000 cycles, had an earliest crack initiation (after only20 000 cycles). No trend can be concluded from Figure 87 as there is a scatter between different set process parameters. Figure 88 illustrates the least square fitted lines or the fatigue crack growth rate curves (*da/daN vs. dk*) for all the test specimens at different laser scan rates.

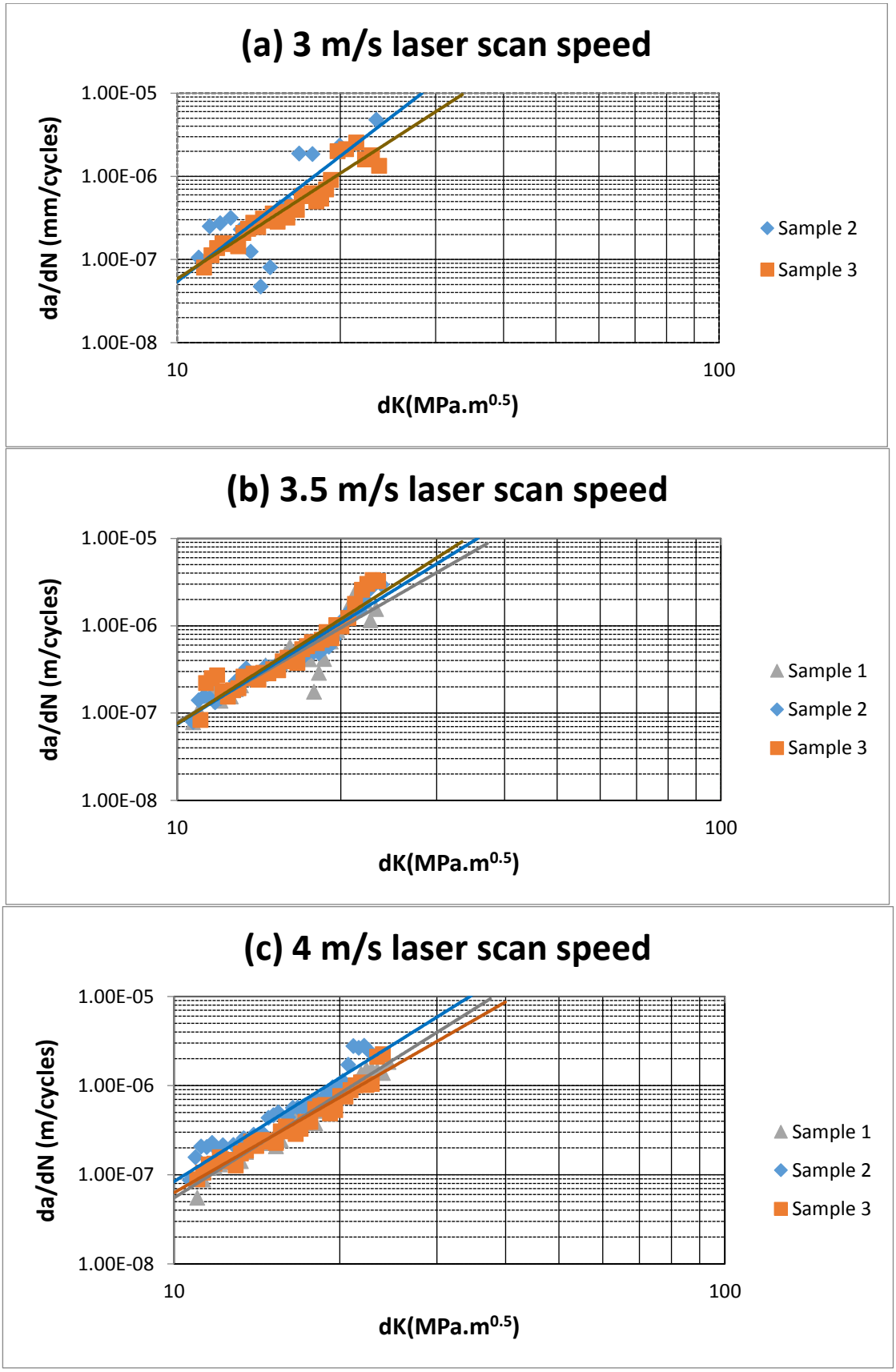


**Figure 88: Crack growth rate da/dN versus the stress intensity factor dK for: (a) 3m/s; (b) 3.5 m/s; (c) 4 m/s**

From the trend line drawn on the data points in Figure 88, the Paris equation (Equation 4) can be solved leading to the Paris constants *C* and *m*, as shown in Table 14.

$$\frac{da}{dN} = C(dK)^m$$ **(Equation 4: Paris equation [25])**

Table 14 shows no relationship between the change in correlation factor (*used to measure the influence of the cyclic stress intensity amplitude experienced by the crack tip on the crack growth rate*) with the increasing laser scan rate. In this regard, the first sample fabricated at 3 m/s is taken as an outlier. The resistance to crack initiation decreased slightly with increasing laser scan speed even though the density of the specimens during fabrication was virtually the same (98% - 99% densification).

**Table 14: Paris parameters and corresponding correlation factors**

| Scan speed (m/s) | Sample number | m | C (m/cycle) | $R^2$ | Number of cycles to 1 mm pre-crack | Number of cycles to failure (N) |
|---|---|---|---|---|---|---|
| **3** | 1 | 5.01 | $5 \times 10^{-13}$ | 0.60 | 33028 | 58872 |
| | 2 | 4.21 | $4 \times 10^{-12}$ | 0.92 | 32499 | 64240 |
| **3.5** | 1 | 3.59 | $2 \times 10^{-11}$ | 0.84 | 34339 | 66601 |
| | 2 | 3.85 | $1 \times 10^{-11}$ | 0.94 | 34390 | 66360 |
| | 3 | 3.98 | $8 \times 10^{-12}$ | 0.90 | 23069 | 50446 |
| **4** | 1 | 3.89 | $7 \times 10^{-12}$ | 0.97 | 26417 | 39699 |
| | 2 | 3.87 | $1 \times 10^{-11}$ | 0.92 | 22465 | 32154 |
| | 3 | 3.56 | $2 \times 10^{-11}$ | 0.95 | 26752 | 63966 |

The resistance to crack propagation was slightly improved as the laser scan rate was increased from 3 m/s to 4 m/s and the value of the constant '*m*', which is basically the gradient of each curve in Figure 88, decreased with increasing laser scan rate. However, given the number of data points available, the above statement cannot be validated and needs further investigation, using sufficient data points.

On the other hand, Figure 89 depicts that, although there seems to be a slight improvement in the resistance to crack propagation from 3 m/s to 4 m/s laser scan speed, there is a point during the test where the crack propagation increases. This is illustrated by a sudden drop in the number of cycles to failure, as illustrated in Figure 89.

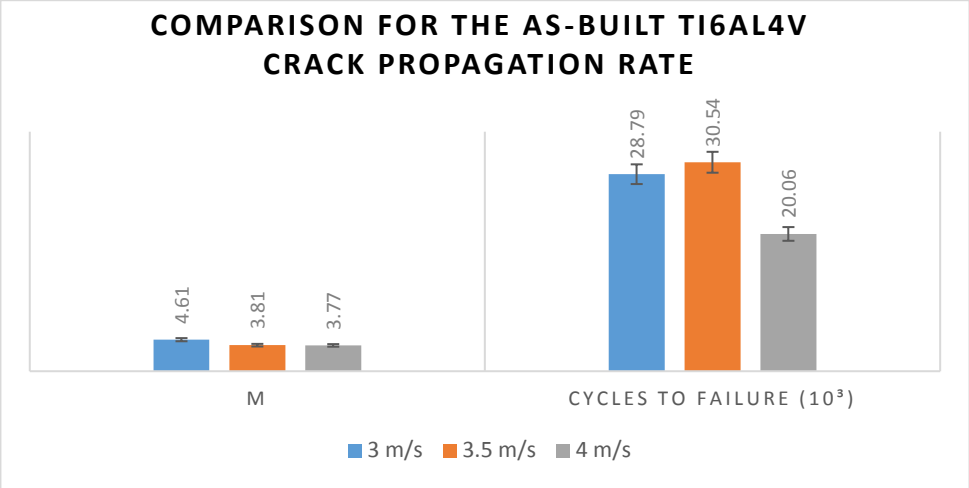


**Figure 89: Comparison of crack propagation rate for the as-built SLM Ti6Al4V alloy**

### 4.2.4. Fatigue crack initiation test results (3-point bend)

The three-point bend fatigue tests were carried at 10 Hz and in compression (R = -0.1). Figures 90 and 91 present a summary of the fatigue tests carried out. Samples were allowed up to 100 000 cycles and a test paused to increase the imposed stress intensity. The main purpose of this experiment was to monitor the effect of pores present in such samples on the crack initiation and propagation, until the samples failed completely. This was followed by fractured surface analysis, in conjunction with the X-ray CT scans made, to identify the crack initiation sites.

The first specimen fabricated at 4 m/s was used for experimental settings as a trial. The stress intensity was first set at 900 MPa and the sample was allowed to complete 100 000 cycles, after which the stress intensity was increased to 1080 MPa. There was no visible crack initiation for another 100 000 cycles. The sample failed when the stress was increased to 1200 MPa and the crack initiation was not observed, as it happened beyond the camera's vision. The latter stress intensity was then used for all samples.

The two Figures (Figure 90 and Figure 91) show the cumulative cycles at different stress levels that eventually led to crack initiation. The total area of the vertical bars in each case demonstrates the relative resistance to crack initiation. Comparison across the test specimen range indicates highly variable resistance to crack initiation.

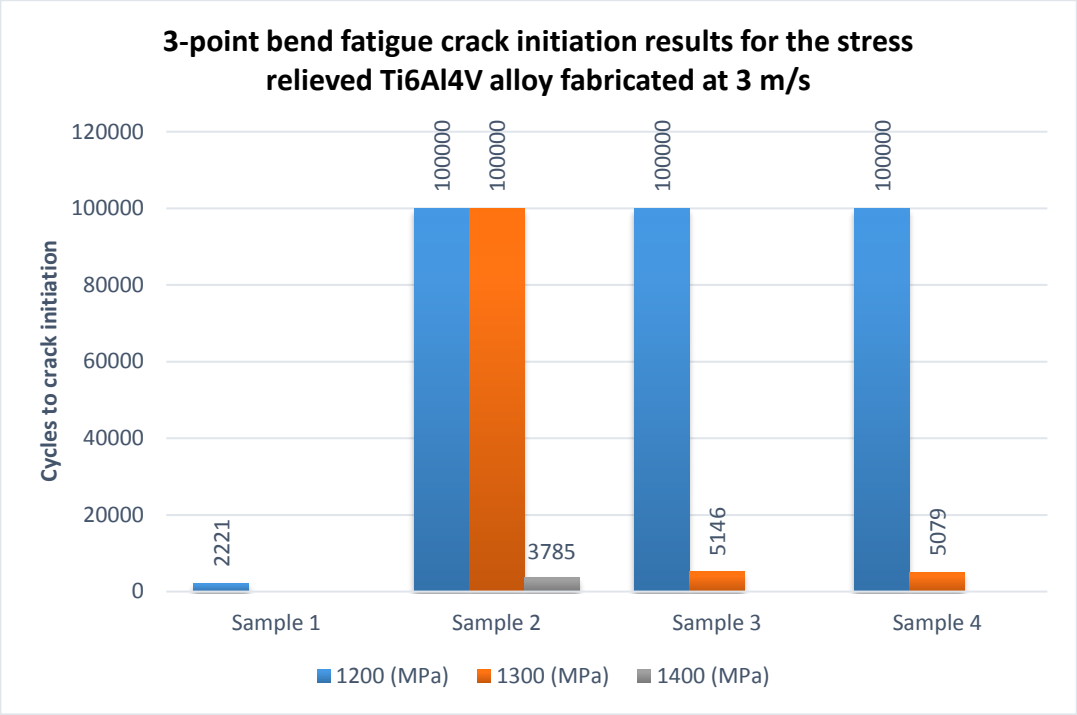


**Figure 90: Number of cumulative cycles at different stress levels for stress relieved SLM Ti6Al4V samples fabricated at 3 m/s.**

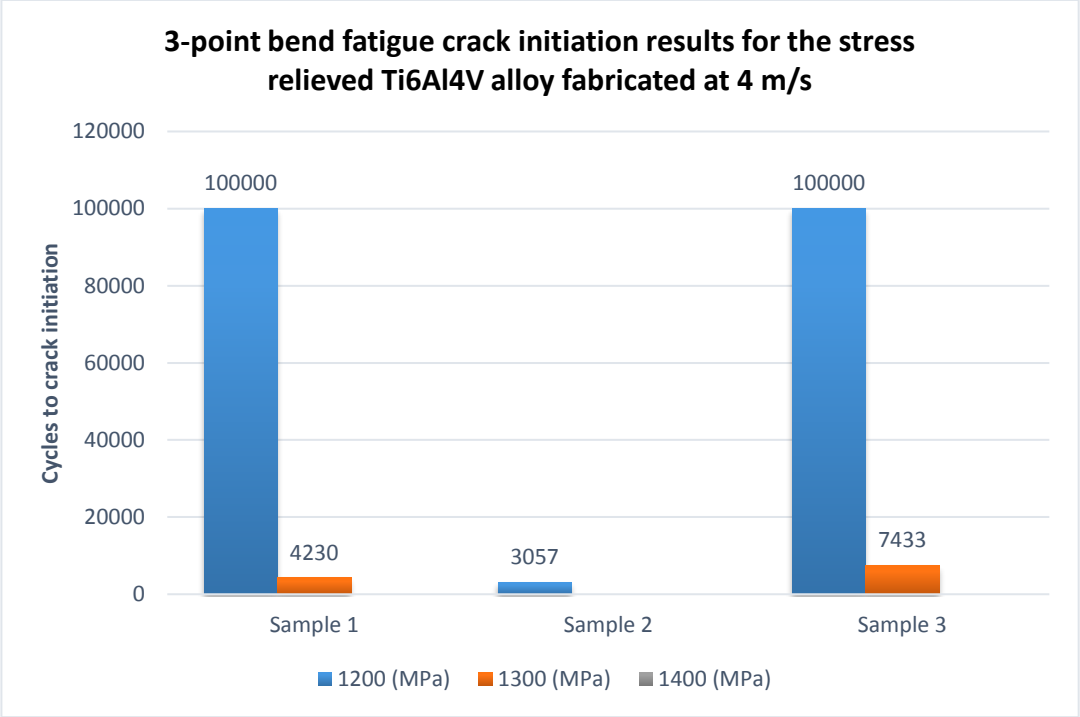


**Figure 91: Number of cumulative cycles at different stress levels for stress relieved SLM Ti6Al4V samples fabricated at 4 m/s.**

## 4.3. REMARKS ON MECHANICAL TESTS RESULTS

There is a significant amount of scatter in the mechanical properties measured and a firm correlation between the laser scan rate and the sample's mechanical properties could not be drawn. Hence, understanding the reasons for the high degree of scatter is important. Further to this, the X-ray CT scans revealed that the presence of pores could not be related to the change in laser scan speed as there was a huge variation in existing pores within specimens fabricated with the same parameter setting.

## 4.4. FRACTOGRAPHY

Secondary electron SEM images were used to investigate fractured surfaces on mechanical testing specimens. This was to assess the fracture mechanisms that led to failure in each specimen.

### 4.4.1. Tensile Fractographs for the as-built SLM Ti6Al4V samples

As the uniaxial tensile stress-strain curves for the as-built SLM Ti6Al4V showed, some specimens, produced using the same process parameters, had inconsistent results, especially in terms of ductility. Therefore, to further elucidate the tensile results, it was necessary to investigate the fractured surfaces on selected specimens to characterise the mode of fracture for each specimen that would have a direct correlation with the ductility observed in the tensile stress-strain curves.

The conventional cup and cone morphology was observed on the tensile fractured surfaces, which indicated a ductile fracture mode, and hence the plastic deformation as shown in Figure 92.

The ductile fracture mode shown in Figure 92 is characterised by the presence of shear edges produced at the last stage of ductile fracture, with the majority of such edges seen with dull surfaces or fibrous morphology.

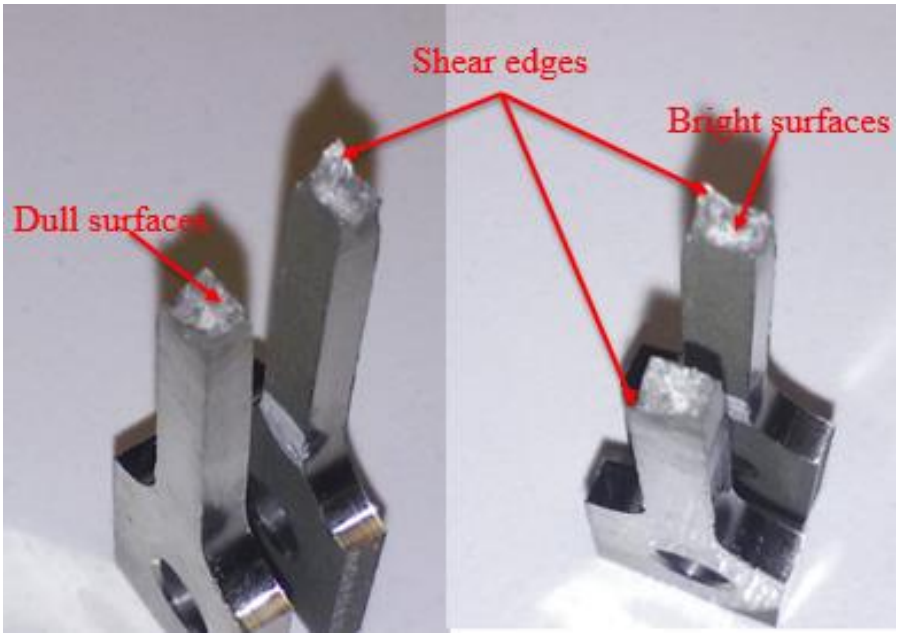


**Figure 92: SLM Ti6Al4V alloy tensile fractured samples fabricated at 1.5 m/s**

The secondary electron SEM images taken on the tensile fractured surface of the SLM Ti6Al4V sample, fabricated using *1.75 m/s* laser scan speed (Specimen 1), are presented in Figure 93 (SLM Ti6Al4V Fractographs).

The presence of circular dimple facets is visible at higher magnifications, as shown in Figure 93 (*circled in red*), indicating ductile fracture mode. The circular dimple facets are the result of pre-existing micro-voids (pores) coalescence to form cracks, owing to the extreme strains experienced caused by the uniaxial forces applied during tensile testing. Fractographs also reveal the presence of several circular pores within the tensile fractured specimen, as indicated by the red arrows in Figure 93. Furthermore, higher magnification into some pores (top right corner in Figure 93) revealed cleavage facets around such pores, which suggests trans-granular brittle fracture, characterised by poor plastic deformation. The yellow dotted lines indicate the undesirable presence of micro cracks.

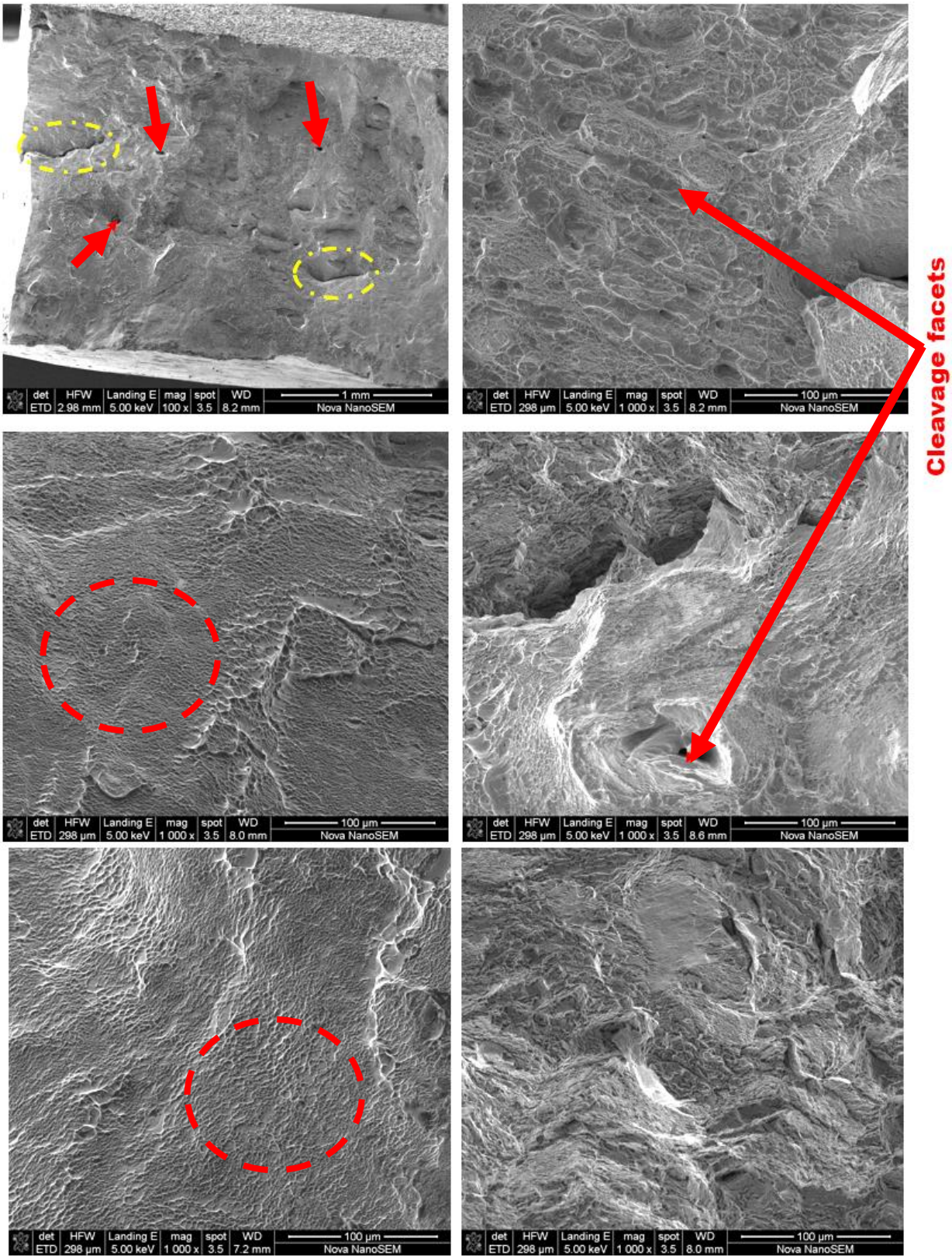


**Figure 93: Fractographs of SLM Ti6Al4V fabricated at 1.75 m/s**

To investigate the sudden loss of ductility in samples produced using the same set process parameters, secondary electron SEM images were taken on the sample, which indicated a substantial loss in ductility during tensile testing (as-built SLM Ti6Al4V fabricated at 2 m/s). The results are shown in Figure 94.

The fractured surface morphology in Figure 94 indicates minor dimple facets and a considerable number of pores and cracks. Furthermore, there exist a substantial number of unfused powder particles, visible throughout the fractured surface, with several voids owing to delamination or unfused regions.

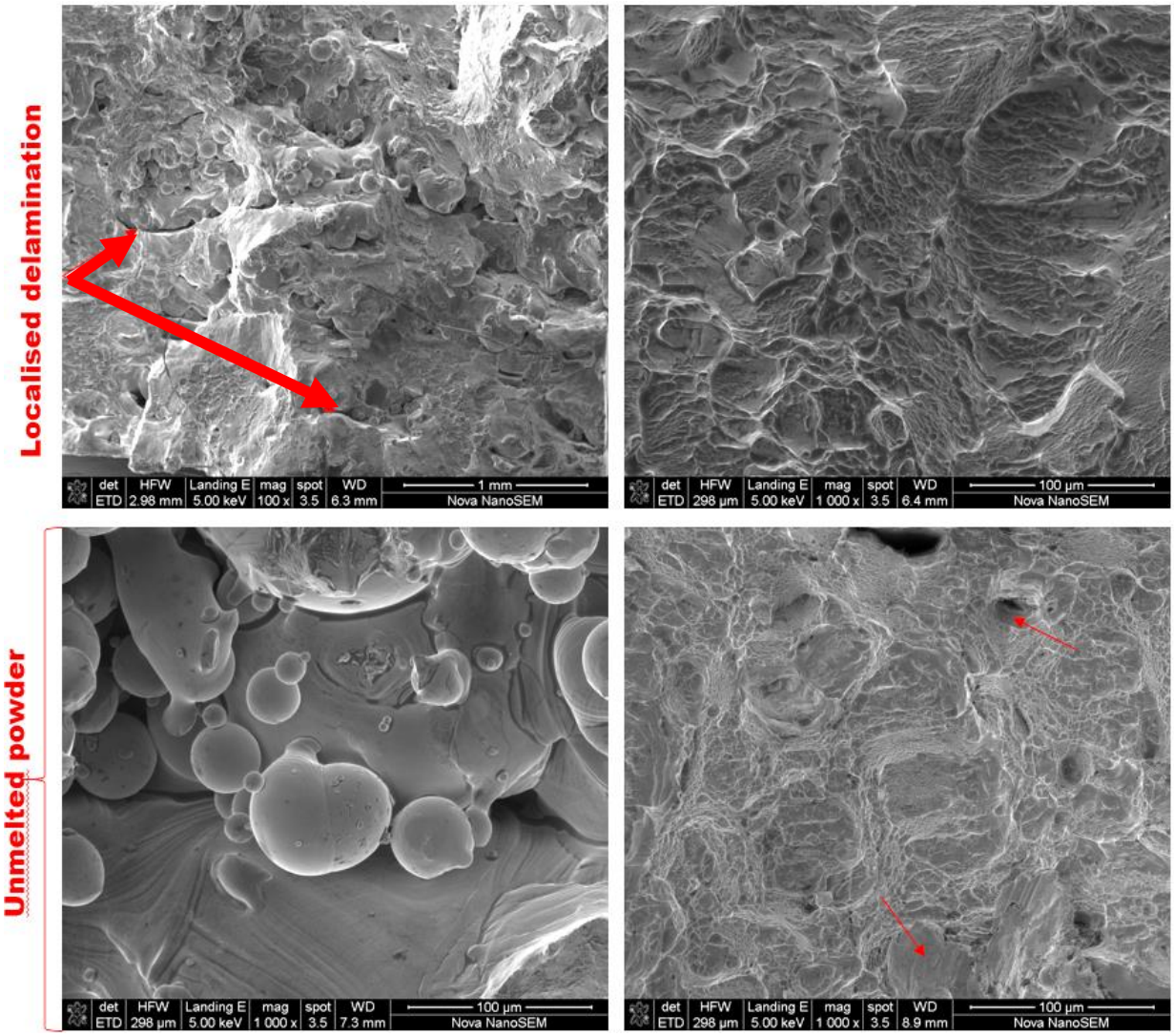


**Figure 94: SLM Ti6Al4V Fractographs fabricated at 2.0 m/s**

A mixed mode fracture morphology (combination of ductile and brittle fracture) is observed on the tensile fractured sample for the as- built SLM Ti6Al4V sample produced at *2.5 m/s* laser scan speed, as shown in Figure 95. Some surfaces mainly reveal dimple fracture morphology at higher magnification, indicating ductile fracture mode, but mostly the cleavage fracture morphology is more dominant. Perhaps this is the reason for the highest UTS with loss in ductility, as indicated in Section 4.2.1 (Figure 80, tensile stress-strain curves for the as-built Ti6Al4V samples fabricated at 2.5 m/s laser scan speed).

On the other hand, in most areas of the same tensile fractured surface, higher magnification indicated a combination of dimple and cleavage fracture morphologies (top right micrograph in figure 95), which clearly indicates that there was a combination of ductile and brittle fracture within the area. Generally, the fractured surface shows the inherent brittle failure character mostly experienced in hard materials.

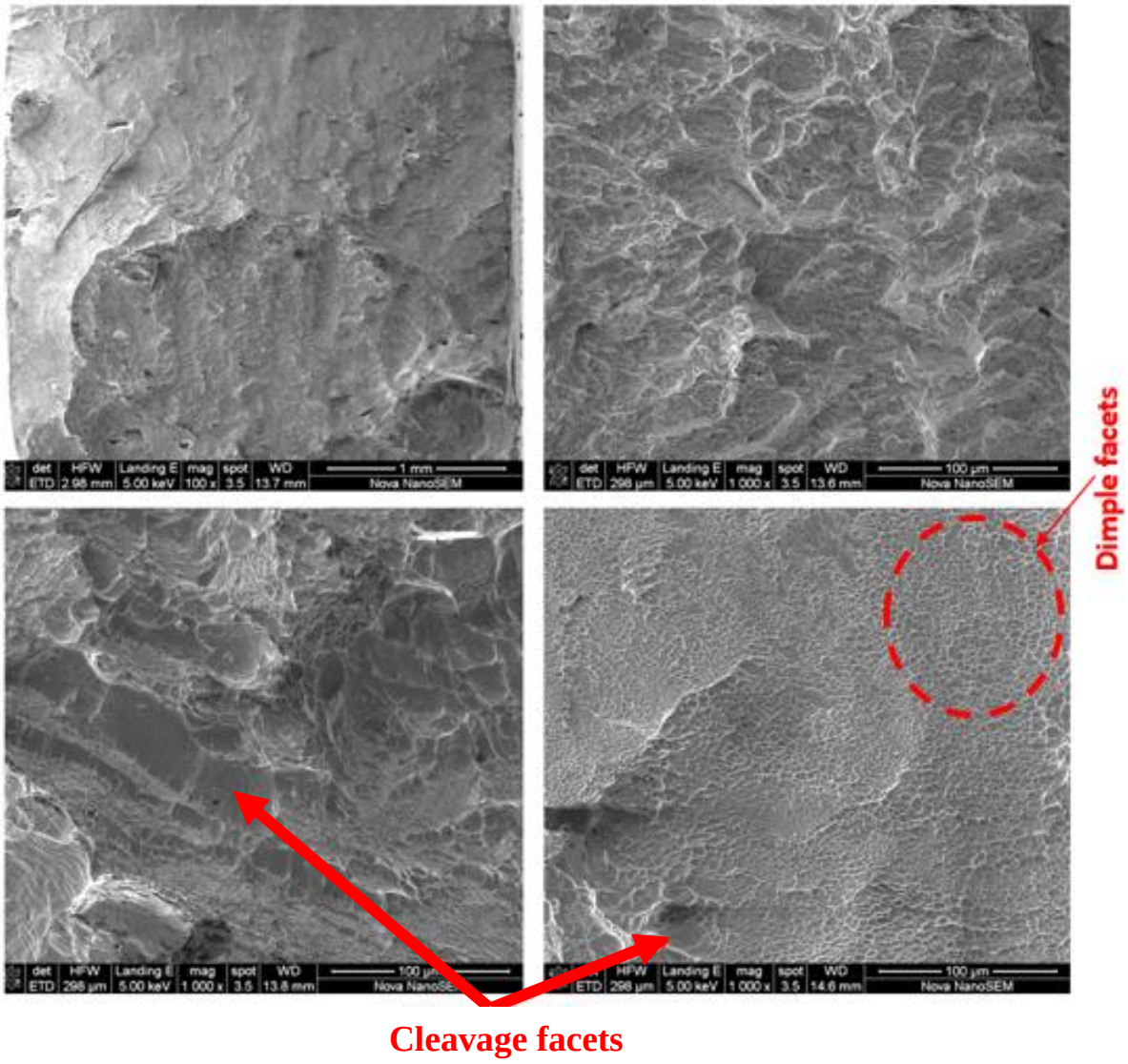


**Figure 95: Secondary SEM micrographs of SLM Ti6Al4V fractured surface fabricated at 2.5 m/s**

### 4.4.2. Tensile Fractographs for the stress relieved SLM Ti6Al4V samples

Fractographs of broken tensile samples taken from the stress relieved SLM Ti6Al4V sample, fabricated at 3 m/s (Specimen 2), showed that the fracture mode was predominately ductile as shown in Figure 96. There is also a noticeable number of open pores on the fractured surface, with minor cleavage facets being visible at lower magnifications.

Although the sample showed better ductility, (*14.8 %*), as compared to the rest of the stress relieved samples, the secondary electron SEM images show that there were still pre-existing micro cracks (cycled in red) and micro pores (indicated by yellow arrows) present.

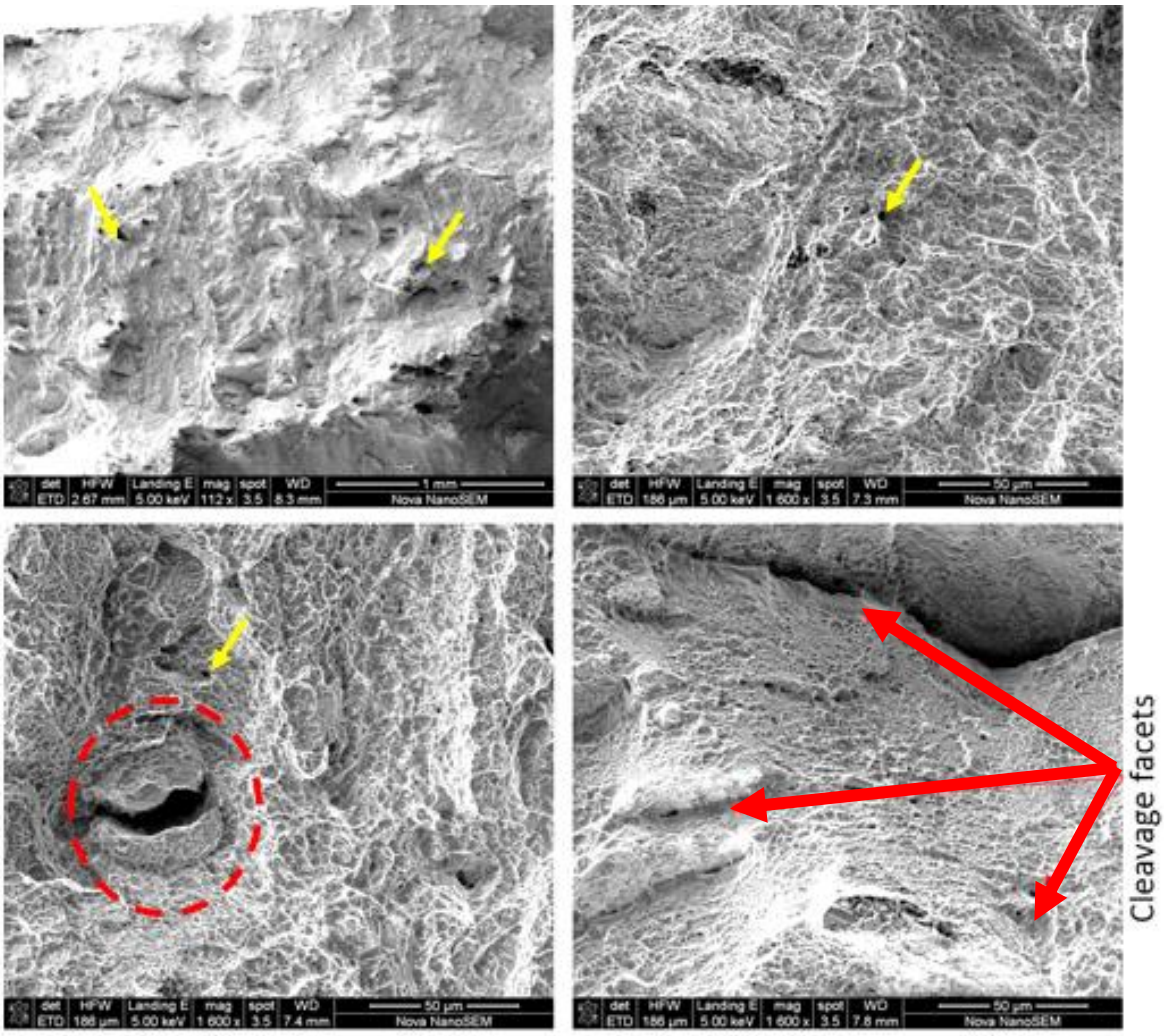


**Figure 96: Tensile fractured surfaces on stressed relieved SLM Ti6Al4V sample fabricated at 3 m/s (sample 2)**

Figure 97 depicts that there was a considerable number of visible existing micro cracks (indicated by the blue arrows) that interlinked as the crack propagated and hence exacerbated the resistance to crack propagation. Figure 97 represents the tensile fractured surface of the stress relieved SLM Ti6Al4V sample fabricated at 4 m/s (Sample 1). There were a considerable number of open pores with unmelted powder particles within the sample, as indicated by the yellow dotted circles. Furthermore, the present of unfused particles is visible in micrographs taken at lower magnifications.

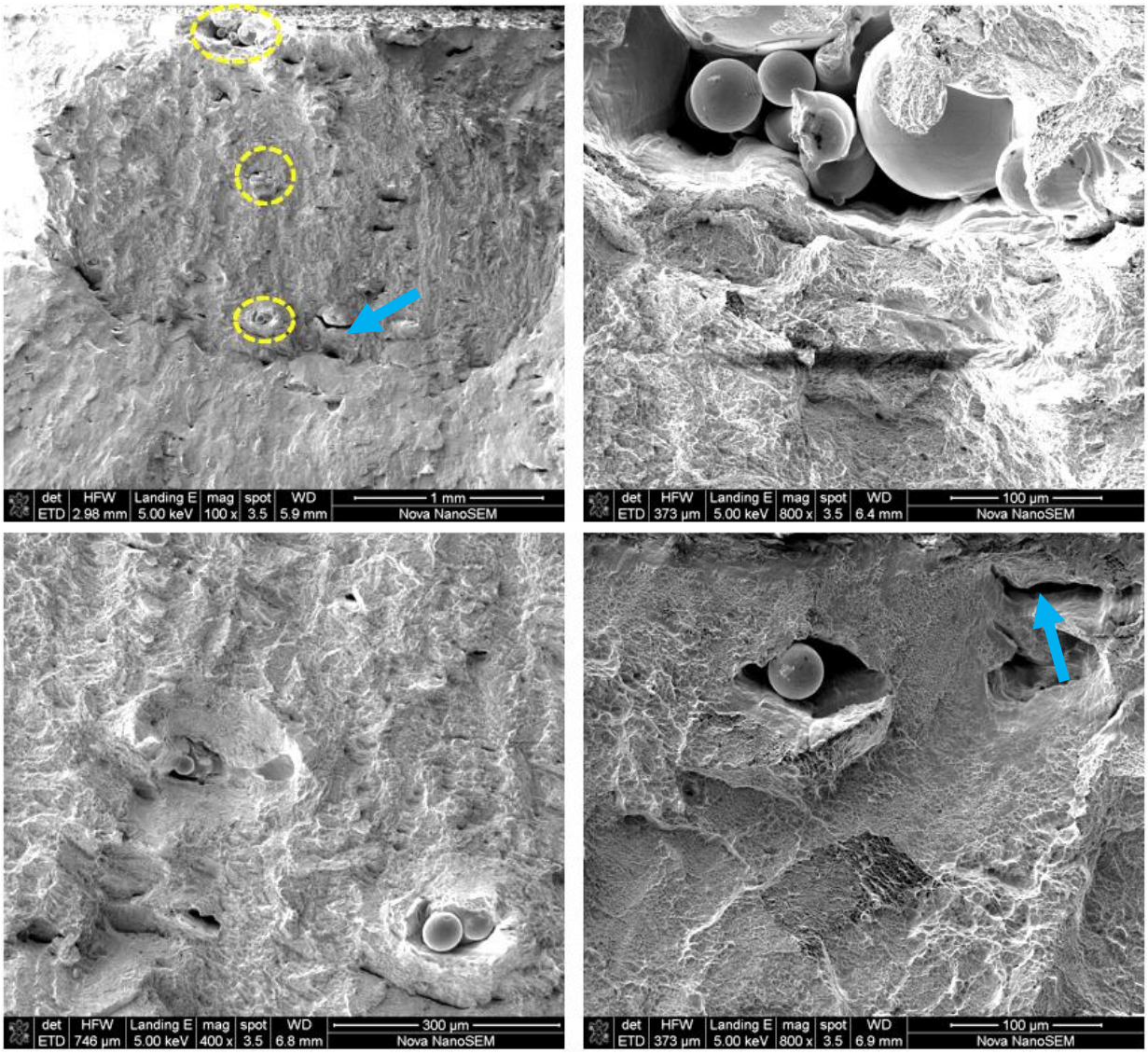


**Figure 97: Tensile fractured surfaces on stressed relieved SLM Ti6Al4V sample fabricated at 4 m/s (sample 1)**

Sample 3, fabricated at 4 m/s, was studied further to investigate loss in ductility as shown in Figure 98. Except for the visible dimple facets observed in some portions on the fractographs, indicating plastic deformation through micro pore coalescence, there exist an alarming number of SLM process defects within the sample, which include localised delamination and large pores, which would have restricted the amount of plastic deformation.

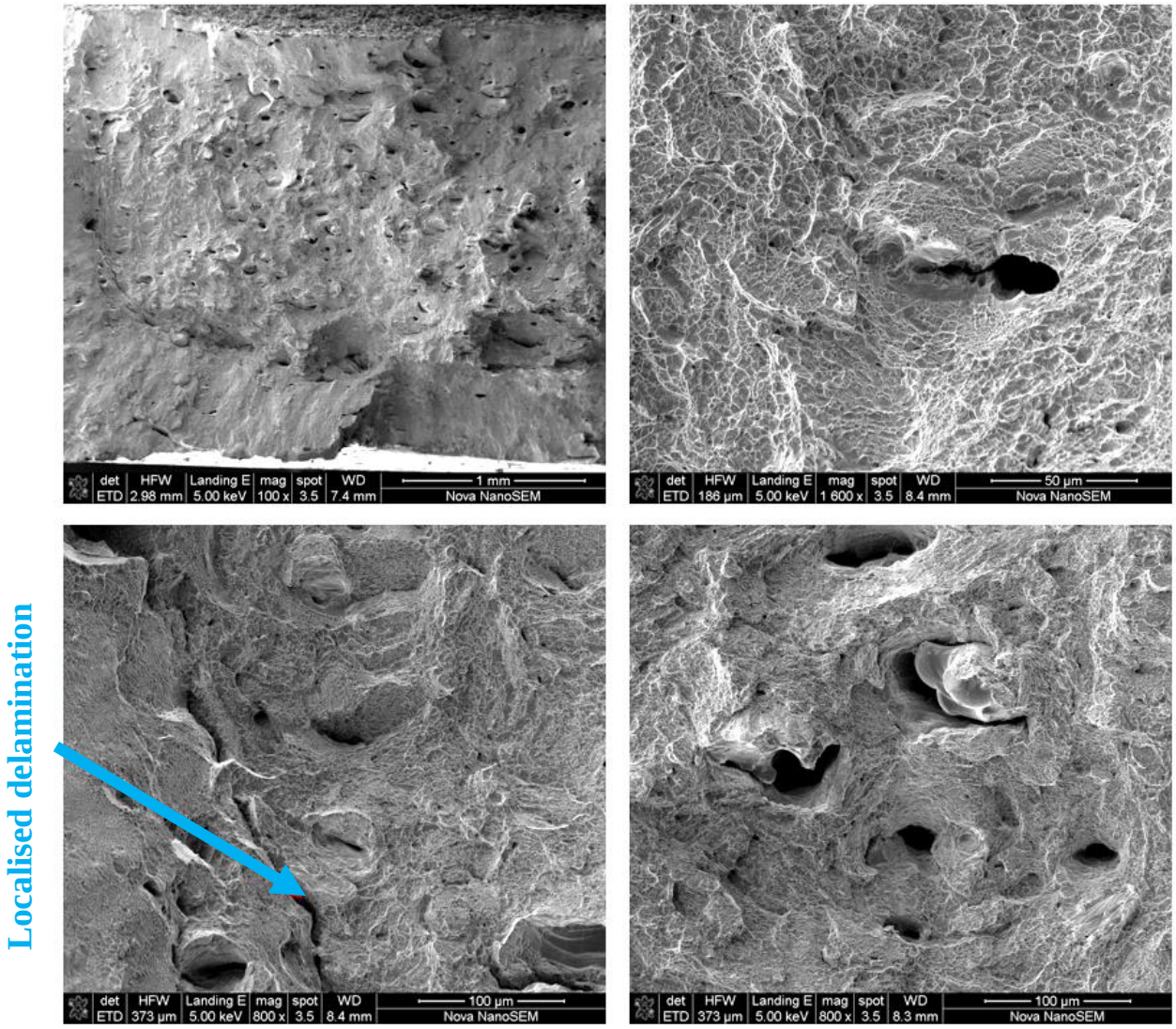


**Figure 98: Tensile fractured surfaces on stressed relieved SLM Ti6Al4V sample fabricated at 4 m/s (sample 3)**

### 4.4.3. Fracture toughness samples fractographs

During pre-cracking, some samples exhibited earliest crack initiation, but the crack propagation rate was slow. This was observed in samples produced at a lower laser scan speed (3 m/s). However, samples produced at higher laser scan rates (3.5 m/s and 4.0 m/s) showed crack initiation at much higher cycles and the crack propagation rate increased as the crack became longer.

Figure 99 depicts the conversional thumbnail crack front profile as a result of stable crack propagation during pre-cracking. The crack propagation was stable and linear during the test and this portion is shown by lighter surfaces in Figure 99.

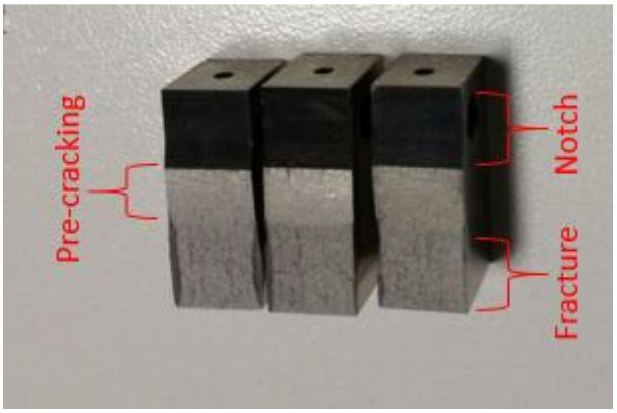


**Figure 99: Crack front on fractured Ti6Al4V samples (stress relieved).**

On the other hand, dull surfaces were due to rapid crack propagation during tensile fracture testing and were therefore characterised by rough surfaces and shear lips, owing to the ductile nature of the sample.

Figure 100 depicts secondary electron SEM images taken on the fractured surface of the fracture toughness sample fabricated at 3 m/s and stress relieved prior to testing. Figure 100(a) shows lower magnification of the crack front and minor pores and internal cracks can be observed.

On the other hand, Figure 100(b and c), shows higher magnifications of some of the defects identified from lower magnification. The presence of cracks and pores within the stress relieved SLM Ti6Al4V sample results in lower resistance to crack propagation. There were minor defects identified in all samples and this may have contributed to the higher fracture toughness values observed in this project after the stress relief heat treatment, comparable to other research [17, 26].

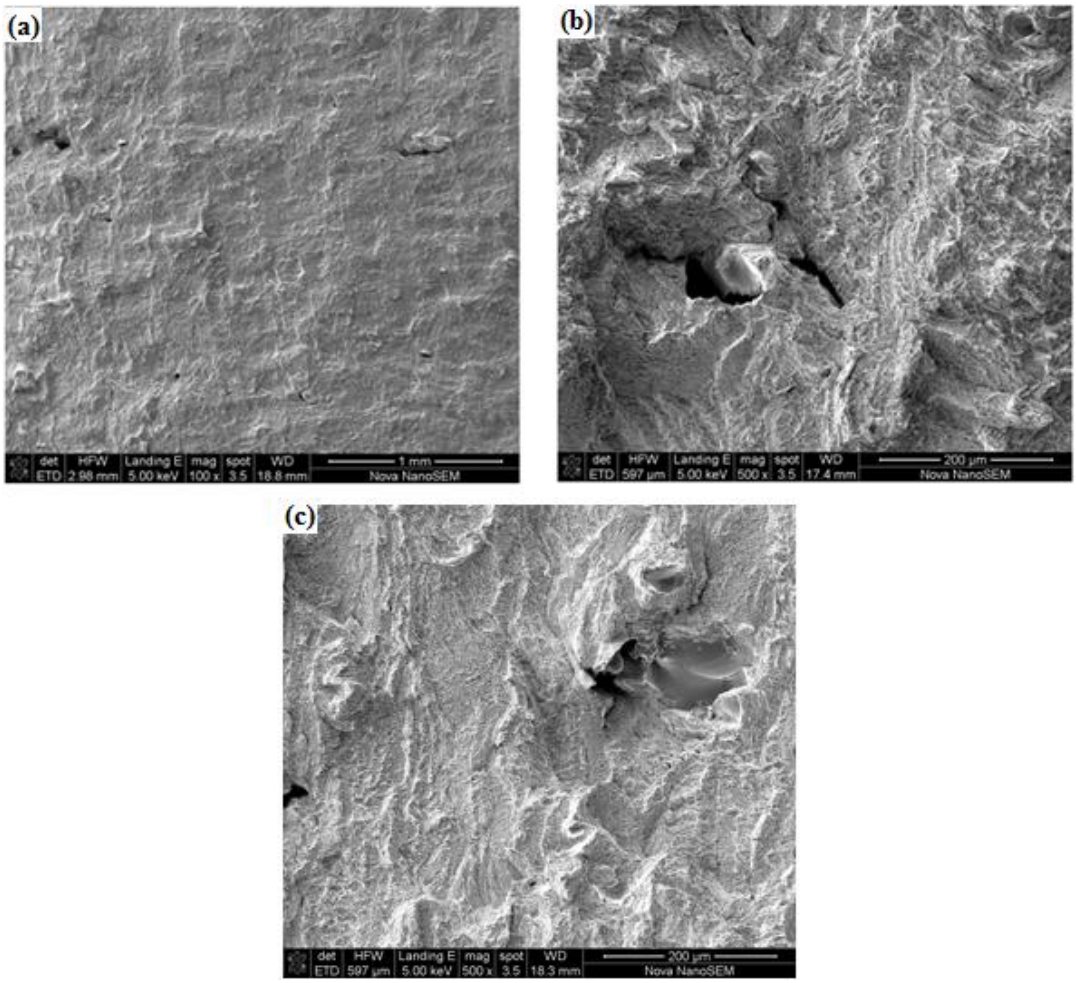


**Figure 100: Fratographs taken on a crack front of a fracture toughness sample fabricated at 3 m/s.**

To investigate the reason behind some samples failing prematurely during pre-cracking, secondary electron SEM images were used, as depicted in Figure 101 (a-d). Comparing these SEM images to those shown in Figure 100, it is apparent that there was a significant number of process defects that contributed to the failure of these fracture toughness samples. The presence of internal cracks (circled in green) and open pores (indicated with yellow arrows) with entrapped unmelted powder particles (circled in red) contributed as multiple stress raisers, which led to multiple crack initiation sites and eventually to rapid crack propagation, with no resistance at all.

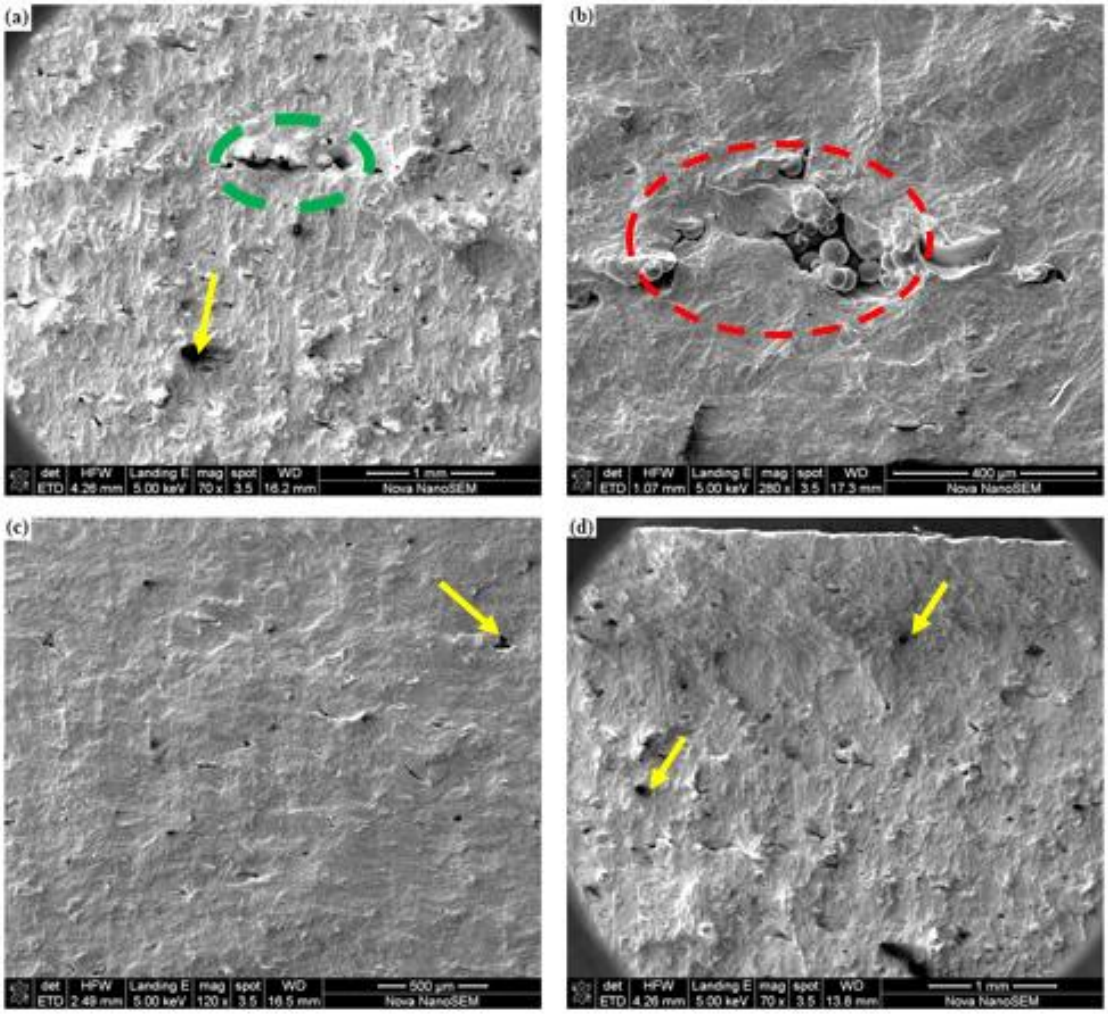


**Figure 101: Fractographs taken on failed fracture toughness samples during pre-cracking**

### 4.4.4. Fractured surfaces on 3-point bend fatigue samples

Fractography in fatigue samples enables the identification of fracture mode and crack initiation sites. Secondary electron SEM images were used for this purpose to compare fractured surfaces on samples that showed poor fatigue results to the sample that endured the fatigue cycles very well. Figure 102 shows the first three-point bend fatigue sample of the stress relieved SLM Ti6Al4V fractured surface. One of the root causes of premature failure at 1200 MPa stress intensity is identified as early crack initiation, owing to a surface pore, as indicated by the blue circle in Figure 102. The lack of crack initiation and propagation resistance is exacerbated by the presence of micro pores and cracks within the sample.

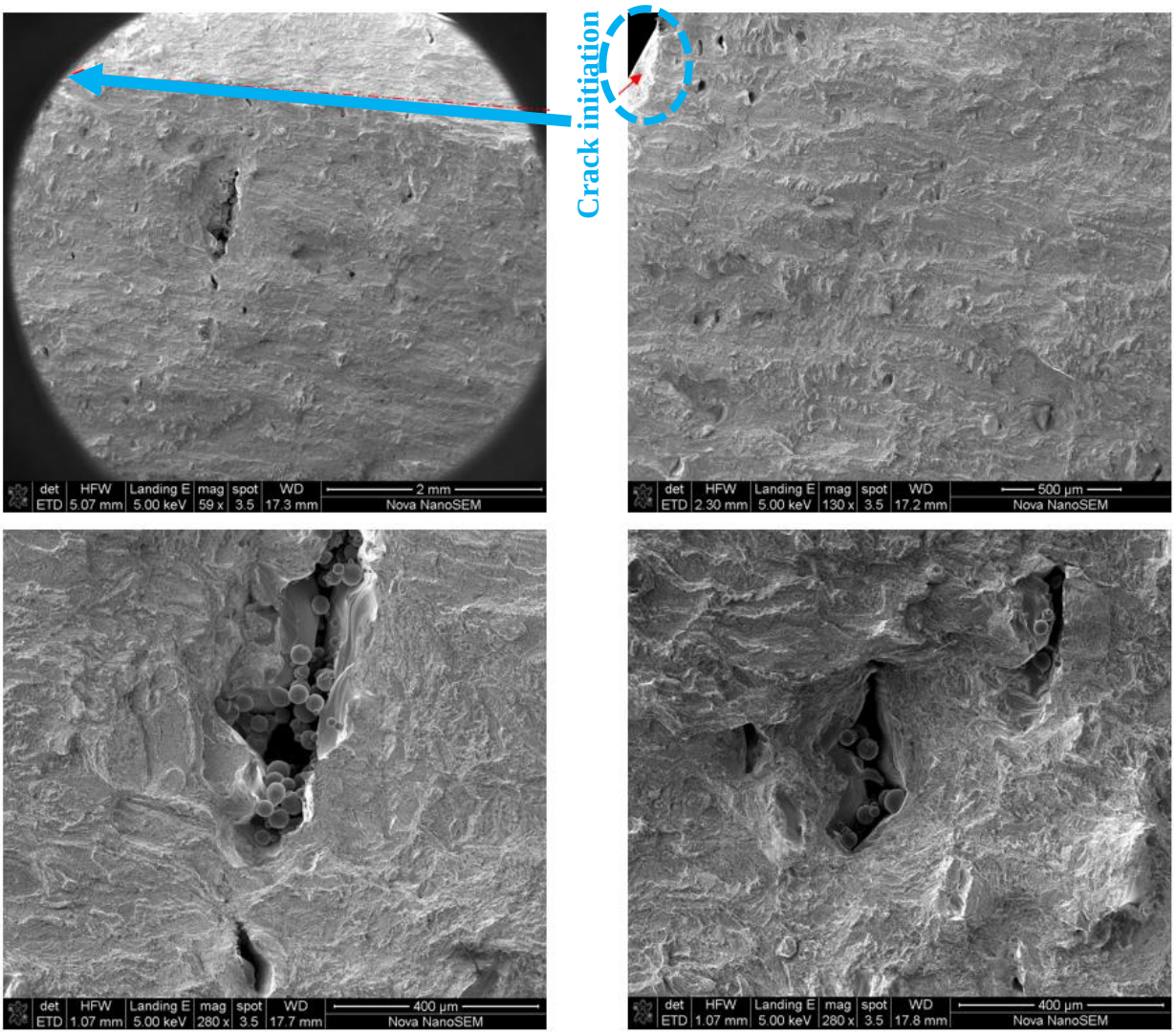


**Figure 102: Fractured surfaces of a stressed relieved SLM Ti6Al4V 3-point bend fatigue sample fabricated at 3 m/s (first sample)**

The chevron tomography shown in Figure 103 supported the above observation, as the second sample fabricated at 4 m/s also responded poorly to the cyclic fatigue three-point bend forces at 1200 MPa. The crack initiation site is shown on the figure and one can identify a process defect, the elongated pore, as the major source. Moreover, the overall tomography has a brittle fracture appearance, which may suggest that there was a rapid crack propagation after initiation.

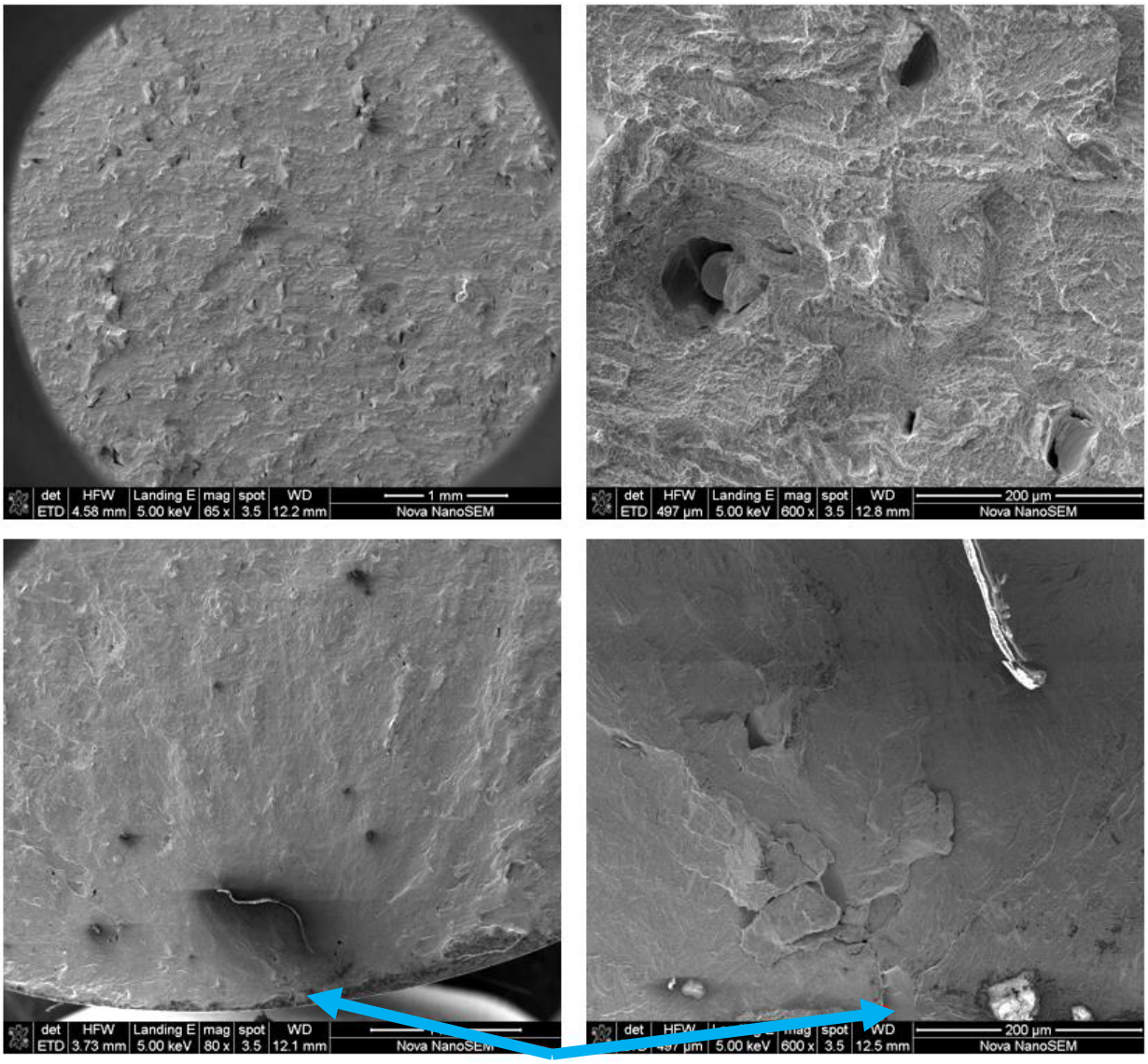


**Figure 103: Fractured surfaces of a stressed relieved SLM Ti6Al4V 3-point bend fatigue sample fabricated at 4 m/s (second sample)**

The secondary electron SEM images shown in Figure 104 illustrate that there are still micro pores visible within this sample, with major defects shown in the figure. The two middle figures in Figure 104 indicate the presence of multiple micro pores (*indicated with black arrows*) and the presence of unfused Ti6Al4V powder particles (*circled in blue*). The sample showed the most fatigue crack initiation resistance compared to other samples, owing to the presence of fewer process defects.

Fractographs taken on all fractured mechanical specimens revealed that the inevitable presence of pores and other process defects led to the poor performance of most of the mechanical specimens. The variation in these process defects mitigates against any correlation with the laser scan rate.

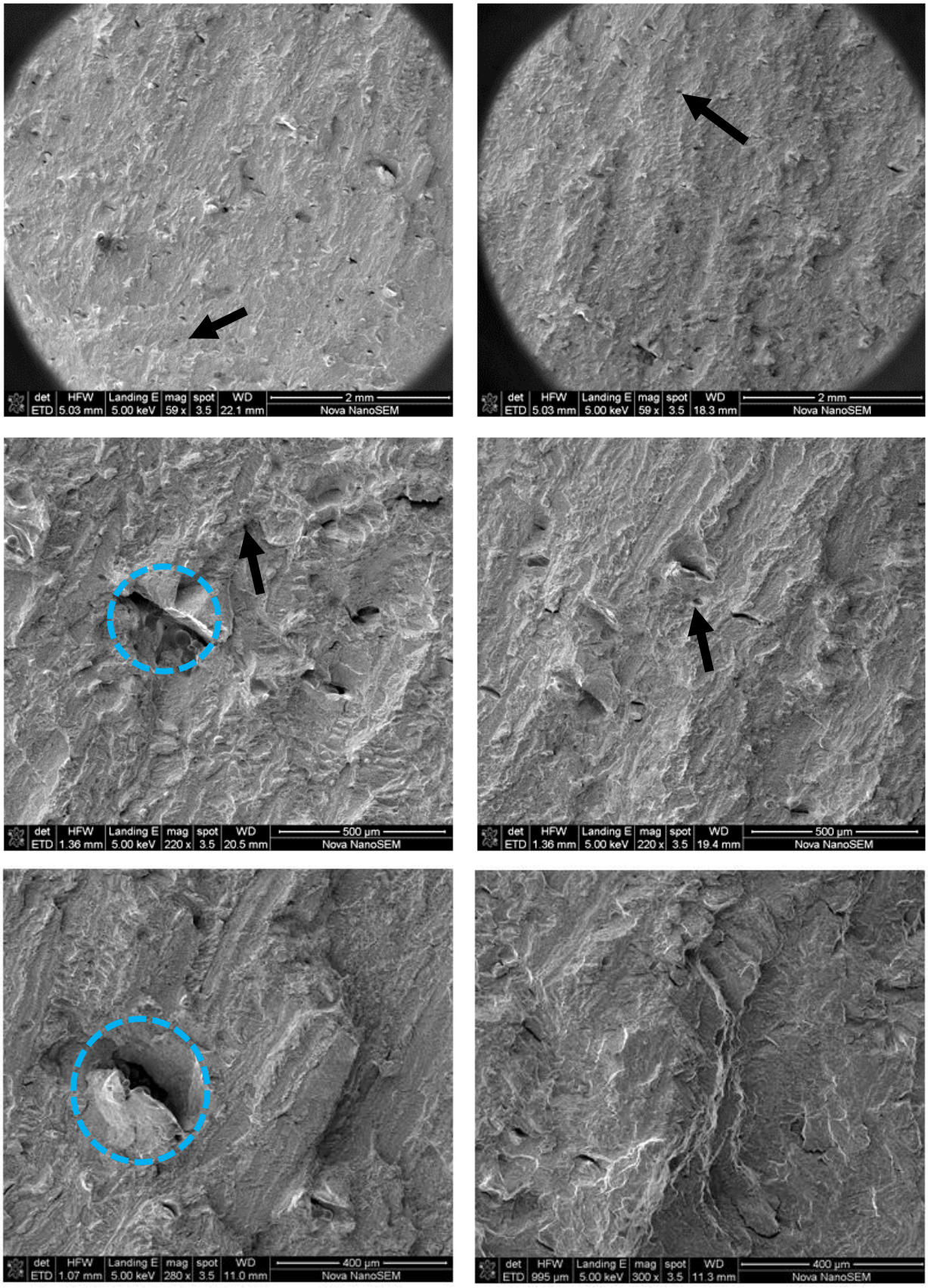


**Figure 104: Fractured surfaces of a stressed relieved SLM Ti6Al4V 3-point bend fatigue sample fabricated at 3 m/s (second sample).**

# 5. DISCUSSIONS

This chapter presents a detailed account and analysis of the mechanical and microstructural results presented in Chapter 4. Moreover, the X-ray CT scans and the secondary electron SEM images were used to identify process defects on fractured surfaces to explain the mechanical behaviour observed in Chapter 4. Comparison is also made with work from other researchers and analysis drawn with respect to the project's results and the findings presented in open literature.

## 5.1. TENSILE TESTING

The uniaxial tensile test results showed a significant scatter in mechanical properties, especially the UTS and ductility within samples produced using the same process parameters. This raised major concerns regarding the repeatability, as well as the reproducibility, of the process itself, especially at laser scan rates exceeding 3 m/s. Gong *et al*. [25] carried out a range of scan rates to fabricate SLM Ti6Al4V samples and observed that there was a sudden deterioration in ductility as the laser scan speed was increased while other process parameters were kept constant. This was attributed to the nature of pores being present at various scan rates, depending on the available energy density. This rapid decrease in ductility on SLM Ti6Al4V products can be attributed to extreme strain localisation caused by an increase in pore size and early crack initiation, which led to fracture of the plane containing the pore and the limiting of the extent of uniform plastic deformation that could be achieved before fracture [54]. The same analogy can be applied to the measured mechanical results found in this project, even though there was considerable scatter; but the nature of pores present within the built SLM Ti6Al4V samples contributed to the mechanical results, as discussed below. Table 15 serves as summary for the samples discussed and can be used for easy reference.

The measured mechanical properties for the as-built SLM Ti6Al4V uniaxial tensile samples, fabricated between 1.5 m/s and 4 m/s laser scan speed, showed a significant scatter in the measured UTS, ductility (% elongation) and the yield strength. For this reason, the relationship between the laser scan rate and the measured mechanical properties could not be established. Figure 80 shows that the scatter in the measured mechanical properties became extreme as the laser scan rate was increased beyond 3 m/s.

The first sample (Sample 1), fabricated at 1.75 m/s, showed better elongation (15%) as compared to the rest of the as-built SLM Ti6Al4V tensile samples and further investigation into

the fractured surface using the secondary electron SEM images (Figure 93) showed that the failure mode was predominantly ductile, as most of the surface morphology had circular dimple facets. This suggested that the sample went through a considerable plastic deformation through micro pore coalescence. Fractographs (Figure 93) also revealed micro cracks and minor cleavage facets on the fractured surface. These pores are believed to be due to entrapped gas because of local over-heating caused by high energy density, as reported by Gong *et al*. [25] and Facchini *et al*. [35]. Furthermore, higher magnification into some pores (Figure 93) revealed cleavage facets around such pores, implicating trans-granular brittle fracture, which is characterised by poor plastic deformation [35].

The as-built SLM Ti6Al4V uniaxial tensile samples fabricated at 2.5 m/s showed a substantial increase in the UTS, with a corresponding deterioration in elongation. This sudden increase in the ultimate tensile strength (UTS) may be attributed to the oxygen or hydrogen embrittlement effect, as this resulted in a corresponding loss in ductility. Furthermore, fractoghraphs (Figure 95) showed that the specimen was mainly dominated by cleavage facets, which are associated with brittle fracture mode. In addition, the general tomography on the fractured surface was mainly flat and showed an inherent brittle failure character. Ferrar *et al*. [34] advocated that the reproducibility of SLM Ti6Al4V samples could be influenced by the method in which the inert gas was delivered across the build platform. Therefore, the embrittlement experienced by samples fabricated at 2.5 m/s may be due to environmental contamination (oxygen embrittlement) across the build platform.

On the other hand, the sudden loss in ductility in some specimens was found to be due to the amount of porosity such specimens exhibited during fabrication. A particular reference can be made to the as-built SLM Ti6Al4V uniaxial tensile specimen produced at 2.0 m/s laser scan speed. The specimen showed a substantial drop in both UTS and ductility (Figure 80) and the secondary electron SEM images on the fractured surface (Figure 94) revealed unfused particles and severe cracks associated with localised delamination. This leads to the conclusion that poor elongation in this sample was mainly due to high porosity within the sample, as could be validated further by its density measurement (92%-94%) in Table 10.

Combining Figure 93, Figure 94 and Figure 95 morphologies, one can say that the sudden loss in ductility for the as-built SLM Ti6Al4V samples was due to the considerable amount of porosity present in the samples, since pores would have acted as stress raisers and the localised delamination interlinked with micro pore coalescence within a short time. This observation correlates well with what Formanoir *et al*. [41] and Sterling *et al*. [40] reported, as the sample

with the most process defects (pores and unmelted particles) was found to exhibit the lowest ductility when compared to the other samples fabricated with the same process parameters.

**Table 15: Summary of the mechanical properties and fractographs for the as-built Ti6Al4V tensile samples.**

| Laser scan speed (m/s) | Energy density ($kJ/mm^3$) | UTS (MPa) | Elongation to failure (%) | Fractographs |
|---|---|---|---|---|
| 1.75 (Sample 1) | 61.91 | 1000 | 15 | 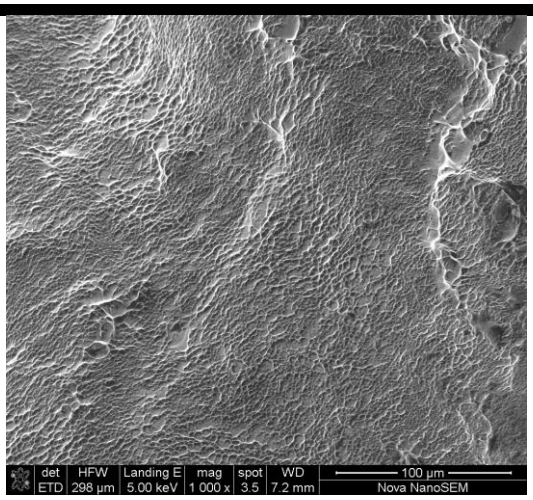 |
| 2.5 | 86.67 | 1333 | 4 | 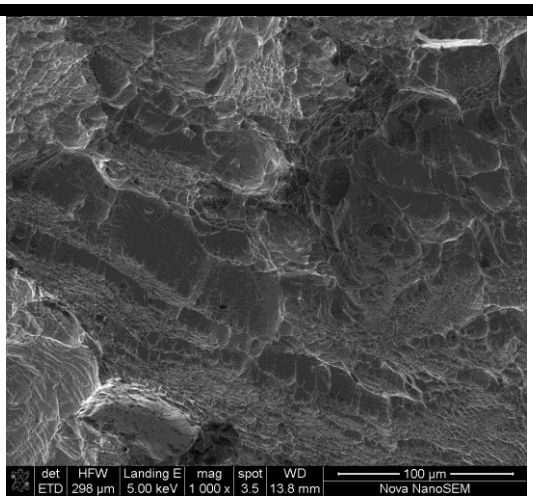 |
| 2.0 | 108.33 | 1007 | 6 | 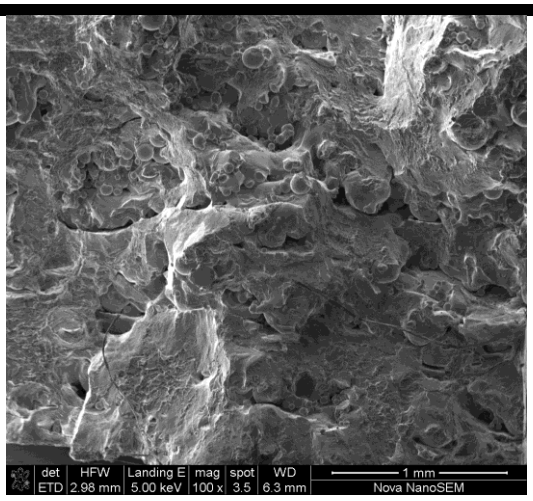 |

One of the major contributors to poor mechanical properties, in addition to those discussed above, is the presence of residual stress within the as-built SLM Ti6Al4V samples. Facchini *et al*. [35] reported that the low ductility observed in SLM samples was attributable to the martensitic morphology, micro cracks and pores, as well as to residual stress inherent in the SLM process. For this reason, SLM Ti6Al4V uniaxial tensile samples were fabricated at 3 m/s and 4 m/s, followed by stress relief heat treatment (650°C for four hours in vacuum and furnace cooled). Furthermore, the X-ray computed tomography (X-ray CT) scans were used for quantitative porosity analysis within the fabricated samples. Table 16 can be used as a quick reference.

There was improvement in the reproducibility and scatter in the measured mechanical properties for the stress relieved SLM Ti6Al4V uniaxial tensile sample fabricated at 3 m/s and 4 m/s, as Figure 83 indicates. Sample 2, fabricated at 3 m/s, showed good ductility compared to other samples and the reason for this could be investigated by the X-ray CT scan analysis, as well as by the fractured surface fractographs. The 3D reconstructed images in Figure 65 show that Sample 2 (Figure 65(a)) had lower porosity compared to the rest of the samples fabricated at 3 m/s. The pore size distribution in Figure 66(a) showed more scattered micro pores throughout the gauge length, with the largest pore at the centre of the sample. The fractured surfaces of Sample 2 showed intensive plastic deformation topography, as there were visible dimple facets with only minor defects observed. On the other hand, Sample 1, fabricated at 3 m/s, showed the lowest ductility, owing to the presence of the largest pore on its surface/edge, as Figure 67(a) and Figure 67b(i) depict. In this case, the plastic deformation was limited by the sudden crack initiation and propagation, owing to the applied stresses on the existing surface crack during the uniaxial tensile testing.

The 2D X-ray CT scan image slices, shown in Figure 67(b), revealed several surface pores in samples fabricated at 3 m/s, while in some other instances the largest pore was seen to be isolated from most of the clustered micro pores. The same observation was done on 2D image slices, shown in Figure 70. Three of the samples fabricated at 4 m/s laser scan speed showed the lowest ductility, as compared to all the stress relieved samples (both 3 m/s and 4 m/s) and the cause of this may be attributed to the number of defects observed, especially next to the surfaces of the samples. Further to this, the secondary electron SEM images in Figure 97 and Figure 98 showed the substantial presence of pores and unmelted powder, most of which were located next to the sample's surface. The poor ductility was due to the extensive presence of pores in these samples. Sample 2, fabricated at 4 m/s, showed better elongation (10%) and the X-ray CT scans, (Figure 68(c), Figure 69(c) and Figure 70(b)), indicated less porosity, as compared to other samples fabricated at 4 m/s.

**Table 16: Summary of the mechanical properties, fractographs and the X-ray CT scans for the stress relieved Ti6Al4V tensile samples.**

| Laser scan speed (m/s) | UTS (MPa) | Elongation to failure (%) | Fractographs | X-ray CT scans |
|---|---|---|---|---|
| 3.0 (Sample2) | 1036 | 14.8 | 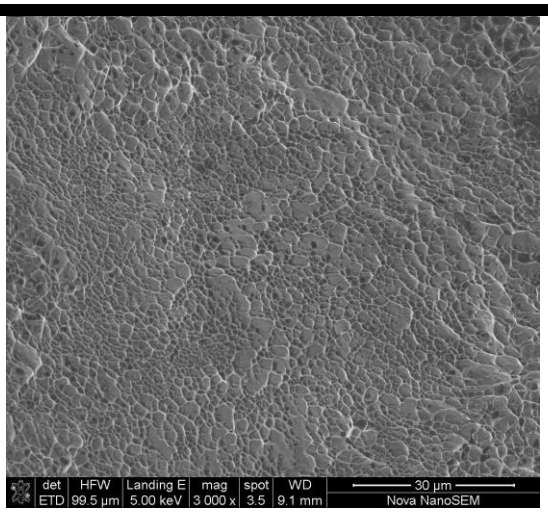  | 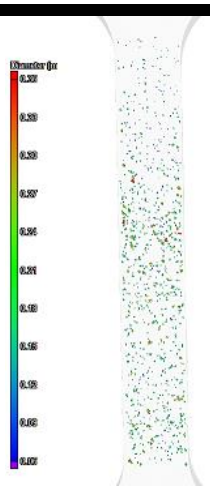 |
| 3.0 (Sample1) | 1000 | 9.7 | 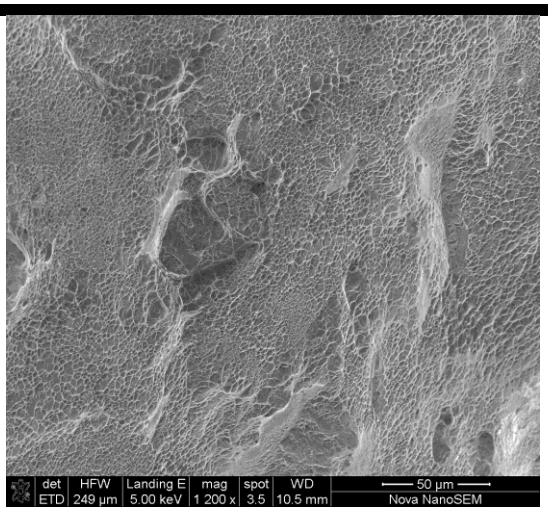  | 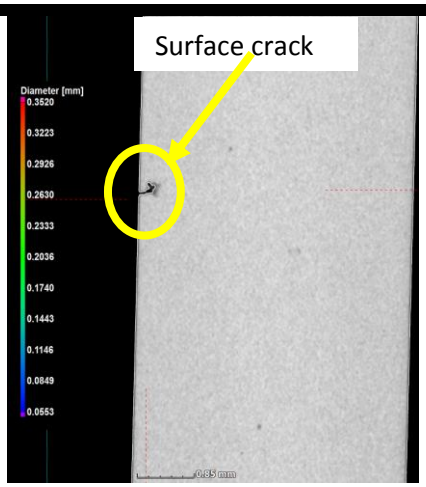  |
| 4.0 (Sample2) | 1060 | 10 | 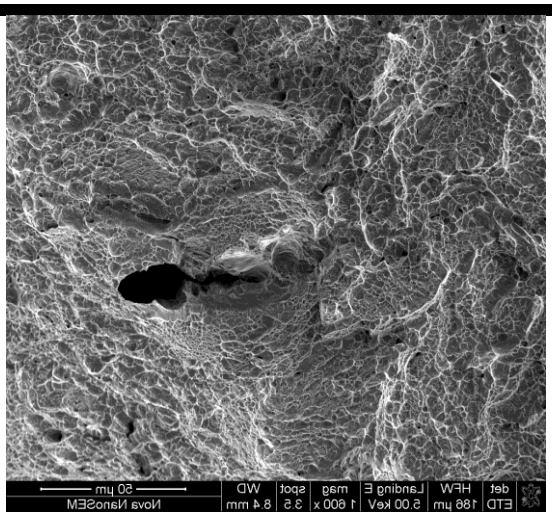 | 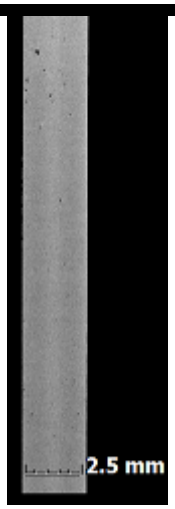  |

Therefore, it is apparent that in this project the measured uniaxial tensile test results depended significantly on a sample's porosity character; the location of porosity within the tensile specimens played a major role on their mechanical response. The scatter in tensile test results was mainly due to an individual samples' porosity character and other SLM process defects, which hampered any correlation to be made between the scan rate, density and the measured tensile tests.

## 5.2. FATIGUE CRACK GROWTH RATE (FCGR) TESTING

The FCGR SLM Ti6Al4V test samples were fabricated using laser speeds between 3 m/s and 4 m/s. The density measurements taken using the Archimedes' principle resulted in the range 97% - 99%. Only nine samples were supplied for this test, of which eight were successfully tested, as presented in Section 4.2.3. It is important to note at this point that the FCGR samples were not stress relieved.

The FCGR measurement taken at different scan rates (3 m/s – 4 m/s) indicated a substantial scatter in individual parameters, as illustrated by Figure 87. This scatter in the FCGR data is further seen in Figure 88, where there are several outlying data points. Perhaps this scenario may be attributed to the presence of residual stresses within samples, as reported by Leuders *et al*. [13]. The fatigue crack growth rate was found to be strongly influenced by the presence of residual stresses. During the 1 mm pre-cracking at the notch root, the fatigue crack initiation was seen to be decreasing with the increasing laser scan rate and this can only be attributed to the escalating residual stresses that were introduced as the scan rate was increased during fabrication, since the density of the samples was the same (±98%) and therefore the effect of porosity to crack initiation should have been the same. This was substantiated by Van Hooreweder *et al*. [26], who advocated that the SLM Ti6Al4V FCGR properties were highly influenced by the microstructural morphology, as all the samples showed anisotropic behaviour in different directions and had the same density. Even though this may be the case, further investigation into the porosity character for each sample needs to be conducted to study the nature and spatial distribution of the defects and pores present.

The FCGR curves in Figure 88 show a slight increase in resistance to crack propagation as the laser scan rate is increased from 3 m/s to 4 m/s. The Paris parameters mimic those observed by Cain *et al*. [17] on the FCGR as-built samples, built in the XY plane, parallel to the X-axis with respect to the build direction (Z-axis). Furthermore, the rapid increase in crack propagation at higher scan rates can be associated with what Van Hooreweder *et al*. [26] observed. It was observed that the fine-grained and martensitic microstructures, like that of the SLM material,

tended to slow the propagation rate of small cracks, owing to the high density of grain boundaries acting as obstacle points. But for cracks larger than 1 mm, the effect was reversed, and crack propagation rate was increased. It is unclear whether this study was carried out on stress relieved samples, resulting in less scatter. To some extent the latter study can be correlated with this project, as samples fabricated at 4 m/s showed rapid crack propagation during the actual FCGR test (after 1 mm pre-crack).

It should be noted that the scatter in some samples may have been as a result of the crack front orientation (direction) with respect to the scan direction. This is a crucial aspect in FCGR tests, as Vrancken *et al*. [20] and Cain *et al*. [17] both observed anisotropic behaviour upon investigation of the fatigue crack growth rate of SLM Ti6Al4V samples carried out in different orientations with reference to the build direction. The crack front direction with respect to the scan orientation were not investigated in this research and this may be the contributing factor for all the scattered data. In addition, the data points are inadequate to reach a conclusive point regarding the influence of the laser scan rate on the FCGR properties for SLM Ti6Al4V.

### 5.3. FRACTURE TOUGHNESS TESTING

The density of the SLM Ti6Al4V fracture toughness samples (bulk) was ±98% before the stress relief heat treatment, which was carried out at 650°C for four hours in a vacuum furnace and left to cool (furnace cooled).

During pre-cracking two samples fractured and failed prematurely. Since the density measurement was 98% for both samples, each fabricated at 3 m/s and 3.5 m/s, the effect of porosity was deemed to be the main contributing factor to the rapid fracture as the samples were stress relieved. The secondary electron SEM images depicted in Figure 101 revealed several SLM process defects that were not picked up by the Archimedes' method. There were cracks that could be associated with localised delamination and clustered micro pores and the combination of these defects resulted in catastrophic failure once a crack had initiated. A study by Jha and Sreekumar [62] on a failed oxidiser tank outlet adaptor using the secondary electron SEM images, revealed that the main cause of failure was due to the presence of shrinkage pores (owing to casting). These shrinkage pores provided crack initiation sites and rapid crack propagation, as the crack inter-linked through pores. In this case, the premature failure of the two samples was found to be due to severe pores and micro cracks experienced during SLM fabrication.

Except for the two samples that failed prematurely during pre-cracking, all the stress relieved SLM Ti6Al4V fracture toughness samples showed the same topographic features under the secondary electron SEM images, as shown in Figure 100. Fractographs showed constant crack propagation and revealed minor cracks and open pores.

Owing to a lack of available data points, the influence of the laser scan rate on fracture toughness behaviour could not be ascertained but, due to the stress relieved state of the fracture toughness samples, there was improvement of the fracture toughness properties compared to the "as built" state of 28 MPa.m$^{0.5}$, as reported by Cain *et al*. [17] and Vrancken *et al*. [20]. Nevertheless, Cain *et al*. [17] carried out stress relief anneal (650°C for four hours), as well as full anneal (890°C for 2 hours) heat treatments, and reported improvement of the fracture toughness properties that were similar to the values observed in this project.

## 5.4. THREE-POINT BEND FATIGUE CRACK INITIATION TESTING

For the fatigue crack initiation test, the stress relieved SLM Ti6Al4V samples were machined into rods (12 mm in diameter and 65 mm in length). The samples were polished to a fine surface finish to eliminate any surface defects prior to the X-ray CT scan and fatigue testing. Work by Wycisk *et al*. [45] showed that the inevitable presence of SLM process defects, both internally and externally, had a negative impact on a sample's fatigue behaviour, as potential early crack initiation sites were provided.

X-ray CT scans and fractographs were used to identify process defects that may have led to the sample's poor fatigue properties. Section 4.2.4 presented three-point bend fatigue tests carried on the stress relieved SLM Ti6Al4V fatigue samples. The first sample had been fabricated at 3 m/s and the second sample at 4 m/s. Both failed prematurely when a stress intensity of 1200 MPa was applied and were investigated for any defects that may have contributed to the poor performance. The two were compared with a second sample fabricated at 3 m/s that had satisfactory endurance (failed at 1400 MPa after completing 100 000 cycles without failure for 1200 MPa and 1300 MPa stress intensities).

The results presented in Figure 90 and Figure 91 indicate that Sample 2, fabricated at 3 m/s, had a good fatigue crack initiation resistance when compared to the rest of the samples, fabricated at 3 m/s and 4 m/s. With reference to Figure 71(b), Figure 72(d) and Figure 73(a), it became apparent that Sample 2 had a better porosity character as compared to the other samples and the largest pore (0.68 mm in diameter) was near the centre of the sample. The

homogenous porosity distribution was mainly dominated by internal pores and less surface pores.

Nevertheless, there were samples that showed poor fatigue crack initiation resistance. Sample 1, fabricated at 3 m/s, and Sample 2, fabricated at 4 m/s laser scan speed, both failed at low cycles at 1200 MPa stress intensity, as shown in Figures 90 and 91.

The 2D images taken from the stacked slices created during the X-ray CT scans in Figure 73 illustrate that most of the pores present in the fatigue specimens with poor properties were clustered and concentrated near the surface. The 3D reconstructed images on the right in Figure 71(c and h) validate the above observation, as it can be seen in both images that pores were close to the sample's surfaces and this may have contributed negatively to the sample's fatigue response. This is further supported by the images captured from the stacked slices depicted by figure 105.

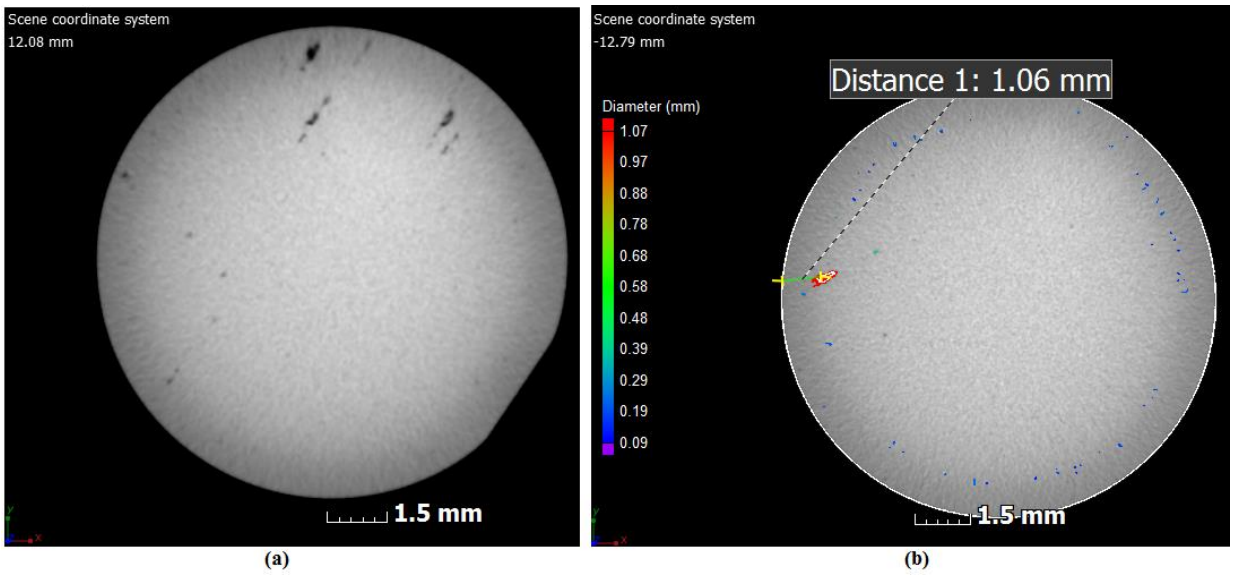


**Figure 105: The 2-D images captured from the stacked slices showing biggest pores near the surfaces: (a) sample 2 fabricated at 4 m/s; (b) sample 1 fabricated at 3 m/s.**

Moreover, both samples encountered heavy process malfunctions, whereby in one case the clustered pores were confined in a single build layer or successive build layers (Figure 71(h)) and in the second case there was a significant number of clustered micro pores distributed throughout the sample (Figure 71(c)).

Sterling *et al* [40] and Chastand *et al*. [44] showed that the size, distribution, location and shape of the pores present in the fatigue samples played a major role in a sample's fatigue properties. Some of their samples showed poor fatigue endurance owing to the surface defects present. The secondary electron SEM images taken on the fractured surfaces of both specimens showed

several process defects and indicated that the crack initiated on the surface of each sample as shown in Figure 102 and Figure 103.

According to the observations made in this project, the ability of a stress relieved SLM Ti6Al4V fatigue sample to have a good resistance to fatigue crack initiation will be dependent on the distribution and position of pores and other SLM defects within such a sample. Most of the samples fabricated by the SLM process had defects and pores, as the X-ray CT scans revealed, but the samples (except the samples discussed above) had good endurance as they reached 100 000 cycles to crack initiation without failing and failed only when the stress intensity was increased to 1300 MPa. The variable resistance to crack initiation among samples was brought about by variable porosities within the SLM processed samples.

## 5.5. MATERIAL CHARACTERISATION

### 5.5.1. The SLM microstructure

The influence of laser scan speed on the resulting microstructure was not investigated in this project. The microstructural morphology of the as-built and stress relieved SLM Ti6Al4V alloy looked the same and no particular difference could be detected. A series of micrographs were taken on the as-built Ti6Al4V samples, fabricated between 1.5 m/s to 4 m/s laser scan speed. A qualitative comparison of micrographs yielded no significant differences, as opposed to the findings of Song *et al*. [2] and Gong *et al*. [29]**,** who reported that increasing the laser scan speed while other process parameters were kept constant resulted in a finer microstructure. Most of the common defects reported in SLM samples were revealed using the light optical microscopy in bright field mode. Localised delamination, satellite particles, unmelted particles, as well as unmelted zones, were common in the samples produced for this project.

### 5.5.2. Density measurements

The density measurement for the SLM sample showed no particular relationship with the laser scan rate. In most instances the density measurement was constant throughout the samples, except for samples that were severely porous (For example, the as-built SLM Ti6Al4V tensile sample, fabricated at 2 m/s, which showed 92% densification). It has become apparent in this project that the density of a mechanical specimen cannot be used as a performance indicator for the SLM process, as the nature/form of pores and their location plays a crucial role in the mechanical response of such specimen. Moreover, the fact that Archimedes' principle is a volume-based method and does not quantify the porosity character of the specimens in question, makes it difficult to predict the mechanical properties of such specimen, as the measured density includes unmelted powder, which does not play any role during mechanical

tests. This was reported by Murr *et al*. [19] and Gong *et al*. [25], who demonstrated that the density observed in SLM parts was critical for the mechanical response/performance and that the porosity within the parts had a detrimental impact on the mechanical properties.

### 5.5.3. The X-ray CT scans

The Archimedes method is a non-destructive method that is inexpensive and quick. However, it offers a limited quantitative measuring capability as compared to the X-ray CT scan, since it can only be used to measure the global density of an SLM product. Nevertheless, a study conducted by Wits *et al*. [36] showed that the X-ray CT scan and the Archimedes method can compare well, even though there may be slight differences in measured densities. The X-ray CT scans in this project were carried out to determine the porosity characteristics of mechanical specimens, to compare the mechanical properties of the stress-relieved SLM Ti6Al4V samples with the porosity revealed by the X-ray scans. This was done since the as-built SLM Ti6al4V tensile samples showed scattered uniaxial tensile measurements, which, it was established, were due to the porosity character in individual samples. The X-ray CT scans carried out for both the uniaxial tensile tests and fatigue crack initiation tests specimens showed variable porosities throughout. However, there was no correlation between the laser scan speed and the porosity character of specimens, as the porosity was random and unpredictable at a given laser scan speed.

# 6. CONCLUSIONS

The relationship between the laser scan rate, density and measured mechanical properties could not be established, owing to the scattered results observed in this project. Furthermore, the following can be noted:

a) There is no correlation between the laser scan rate, densification and mechanical properties in the samples produced in this research. The extensive and highly varied porosity caused substantial scatter in the mechanical properties and this impeded any correlation to be made between the laser scan speed and the measured mechanical properties.

b) The density measurement by Archimedes' principle of the SLM Ti6Al4V alloy can be used only as a qualitative indication of SLM process optimisation. In most instances, the density measurement by Archimedes' principle of the SLM Ti6Al4V alloy included unfused powder particles that could not take part during mechanical tests, but exacerbate the SLM Ti6Al4V alloy's mechanical response.

c) The elongation and UTS of the SLM Ti6Al4V alloy depended significantly on the size, spatial distribution and location of pores within the product. Samples that showed good mechanical tensile properties were found to possess minor process defects, as pores were seen scattered over the samples' gauge lengths. On the other hand, samples with poor mechanical properties had both clustered pores and extremely large pores closer to one another and/or on the sample's surface.

d) The largest pore within the SLM Ti6Al4V alloy would have been significant only if such a pore is closer to either the surface of the material or to clustered micro pores. In some of the mechanical test results, the largest pore was isolated and was seen not to have played any role in the sample's response to mechanical tests, but some other mechanisms had taken place, such as micro pores coalescence.

e) The presence of SLM process defects, such as pores and cracks, exacerbated the fatigue response of SLM samples. The X-ray CT scans revealed that samples with poor fatigue properties had both clustered pores and large pores close enough to the samples' surface and could have acted as surface pores/cracks.

f) With reference to the as-built SLM Ti6Al4V uniaxial tensile samples fabricated at 2.5 m/s, which showed substantial increase in UTS with a drop in elongation, it was clear

by studying the fractured surfaces that the fracture mechanism was mainly inherent metal brittle fracture, which could only happen if there was embrittlement during fabrication.

# 7. RECOMMENDATIONS

As a result of the findings and conclusions as presented in previous sections, the following recommendations are made:

- There is a great deal of SLM process inconsistency and irreproducibility in samples produced using the same process parameters. This calls for a more controlled and optimised process to produce reliable samples with better microstructural integrity.

- The role of porosity in the mechanical properties of SLM Ti6Al4V can be further quantitatively studied using the finite elements analysis (FEA), to investigate the amount of stress needed for crack initiation, especially on the largest pore, as revealed by the X-ray CT scans.

# 8. BIBLIOGRAPHY

[1]. B. Ross, "Investigating Mechanical Failures". Chapman and Hall First edition (1995). Pages 34-36, 54-63.

[2]. W.T. Becker, University of Tennessee, Emeritus; S. Lampman, ASM International. "Fracture Appearance and Mechanisms of Deformation and Fracture".

[3]. R. W. K Honeycombe, "The plastic deformation of metals". Edward Arnold Publishers (1968). Pages 427-457 (Chapter 15 – Fracture).

[4]. B. A. Bilby, K. J. Miller and J. R. Willis. "Fundamentals of deformation and fracture". International union of theoretical and applied mechanics, Elshelby Memorial Symposium, Sheffield (April 1984). Cambridge University Press (1985). Pages 233 – 236.

[5]. L. Li. "Repair of directionally solidified super-alloy GTD-111 by laser-engineered net shaping" Journal of Material Science (2006) 41:7886–7893.

[6]. M.G. Moletsane, P. Krakhmalev, N. Kazantseva, A. Du Plessis, I. Yadroitsava & I. Yadroitsev. "TENSILE PROPERTIES AND MICROSTRUCTURE OF DIRECT METAL LASER-SINTERED TI6AL4V (ELI) ALLOY". South African Journal of Industrial Engineering November 2016 Vol 27(3) Special Edition, pp 110-121.

[7]. A. Du Plessis, S. Gerhard le Roux, G. Booysen, Johan Els. "Quality control of a laser additive manufactured medical implant by X-ray tomography". 3D printing and additive manufacturing, volume 3, 2016. Mary Ann Liebert, Inc.

[8]. H.E. Boyer. "Atlas of Fatigue Curves, Fatigue Testing". Copyright © 1986 ASM International®, www.asminternational.org.

[9]. D. J. Wulpi, FASM. "General procedures for failure analysis". A lesson from principle of failure analysis. ASM international & MEI. Course 13, Test 1.

[10]. D. J. Wulpi, FASM. "Ductile and brittle fractures, fatigue failures". A lesson from principle of failure analysis. ASM international & MEI. Course 13, Test 3 and Test4.

# 9. REFERENCES


[1]. I. Yadroitsev, I. Smurov. "Selective laser melting technology: from the single laser melted track stability to 3D parts of complex shape". Physics Procedia 5 (2010) 551–560.

[2]. B. Song, S. Dong, B. Zhang, H. Liao, C. Coddet. "Effects of processing parameters on microstructure and mechanical property of selective laser melted Ti6Al4V". Materials and Design 35 (2012) 120–125.

[3]. L. Thijs, F. Verhaeghe, T. Craeghs, J. Van Humbeeck, J.Kruth. "A study of the microstructural evolution during selective laser melting of Ti–6Al–4V". Acta Materialia 58 (2010) 3303–3312.

[4]. B. Vrancken, L. Thijs, J.Kruth, J. Van Humbeeck. "Heat treatment of Ti6Al4V produced by Selective Laser Melting: Microstructure and mechanical properties". Journal of Alloys and Compounds 541 (2012) 177–185.

[5]. P. Edwards, M.Ramulu. "Fatigue performance evaluation of selective laser melted Ti–6Al–4V". Materials Science & Engineering A598 (2014)327–337.

[6]. H. Gong, H. Gu, K. Zeng, J.J.S. Dilip, D. Pal, B. Stucker, D. Christiansen, J. Beuth, J. J. Lewandowski. "Melt Pool Characterization for Selective Laser Melting of Ti-6Al-4V Pre-alloyed Powder". Additive Manufacturing 1–4 (2014) 256-267.

[7]. ASTM-International, ASTM Standard F2792-12a: standard terminology for additive manufacturing technologies, (2012).

[8]. R. Wauthle, B. Vrancken, B. Beynaerts, K. Jorissen, J. Schrooten, J.Kruth, J. Van Humbeeck. "Effects of build orientation and heat treatment on the microstructure and mechanical properties of selective laser melted Ti6Al4V lattice structures". Additive Manufacturing 5 (2015) 77–84.

[9]. H. Galarraga, D. A. Lados, R. R. Dehoff, M. M. Kirka,P. Nandwana. "Effects of the microstructure and porosity on properties of Ti-6Al-4VELI alloy fabricated by electron beam melting (EBM)". Additive Manufacturing 10 (2016) 47–57.

[10]. A. J. Pinkerton. "Lasers in additive manufacturing". Optics & Laser Technology. 78 (2016) 25–32.

[11]. B. A. Szost, S. Terzi, F. Martina, D. Boisselier, A. Prytuliak,T. Pirling, M. Hofmann, D. J. Jarvis. "A comparative study of additive manufacturing techniques: Residual stress and microstructural analysis of CLAD and WAAM printed Ti–6Al–4V components". Materials and Design 89 (2016) 559–567.

[12]. L. E. Murr, E Martinez, K N. Amato, S. M. Gaytan, J Hernandez, D. A. Ramirez, P. W. Shindo, F. Medina, R. B. Wicker. "Fabrication of Metal and Alloy Components by Additive Manufacturing: Examples of 3D Materials Science". Journal of Materials Research and Technology. Volume 1(1) (2012) 42 – 54.

[13]. S. Leuders, M. Thöne, A. Riemer, T. Niendorf, T. Tröster, H.A. Richard, H.J. Maier. "On the mechanical behaviour of titanium alloy TiAl6V4 manufactured by selective laser melting: Fatigue resistance and crack growth performance". International Journal of Fatigue 48 (2013) 300–307.

[14]. L E. Murr, S M. Gaytan, D. A. Ramirez, E. Martinez, J. Hernandez, Krista N. Amato, P. W. Shindo, F. R. Medina and R. B. Wicker. "Metal Fabrication by Additive Manufacturing Using Laser and Electron Beam Melting Technologies". J. Mater. Sci. Technol., 2012, 28(1), 1–14.

[15]. I. Yadroitsev, P. Krakhmalev, I. Yadroitsava. "Selective laser melting of Ti6Al4V alloy for biomedical applications: Temperature monitoring and microstructural evolution". Journal of Alloys and Compounds 583 (2014) 404–409.

[16]. ASTM international, ASTM F1472-14 Standard Specification for Wrought Titanium-6Aluminum-4Vanadium Alloy for Surgical Implant Applications (UNS R56400). (2014)

[17]. V. Cain, L. Thijs, J. Van Humbeeck, B. Van Hooreweder, R. Knutsen. "Crack propagation and fracture toughness of Ti6Al4V alloy produced by selective laser melting". Additive Manufacturing 5 (2015) 68–76.

[18]. Askeland, Fulay, Wright and Balani, "The science and engineering of materials", 6th edition (Cengage Learning), (2010) pages 558 – 560.

[19]. L.E. Murr, S.A. Quinones, S.M. Gaytan, M.I. Lopez, A. Rodela, E.Y. Martinez, D.H. Hernandez, E. Martinez, F. Medina, R.B. Wicker. "Microstructure and mechanical behavior of Ti–6Al–4V produced by rapid-layer manufacturing, for biomedical applications". Journal of the mechanical behaviour of biomedical materials (2009) 20 – 32.

[20]. B. Vrancken, V. Cain, R. Knutsen and J. Van Humbeeck. "Residual stress via the contour method in compact tension specimens produced via selective laser melting". Scripta Materialia 87 (2014) 29–32.

[21]. M. Seifi, A. Salem, J. Beuth, O. Harrysson, J. J. Lewandowski. "Overview of Materials Qualification Needs for Metal Additive Manufacturing". JOM, Vol. 68, No. 3, 2016.DOI: 10.1007/s11837-015-1810-0. 2016 The Minerals, Metals & Materials Society.

[22]. M.Speirs, J.Van.Humbeeck, J.Schrooten, J.Luyten, J.P.Kruth. "The effect of pore geometry on the mechanical properties of selective laser melted Ti-13Nb-13Zr scaffolds". Procedia CIRP 5 (2013) 79 – 82.

[23]. Prof. Dr. Ir. J.P. Kruth, Ir. P. Mercelis, Prof. Dr. Ir. L. Froyen, Ir. Marleen Rombouts. "Binding Mechanisms in Selective Laser Sintering and Selective Laser Melting". Available at: http://edge.rit.edu/edge/P10551/public/SFF/SFF%202004%20Proceedings/SFF%20Papers%202004/06-Kruth.pdf
Accessed on the: 10th March 2016.

[24]. Dr. W. N. Watson, US DEPARTMENT OF ENERGY. "In the OSTI Collections: 3-D Printing and Other Additive Manufacturing Technologies". Available at: http://www.osti.gov/home/osti-collections-3-d-printing-and-other-additive-manufacturing-technologies
Accessed on the: 10th March 2016

[25]. H. Gong, K. Rafi, H. Guc, G.D. Janaki Ramd, T. Starr, B. Stucker. "Influence of defects on mechanical properties of Ti–6Al–4 V components produced by selective laser melting and electron beam melting". Materials and Design 86 (2015) 545–554.

[26]. B. Van Hooreweder, D. Moens, R. Boonen, J. Kruth and P. Sas. "Analysis of Fracture Toughness and Crack Propagation of Ti6Al4V Produced by Selective Laser Melting". Advanced engineering materials 2012, 14, (No. 1-2) 92 – 97.

[27]. W. Shifeng, L. Shuai, W. Qingsong, C. Yan, Z. Sheng, S. Yusheng. "Effect of molten pool boundaries on the mechanical properties of selective laser melting parts". Journal of Materials Processing Technology 214 (2014) 2660–2667.

[28]. F. Bartolomeu, S.Faria, O.Carvalho, E.Pinto , N.Alves, F.S.Silva, G.Miranda. "Predictive models for physical and mechanical properties of Ti6Al4V produced by Selective Laser Melting". Materials Science & Engineering A663 (2016)181–192.

[29]. H. Gong, K. Rafi, H. Gu, T. Starr, B. Stucker. "Analysis of defect generation in Ti–6Al–4V parts made using powder bed fusion additive manufacturing processes". Additive Manufacturing 1–4 (2014) 87–98.

[30]. J. Sun, Y. Yang, D. Wang. "Parametric optimization of selective laser melting for forming Ti6Al4V samples by Taguchi method". Optics & Laser Technology 49 (2013) 118–124.

[31]. G. Kasperovich, J. Haubrich, J. Gussone, G. Requena. "Correlation between porosity and processing parameters in TiAl6V4 produced by selective laser melting". Materials and Design 105 (2016) 160–170.

[32]. P.A. Kobryn, E.H. Moore and S.L. Semiatin. "The effect of laser power and traverse speed on microstructure, porosity, and build height in laser-deposited Ti-6Al-4V". Scripta mater. 43 (2000) 299–305.

[33]. B. Song, S. Dong, S. Deng, H. Liao, C. Coddet. "Microstructure and tensile properties of iron parts fabricated by selective laser melting". Optics & Laser Technology 56 (2014) 451–460.

[34]. B. Ferrara, L. Mullena, E. Jonesb, R. Stampb, C.J. Sutcliffe. "Gas flow effects on selective laser melting (SLM) manufacturing performance". Journal of Materials Processing Technology 212 (2012) 355– 364.

[35]. L. Facchini, E. Magalini, P. Robotti, A. Molinari, S. Ho¨ges and K. Wissenbach. "Ductility of a Ti-6Al-4V alloy produced by selective laser melting of pre-alloyed powders". Rapid Prototyping Journal 16/6 (2010) 450–459.

[36]. W. W. Wits, S. Carmignato, F. Zanini, T. H.J. Vaneker. "Porosity testing methods for the quality assessment of selective laser melted parts". CIRP Annals - Manufacturing Technology 65 (2016) 201–204.

[37]. J.P. Kruth, L. Froyen, J. Van Vaerenbergh, P. Mercelis, M. Rombouts, B. Lauwers. "Selective laser melting of iron-based powder". Journal of Materials Processing Technology 149 (2004) 616–622.

[38]. M. Xia, D. Gu, G. Yu, D. Dai, H. Chen, Q. Shi. "Porosity evolution and its thermodynamic mechanism of randomly packed powder-bed during selective laser melting of Inconel 718 alloy". International Journal of Machine Tools & Manufacture 116 (2017) 96–106.

[39]. D. Gu, Y.Hagedorn, W. Meiners, G. Meng, R. Joa˜o Santos Batista, K. Wissenbach, R. Poprawe. "Densification behavior, microstructure evolution, and wear performance of selective laser melting processed commercially pure titanium". Acta Materialia 60 (2012) 3849–3860.

[40]. A. Sterling, N. Shamsaei, B. Torries, S. M. Thompson. "Fatigue Behaviour of Additively Manufactured Ti-6Al-4V". Procedia Engineering 133 (2015) 576 – 589.

[41]. C. de Formanoir, S. Michotte, O. Rigo, L. Germain, S. Godet. "Electron beam melted Ti–6Al–4V: Microstructure, texture and mechanical behavior of the as-built and heat-treated material". Materials Science & Engineering A652 (2016) 105–119.

[42]. R. Casati, J. Lemke, M. Vedani. "Microstructure and Fracture Behavior of 316L Austenitic Stainless Steel Produced by Selective Laser Melting". Journal of Materials Science & Technology 32 (2016) 738–744.

[43]. P. Krakhmalev, G. Fredriksson, I. Yadroitsava, N. Kazantseva, A. du Plessis, I. Yadroitsev. "Deformation behaviour and microstructure of Ti6Al4V manufactured by SLM". Physics Procedia 83 (2016) 778 – 788.

[44]. V. Chastand, A. Tezenas, Y. Cadoret, P. Quaegebeur, W. Maia, E. Charkaluk. "Fatigue characterisation of Titanium Ti-6Al-4V samples produced by Additive Manufacturing". Procedia Structural Integrity 2 (2016) 3168 – 3176.

[45]. E. Wycisk, A. Solbach, S. Siddique, D. Herzog, F. Walther, C. Emmelmann. "Effects of Defects in Laser Additive Manufactured Ti-6Al-4V on Fatigue Properties". Physics Procedia 56 (2014) 371 – 378.

[46]. T. M. Mower, M. J. Long. "Mechanical behavior of additive manufactured, powder-bed laser-fused materials". Materials Science & Engineering A651 (2016) 198–213.

[47]. I. Maskery, N.T. Aboulkhair, M.R. Corfield, C. Tuck, A.T. Clare, R.K. Leach, R.D.Wildman, I.A. Ashcroft, R.J.M. Hague. "Quantification and characterisation of porosity in selectively laser melted Al–Si10–Mg using X-ray computed tomography". Materials Characterization 111 (2016) 193–204.

[48]. P. Hermanek, S. Carmignato. "Reference object for evaluating the accuracy of porosity measurements by X-ray computed tomography". Case Studies in Nondestructive Testing and Evaluation 6 (2016) 122–127.

[49]. S. Tammas-Williams, H. Zhao, F. Léonard, F. Derguti, I. Todd, P.B. Prangnell. "XCT analysis of the influence of melt strategies on defect population in Ti–6Al–4V components manufactured by Selective Electron Beam Melting". Materials Characterization 102 (2015) 47–61.

[50]. G. Ziółkowski , E. Chlebus, P. Szymczyk, J. Kurzac. "Application of X-ray CT method for discontinuity and porosity detection in 316L stainless steel parts produced with SLM technology". Archives of civil and mechanical engineering14 (2014) 608 – 614.

[51]. S.D. Zhang, W.L. Zhang, S.G. Wang, X.J. Gu, J.Q. Wang. "Characterisation of three-dimensional porosity in Fe-based amorphous coating and its correlation with corrosion behaviour". Corrosion Science 93 (2015) 211–221.

[52]. M. Wicke, M. Luetje, I. Bacaicoa, A. Brueckner-Foit. "Characterisation of casting pores in a Fe-rich Al-Si-Cu alloys by micro tomography and finite element analysis". Procedia Structural Integrity 2 (2016) 2643 – 2649.

[53]. A.Niklas, S.Orden, A.Bakedano, M.daSilva, E.Nogués, A.I.Fernández-Calvo. "Effect of solution heat treatment on gas porosity and mechanical properties in a die cast step test part manufactured with a new AlSi10MnMg (Fe) secondary alloy". Materials Science & Engineering A667 (2016) 376–382.

[54]. P. Kumar, K.S. Ravi Chandran, F. Cao, M. Koopman, and Z. Zak Fang, "The Nature of Tensile Ductility as Controlled by Extreme-Sized Pores in Powder Metallurgy Ti-6Al-4V Alloy". Metallurgical And Materials Transactions A Volume 47a, May 2016—2151.

[55]. T. Taxer, C. Schwarz, W. Smarsly, E. Werner. "A finite element approach to study the influence of cast pores on the mechanical properties of the Ni-base alloy MAR-M247". Materials Science & Engineering A575 (2013) 144–151.

[56]. M. Benedetti, M. Cazzolli, V. Fontanari, M. Leoni. "Fatigue limit of Ti6Al4V alloy produced by Selective Laser Sintering". Procedia Structural Integrity 2 (2016) 3158 – 3167.

[57]. L. Wang, N. Limodin, A. El Bartali, J. Witz, R Seghir, J. Buffiere, E. Charkaluk. "Influence of pores on crack initiation in monotonic tensile and cyclic loadings in lost foam casting A319 alloy by using 3D in-situ analysis". Materials Science & Engineering A673 (2016) 362–372.

[58]. G. Lütjering. "Influence of processing on microstructure and mechanical properties of (α + β) titanium alloys". Materials Science and Engineering A243 (1998) 32–45.

[59]. M.Simonelli, Y.Y.Tse, C.Tuck. "Effect of the build orientation on the mechanical properties and fracture modes of SLM Ti–6Al–4V". Materials Science &Engineering A616 (2014)1–11.

[60]. U. Tradowsky, J. White, R. M. Ward, N. Read, W. Reimers, M.M. Attallah. "Selective laser melting of AlSi10Mg: Influence of post-processing on the microstructural and tensile properties development". Materials and Design 105 (2016) 212–222.

[61]. A. Du Plessis, S. Gerhard le Roux, A. Guelpa. The CT Scanner Facility at Stellenbosch University: An open access X-ray computed tomography laboratory. Nuclear Instruments and Methods in Physics Research B 384 (2016) 42 – 49.

[62]. Abhay K. Jha, K. Sreekumar. "Effect of pores and acicular eutectic silicon particles on the performance of Al–Si–Mg (AS7G03) casting". Engineering Failure Analysis 16 (2009) 2433–2439.

# 10. APPENDICES

## 62.1. APPENDIX A: MECHANICAL TESTS

### 62.1.1. Fatigue crack growth rate

**Table 17: Cyclic loading conditions used for SLM Ti6Al4V FCGR samples**

| Load Force (kN) | Frequency (Hz) | Max load (kN) | Min load (kN) | Mean load (kN) | Amplitude (kN) | Frequency (Hz) |
|---|---|---|---|---|---|---|
| 2,925 | 27998,208 | 3,250 | 0,325 | 1,788 | 1,463 | 7 |

**Table 18: The crack growth rate and cyclic stress intensity amplitude for Ti6Al4V sample (3.5 m/s)**

| Number of Cycles, N | Crack Length, a | Actual Crack Length | Crack Growth Rate, da/dN (m/cycle) | $P_{max}$, kN | $P_{min}$, kN | Cyclic Stress intensity amplitude ΔK, (Mpa.$m^{0.5}$) |
|---|---|---|---|---|---|---|
| 0 | 0 | 4,7 | #DIV/0! | 3,25 | 0,325 | 9,39490343 |
| 34390 | 1 | 5,7 | 2,91E-08 | 3,25 | 0,325 | 10,42030719 |
| 37148 | 1,25 | 5,95 | 9,06E-08 | 3,25 | 0,325 | 10,67904834 |
| 39260 | 1,5 | 6,2 | 1,18E-07 | 3,25 | 0,325 | 10,93907737 |
| 40439 | 1,75 | 6,45 | 2,12E-07 | 3,25 | 0,325 | 11,20057517 |
| 42239 | 2 | 6,7 | 1,39E-07 | 3,25 | 0,325 | 11,46373185 |
| 44859 | 2,25 | 6,95 | 9,54E-08 | 3,25 | 0,325 | 11,72874729 |
| 46378 | 2,5 | 7,2 | 1,65E-07 | 3,25 | 0,325 | 11,99583158 |
| 47756 | 2,75 | 7,45 | 1,81E-07 | 3,25 | 0,325 | 12,26520559 |
| 49261 | 3 | 7,7 | 1,66E-07 | 3,25 | 0,325 | 12,53710156 |
| 51071 | 3,25 | 7,95 | 1,38E-07 | 3,25 | 0,325 | 12,81176367 |
| 51710 | 3,5 | 8,2 | 3,91E-07 | 3,25 | 0,325 | 13,08944877 |
| 52679 | 3,75 | 8,45 | 2,58E-07 | 3,25 | 0,325 | 13,37042702 |
| 53442 | 4 | 8,7 | 3,28E-07 | 3,25 | 0,325 | 13,65498266 |
| 55210 | 4,25 | 8,95 | 1,41E-07 | 3,25 | 0,325 | 13,94341485 |
| 55959 | 4,5 | 9,2 | 3,34E-07 | 3,25 | 0,325 | 14,23603852 |
| 56740 | 4,75 | 9,45 | 3,20E-07 | 3,25 | 0,325 | 14,53318529 |
| 57390 | 5 | 9,7 | 3,85E-07 | 3,25 | 0,325 | 14,83520447 |
| 58242 | 5,25 | 9,95 | 2,93E-07 | 3,25 | 0,325 | 15,14246416 |
| 58920 | 5,5 | 10,2 | 3,69E-07 | 3,25 | 0,325 | 15,45535239 |
| 59477 | 5,75 | 10,45 | 4,49E-07 | 3,25 | 0,325 | 15,77427836 |
| 60339 | 6 | 10,7 | 2,90E-07 | 3,25 | 0,325 | 16,0996738 |
| 60755 | 6,25 | 10,95 | 6,01E-07 | 3,25 | 0,325 | 16,43199439 |
| 61309 | 6,5 | 11,2 | 4,51E-07 | 3,25 | 0,325 | 16,77172138 |
| 61792 | 6,75 | 11,45 | 5,18E-07 | 3,25 | 0,325 | 17,11936322 |
| 62431 | 7 | 11,7 | 3,91E-07 | 3,25 | 0,325 | 17,47545741 |
| 62839 | 7,25 | 11,95 | 6,13E-07 | 3,25 | 0,325 | 17,84057251 |
| 63340 | 7,5 | 12,2 | 4,99E-07 | 3,25 | 0,325 | 18,21531024 |
| 64060 | 7,75 | 12,45 | 3,47E-07 | 3,25 | 0,325 | 18,60030787 |
| 64372 | 8 | 12,7 | 8,01E-07 | 3,25 | 0,325 | 18,99624069 |

| | | | | | | |
|---|---|---|---|---|---|---|
| 64799 | 8,25 | 12,95 | 5,85E-07 | 3,25 | 0,325 | 19,40382482 |
| 65139 | 8,5 | 13,2 | 7,35E-07 | 3,25 | 0,325 | 19,82382017 |
| 65299 | 8,75 | 13,45 | 1,56E-06 | 3,25 | 0,325 | 20,25703375 |
| 65487 | 9 | 13,7 | 1,33E-06 | 3,25 | 0,325 | 20,7043232 |
| 65658 | 9,25 | 13,95 | 1,46E-06 | 3,25 | 0,325 | 21,16660073 |
| 65849 | 9,5 | 14,2 | 1,31E-06 | 3,25 | 0,325 | 21,64483738 |
| 65995 | 9,75 | 14,45 | 1,71E-06 | 3,25 | 0,325 | 22,14006766 |
| 66080 | 10 | 14,7 | 2,94E-06 | 3,25 | 0,325 | 22,65339476 |
| 66155 | 10,25 | 14,95 | 3,33E-06 | 3,25 | 0,325 | 23,18599611 |
| 66222 | 10,5 | 15,2 | 3,73E-06 | 3,25 | 0,325 | 23,73912966 |
| 66360 | 10,75 | 15,45 | 1,81E-06 | 3,25 | 0,325 | 24,31414063 |

### 62.1.2. Fracture toughness

As mentioned in previous sections, fracture toughness testing involves two stages, namely, pre-cracking stage up to a predetermined crack length followed by force increment until the specimen fractures. The two tables (**Table 16 and Table 17**) serve as examples of the data captured during the pre-cracking stage.

**Table 19: Data capture during SLM Ti6Al4V sample (stress relieved) fabricated at 3 m/s.**

| Number of Cycles, N | Crack Length, a | Actual Crack Length | Crack Growth Rate, da/dN (m/cycle) | $P_{max}$, kN | $P_{min}$, kN | Cyclic Stress intensity amplitude ΔK, (Mpa.$m^{0.5}$) |
|---|---|---|---|---|---|---|
| 0 | 0 | 4,7 | #DIV/0! | 8,7 | 0,87 | 16,32883322 |
| 16500 | 0,5 | 5,2 | 3,03E-08 | 8,7 | 0,87 | 17,33545394 |
| 19340 | 1 | 5,7 | 1,76E-07 | 8,7 | 0,87 | 18,35881468 |
| 24670 | 1,5 | 6,2 | 9,38E-08 | 8,7 | 0,87 | 19,40406034 |
| 28460 | 2 | 6,7 | 1,32E-07 | 8,7 | 0,87 | 20,47702644 |
| 29100 | 2,5 | 7,2 | 7,81E-07 | 8,7 | 0,87 | 21,58433825 |
| 30850 | 3 | 7,7 | 2,86E-07 | 8,7 | 0,87 | 22,73352837 |
| 33670 | 3,5 | 8,2 | 1,77E-07 | 8,7 | 0,87 | 23,93317692 |
| 35890 | 4 | 8,7 | 2,25E-07 | 8,7 | 0,87 | 25,19307941 |
| 36870 | 4,5 | 9,2 | 5,10E-07 | 8,7 | 0,87 | 26,5244491 |
| 38176 | 5 | 9,7 | 3,83E-07 | 8,7 | 0,87 | 27,94016208 |
| 38900 | 5,5 | 10,2 | 6,91E-07 | 8,7 | 0,87 | 29,45505617 |
| 40000 | 6 | 10,7 | 4,55E-07 | 8,7 | 0,87 | 31,08629767 |
| 40450 | 6,5 | 11,2 | 1,11E-06 | 8,7 | 0,87 | 32,85383449 |
| 40887 | 7 | 11,7 | 1,14E-06 | 8,7 | 0,87 | 34,78096027 |
| Crack initiation at 7000 cycles | | | | | | |

**Table 20: Data capture during SLM Ti6Al4V sample (stress relieved) fabricated at 3.5 m/s.**

| Number of Cycles, N | Crack Length, a | Actual Crack Length | Crack Growth Rate, da/dN (m/cycle) | $P_{max}$, kN | $P_{min}$, kN | Cyclic Stress intensity amplitude ΔK, (Mpa.$m^{0.5}$) |
|---|---|---|---|---|---|---|
| 0 | 0 | 4,7 | #DIV/0! | 8,7 | 0,87 | 16,32883322 |
| 23340 | 0,5 | 5,2 | 2,14E-08 | 8,7 | 0,87 | 17,33545394 |
| 25980 | 1 | 5,7 | 1,89E-07 | 8,7 | 0,87 | 18,35881468 |
| 30035 | 1,5 | 6,2 | 1,23E-07 | 8,7 | 0,87 | 19,40406034 |
| 32760 | 2 | 6,7 | 1,83E-07 | 8,7 | 0,87 | 20,47702644 |
| 35760 | 2,5 | 7,2 | 1,67E-07 | 8,7 | 0,87 | 21,58433825 |
| 37240 | 3 | 7,7 | 3,38E-07 | 8,7 | 0,87 | 22,73352837 |
| 39197 | 3,5 | 8,2 | 2,55E-07 | 8,7 | 0,87 | 23,93317692 |
| 39900 | 4 | 8,7 | 7,11E-07 | 8,7 | 0,87 | 25,19307941 |
| 40800 | 4,5 | 9,2 | 5,56E-07 | 8,7 | 0,87 | 26,5244491 |
| 41250 | 5 | 9,7 | 1,11E-06 | 8,7 | 0,87 | 27,94016208 |
| 41870 | 5,5 | 10,2 | 8,06E-07 | 8,7 | 0,87 | 29,45505617 |
| 42180 | 6 | 10,7 | 1,61E-06 | 8,7 | 0,87 | 31,08629767 |
| 42230 | 6,5 | 11,2 | 1,00E-05 | 8,7 | 0,87 | 32,85383449 |
| Premature Fracture | 7 | 11,7 | #VALUE! | 8,7 | 0,87 | 34,78096027 |
| Crack initiation at 19000 cycles followed by rapid propagation after 42230 cycles and premature fracture | | | | | | |